Chemically selective microspectroscopy with broadband shaped femtosecond laser pulses

Dissertation
zur Erlangung des Doktorgrads
der Naturwissenschaften
(Dr. rer. nat.)

Bernhard von Vacano

Fachbereich Chemie
Philipps-Universität Marburg

Marburg an der Lahn 2008

Chemically selective microspectroscopy with broadband shaped femtosecond laser pulses

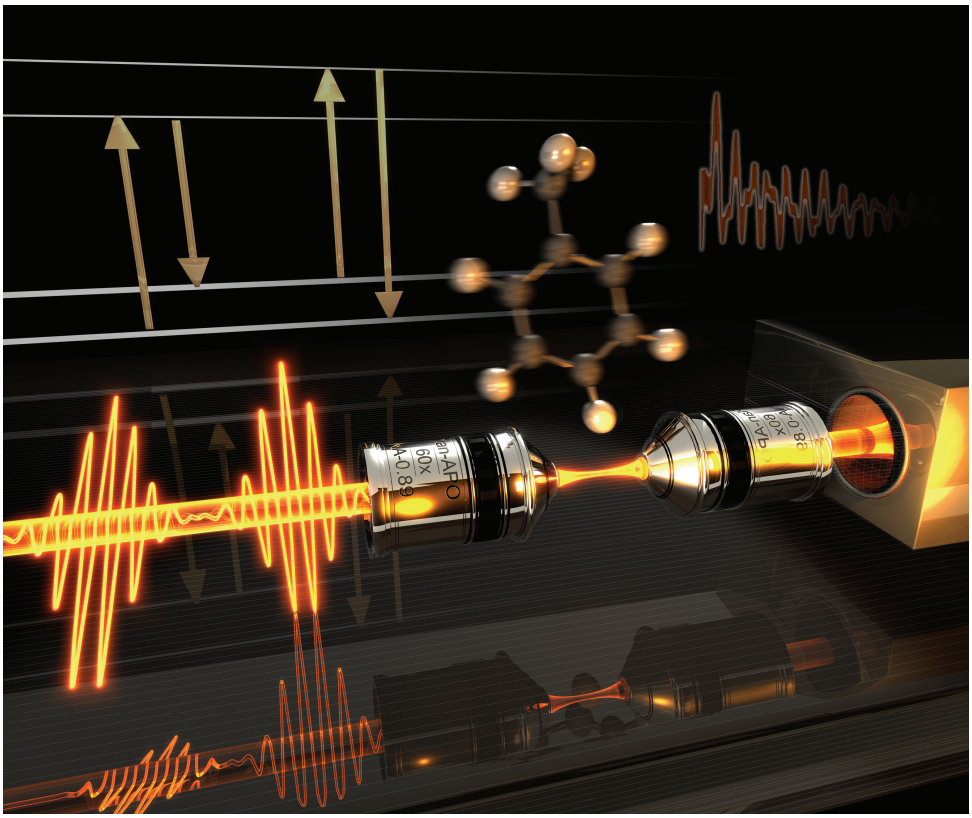

Dissertation
zur Erlangung des Doktorgrads
der Naturwissenschaften
(Dr. rer. nat.)

Bernhard von Vacano

Fachbereich Chemie
Philipps-Universität Marburg

Marburg an der Lahn 2008

Erster Gutachter: Prof. Dr. Marcus Motzkus (FB Chemie)
Zweiter Gutachter: Prof. Dr. Ulrich Höfer (FB Physik)

Tag der mündlichen Prüfung : 03.03.2008
Weitere Prüfer: Prof. Dr. Norbert Hampp und Prof. Dr. Andreas Seubert (beide FB Chemie)

Abstract

This doctoral thesis presents a new, unified approach to nonlinear microspectroscopy employing tailored broadband femtosecond laser radiation. The key concept is to functionalize the femtosecond excitation in order to implement a series of multiphoton spectroscopy techniques, especially for microscopic imaging. The most important application is coherent anti-*Stokes Raman* scattering (CARS) spectroscopy, which allows chemical identification of untreated samples in microscopy due to their characteristic vibrational spectra. The presented approach allows huge experimental simplifications of CARS, schemes for very rapid spectral acquisition and determination of the chemical composition (based on the quantitative analysis of entangled multiplex spectra by evolutionary algorithm fitting), as well as new methods for microscopic CARS measurements in the time-domain, resolving molecular vibrations temporally. This is possible, because coherent control of the signal generation is applied, manipulating the quantum mechanical processes of the underlying light-matter interaction by shaping the excitation light field in phase, amplitude and polarization. Thus, spectroscopic function and even molecular control is imprinted on the excitation pulses. It is shown that this idea of functional "photonic integration" can be pursued even further by incorporating an interferometric detection scheme in the same pulses without any additional optical elements in the experimental setup, drastically improving the measurement sensitivity by more than three orders of magnitude. In addition to these novel conceptual findings, new technological developments have been invented and pushed forward. These include the generation of ultrabroadband femtosecond radiation in microstructured optical fibres and its precise phase measurement and management, which is a prerequisite for coherent control. In this context, a new pulse-shaper enabled variant of SPIDER was developed, allowing very rapid compression in collinear beam geometry in the microscope. Employing the developed set of tools and concepts, application examples are given ranging from quantitative chemical imaging of polymer blend samples, to the chemical identification of potentially hazardous powdery substances and the microanalytical sensing of the chemical composition in a microfluidic device.

Kurzzusammenfassung

In dieser Arbeit wird ein neuer, umfassender Ansatz für nichtlineare Spektroskopie im Fokus eines Mikroskops vorgestellt. Dabei wird Laserstrahlung mit gezielt geformten Femtosekunden-Impulsen verwendet. Das grundlegende Konzept ist die Funktionalisierung der Femtosekunden-Laseranregung, um eine Reihe von Multiphotonen-Spektroskopie-Methoden in ein und demselben Aufbau umzusetzen, und für die mikroskopische Bildgebung verfügbar zu machen. Die wichtigste Methode dabei ist kohärente anti-*Stokes Raman* Streuung (CARS), die das Vibrationsspektrum einer Probe nutzt, um sie chemisch spezifisch zu identifizieren. Der hier verfolgte Ansatz stellt eine immense Vereinfachung von CARS-Spektroskopie dar. Dabei wird zum einen ein Schema zur sehr rasche Spektrenaufnahme und quantitativen Analyse komplexer Mehrkomponenten-Spektren vorgestellt, das auf der Anpassung eines physikalischen Modells mittels eines evolutionären Algorithmus basiert. Zudem werden neue Methoden entwickelt, die zum Beispiel CARS-Messungen in die Zeitdomäne verlagern und in der Tat die Molekülschwingungen zeitaufgelöst verfolgen. Das wird nur dadurch möglich, dass durch kohärente Kontrolle mit in Phase, Amplitude und Polarisation geformten Anregungsimpulsen die Licht-Materie-Wechselwirkung auf quantenmechanischem Niveau gezielt beeinflusst wird. Auf diese Weise können die Laserimpulse selbst mit spektroskopischen Funktionen versehen werden. Es wird gezeigt, dass diese funktionale „photonische Integration“ noch weiter getrieben werden kann, indem auch interferometrische Detektion ohne weitere optische Bauelemente durch Formung der Anregungsimpulse verwirklicht wird. Dies vereinfacht Experimente deutlich und erhöht gleichzeitig die Empfindlichkeit von CARS drastisch um mehr als drei Größenordnungen. Zusätzlich zu diesen neu entwickelten Konzepten werden für die Verwirklichung notwendige technische Neuentwicklungen vorgestellt, darunter die Erzeugung von Breitband-Femtosekunden-Impulsen in mikrostrukturierten Fasern und deren genaue Charakterisierung und Kompression durch eine neue, Impulsformer-basierte Variante der SPIDER-Methode. In der Anwendung der neuen Spektroskopietechniken werden Beispiele gezeigt, die von der quantitativen chemischen Bildgebung von Polymer-Blends, über die selektive Detektion von Markermolekülen für biologische Kampfstoffe (Anthrax) bis zu ersten analytischen Anwendungen bei der Messung chemischer Zusammensetzungen in einer mikrofludischen Zelle.

Eine ausführliche Zusammenfassung in deutscher Sprache findet sich in Kapitel 8 am Ende der Arbeit.

Diese Arbeit wurde durch ein Promotionsstipendium des „Fonds der chemischen Industrie“ gefördert.

List of publications in the context of this thesis

In peer-reviewed international journals:

- "Single-beam CARS spectroscopy applied to low-wavenumber vibrational modes", B. von Vacano, W. Wohlleben and M. Motzkus, J. Raman Spectroscopy, 37 (2006) 404-410.
- "Actively Shaped Supercontinuum from a Photonic Crystal Fiber for Nonlinear Coherent Microspectroscopy", B. von Vacano, W. Wohlleben and M. Motzkus, Optics Letters, 31 (2006) 413-415.
- "In-situ broadband pulse compression for multiphoton microscopy using a shaper-assisted collinear SPIDER", B. von Vacano, T. Buckup and M. Motzkus, Optics Letters, 31 (2006) 1154-1156.
- "Time resolved two color single beam CARS employing supercontinuum and femtosecond pulse shaping", B. von Vacano and M. Motzkus, Optics Comm., 264 (2006) 488-493.
- "Highly sensitive single-beam heterodyne coherent anti-Stokes Raman scattering (CARS)", B. von Vacano, T. Buckup and M. Motzkus, Optics Letters, 31 (2006) 2495-2497.
- "Shaper-assisted collinear SPIDER: fast and simple broadband pulse compression in nonlinear microscopy", B. von Vacano, T. Buckup and M. Motzkus, J. Opt. Soc. Am. B, 24 (2007), 1091-1100.
- "Rapid polymer blend imaging with quantitative broadband multiplex-CARS microscopy", B. von Vacano, L. Meyer and M. Motzkus, J. Raman Spectroscopy, 38 (2007) 916-926.
- "Molecular discrimination of a mixture with single-beam Raman control", B. von Vacano and M. Motzkus, J. Chem. Phys., 127 (2007), 144514.
- "Parametrically amplified ultrashort pulses from shaped photonic crystal fiber supercontinuum" J. Möhring, T. Buckup, B. von Vacano and M. Motzkus, Optics Letters 33 (2008), 186-188.
- "Time-resolving molecular vibration for microanalytics: single laser beam nonlinear Raman spectroscopy in simulation and experiment", B. von Vacano and M. Motzkus, Phys. Chem. Chem. Phys., 10 (2008), 681-691.

Submitted / In press:

- "Microanalytical nonlinear single-beam spectroscopy combining an unamplified femtosecond fibre laser, pulse shaping and interferometry", B. von Vacano, J. Rehbinder, T. Buckup and M. Motzkus, Applied Physics B, submitted.
- "Advanced multiphoton and CARS microscopy with broadband shaped femtosecond laser pulses", B. von Vacano and M. Motzkus, chapter for book on "Biochemical Applications of Nonlinear Optical Spectroscopy" by V. Yakolev (ed.), Taylor and Francis, scheduled for 2008.

In Proceedings:

- "Actively shaped Supercontinuum from a Photonic Crystal Fibre for Quantum Control Microspectroscopy", B. von Vacano, W. Wohlleben and M. Motzkus, Proceedings of the Conference on Lasers and Electro-Optics, Optical Society of America (2006), CTuA2.
- "Shaper-Assisted Collinear SPIDER for Broadband Pulse Compression in Multiphoton Microscopy",
  B. von Vacano, T. Buckup and M. Motzkus, Proceedings of the Conference on Lasers and Electro-Optics, Optical Society of America (2006), CTuC1.
- "Time-resolved single-beam CARS with shaped Supercontinuum from a Photonic Crystal Fiber",
  B. von Vacano, W. Wohlleben, and M. Motzkus, Ultrafast Phenomena XV, Springer, Berlin (2007), 813.
- "Design and application of shaper-assisted collinear (SAC-) SPIDER for pulse compression in high contrast multiphoton microscopy", B. von Vacano, T. Buckup and M. Motzkus, CLEO Europe Conference Proceedings, Optical Society of America, European Physical Society (2007), CL-4-WED
- "Sensitive single-beam heterodyne CARS microscopy with independently phase controlled local oscillator", B. von Vacano, T. Buckup and M. Motzkus, CLEO Europe Conference Proceedings, Optical Society of America, European Physical Society (2007), CL4-3-THU.
- "Robust multiplex CARS microscope based on photonic crystal fibre supercontinuum",
  B. von Vacano, L. Meyer and M. Motzkus, CLEO Europe Conference Proceedings, Optical Society of America, European Physical Society (2007), CH3-4-FRI.

Oral presentations:

- Invited talk "Actively Shaped Supercontinuum for Coherent Control Applications",
  B. von Vacano, W. Wohlleben und M. Motzkus, 4th International Workshop on Optimal Control of Quantum Dynamics, Ringberg/Tegernsee, 07.12.2005.
- Invited talk "Microscopic chemical imaging with shaped femtosecond pulses",
  B. von Vacano, FCI-Stipendiatentreffen Göttingen, 20.01.2006.
- Invited talk "Kompression von Superkontinuum aus einer mikrostrukturierten Faser, Pulsformung und Anwendung für nichtlineare Mikro-Spektroskopie",
  B. von Vacano, IAP Institutsseminar, Universität Bern (CH), 15.06.2006.
- Invited talk "Nonlinear Raman Microscopy with tailored broadband femtosecond laser pulses: Novel approaches to label-free microscopic chemical imaging",
  B. von Vacano, Physics Seminar, School of Physics and Astronomy, University of Cardiff, Cardiff (UK), 24.10.2007.
- "Single-beam CARS mit geformten Femtosekunden-Pulsen",
  B. von Vacano, W. Wohlleben and M. Motzkus, DPG-Frühjahrstagung, Berlin, 07.03.2005.
- "In situ Measurement and Active Phase Control of Broadband Pulses for Multiphoton Microscopy", B. von Vacano, T. Buckup and M. Motzkus DPG-Frühjahrstagung, Frankfurt, 14.03.2006.
- "Coherent Control with Actively Shaped Supercontinuum from a Photonic Crystal Fiber",
  B. von Vacano, W. Wohlleben and M. Motzkus DPG-Frühjahrstagung Frankfurt, 16.03.2006.

- "Shaper-Assisted Collinear SPIDER for Broadband Pulse Compression in Multiphoton Microscopy", B. von Vacano, T. Buckup and M. Motzkus, CLEO, Long Beach (USA), 23.05.2006.
- "Time-resolved Single-beam CARS with Shaped Supercontinuum from a Photonic Crystal Fiber", B. von Vacano, W. Wohlleben and M. Motzkus, OSA Ultrafast Phenomena, Pacific Grove (USA), 03.08.2006.
- Presentation at the „Schülerworkshop": „Chemische Bildgebung mit Laser-Impulsen", B. von Vacano, Universität Marburg, 08.03.2007.
- „Broadband Multiplex CARS Microscopy employed for Polymer Analytics", B. von Vacano, L. Meyer and M. Motzkus, DPG-Frühjahrstagung, Düsseldorf, 22.03.2007.
- „Single-beam Heterodyne CARS for Sensitive Chemically Selective Microscopy", B. von Vacano, T. Buckup and M. Motzkus, DPG-Frühjahrstagung, Düsseldorf, 23.03.2007.
- "Sensitive single-beam heterodyne CARS microscopy with independently phase controlled local oscillator", B. von Vacano, T. Buckup and M. Motzkus, CLEO Europe, München, 21.06.2007.
- "Robust multiplex CARS microscope based on photonic crystal fibre supercontinuum", B. von Vacano, L. Meyer and M. Motzkus, CLEO Europe, München, 22.06.2007.

Poster presentations:

- "Single-beam CARS spectroscopy with shaped Femtosecond Laserpulses", B. von Vacano, W. Wohlleben und M. Motzkus, GDCh-Tagung Fachgruppe "Photochemie", Jena, 30.03.2005
- "Nichtlineare chemisch selektive Raman-Mikroskopie mit geformten Femtosekunden-Laserpulsen", B. von Vacano, W. Wohlleben und M. Motzkus, Universität Marburg - Tag der PC, Schloss Rauischholzhausen, 28.02.2006.
- "Single-beam CARS Microscopy employing Coherent Control Schemes", B. von Vacano, W. Wohlleben, M. Motzkus, DPG-Frühjahrstagung Frankfurt, 14.03.2006.
- „Nichtlineare chemisch selektive Raman-Mikroskopie mit Femtosekunden-Laserpulsen", B. von Vacano, L. Meyer and M. Motzkus, Materialforschungstag Mittelhessen, Schloss Rauischholzhausen, 30.06.2006.
- "High-contrast Multiphoton Microscopy based on Shaper-assisted Collinear SPIDER Pulse Compression", B. von Vacano, T. Buckup, M. Motzkus, DPG-Frühjahrstagung Düsseldorf, 20.03.2007.
- "Design and application of shaper-assisted collinear (SAC-) SPIDER for pulse compression in high contrast multiphoton microscopy", B. von Vacano, T. Buckup and M. Motzkus, CLEO Europe, München, 20.06.2007.
- "Selective Microscopic Imaging Using Femtosecond Coherent Anti-Stokes Raman Scattering (CARS) Techniques", B. von Vacano, C. Pohling, L. Meyer and M. Motzkus, Nanobionics IV Conference, Marburg, 19.09.2007.
- "Advanced multiphoton microspectroscopy with broadband shaped femtosecond laser pulses", B. von Vacano, T. Buckup, M. Motzkus, 5th International Ringberg Workshop on Optimal Control of Quantum Dynamics, Ringberg/Tegernsee, 29.11.2007.

Table of Contents

1 Introduction to coherently controlled nonlinear microscopy

Optical microscopy today still is one of the most important technologies for the advancement of science, especially as workhorse in biology and life sciences, but also in material science, forensics, archaeology, microfabrication and many other areas. Despite its ubiquitous usage and the age of the basic technology, optical microscopy remains an extremely vital field of modern research. One main challenge is to improve the spatial resolution; to push the capabilities of optical microscopy towards the nanoscale, exemplified by the recent work on far-field "nanoscopy"[1] Another very important aspect is the image contrast achievable. Classically, sample absorption and refractive index changes are exploited. As this is by far not enough to reveal the microscopic structure of many samples of interest, techniques for selective staining have emerged, and modern fluorescent markers have led to a second "microscopic revolution" in biology. However, there is still a need for new concepts: Staining is restricted to cases where suitable dyes are available. Inevitable bleaching of the labelled samples severely restricts observation time. Furthermore, in the life sciences dyes and their photo-degraded products are often toxic and prevent imaging of living cells, while in the material sciences the introduction of a dye can severely alter the material properties under study. And still, the information about the true chemical composition obtainable is very limited. Therefore, a different contrast mechanism is highly wanted, which is chemically selective and does not require modification of the sample. This is fulfilled by vibrational spectroscopy, which uses the intrinsic physical properties of molecules having characteristic vibrational resonances. Employing infrared absorption to visualize the chemical composition directly in microscopy, for example of polymers,[2, 3] is challenging: It is difficult to obtain suitable light sources and optical components for such large wavelengths, the samples have to be very thin due to their high absorption, and the spatial resolution necessarily remains much lower than known from conventional microscopy. On the other hand, visible light and standard optical components can be used in *Raman* spectroscopy. Implemented in a confocal microscope, *Raman* allows selective chemical imaging with high three-dimensional spatial resolution. The drawbacks of *Raman* spectroscopy are, however, weak signals which require long acquisition and therefore prolonged illumination times to obtain a spectrum, and a possible background due to fluorescence from the sample.

With the availability of high intensity pulsed laser sources, optical microscopy has entered yet another new field: New phenomena with nonlinear intensity dependence have been discovered and have led to the development of new and powerful multiphoton spectroscopy techniques (Fig. 1.1).[4, 5] This includes fluorescence imaging with highly reduced photobleaching of the labelling dyes, bright images with very high three-dimensional resolution, deep-tissue imaging and novel contrast mechanisms. In the most commonly employed two-photon fluorescence microscopy, labelling fluorophores are excited simultaneously with two

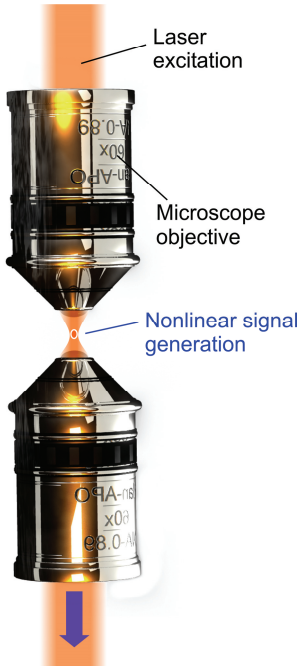

Fig. 1.1: Schematic depiction of nonlinear microscopy

photons, which can roughly be understood as equivalent to an excitation with a single photon of the double energy, or half the wavelength (Fig. 1.2a). The use of long excitation wavelengths in the near-infrared spectral region is the reason, why multiphoton techniques usually achieve much higher penetration depths, as scattering is highly reduced.[4, 6] Still, multiphoton fluorescence is limited to stained samples and the contrast offered by the dyes used.

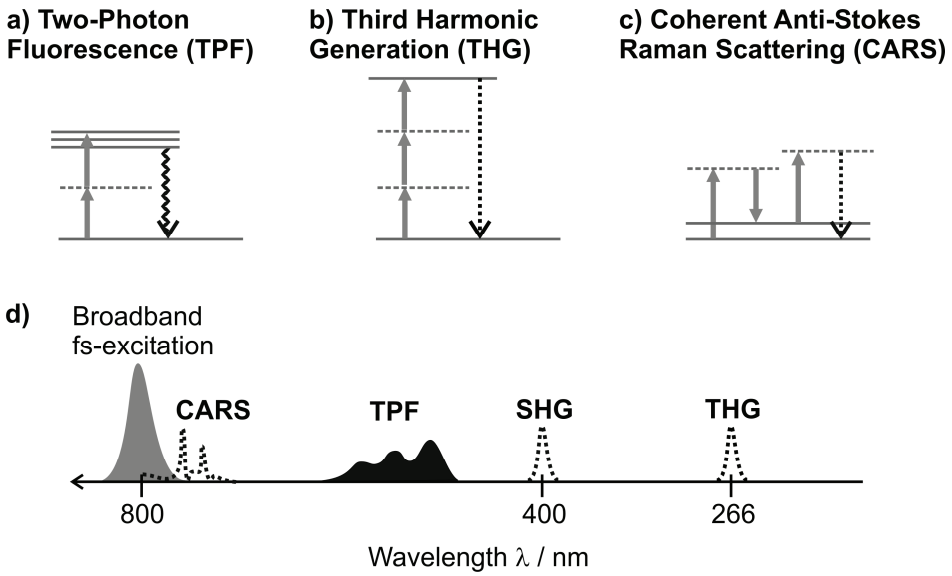

Fig. 1.2: Multiphoton spectroscopy schemes with corresponding energy level diagrams **(a-c)**. Black solid arrows always indicate the energy equivalent of one excitation laser photon. **d)** Sketch of possible excitation and signal spectra, demonstrating their relative spectral positions. Excitation with a fs-laser with a *Gaussian* spectrum around 800 nm has been assumed. Possible multiphoton signals include CARS, two-photon fluorescence (TPF), second harmonic generation (SHG) and third harmonic generation (THG).

Other, still less commonly employed multiphoton techniques image native, untreated samples. One class is harmonic generation,[7] be it second harmonic generation (SHG) [8, 9] or third harmonic generation (THG, Fig. 1.2b).[10] In SHG and THG imaging, two or three photons combine in the sample in a nonlinear optical process. This intrinsically occurs in some materials, yielding imaging contrast.

Despite the usefulness of fluorescence, SHG and THG, another nonlinear optical spectroscopy method is even more powerful for functional imaging of unlabelled samples, and draws on the unique advantage of vibrational spectroscopy as contrast mechanism: CARS.[11, 12] CARS refers to "coherent anti-*Stokes Raman* Scattering", and is a three-photon process carrying information about the sample due to the involvement of a vibrational energy level (Fig. 1.2c). In principle, CARS yields the same information as linear *Raman* microscopy, but has huge advantages: The three-dimensional sectioning capabilities are superior due to the nonlinearity of CARS, and the signal can be several orders of magnitudes stronger when using short-pulse lasers. In CARS, a pair of photons of different energy coherently excites a molecular vibration, which is then probed by the third photon. The signal created is a photon of higher energy, blue-shifted with respect to the probe photon by the energy of the vibrational level of the molecule (see also Fig. 1.2d). As

mentioned before, the vibrational levels of a molecule are highly specific and CARS thus allows chemical identification and imaging based on the true chemical composition of the sample. CARS requires photons at least at two different wavelengths, which are usually provided by the combination and synchronization of different lasers. In addition, the sensitivity of CARS is low, as the signal strength of an analyte scales quadratically with its concentration. All the mentioned facts make CARS, despite its great potential, rather unflexible, experimentally very demanding and as such prevent wide-spread use.

This situation is the starting point of this thesis. The aim is to integrate CARS microscopy in a general scheme for flexible nonlinear microspectroscopy, simplifying the setup, solving the issue of low sensitivity and paving the way for applications. This requires implementing CARS in a single beam of femtosecond laser pulses with sufficient bandwidth to contain both photons.[13-17] The approach therefore calls for excitation lasers with high optical bandwidth (exceeding thousands of wavenumbers), and thus ultrashort pulse duration in the sub-20 fs regime.

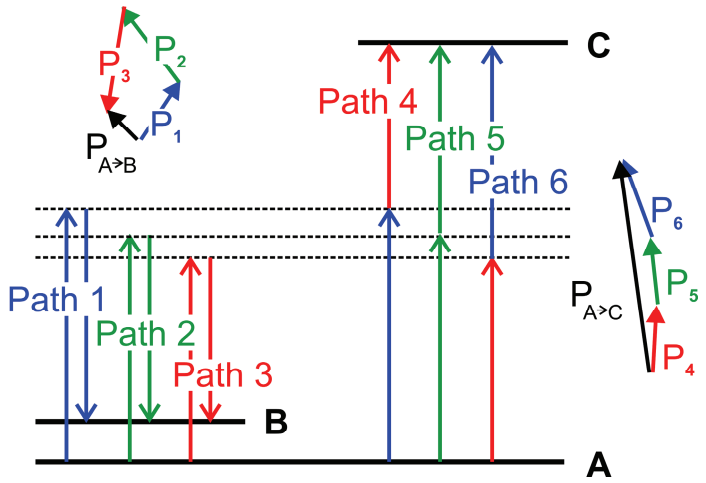

Fig. 1.3: Coherent control of multiphoton processes. As an example, quantum interference between pathways leading from state A to state B in a *Raman*-type transition are shown (Paths 1-3), as well as pathways leading from the same initial state A to a target state C in a two-photon-absorption type transition (Paths 4-6). Depending on the quantum mechanical phases between the different pathways leading to the same target state, destructive or constructive interference can be induced, which is the foundation of coherent control. In this example, the probability amplitudes P_1, P_2, P_3 for the transition $A \rightarrow B$ add up almost completely destructively, while P_4, P_5, P_6 for the process $A \rightarrow C$ interfere constructively, leading to a large probability $P_{A \rightarrow C}$. Thus, coherent control allows selectively exciting a desired multiphoton process by applying correct phases for the different pathways.

Such a sub-20 fs broadband laser pulse containins all the different photon energies (corresponding to the arrows in the level diagrams in Fig. 1a-c) and excites all possible nonlinear processes at once. Therefore, the second essential ingredient in this thesis is coherent control. Coherent control is a very powerful concept, aiming at selectively manipulating quantum states through the interaction with laser light.[18-21] Methods of coherent control have found widespread applications in nonlinear optics,[22-24] atomic and molecular physics [25-27] and even for steering chemical reactions [28] and processes

in photobiology.[29] In addition, coherent control has proved a very valuable addition to spectroscopy [30-32] and allows the extremely flexible implementation of nonlinear spectroscopy, where the desired multiphoton process can simply be selected by inducing the appropriate quantum interferences. From a fundamental point of view, all multiphoton transitions can be understood as light-matter interactions taking the system under study from an initial level via intermediate states to a certain target state. As light-matter interaction is a quantum mechanical phenomenon, the different processes and thus "pathways" not only occur simultaneously, but give rise to quantum interferences (Fig. 1.3). The probability, with which a certain transition (for example TPF, CARS, …) can take place is determined by the sum of the probability amplitudes of all indistinguishable pathways connecting the initial and target level.[25, 33] In Fig. 1.3, this has schematically been depicted for a *Raman*-like transition and two-photon absorption. The indistinguishable pathways are given by all suitable combinations of photon energies in a broadband femtosecond pulse. If the phases of the pathways are arbitrarily controlled in order to select one target state over the other, one exerts coherent control.

This is the key to the broadband femtosecond approach to nonlinear microspectroscopy presented here. From the point of view of coherent control, it becomes clear that high spectral bandwidths are beneficial: Providing a huge number of photon energies and as such interfering pathways is necessary to be able to achieve high interference contrast, and thus good controllability of optical processes.

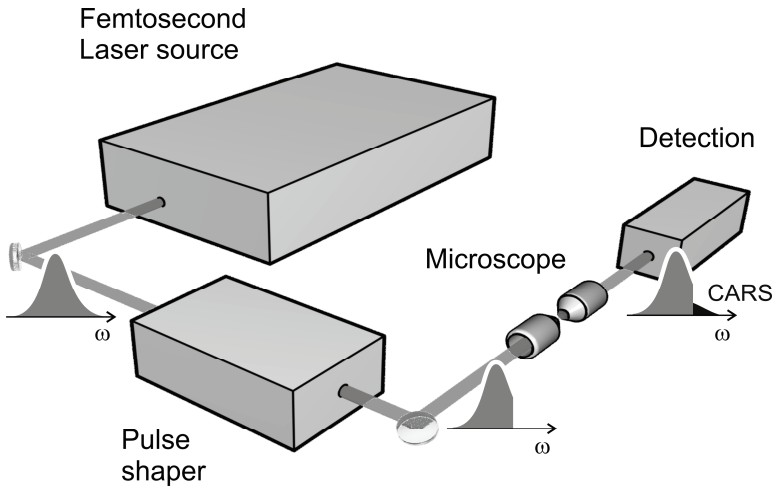

Fig. 1.4: General scheme of the versatile next-generation broadband multiphoton laser-scanning microscope developed and investigated in this thesis. A broadband femtosecond laser acts as the excitation source, which can be used for a multitude of nonlinear spectroscopic imaging techniques, such as TPF, SHG, THG and CARS. The fs-pulse shaper ensures highest excitation efficiency in the microscope by compensating pulse distortions due to dispersion, and allows tailoring the excitation to improve contrast or enable spectroscopic acquisition despite the broadband excitation, as in the case of single-beam CARS. Detection can be performed in forward or backward (epi-)direction, depending on the application (Only forward detection is shown in this figure).

All processes are therefore carried out in the same experimental setup: What is needed, is a broadband laser source, the capability to deliver the femtosecond pulses *in situ* in the

microscope with highest possible intensity and to control the phase to select the desired process, and finally a multichannel detection unit. In a schematic way, this is shown in Fig. 1.4. Hitherto, this approach is confronted with several critical issues: If unaccounted for, material dispersion in the microscope objectives will severely distort ultrashort fs-pulses. Boadband excitation cannot be expected *per se* to offer useful spectral resolution, while it was claimed[11] that fs-pulses at the same time have a very unfavourable ratio of CARS signal versus background. Also, the relatively poor sensitivity of CARS also has to be addressed.

In this thesis, it will be demonstrated that the combination of broadband laser excitation with fs-pulse shaping and coherent control resolves all these issues by exploiting coherent control. To achieve this, the milestones to fulfil are the efficient generation of broadband femtosecond radiation, its tailoring and compression to very short pulses *in situ* in the microscope, development of coherently controlled spectroscopy schemes and their application. All these issues will be addressed in detail as follows:

- **Chapter 2** introduces description and properties of femtosecond laser pulses. The scope in this pursuit is not comprehensive, but limited to aspects in the context of broadband nonlinear microscopy, in order to motivate the use of broadband femtosecond pulses and establish underlying ideas and formalisms for the reader. As it will be essential to have laser sources at hand with a maximum of achievable optical bandwith, furthermore a novel approach to the spectral broadening of existing fs-laser sources will be presented. This "broadband upgrade" using special microstructured optical fibers is the key technology enabling applications in later chapters.

- One important use of this so far uncompressed, yet spectrally extremely broadened fs-radiation is described in **Chapter 3**. Employing the broadband fibre laser source, a first scheme for chemically selective microscopy can be implemented. The unique properties of the laser source allow imaging with very rapid, multiplex spectral acquisition, which will be used for the quantitative chemical mapping of complex polymer blend samples.

- To introduce further functionality in the fs-laser spectroscopy, the broadband light source is finally merged with advanced pulse shaping in **Chapter 4**. The active tailoring of the spectral and temporal shape of the broadband laser pulses from the microstructured fibers and the development of a new fast scheme for its compression make it possible to use the ultrashort fs-pulses in a nonlinear microscope, which otherwise could not be achieved. It will be shown in a first example that compressed broadband pulses are by far superior in terms of nonlinear spectroscopic signal strength and therefore image contrast.

- **Chapter 5** makes use of all the technological achievements, and puts them to use in coherently controlled molecular spectroscopy. To accomplish this, the prior established capabilities to shape broadband pulses in phase, amplitude and polarization are exploited and schemes developed theoretically for coherently controlled CARS spectroscopy. As a conceptually novel approach, the fs-laser excitation is tailored in such a way that ultrafast molecular vibrations are resolved in

time. Even a scheme for pump-probe-type coherent control experiments in a microenvironment is implemented. A thorough comparison of different control approaches in simulation and experiment will finally yield first examples of chemical imaging and the discrimination of potentially hazardous components in a powdery matrix.

- Still, the issue of sensitivity remains. Therefore, another function is integrated into the shaped fs-laser pulses in **Chapter 6**. The perfect coherence of the broadband spectrum and the high flexibility of the pulse-shaping approach make it possible to introduce a novel interferometric detection scheme, which helps detect chemically selective spectroscopy at a 5000 times improved sensitivity. These results impressively demonstrate the great potential of the integrated approach pursued, combining the broadband fs-source, pulse shaper and a nonlinear microscope.

The thesis finally ends with a summary, placing the findings made in perspective, and giving an outlook on future directions of research and further potential applications.

2 Ultrabroadband femtosecond laser pulses for microspectroscopy

In this chapter, a general introduction to ultrashort femtosecond laser pulses, their description and application shall be given.[34, 35] The emphasis will be on introducing the quantities necessary for later describing pulse-shaping and spectroscopy applications, as well as giving an account of coherent spectral broadening mechanisms in photonic crystal fibers - one of the foundations of this work.

2.1 Properties and description of ultrashort laser pulses

Femtosecond laser sources periodically emit ultrashort bursts of light with no emission of radiation in between pulses. This leads to very high peak intensities at low average laser power and is the reason why such lasers are ideal for efficient excitation of nonlinear optical processes. For typical fs-oscillators, pulse repetition frequencies f_{rep} are in the range of tens to a hundred MHz. The gain G in peak intensity I_p over a continuous wave laser with the same average intensity $\langle I \rangle$ is given by

$$G = \frac{I_p}{\langle I \rangle} = \frac{T_{rep}}{\tau_p} = \frac{1}{\tau_p \cdot f_{rep}}, \tag{2.1}$$

with the ultrashort pulse duration τ_p and the period T_{rep} of pulse repetitions at a rate $f_{rep} = T_{rep}^{-1}$. The respective quantities are summarized in Fig. 2.1. For *cw* lasers, G always equals unity, while for an assumed 12 fs pulse at 80 MHz repetition rate, G is about one million! Considering a nonlinear optical signal with intensity dependence to the power of n (examples have been introduced in chapter 1), it can be calculated as follows:

$$\left\langle I_{Sig} \right\rangle \propto f_{rep} \cdot \int dt \left[I(t) \right]^n \approx f_{rep} \cdot \left[I_p \right]^n \cdot \tau_p = \langle I \rangle^n \cdot G^{(n-1)}, \tag{2.2}$$

where $\left\langle I_{Sig} \right\rangle$ is the time-averaged signal intensity. This relation quantitatively substantiates the immense efficiency gain of using ultrashort pulsed lasers for nonlinear processes with $n > 1$.

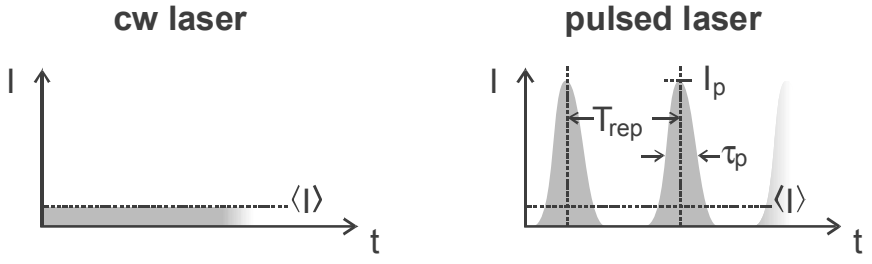

Fig. 2.1: Continuous wave (*cw*) versus pulsed laser. Indicated are the average intensity $\langle I \rangle$, peak intensity I_p, pulse duration τ_p and pulse repetition period T_{rep}.

Furthermore, beyond the mere increase in efficiency, the very short duration of femtosecond laser pulses offers a whole new quality and gives access to the measurement of equally fast events, such as atomic motion in a molecular vibration, which will be exploited extensively later in this work.

In contrast to a continous-wave laser, where the laser emission is described by an almost infinitely extended sine wave of the electric field (Fig. 2.2a), ultrashort laser pulses consist of only a short section of such a sine wave (usually with a smooth envelope) with a few optical cycles (Fig. 2.2c). This fact immediately illustrates why ultrashort laser pulses necessarily cannot have a single defined frequency, but a broader spectrum (Fig. 2.2d). Therefore, the most important notion of ultrashort pulses is the *Fourier* transform relation between the temporal shape of a pulse and the spectrum necessary to create it. The electric field of a laser pulse can equivalently be described in frequency and time domain:

$$\begin{aligned} E(t) &= |E(t)| \cdot \exp[i\phi_I(t)] = |E(t)| \cdot \exp\left[i\left(\phi(t) - \omega_0 t\right)\right] = FT\left\{\tilde{E}(\omega)\right\} \\ \tilde{E}(\omega) &= \left|\tilde{E}(\omega)\right| \cdot \exp[i\varphi(\omega)] = FT^{-1}\{E(t)\} \end{aligned} \quad , \tag{2.3}$$

where $E(t)$ represents the complex electric field in the time domain with amplitude $|E(t)|$, also termed the temporal field envelope, and instantaneous temporal phase $\phi_I(t)$. It is convenient to separately account for the continuous phase change due to the oscillation of the electric field with $exp[-i\omega_0 t]$ and define a temporal phase $\phi(t) = \phi_I(t) + \omega_0 t$. $\tilde{E}(\omega)$ is the *Fourier* transform of $E(t)$, and thus the pulse representation in frequency domain with amplitude $|\tilde{E}(\omega)|$ and spectral phase $\varphi(\omega)$. Exemplarily, these quantities are shown in Fig. 2.2.

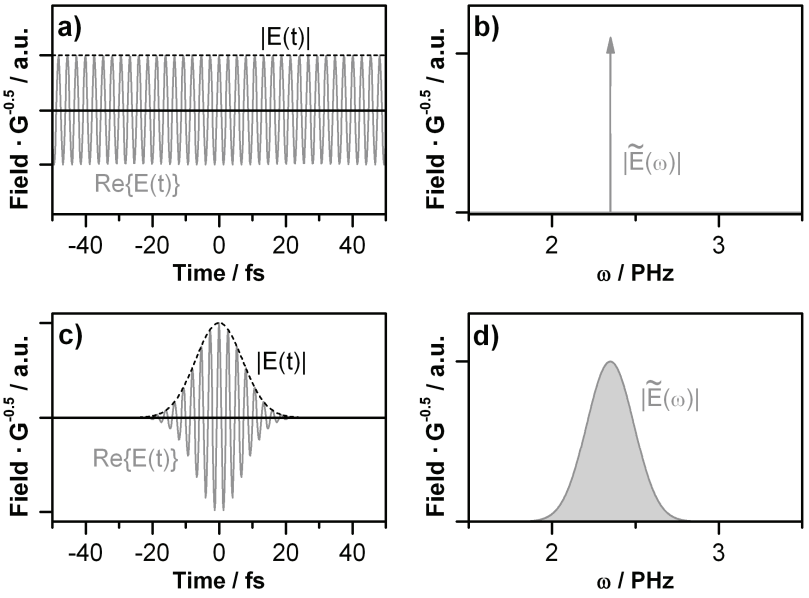

Fig. 2.2: Electric field in the time domain [panels (**a**) and (**c**)] and in the frequency domain [panels (b) and (d)]. **a)** A continuous-wave laser approximately emits an infinite wave *Re{E(t)}* with a constant amplitude $|E(t)|$. **b)** This results in a single defined frequency in its spectrum $|\tilde{E}(\omega)|$. **c)** Amplitude $|E(t)|$ and field *Re{E(t)}* for a 12 fs laser pulse. **d)** Correspondingly, its spectrum is broad and has a FWHM of $\Delta\omega \sim 330$ THz. In this comparison, the electric fields have been scaled by $\sqrt{G}$ [see Eqn. (2.1)] to be able to show them on the same scale. The center frequency ω_0 is 2350 THz in both cases, which corresponds to a wavelength λ_0 of 800 nm.

The *Fourier* relationship leads to the well-known time-bandwidth product (TBP), stating that the pulse temporal width (measured as full width at half maximum, FWHM) τ_p multiplied by the pulse spectral width in the frequency domain $\Delta\omega$ is given by a constant *TBP*:

$$\tau_p \cdot \Delta\omega = 2\pi \cdot TBP \tag{2.4}$$

TBP depends on the pulse profile (for the most commonly assumed *Gaussian* pulses *TBP* is 0.44). Relation (2.4) has the important consequence mentioned before that very short femtosecond pulses necessarily require very broad laser pulse spectra. However, a broad pulse spectrum alone does not guarantee short pulses: Equation (2.4) only holds for "*Fourier*-Transform limited" (FTL) pulses, meaning that the spectral phase $\varphi(\omega)$ and as such the temporal phase $\phi(t)$, see Eqn. (2.3), have to be zero or purely linear.

The influence of the spectral phase on the temporal shape (and temporal phase) of the pulses is of utmost importance, as this is the experimental lever to create ultrashort light pulses with a desired shape and function. On the other hand, linear and nonlinear effects of pulse propagation can also alter the spectral phase of an ultrashort laser pulse. To describe and understand such phenomena, it is common and very instructive to expand typical spectral phase functions in a *Taylor* series around the central frequency ω_0 of a laser pulse:

$$\begin{aligned}\varphi(\omega) &= \varphi_0 + \left.\frac{\partial\varphi(\omega)}{\partial\omega}\right|_{\omega_0} \cdot (\omega-\omega_0) + \frac{1}{2}\left.\frac{\partial^2\varphi(\omega)}{\partial\omega^2}\right|_{\omega_0} \cdot (\omega-\omega_0)^2 + \cdots \\ &= \varphi_0 + \varphi' \cdot (\omega-\omega_0) + \frac{1}{2}\varphi'' \cdot (\omega-\omega_0)^2 + \cdots\end{aligned} \tag{2.5}$$

Similarly, the temporal phase $\phi(t)$ can be written down as follows, expanded around the pulse arrival at time t_0:

$$\phi(t) = \phi_0 + \phi' \cdot (t-t_0) + \frac{1}{2}\phi'' \cdot (t-t_0)^2 + \cdots \tag{2.6}$$

What is the effect of the expansion coefficients of the spectral phase on the temporal shape and phase of the laser pulse? The constant φ_0 in Eqn. (2.5) is only a phase offset for the whole pulse and does not alter its shape. The linear contribution φ' to the spectral phase does also not alter the shape of the pulse, but leads to a shift of the pulse in time with respect to t_0 (Fig. 2.3c+d). Plugging Eqn. (2.5) into Eqn. (2.3) it can be shown that φ' (which possesses the unit of time) directly gives this temporal shift. Therefore, often group delay $T_g(\omega)$ is discussed instead of the spectral phase $\varphi(\omega)$. The group delay $T_g(\omega)$ is the derivative of the spectral phase and can directly be understood as the arrival time of each frequency component ω in the pulse relative to t_0:

$$T_g(\omega) = \frac{d\varphi(\omega)}{d\omega} = \varphi' + \varphi'' \cdot (\omega-\omega_0) + \cdots \tag{2.7}$$

As shown by (2.7), the second-order coefficient of Eqn. (2.5) φ'' leads to a linear frequency-dependent delay of the pulse. This is called a *chirp*, as any laser pulse exhibiting a nonzero φ'' will have a time-dependent instantaneous frequency - like the characteristic chirping of a

bird in acoustics. The instantaneous frequency $\omega_I(t)$ is defined for the temporal phase in analogy to the group delay for the spectral phase:*

$$\omega_I(t) = -\frac{d\phi_I(t)}{dt} = \omega_0 - \left(\phi' + \phi'' \cdot (t - t_0) + \cdots\right) \tag{2.8}$$

If an ultrashort pulse propagates through a dispersive medium, each frequency component of the pulse experiences a different refractive index and thus a different phase velocity. For a laser pulse in the visible spectral region and a normal transparent material this leads to the red frequency components arriving earlier than the blue ones: the pulse becomes chirped and $\varphi'' > 0$ (Fig. 2.3e+f). For applications of ultrashort lasers, this causes inevitable temporal broadening of the pulses passing through transparent bulk media. One can, however create materials which exhibit no or even anomalous dispersion in the visible and NIR spectral region. To characterize such materials, the group velocity dispersion $GVD(\omega)$ is commonly used, which is the first derivative of $T_g(\omega)$ [and as such the second derivative of $\varphi(\omega)$] per propagation distance l:

$$GVD(\omega) = \frac{\partial}{\partial l}\left[\frac{\partial}{\partial \omega} T_g(\omega)\right] \tag{2.9}$$

Therefore, if $GVD(\omega)$ is known for a specific material, the spectral phase accumulated upon propagation can be precisely predicted using the relations presented above. For practical applications, the group velocity dispersion is often given in units of wavelength as GVD_λ:[36]

$$GVD_\lambda(\lambda) = -\frac{2\pi c}{\lambda^2} \cdot GVD\left(\frac{2\pi c}{\lambda}\right). \tag{2.10}$$

* Note that the occurrence of the negative sign in Eqn. (2.8) is a consequence of the definition of the exponent containing the temporal phase in Eq. (2.3).

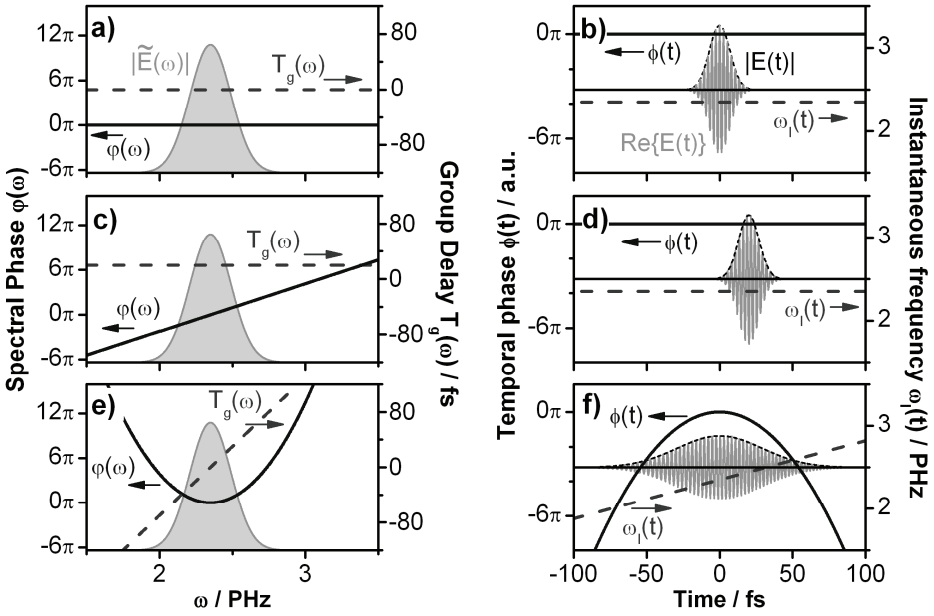

Fig. 2.3: Influence of simple polynomial spectral phases on the temporal shape of a pulse. Shown is the spectrum $|\tilde{E}(\omega)|$, the spectral phase φ(ω), the group delay $T_g(\omega)$, the temporal field $Re\{E(t)\}$, the field amplitude $E(t)$ and the instantaneous frequency $\omega_I(t)$. **a-b)** *Fourier*-transform limited pulse with φ(ω) = 0. This is the same pulse as shown in Fig. 2.2c+d). **c-d)** Linear spectral phase with φ' = 20 fs leading to a temporal shift. **e-f)** Quadratic phase with φ'' = 100 fs^2, leading to a temporal broadening and a time-dependent instantaneous frequency (chirp).

2.2 Coherent spectral broadening in photonic crystal fibers

For applications of ultrafast lasers in spectroscopy, it is highly desirable to use the shortest pulses available with their concomitant high bandwidth, *e. g.* to maximize temporal resolution of molecular dynamics under study. However, generally shorter pulses and the support of larger bandwidths require more and more complex and expensive laser systems. Recently, fs-oscillators emitting pulses in the range of 10 fs pulses have become commercially available.[37] However, the majority of technically mature femtosecond lasers installed in laboratories are of the τ_p = 100 fs pulse duration class. Also, the recently developed fs-fiber laser sources, which feature still increased robustness, very compact design and unbeatably low costs of operation, are so far available only with pulses equal or longer than this.[38-40] According to Eqn. (2.4) , the pulse duration τ_p of a given source could be shortened, if the pulse bandwidth Δω was increased by some optical process.

It is clear that this requires a nonlinear interaction, as linear propagation through an optical medium will always conserve frequency. A very successful strategy is to use nonlinear self-phase modulation (SPM) to increase the bandwidth of a laser source. For an efficient coherent broadening of low-power fs-oscillator pulses, focussing for highest peak intensities and at the same time achieving long interaction distances is necessary. Therefore, successful SPM broadening in this case involves the use of optical fibers with micrometer-sized cores. Like this, the pulse energy is confined in a tight focal spot throughout the length of the fiber, allowing continuously very high peak intensities. Of course, dispersion broadening (chirping) of the pulses in the fiber has to be minimized – otherwise the peak intensity will

drop dramatically upon propagation. Novel microstructured fibers, such as photonic crystal fibers (PCF), allow maximizing nonlinearities and at the same time tailoring the dispersion properties, namely the group velocity dispersion $GVD(\omega)$, to minimize pulse broadening. Therefore, PCF will be used throughout this thesis for coherent spectral broadening. But before, the principle mechanism of SPM shall be elucidated, and a brief introduction be given to the properties and applications of PCF.

2.2.1 Self-phase modulation (SPM)

The origin of SPM is a temporal variation of the refractive index n of a medium through which the pulse propagates. The reason for the modulation of n is the *Kerr* effect, which describes the dependence of the refractive index on an applied strong electric field. In the case of SPM, the applied field is the high intensity ultrashort laser pulse itself. The important consequence is an intensity-dependent component $\Delta n(t)$ of the refractive index:

$$\begin{aligned} n &= n_0 + n_{NL} \cdot I(t) \\ \Delta n(t) &= n_{NL} \cdot |E(t)|^2, \end{aligned} \tag{2.11}$$

with n_0 the unperturbed refractive index, n_{NL} the refractive index nonlinearity and $I(t) = |E(t)|^2$ the temporal intensity of the pulse. The variation of the refractive index $\Delta n(t)$ causes an additional term in the temporal phase of the pulse

$$\phi_{NL}(t) = \Delta n(t) \cdot L \cdot \frac{\omega_0}{c}, \tag{2.12}$$

proportional to the propagation length L in the medium. This quantitatively shows that effective SPM requires focusing to achieve high intensities $I(t)$ and as such high variations $\Delta n(t)$, and a long interaction length L, as reasoned before. Due to the small value of the index of refraction nonlinearity n_{NL}, intensities in the order of >0.1 TW/cm^2 are needed for significant SPM to occur. Focusing a standard 100 fs-oscillator pulse with nanojoule energy down to a micrometer spot, the peak intensity I_{peak} reaches 10 TW/cm^2. As can be seen from Eqn. (2.12), the addition $\phi_{NL}(t)$ to the temporal phase directly reflects the temporal intensity profile of the pulse: a *Gaussian* pulse will create a *Gaussian* phase modulation. This is shown in Fig. 2.4 for two cases, resulting in a peak self-phase modulation of less than π (a-c), and in the other case of ~7.5π (d-f).

Parameters used for the simulation in Fig. 2.4 correspond to 5 nJ pulses of 100 fs duration, focussed in a fibre with a diameter of 1.5 µm made from quartz glass. For the case of low SPM, a fibre length L of only 0.4 mm was assumed, while the ten-fold fibre propagation distance of 4 mm was chosen for the strong SPM example. Note that according to Eqn. (2.12) the product $I_{peak} \cdot L$ determines the amount of SPM, so that the same normalized values of $I_{peak} \cdot L$ could also be obtained by changing the pulse energy respectively. A pulse spectrally broadened by SPM retains its temporal profile, and is as such not *Fourier*-limited, obeying Eqn.(2.4). If one manages to compensate for the distortion of the spectral phase of the broadened pulses, one can obtain TL pulses significantly shorter than the input pulses. For example, the case given in Fig. (d-f) corresponds to a shortening of the initial 100 fs pulse to below 10 fs by SPM and subsequent perfect phase compensation. The application of

such a process will be the foundation of most of the broadband femtosecond laser spectroscopy methodology presented in this thesis.

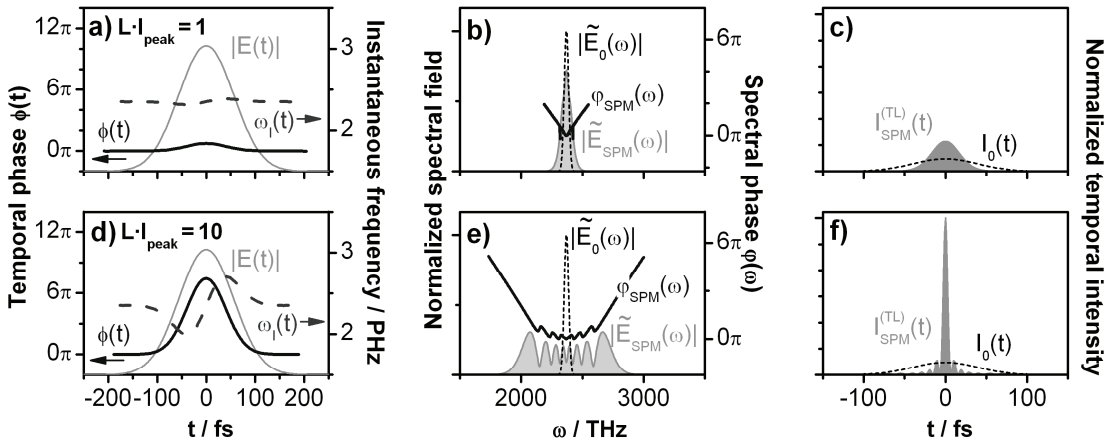

Fig. 2.4: Effect of pure self-phase modulation (SPM) on a 100 fs pulse. Shown are two cases, one of weak SPM (a-c) and of a ten times stronger SPM (d-f). Indicated are the temporal field $|E(t)|$ in the first column (a, d) together with the modulated spectral phase $\phi(t)$ and the resulting instantaneous frequency $\omega_I(t)$. Note that SPM retains the temporal shape of the pulse. This is different for the spectral field, shown in the second column (b, e). Compared to the initial amplitude spectrum $|\tilde{E}_0(\omega)|$ (dashed curve), symmetric spectral broadening occurs. Also, the spectral phase $\varphi_{SPM}(\omega)$ becomes modulated. If one manages to compensate for this spectral phase and restore a flat $\varphi(\omega)$, *Fourier*-transform limited pulses $I_{SPM}^{(TL)}(t)$ of much shorter duration (c, f) than the input pulse $I_0(t)$ (dashed curve) are obtained.

2.2.2 Properties of Photonic Crystal Fibres (PCF)

Photonic crystal fibres form a new class of optical material with unique properties. In principle, a PCF always consists of a periodic one-dimensional arrangement of structural elements on a length scale comparable to the wavelength of light. PCF principles and design has been summarized in an article by *Russel*,[41] while the physics of ultrashort pulse propagation and spectral broadening can be found in an comprehensive review by *Dudley et al.*[42] Here, only a very brief outline shall be given to place the experimental findings in context.

A typical index-guiding PCF is made from standard fused silica and features a periodic arrangement of air-filled holes around a solid core. To obtain polarization maintaining fibres, a symmetry breaking in the pattern is necessary (Fig. 2.5a). The periodic microstructure introduces a completely novel degree of freedom for material design, compared to bulk materials and *e. g.* conventional step-index fibres, in which optical properties such as the dispersion profile can only be modified within narrow boundaries by exchanging the material. In PCF, this limitation is lifted. It was found that PCF with micrometer sized cores and a high fraction of air-filling around it allow a dramatic shift of the dispersion curve, so that the fibre exhibits the transition from normal to anomalous dispersion already in the visible spectrum. Additionally, the reduced effective mode area in such fibres leads to an enhanced *Kerr* nonlinearity in the PCF compared to a standard fibre.

Both facts together are the foundation of supercontinuum generation even with weak ultrashort pulses, as strikingly demonstrated in the seminal work of *Ranka et al.*[43] For practical applications, the ability to tune the transition of normal to anomalous dispersion, characterized by the zero-dispersion wavelength ZDW, is of utmost importance. Pumping a fibre in the region of anomalous dispersion, leads to the broadest spectra generated at a given pump energy due to a multitude of nonlinear processes possible in this regime, including soliton dynamics.[42] However, these processes are also highly susceptible to noise amplification and therefore not the prime choice for a most stable compressible laser source. Matching the ZDW directly to the laser pump wavelength leads to highly diminished contributions of such processes, as only a fraction of the laser spectrum overlaps with the anomalous dispersion region. At the same time, the gross dispersion upon propagation is very low, which is of course advantageous for maintaining the high peak intensity of the pump femtosecond pulses in the process of broadening. Pumping entirely in the normal dispersion region restricts nonlinear processes almost exclusively to self-phase modulation, resulting in very stable spectra, but not reaching the enormous octave-spanning optical bandwidths of typical supercontinua generated by solitonic processes in the anomalous pumping regime. Another important factor is the fibre length. Even when pumping in the anomalous dispersion region, a very short fibre does not allow solitonic processes to come into play and emphasises only the initial self-phase modulation. Generally, spectral broadening of femtosecond pulses typically already saturates at lengths of several centimetres, whereas spectral coherence (and as such compressibility) diminishes markedly for long fibres. Thus, to achieve as high coherence as possible, the fibre length has to be kept at a minimum for a given spectral broadening required.

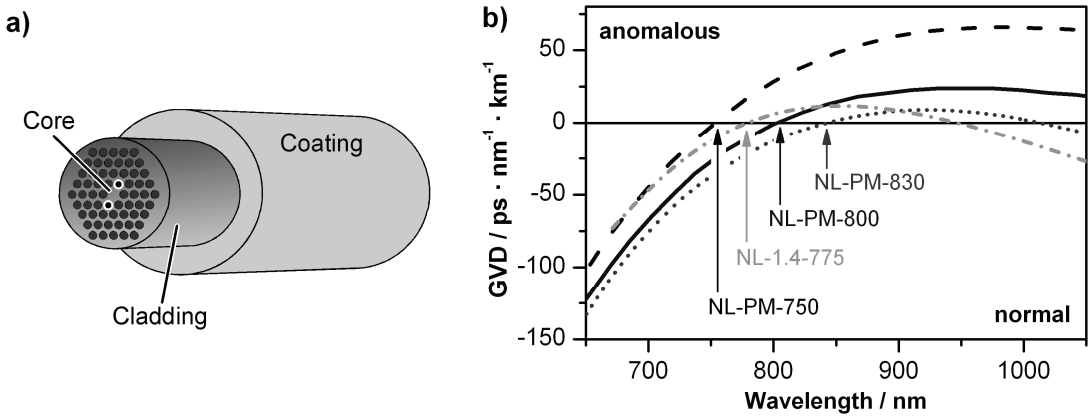

Fig. 2.5: a) Schematic drawing of an index-guiding PCF, featuring a micrometer-sized solid core, surrounded by air-filled holes in the cladding region. Two filled holes (or alternatively larger air-filled holes) introduce birefringence, and thus make this PCF polarization maintaining. A polymer coating provides mechanical stability and allows bending the fibre without breaking it. **b)** Group velocity dispersion curves for a set of PCF commercially available from *Crystal Fibre A/S* (Denmark). The fibres shown have zero-dispersion wavelengths (ZDW) at 750 nm (dashed curve), 775 nm (dash-dotted curve), 800 nm (solid curve) and 830 nm (dotted curve). Note that fibre type NL-1.4-775 is the only one without polarization maintaining (PM) design, but as a particularity has the second ZDW very close in the NIR.

In Fig. 2.5b, a selection of commercially available fibres is shown which have been used in this thesis. For a pump wavelength given by the maximum Ti:sapphire emission around 795 nm, these fibers allow covering from pumping fully in the anomalous dispersion regime (PCF NL-PM-750, dashed curve) to fully in the normal region (PCF NL-PM-830). The preferred fibres were all polarizazion maintaining, as this allows efficient continuum generation as well as use of the fibre output for pulse shaping and spectroscopy. Only the fibre of type PCF NL-1.4-775 does not preserve polarization, but is specifically designed to have a very closely lying second ZDW at 945 nm. This leads to continua relatively robust towards pump pulse variations, with a double peaked spectrum at the two zero-dispersion wavelengths. Therefore, significant spectral energy is converted to the NIR part of the spectrum, which – together with the mentioned robustness – will make this fibre a good choice for experiments relying on broad coverage in the NIR, as will be seen in the next chapter (3.4).

2.3 Experimental creation of PCF continua

After having given a brief account of the physical mechanism and the desired fibre properties for coherent spectral broadening, a series of experimental findings shall be laid out to corroborate the theoretical considerations. The experimental realization is straight forward and shown in Fig. 2.6. It consists of a 100 fs laser oscillator as pump source protected from backreflections, which would interrupt the mode-locked operation, by a Faraday isolator (FI). The fs-laser light has to be coupled into the micrometer sized core of the PCF. This requires lenses with focal distances in the millimetre range. To avoid unnecessary dispersion of the pump pulses and yet achieve a diffraction-limited spot without spherical aberrations, the input coupling lens (L1) is chosen to be a single aspheric lens (*New Focus*, $f = 6.2$ mm, *NA* 0.40). For highest coupling efficiency it is important to match both the spot size and the numerical aperture *NA* of the input coupling to the PCF core diameter and aperture of acceptance. For example, the typical PCF type NL-PM-800 has a core diameter of 1.8μm and *NA* 0.38. To optimize the focussed spot size, a lens telescope can be used to adjust the beam diameter in front of L1. In the case of the laser used in this thesis, the input beam was already in the range of 3-4 mm, which leads to foci between 2.1 μm and 1.6 μm, well suited for the PCF.

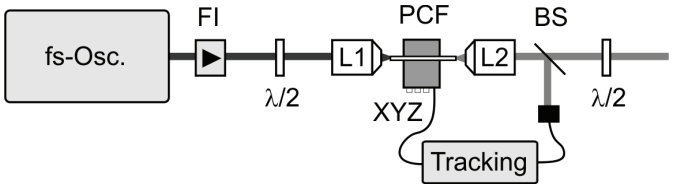

Fig. 2.6: Experimental setup of PCF continuum generation. The fs-laser oscillator is sent through a *Faraday* isolator (FI) and coupled into the PCF by an aspheric lens (L1). The PCF is mounted on a piezo-driven three-axis stage with active tracking on highest coupling efficiency. The generated broadband light is coupled out of the fibre by a microscope objective (L2). To accommodate for the birefringence of the polarization-maintaining fibre, λ/2 wave plates are placed on either side of the PCF.

The PCF itself is mounted on a 3 axis micrometer stage (XYZ), which can be operated manually and fine-tuned automatically by piezo actuators. The feedback signal for piezo stabilization is provided by a commercial fibre tracking system (*Thorlabs NanoTrack*), which allows increased long-term stability and very high day-to-day reproducibility of the PCF fibre source. Coupling of the continuum out of the fibre is performed with a microscope objective (40x, achromatic), again mounted on a three-axis stage. Due to the increased bandwidth, an aspheric lens cannot be used here due to its chromatic aberration, and the additional dispersion of a microscope objective has to be put up with.

To assess the pulse-to-pulse intensity stability of the 80 MHz PCF source including the active tracking system, output pulse trains of several µs duration were recorded with a fast photodiode and a GHz-oscilloscope. A statistical analysis resulted in 1-2% fluctuations of the output, while the fs-oscillator itself showed ~1% fluctuations. This proves that the insertion of the PCF does not introduce significant instabilities, which is the reason why it will successfully be used as broadband spectroscopy source. On this short timescale, switching off the tracking system did not deteriorate stability, being only effective for long-term drifts as mentioned before.

From the introduction in 2.2.2, the main experimental parameters to optimize PCF continuum generation under the pretext of using the maximum pump energy of ~3 nJ in our system clearly are the fibre length and the relative spectral position of the pump with respect to the zero-dispersion wavelength. Both parameters are examined in Fig. 2.7.

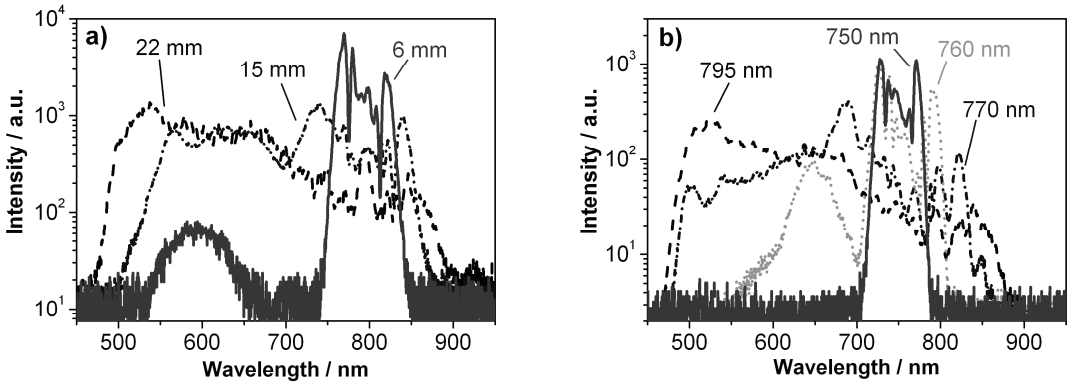

Fig. 2.7: PCF continuum generation dependence on experimental parameters. The fibre used for this comparison was always of the type NL-PM-750. **a)** Dependence on the length of the PCF, pumped in the anomalous dispersion region at 795 nm, starting from pure self-phase modulation at 6 mm length (solid curve) to broader spectra at 15 mm (dash-dotted curve) and 22 mm (dashed curve). In the latter cases, clearly solitonic broadening processes have begun to play a major role generating the huge increase in bandwidth. **b)** Dependence of continuum generation in a 22 mm long PCF on the pump wavelength used. As shown in a), pumping this fibre length at 795 nm (dashed curve) results in the broadest continuum. Shifting the pump wavelength to 770 nm (dash-dotted curve) or 760 nm (dotted curve), thus closer to the zero dispersion wavelength (ZDW), results in reduced bandwidth. Finally, pumping directly at the ZDW of 750 nm - even at this length - leads to broadening purely by self-phase-modulation (solid curve).

The experimental findings substantiate that the desired, highly coherent yet moderately broadened SPM spectra can be achieved in short fibre lengths and with pumping close to, or at the zero-dispersion wavelength. Consequently, if pumping in the anomalous dispersion region, the choice of very short pieces of PCF is mandatory.

The broadband light out of the fibre does not correspond to ultrashort pulses, as the spectral phase is not flat due to the self-phase modulation origin (see 2.2.1), additional nonlinear broadening processes and dispersion. If the spectra are fully coherent and have a stable phase, they can be measured and compressed to ultrashort pulses by active phase shaping, as will be shown later. In the case of extremely broad continua with solitonic origin, often intensity and phase fluctuations on the pulse-to-pulse scale are such that ultrashort compression is not possible. However, such spectra can still be very useful for spectroscopy in the frequency domain, if temporal fluctuations of the pulse shape can be tolerated. The most prominent example is their use for absolute frequency measurements,[44] for which *T. Hänsch* was awarded the Nobel Prize in 2005.

Tolerance towards temporal fluctuations is also the case in the broadband frequency-domain multiplex-CARS implementation described in the following chapter.

3 Broadband multiplex-CARS microscopy with a single laser source†

The implementation of CARS microscopy for label-free chemical imaging (see chapter 1) poses some technical challenges, which will be explained in the following sections. However, if a femtosecond laser is used and its spectrum tailored by means of filtering and spectral conversion in a photonic crystal fibre (PCF), a robust and comparably simple CARS microscope can be constructed. Such an approach will be described in this chapter. The presented engineering of the excitation spectrum is a first step on the way of introducing function to broadband excitation in order to exploit it for selective extraction of spectroscopic information.

3.1 Introduction to multiplex coherent anti-Stokes Raman Scattering

In CARS, three laser fields of different frequencies ω_p, ω_s and $\omega_{p'}$ create a signal emission blue-shifted with respect to the excitation by the energy spacing Ω_R of the vibrational level probed (Fig. 3.1a).

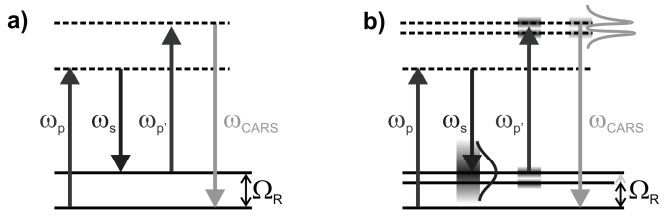

Fig. 3.1: a) Energy level representation of a CARS process. The frequency pair ω_p, ω_s coherently excites a vibrational level of the sample at the energy spacing $\omega_p - \omega_s = \Omega_R$, which is probed by $\omega_{p'}$ to generate the CARS signal at $\omega_{CARS} = \omega_{p'} + \Omega_R$. **b)** Schematic depiction of a multiplex CARS process. Instead of one frequency ω_s, a broader spectrum is used which allows to excite several vibrational levels at once. This leads to a blue-shifted CARS-signal which mirrors the vibrational spectrum.

The fact that the CARS process involves three laser fields interacting with the sample leads to an intensity dependence of the CARS signal to the power of three. Using ultrashort pulsed lasers to achieve high peak intensities at low average irradiation power, the CARS signal can be several orders of magnitudes stronger than a corresponding spontaneous *Raman* signal. This requirement of ultrashort lasers, together with the fact that up to three laser colors have to be provided for CARS, makes this nonlinear *Raman* process seem much more complex to implement. In fact, much effort has been put into synchronizing several pulsed lasers,[45] or to use rather complicated parametric optical processes to convert laser frequencies.[46] A conventional CARS setup still provides only a frequency combination (ω_p, ω_s) matching one specific vibrational level. The magnitude of the blue CARS signal is then an indicator of how many molecules with a matching vibrational spectrum are present

† This chapter has been published as a regular article "*Rapid polymer blend imaging with quantitative broadband multiplex CARS microscopy*" by B. von Vacano, L. Meyer and M. Motzkus in Journal of Raman Spectroscopy **38**, 916-926 (2007).

in the sample. To obtain a full vibrational spectrum, the laser colors have to be tuned sequentially. Alternatively, instead of providing only a single color of frequency ω_s within the set of laser frequencies in the CARS scheme (Fig. 3.1a), a broad spectrum containing different "ω_s" at the same time can be sent into the sample (Fig. 3.1b). This leads to a blue CARS emission, which contains the whole vibrational spectrum that can be probed within the bandwidth of ω_s. This technique is termed Multiplex CARS (MCARS). MCARS is well known in combustion diagnostics[47] and has first been developed for microscopy using a setup of synchronized ps- and fs-lasers.[48-50]

Multiplex CARS is very advantageous, as it allows acquiring entire vibrational spectra within a very short time of around hundred milliseconds. This way, rapid hyperspectral imaging can be performed to record the complete vibrational spectrum of every position in a sample. From this data, the chemical composition can be determined in its spatial variation, and thus real chemical mapping be achieved. However, for a routine usage of MCARS, several issues have to be addressed concerning the instrumental implementation: Only one laser should be needed, which should emit ultrashort light pulses and operate reliably. These requirements can be fulfilled by standard femtosecond laser oscillators. From this source, all frequencies necessary for MCARS have to be derived: This requires narrowing the spectrum of the fs-oscillator for the frequency component in the CARS process termed "pump" in the following (ω_p and $\omega_{p'}$, see Fig. 3.1b), and broadening it for the other, termed "*Stokes*" (broad range of frequencies ω_s), to obtain multiplexing over the whole range of chemically interesting vibrational energies (~ 400 - 4000 cm^{-1}). This is in contrast to the earlier MCARS microscopy studies,[48-50] which were only able to cover a range of a few hundred cm^{-1} around a selected *Raman* shift. Broadband MCARS acquisition with one laser can be accomplished using a combination of spectral filters and generation of supercontinuum radiation. The key feature is the spectral broadening of the low-energy femtosecond oscillator pulses, with spectral widths of only some nanometers, into supercontinuum spectra ranging over several hundreds of nanometers. Only recently this has become possible with the use of photonic crystal fibers (PCF, see previous chapter)[43, 51] or tapered fibers[52, 53]. This technologic development paved the way for a compact, one-laser implementation of CARS-[54] and broadband MCARS-microscopy, the latter of which has only recently been introduced independently by *Kee* and *Cicerone*[55] as well as *Kano* and *Hamaguchi*[56, 57].

In the following sections, the design considerations for a robust implementation of broadband MCARS for applications in material science and polymer analytics are developed and a prototypical experimental setup[58] is presented. Its operating parameters are characterized and successful MCARS spectroscopy and three-dimensional microscopic chemical imaging of polymer samples is demonstrated. For imaging, even complex MCARS spectra are decomposed quantitatively with a data analysis scheme which has been developed to obtain high-contrast images of the different chemical components. The analysis scheme allows decomposing the complex MCARS spectra, which contain interference terms form nonresonant background and the overlaid dispersive CARS line shapes into linear fields. This requires fitting of a physical model, as direct analytical inversion is impossible due to the detected square-law intensity. With the experimental simplifications and improvements and the availability of the powerful data analysis made available in this thesis, the setup proved so attractive, that it is subject of a beginning

industrial cooperation with the aim of establishing MCARS for the study of polymer samples.

3.2 Theory and Implementation considerations

The key challenge for MCARS is the generation of the laser excitation light needed to drive the nonlinear *Raman* process. The CARS signal generation is described by Eq.(3.1):

$$S_i(\omega) = N_i \cdot \int_0^\infty d\Omega \int_0^\infty d\omega' \left[\chi^{(3)}_{res,i}(\Omega) + \chi^{(3)}_{NR,i} \right] E_{p'}(\omega - \Omega) E_s^*(\omega') E_p(\omega' + \Omega), \tag{3.1}$$

where $S_i(\omega)$ is the complex electric CARS field of a pure sample *i*, which leads to the measurable CARS spectrum $|S_i(\omega)|^2$. *N* is the number of scattering molecules, $\chi^{(3)}_{res}$ the respective resonant and $\chi^{(3)}_{NR}$ the nonresonant part of the third-order susceptibility of the material, and $E_{p'}$, E_s and E_p are the components of the electrical field taking part in the CARS process as designated in Fig. 3.1 with their corresponding frequencies $\omega_{p'}$, ω_s and ω_p.

For an implementation of the CARS process, the fields E_p and $E_{p'}$ typically stem from the same laser source (frequency $\omega_p = \omega_{p'}$). The spectral width of this laser field then determines the minimal linewidth achievable in the MCARS signal, and therefore the spectral resolution of the experiment. For typical samples in the condensed phase, the width of vibrational *Raman* lines is in the range of a few wavenumbers. If a femtosecond oscillator output with a spectral width of typically 200 cm^{-1} bandwidth was used directly as E_p and $E_{p'}$ in a MCARS setup, the achieved spectral resolution of the apparatus would be rather poor compared to the vibrational line width. Therefore, it is necessary to spectrally filter only a smaller portion of the fundamental laser beam for use as E_p and $E_{p'}$. This can be done using specifically designed optical bandpass interference filters. Assuming that the pump spectrum is reasonably narrow, it can be approximated with $E_p(\omega) = E_{p'}(\omega) = E_p \cdot \delta(\omega - \omega_p)$, which simplifies Eq. (3.1):

$$S_i(\omega_p + \Omega) = N_i \cdot \left[\chi^{(3)}_{res,i}(\Omega) + \chi^{(3)}_{NR,i} \right] E_p^2 E_s^*(\omega_p - \Omega) \tag{3.2}$$

$$\left| S_i(\omega_p + \Omega) \right|^2 = N_i^2 \cdot \left| \left[\chi^{(3)}_{res,i}(\Omega) + \chi^{(3)}_{NR,i} \right] \right|^2 I_p^2 I_s(\omega_p - \Omega), \tag{3.3}$$

where I_p and I_s have been introduced as the intensities of the pump and *Stokes* beam, and $\Omega = \omega - \omega_p$ is the CARS shift. It has to be taken into account that Eq. (3.3) also gives an intensity dependence of the CARS signal proportional to I_p^2, and thus to the square of the intensity of the filtered beam. This means that while the spectral resolution increases linearly with a narrower spectral filter, the CARS signal intensity drops quadratically. Therefore, a reasonable compromise between resolution and signal strength with the given laser power has to be made.

As can also be seen from Eq. (3.3), the CARS-signal $|S_i(\omega_p + \Omega)|^2$ is only generated if the respective *Stokes* spectrum I_s is non-zero at the frequency $\omega_p - \Omega$, which means that its spectral width determines the range of wavenumbers that can be covered in MCARS. For broadband multiplexing, this spectral coverage has to be matched with the range of vibrational resonances occurring in chemical compounds, which is roughly 3500 cm^{-1}. In the case of a pump wavelength of 785 nm, a continuum of wavelengths ranging from the

pump wavelength to above 1050 nm has to be provided. We have seen in chapter 2 that such a massive frequency conversion can be achieved in photonic crystal fibres (PCF). As stated there, the choice of PCF has to be carefully made to generate a smooth and intense spectrum in the NIR, based on the available laser power, pulse length and on maximal operation stability. For the experimental implementation thus PCF with two closely lying zero-dispersion wavelengths are well suited.[59]

The need for high intensities in the CARS process makes it imperative to make efficient use of the available laser power. Therefore, the optimal solution is to either actively narrow the spectrum of the pump, which has been demonstrated for MCARS by *Andresen*, *Paulsen et al.*,[60] or to generate the narrowband pump beam from spectral filtering of the entire laser output, and to use the rejected light to generate the supercontinuum. The latter approach has been taken by *Kee* and *Cicerone*,[55] however it was achieved only with a rather complicated setup for the spectral filtering. On the other hand, commercially available interference band pass filters are much more robust and do not require any additional optical setup. Therefore, the alternative approach by *Kano* and *Hamaguchi*[56] included such simple filters, but was also based on a splitting of the fundamental laser beam into two portions, using one for supercontinuum generation and filtering the other, rejecting a reasonable amount of unused laser power. It would be ideal to achieve an experimental setup which uses simple optical interference filters, but still maintains the highest energy efficiency possible. These considerations are the starting point for the experimental implementation of broadband MCARS in this thesis, which is presented in the following section.

3.3 Experimental Implementation

A schematic representation of the experimental setup is shown in Fig. 3.2. The primary laser source used in this study is a Ti:Sapphire femtosecond laser oscillator (*Clark-MXR NJA-5*) pumped by a Nd:YAG–Laser (*Spectra Physics Millennia*), which emits 100 fs pulses centred at ~785 nm with pulse energies of ~3 nJ at a repetition rate of 80 MHz. The laser beam is sent through an optical faraday isolator (FI), which prevents the disruption of the mode-locked laser operation by any backreflections from the coupling into the PCF or from the microscope. It is then incident on the first of a set of interference filters (F1-F3), which have filtering characteristics matching each other. The first filter (F1) transmits only a narrow portion of the oscillator laser beam, namely an almost rectangular spectrum with a width of ~3 nm, which corresponds to ~50 cm^{-1} at the center wavelength of 783 nm (0.4 nJ, duration >500 fs). The filter works such that the rejected spectral portions are reflected. This reflected light (2.2 nJ) is used to create supercontinuum in 230 mm of a photonic crystal fiber (PCF) type NL-1.4-775 (*Crystal Fibre A/S*), which has two zero-dispersion wavelengths at 775 nm and 945 nm. The supercontinuum, ranging from below 700 to over 1100 nm, is recombined with the narrow pump beam, which can be delayed by τ with a linear stage, at an interference long pass filter (F2). This filter transmits wavelengths longer than 785 nm and reflects light with shorter wavelengths. Therefore, only the NIR part of the supercontinuum is transmitted. The spectrally narrow beam, which hits the filter on the opposite surface, is reflected, collinearly overlaying both beams.

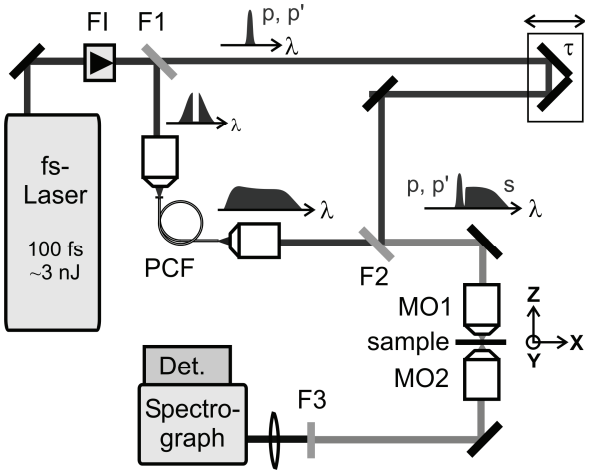

Fig. 3.2: Schematic drawing of the experimental broadband MCARS setup. FI: Faraday Isolator, F1: bandpass interference filter, PCF: Photonic crystal fiber, F2: longpass interference filter, MO1: microscope objective (60x, NA 0.7), MO2: microscope objective (40x, NA 0.6), F3: shortpass interference filter.

The collinearly propagating beams are sent to the microscope setup, consisting of the pair of microscope objectives MO1 (60x, NA 0.7) and MO2 (40x, NA 0.6). Finally, the blue-shifted CARS signal with wavelengths <760 nm is transmitted through a short pass interference filter (F3) for detection, while the excitation light is rejected. The ability to delay the narrow pump beam with respect to the supercontinuum is needed to be able to use the experimental setup with fibres of different length, and to choose an optimal temporal overlap between the two beams.

The detection of the blue-shifted MCARS-signal, which contains the complete vibrational spectrum of the sample at once, can on the one hand simply be carried out sequentially with a photomultiplier tube (PMT). This allows detection with very high sensitivity and rapid acquisition for single-wavenumber images, but has, for hyperspectral imaging, the disadvantage of giving away the time advantage of multiplexed acquisition, as now the spectrograph has to be scanned to acquire complete spectra. On the other hand, fast acquisition of the complete spectrum is achieved when using the spectrograph with a sensitive CCD multichannel detector (*Andor iDus DV420*), which can be Peltier-cooled to -70 C to suppress thermal noise.

The sample in the microscope can be scanned with a three-axis piezo translation stage (*Thorlabs PiezoBlock*) with a travelling range of 90 µm in each direction to obtain spatially resolved microscopic information. For reasons of stability even over very long measurement periods, and to compensate mechanical shocks that might occur, the coupling into the PCF is currently actively stabilized with a piezo positioning stage. The feedback of the intensity transmitted intensity through the fibre is used to drive the piezo voltages such that optimal coupling is maintained.

3.4 Characterization of the broadband MCARS setup

First of all, the successful creation of all frequency components necessary for MCARS has to be confirmed. Considering a spectrum of the combined narrow-band and broad-band beams (Fig. 3.3) recorded after the long pass filter (F2 in Fig. 3.2) shows an intense narrow peak around 785 nm, originating from the spectrally filtered fundamental oscillator beam. For wavelengths shorter than 785 nm, no intensity is detected, according to the steep cut-off of the long pass filter in this spectral region. On the side of larger wavelengths, a broad spectrum ranging into the NIR can be seen. While the spectral intensity in Fig. 3.3 for wavelengths smaller than 800 nm was determined with a fibre spectrometer (*Ocean Optics, USB-2000*), the data shown for wavelengths longer than 800 nm was obtained indirectly, as the sensitivity of the spectrometer was not sufficient in this wavelength range. Therefore, the NIR-part of the spectrum was determined from a spectrum of the sum-frequency between the narrowband pump (785 nm) and the supercontinuum from the fibre. It becomes visible that the spectral broadening achieved in the PCF reaches to wavelengths larger than 1050 nm and is sufficient to cover *Raman* shifts well up to 3500 cm^{-1}.

This can be corroborated by looking at the CARS signal generated with this excitation spectrum as described in the following. The CARS signal generation is dependent on the frequency components of both beams overlapping in space and time. Spatial overlap is established by carefully combining the narrowband and broadband beams in a collinear geometry. Temporal overlap of the pulses in both beams has to be found due to their differing optical path lengths. Furthermore, the new frequency components in the supercontinuum do not necessarily all arrive at the same time. Depending on the type of fiber, its length and all optical elements used in the beam path, the supercontinuum exhibits a time dependent momentary spectrum, called a chirp. For the application in CARS spectroscopy this translates into a spectral coverage of vibrational modes that is dependent on the relative delay τ of the narrow pump and the broad *Stokes* beam. In order to characterize the properties of the MCARS excitation, first CARS spectra are taken as a function of the delay τ between pump and *Stokes*. Such datasets are shown in Fig. 3.4.

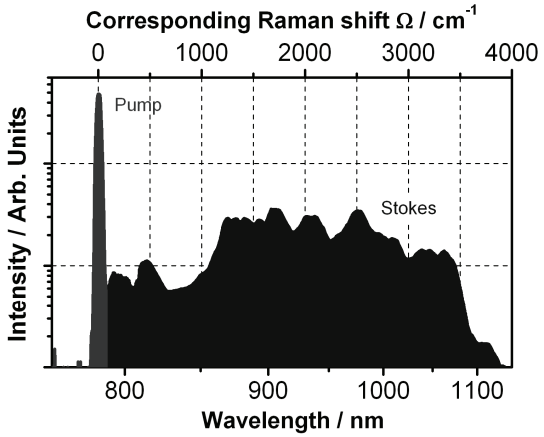

Fig. 3.3: Excitation spectrum measured after combining the beams at the longpass interference filter (F2 in Fig. 3.2). The intensity is shown on a logarithmic scale. Intensities for wavelengths larger than ~800 nm have been determined indirectly by sum-frequency mixing of the supercontinuum with the narrowband pump.

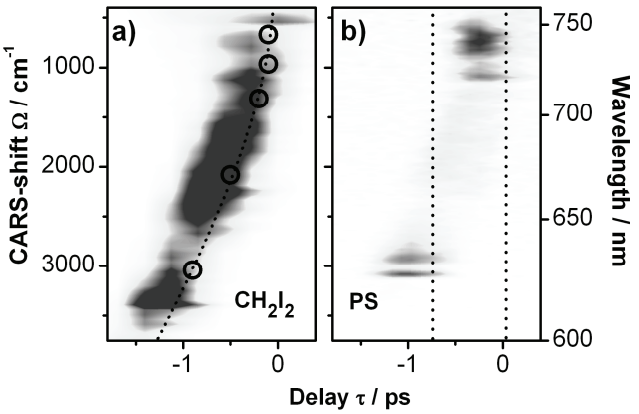

Fig. 3.4: a) Blue-shifted CARS signal obtained in CH_2I_2, dominated by nonresonant background. This measurement, performed with the photomultiplier, demonstrates a spectral coverage of the CARS signal from below 600 nm to above 760 nm, which corresponds to a anti-*Stokes* shift range of more than 3500 cm^{-1}, and clearly shows the chirp of the supercontinuum presently used. **b)** The same measurement for polystyrene (PS). For this sample it is obvious that there is almost only resonant CARS signal at 630 nm, 640 nm, and around 740 nm, corresponding to molecular vibrations at 3100 cm^{-1}, 2900 cm^{-1}, and around 1000 cm^{-1} respectively. The vertical dashed lines indicate two delays used for CCD acquisition of the complete spectral range.

A peculiarity of the CARS process is the presence of a nonresonant background signal due to $\chi^{(3)}_{NR}$ in equations (1) and (2), which does not contain information about the vibrational resonances of the sample. It is rather a smoothly varying offset in the CARS signal reflecting the *Stokes* spectrum I_s, and mostly unwanted. Normally in MCARS, the experimental conditions are such that the nonresonant background is weak enough to be able to discern the underlying vibrational resonances. There are cases, however, in which this is not the case and the vast majority of the signal is due to the nonresonant background. This is especially true for molecules which have strong electronic two-photon resonances near the excitation wavelengths used, for example Diiodomethane (CH_2I_2). The dominantly nonresonant signal from this molecule is very well suited to characterize the properties of the MCARS setup, especially how much spectral coverage can be achieved. Due to its independence from the presence of vibrational resonances in the sample, the nonresonant background directly shows which *Raman* modes would be detectable with the supercontinuum for a given delay τ. As can be seen in Fig. 3.4a, there is a continuous signal trace ranging from above 3800 cm^{-1} to below 500 cm^{-1} proving the complete coverage of chemically interesting vibrational modes with the established setup. It is also clear that this spectral range cannot be covered for only one given delay τ, because the supercontinuum is chirped. For a multiplexed CARS acquisition, this is a disadvantage. It can be mitigated either by scanning τ,[55] or be completely avoided if the chirp of the supercontinuum is removed by a careful choice of the PCF[61] or by chirp compensation, e.g. with pulse shaping,[17, 62] in an additional optical setup.

The same plot of the CARS signal versus τ looks markedly different for a polystyrene (PS) sample (Fig. 3.4b. In this case, there is - apart from a weak contribution - no continuous

signal trace, but only several bands with a constant CARS wavelength, parallel to the τ-axis. This is clearly indicative of a resonant CARS signal, and therefore of the vibrational spectrum of PS. In fact, the signals perfectly match the known *Raman* resonances at ~3100 cm^{-1} (C-H stretching on unsaturated carbon atoms), 2900 cm^{-1} (C-H stretching on saturated carbon atoms) and fingerprint signals around 1000 cm^{-1} (characteristic for aromatic rings).

This data proves the successful implementation of MCARS spectroscopy. With the current chirp properties of the supercontinuum, a delay τ can be chosen that allows either monitoring the high- or low-wavenumber range of vibrational spectra. To cover the whole spectrum in one run, the wavelength-scanning can be coupled to a simultaneous scanning of τ in the MCARS implementation with a single-channel detector (PMT) . Such spectra correspond to a section of the plots in Fig. 3.4 along a curve. This (τ, λ)-coupling was achieved here with a polynomial fit through a set of points obtained from Fig. 3.4a. For an implementation with a multichannel detector (CCD camera), sections are necessarily made parallel to the frequency axis, as indicated by the dashed lines in Fig. 3.4b. This pair of lines shows that the complete spectral range can however be covered with two subsequent acquistions at τ = -0.8 ps and τ = 0.05 ps.

3.5 Rapid MCARS Microscopy of Polymer blends

An important class of materials, where the knowledge of the spatial variation of chemical composition is vital for the understanding of their properties, are polymer blends. The blending of established polymers allows the development of new materials with tailored properties. However, many blends are characterized by a composition of polymers which are thermodynamically not miscible. This means that the mechanical properties, for example, are very much dependent on the morphology of the blend on the micrometer scale. At the same time, the phase separation behaviour and compatibility are sensitive to the addition of any other component, including dyes. *Raman* microscopy has been utilized to reveal the chemical distribution and domain size in various polymer blend systems.[63-67] However, due to the long integration times of up to tens of seconds per pixel, such studies are very time consuming. MCARS can dramatically accelerate such measurements and allows rapid acquisition of larger areas with higher pixel numbers. A polymer blend was also used for a first demonstration of chemical mapping in broadband MCARS.[55]

The polymer blend samples studied were provided by *BASF AG* as thin, opaque foils (size approximately 2 × 5 cm), partly with visible inhomogeneities on the millimetre scale. For the microscopy experiments, rectangles in the size of 3 × 4 mm were cut out, placed on a microscope slide and protected with a coverslip. For this rectangular clipping, regions were selected which did not exhibit visible inhomogeneity. The polymers examined (Fig. 3.5) include polyethylene (PE), polystyrene (PS), polymethylmethacrylate (PMMA) and polyethyleneterephthalate (PET). Tertiary blends consisting of PS, PET, PMMA, and PS, PMMA, PE were prepared by annealing the mixtures at 250°C and 230°C respectively for approximately two minutes and subsequent melt pressing at that temperature.

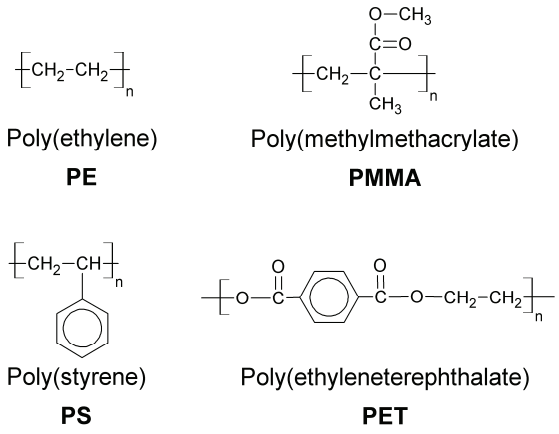

Fig. 3.5: Chemical structures and abbreviations of the polymers used in this study. The selection comprises polymers with saturated carbon atoms (only single bonds), such as polyethylene (PE) and polymethylmethacrylate (PMMA), as well as polymers with unsaturated aromatic rings in polystyrene (PS) and polyethyleneterephthalate (PET).

3.5.1 MCARS spectra of neat polymer samples

In Fig. 3.6 broadband MCARS spectra are shown for pure samples of PE, PS, PMMA and PET (Fig. 3.5). The data shown as solid black curves (hatched in grey) were obtained with single-channel acquisition and subsequent coupled scanning of τ and λ according to the fitted path shown in Fig. 3.4a (dashed curve). It can be seen that characteristic *Raman* resonances are found over the complete spectral range from 500 cm^{-1} to above 3200 cm^{-1}. The spectral resolution, determined from the smallest linewidth, is better than 60 cm^{-1}, in accordance with the spectral filtering scheme described in the experimental section. The spectra, which have been obtained without further data processing, show only a very weak nonresonant background, which manifests itself in the typical CARS-"dips" at the high wavenumber side of the CARS lines. This favourable ratio of resonant signal over nonresonant background was achieved by the optimized choice of the delays τ for each wavenumber, which in the fitting of τ versus λ in Fig. 3.4a) does not correspond to a trace following the maximum of the nonresonant signal, but is shifted about 0.2 ps towards a positive delay. This effect of a reduced nonresonant background can be understood by the temporal behaviour of the resonant and the nonresonant CARS signal (Fig. 3.7).

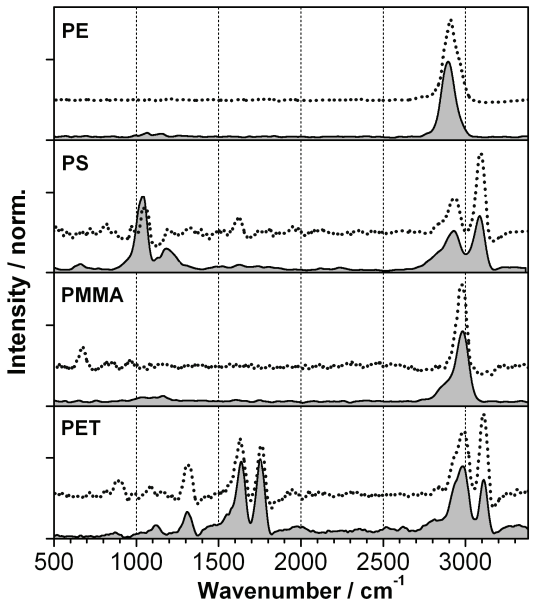

Fig. 3.6: Normalized broadband MCARS spectra from neat samples of polymer foils. The spectra shown as solid curves hatched in grey are obtained with single-channel detection, and simultaneous scanning of the wavenumber and the delay τ between pump and *Stokes*. The spectra shown as dotted curves are from multichannel acquisition with the CCD detector at two different delays τ, with subsequent removal of the nonresonant background (see Fig. 3.8 for details).

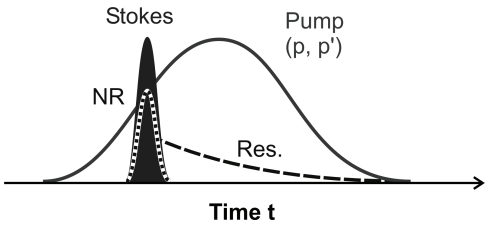

Fig. 3.7: Schematic depiction of the nonresonant background suppression by chosing a slightly positive delay between pump and *Stokes* pulse. The nonresonant response of the sample (dotted curve) is only probed during the temporal overlap of pump (solid curve) and *Stokes* (solid hatched curve), while the long-lived resonant signal (dashed curve) can be probed during the complete duration of the pump pulse.

While the nonresonant signal is only generated instantaneously during the temporal overlap of pump and *Stokes* pulse, the coherent resonant excitation of a vibrational level in the condensed phase lasts up to several picoseconds. Shifting the spectrally narrow and therefore temporarily long Pump pulse to a larger delay τ allows temporal overlap of the broadband *Stokes* pulse, which is much shorter in time, only with the leading edge of the pump. This favours the resonant contribution, because it can be probed during the remaining duration of the pump pulse, whereas the nonresonant contribution cannot.

Spectra recorded with the CCD camera necessarily correspond to vertical sections through the (τ,λ)-representation of the CARS spectrum. As mentioned before, to cover the complete spectral range, two acquisitions at different delays τ are necessary (dashed vertical lines in Fig. 3.4b), which can then digitally be stitched together to obtain the broadband MCARS spectrum. Such a spectrum for PET is shown in Fig. 3.8 as black solid line; the stitching has been performed around 2000 cm^{-1} (dashed vertical line in Fig. 3.8). It is obvious that in this case the nonresonant background is not negligible. Due to the acquisition at two different delays τ, the nonresonant signal has two maxima at 700 cm^{-1} and 2900 cm^{-1}. To remove the background, in a simple approach it can be fitted by a smoothly varying curve (grey shaded area in Fig. 3.8) through nodes at spectral positions, where no *Raman* resonances are to be seen. This background corresponds to a contribution which is, according to Eq. (3.3), directly proportional to $|\chi^{(3)}_{NR}|^2$ (which is practically constant), and to the *Stokes* spectrum I_s for a given delay τ. Therefore, it can be subtracted from the raw MCARS data and then used to perform an intensity correction of the MCARS spectrum (which is also proportional to I_s) by division. Such a procedure has also been applied in earlier broadband MCARS literature.[55, 56] The resulting intensity corrected spectrum is shown as dotted curve in Fig. 3.8 and, for comparison with the single-channel detector spectra, also for each polymer in Fig. 3.6.

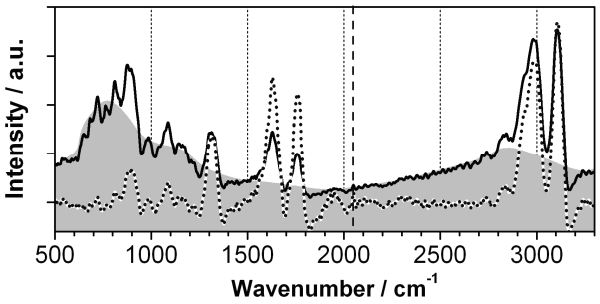

Fig. 3.8: Demonstration of the removal of nonresonant background from a PET broadband MCARS spectrum recorded at two different delays τ with the CCD camera. The two spectra were stitched at around 2000 cm^{-1}, as indicated by the dashed vertical line. The raw spectrum obtained is shown as black solid curve, the nonresonant background as grey shaded area. The nonresonant background can then be used to obtain the background-subtracted and intensity-corrected MCARS-spectrum of PET, shown as dotted line.

3.5.2 Quantitative analysis of MCARS spectra

The procedure described so far gives intensity-corrected spectra, which are in most cases well suited for the characterization of neat samples. The problem is, however, that this simple approach does not take fully into account the coherent nature of the measured CARS signal. For quantitative analysis of MCARS spectra, a more elaborate procedure has to be employed.[68] This becomes evident when considering the CARS signal $|S_{mix}(\omega_p + \Omega)|^2$ from a mixture of components: The total CARS signal is a coherent sum over all complex S_i:

$$\left|S_{mix}\left(\omega_p+\Omega\right)\right|^2=\left|\sum_i c_i\cdot S_i\left(\omega_p+\Omega\right)\right|^2, \tag{3.4}$$

where the coefficients c_i are the relative contents of the components i in the sample.

Eq. (3.4) gives rise to interferences between the contributions of all components, which has to be taken into account to determine quantitatively the coefficients c_i, and therefore the chemical composition from a measured spectrum $|S_{mix}(\omega_p + \Omega)|^2$.

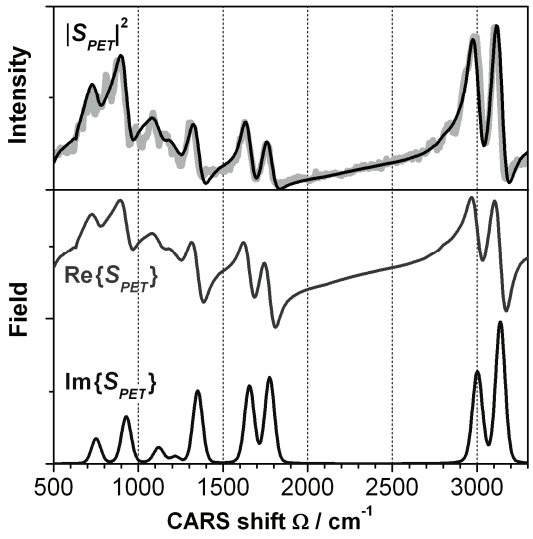

Fig. 3.9: Fitting of a complex CARS field to the measured raw MCARS spectrum (thick grey curve). The fit (black solid curve), shown here for the example of PET, allows reconstructing the real and imaginary parts of the field (see text for details). This is necessary for the quantitative analysis of MCARS spectra of mixtures.

In a first step, the complex electric fields $S_i(\omega_p + \Omega)$ are fitted to the raw MCARS spectra of neat PS, PE, PMMA and PET. The nonresonant susceptibility $\chi^{(3)}_{NR,i}$ in Eq. (3.1) was assumed constant for each polymer, and the resonant part $\chi^{(3)}_{res,i}$ described by a sum of complex dispersive lines of the following form:

$$\chi^{(3)}_{res,i}(\Omega)=\sum_n\frac{f_n}{\Omega_n-\Omega+i\Gamma_n}, \tag{3.5}$$

where Ω_n is the spectral position of a *Raman* resonance with amplitude f_n and linewidth Γ_n. The starting values for Ω_n and Γ_n were taken from the corresponding spontaneous *Raman* spectra of the polymers.[69] As an example of this fitting procedure, in Fig. 3.9 the raw experimental MCARS-spectrum (grey solid curve) is shown for PET together with the fit result $|S_{PET}(\omega_p + \Omega)|^2$ (black solid curve, see Table 3.1). In the lower part, the real and imaginary parts of $S_{PET}(\omega_p + \Omega)$ can be seen.

Table 3.1: Fitting coefficents for modeling the MCARS spectrum of polyethyleneterephthalate (PET) according to Eqs. (3.4) + (3.5). Starting values were obtained from literature.[69]

n	Vibrational energy Ω_n / cm^{-1}	Relative Amplitude f_n	Linewidth Γ_n / cm^{-1}
1	3134	2.5	5.1
2	2999	2.1	7.4
3	1772	3.8	5.3
4	1652	3.3	6.2
5	1347	3.0	5.2
6	1215	0.5	5.0
7	1117	1.0	11
8	925	1.2	17
9	747	0.5	7.0

When the complex CARS-fields $S_i(\omega_p + \Omega)$ of each component is known, the spectrum of any mixture of them can be described by Eq. (3.4) and a set of coefficients c_i. This procedure is used to obtain chemical maps from hyperspectral MCARS microscopic images: For each pixel the respective spectrum $|S_{mix}(\omega_p + \Omega)|^2$ is fitted using an evolutionary algorithm[70] to yield the coefficients c_i, which give the chemical composition of the sample at that position and therefore the chemical map.

3.5.3 Chemical mapping and virtual sectioning of polymer blends

The first polymer blend under study is a ternary mixture of PS, PET and PMMA. For this sample, broadband MCARS spectra were taken in the lateral *XY*-plane with an acquisition time of the CCD camera of 150 ms and a step size of $\Delta X = \Delta Y = 500$ nm. The delay τ was set such that spectra could be acquired from 1500 cm^{-1} to 3200 cm^{-1}. Again, a chemical map for the three components was constructed according to a fit of Eq. (3.4). Maps for PS, PET and PMMA, where the magnitude of the coefficients c_i is encoded in brightness, are shown in Fig. 3.10. Separate domains of the different polymers can clearly be seen revealing the morphology of the phase separation in the blend. From the smallest resolved features, the lateral spatial resolution achieved is estimated to be better than 1 µm.

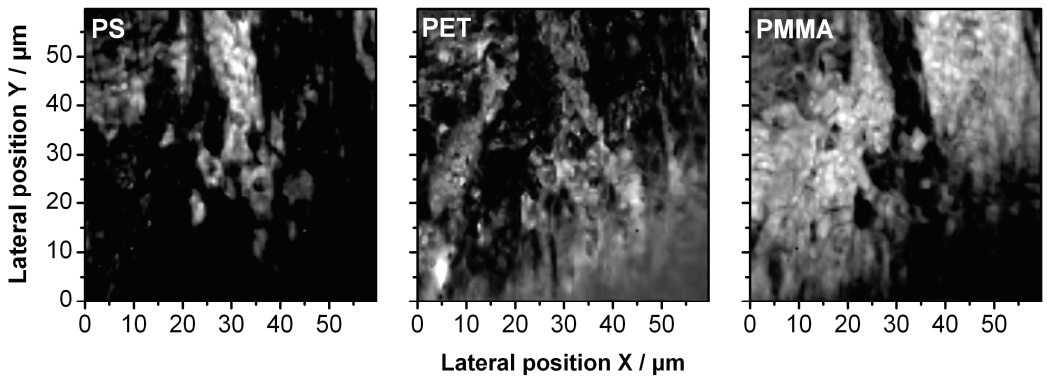

Fig. 3.10: Chemical map of a polymer blend consisting of PS, PET and PMMA. In each panel, the brightness of every pixel represents the magnitude of the fitted coefficients c_i, and hence the respective polymer concentration.

Further insight into the structure of the sample can be gained by a virtual sectioning of this sample along the *XZ*-plane. Such a section, recorded with step sizes $\Delta X = 600$ nm and $\Delta Z = 1$ µm, is shown in Fig. 3.11, revealing a rough surface and an average sample thickness of 22 µm.

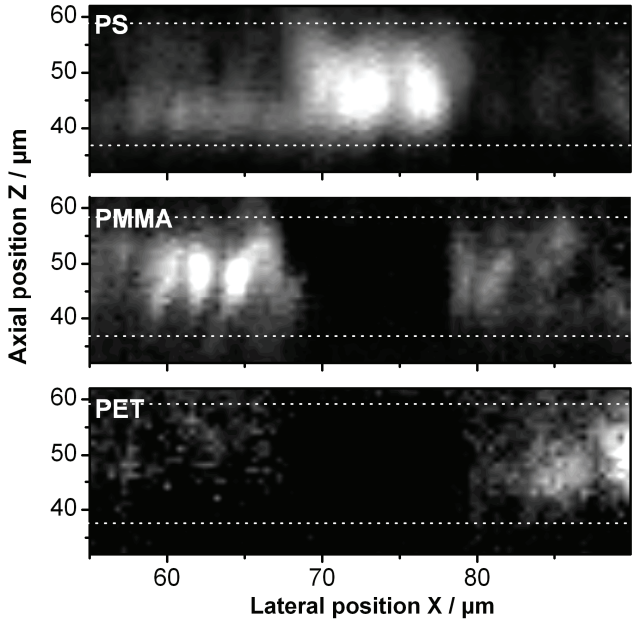

Fig. 3.11: Chemical map of a virtual sectioning through a polymer blend consisting of PS, PMMA and PET. The dashed white lines are guides to the eye, indicating the average sample thickness of 22 µm.

The second polymer blend sample consists of PS, PMMA and PE. The same experimental parameters were used to obtain chemical maps (Fig. 3.11). It can be seen that the region of the sample imaged consists mostly of PS and PE, which do not exhibit such sharp phase boundaries as was the case in the previous blend (Fig. 3.10). Some PMMA is also being found in the region for *X* around 40 µm. In this set of ingredients and at the given experimental parameters, PMMA and PE can only be discriminated by the spectral position

of the saturated C-H-stretching band at 2890 cm^{-1} (PMMA) and 2980 cm^{-1} (PE) respectively (Fig. 3.6).

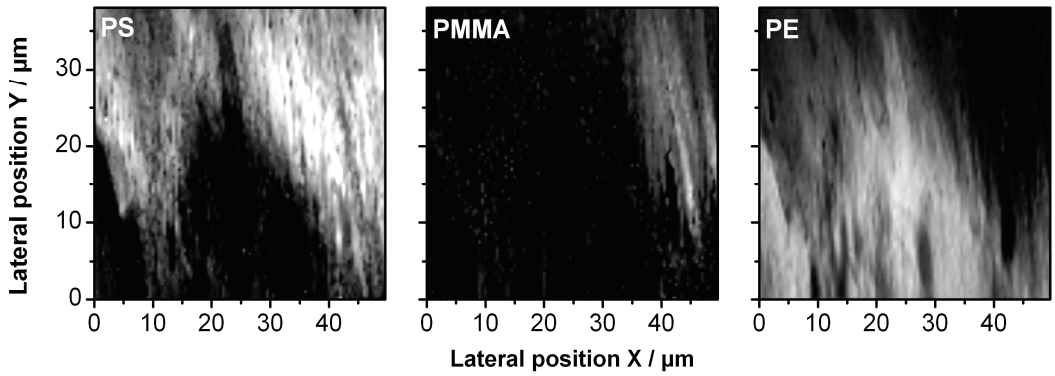

Fig. 3.12: Chemical map of a polymer blend consisting of PS, PMMA and PE. In each panel, the brightness of every pixel represents the magnitude of the fitted coefficients c_i, and hence the respective polymer concentration.

3.5.4 Chemical mapping and virtual sectioning of an unknown layered polymer sample

As an example of chemical mapping and virtual sectioning of a sample with unknown composition, a completely transparent adhesive tape (commercial *Beiersdorf AG "TESA film"*) was attached on a glass microscope slide and a hyperspectral MCARS image was taken as a section in the *XZ*-plane (Fig. 3.13). The step sizes were $\Delta X = \Delta Z = 1$ µm, and CCD multiplex spectra were recorded with an acquisition time of only 50 ms per pixel. In this example, a delay τ was chosen covering a spectral range from 2500 cm^{-1} to 3600 cm^{-1}. From the raw spectral data, it can be concluded that the tape consists of two layers with different chemical composition, *i.e.* the carrier film and an adhesive layer. The *XZ*-data was fitted according to eq. 3 with the procedure described in the previous section and a chemical map of the two components is obtained. The respective MCARS spectra of the carrier film and the adhesive are shown in the right panel in Fig. 3.13. It can be seen that the spectral signatures of both components overlap almost completely, but have a different shape. This difference is enough to obtain high-contrast chemical maps in the fitting procedure, clearly showing the layered structure in the left panels of Fig. 3.13. From this data, also the achieved axial resolution (in *Z* direction) can be estimated to be around 3 µm.

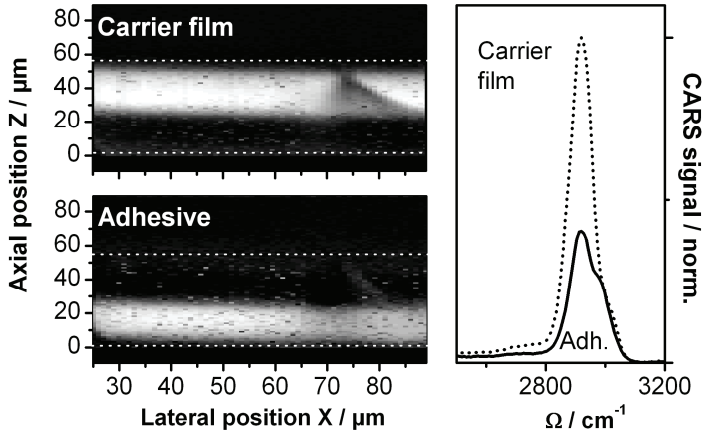

Fig. 3.13: Chemical map of a virtual sectioning through a transparent adhesive film. The left panels show the layered spatial distribution of the carrier film and the adhesive, the right panel the respective MCARS spectra of both components. The dashed white horizontal lines are guides to the eye.

3.6 Perspectives and further developments

The chemical maps obtained from the polymer blends, and from the adhesive film of unknown composition, confirm successful MCARS microscopy with chemical contrast in complex samples. Also, the fitting procedure to obtain the images has proven to be able to retrieve the chemical composition of mixtures from the broadband MCARS spectra even with heavily overlapping spectral signatures. The spatial resolution better than 1 μm in lateral and 3 μm in axial dimensions, while still offering room for improvement, is already sufficient to study the microscopic phase separation morphology of polymer blends and also to allow virtual sectioning. In the future, the setup can be optimized with respect to the chirp of the supercontinuum and the spatial resolution by applying changes to the optical layout. Furthermore, an even more compact and modular set-up could be devised. If the spectral resolution is to be improved, a narrower spectral filter or spectral compression[60] will be needed, which can be easily integrated in the setup. However, it is likely that in this case higher input laser powers are also required to maintain high enough CARS signal levels. Higher excitation intensities will also facilitate detection in backwards (epi-) direction, which is very attractive for many samples, as they can be highly scattering (like biological tissue) or even completely opaque (like many material samples). First work is presently underway to explore the potential of epi-MCARS microscopy with the presented setup, and has already shown promising results. However, the signal strengths are markedly lower and therefore longer integration times seem necessary. The mechanisms leading to CARS emission in epi-direction are also still subject of study,[71] as almost all detected signal seems to stem from backscattered forward signal, and not – as naïvely expected – from true epi-CARS emission. Applications of this broadband MCARS-setup beyond material analysis are of course also of great interest. In this direction, work is under way to explore imaging of biological material and cells. Also, the chemical selectivity of broadband MCARS has been shown in a proof-of-principle study to be suited for a rapid detection of microcrystals containing an anthrax marker molecule. This use of CARS for threat detection will be discussed in some more depth in section 5.5.2.

In summary, a detailed account of the implementation of a broadband MCARS setup has been given for the chemical mapping of polymer samples. The spectral resolution of 60 cm^{-1} is well suited to discriminate different polymers based on their CARS profiles, while the spectral coverage of the *Stokes* pulse, exceeding a bandwidth of 3500 cm^{-1}, allows detection of the complete range of chemically significant wavenumbers. Using the spectral information, the complex CARS fields can be reconstructed from the MCARS spectra of the pure polymer components, and this information used to perform a fully quantitative analysis of MCARS spectra of mixtures using an evolutionary algorithm. The resulting chemical maps show the spatial distribution of the components with high contrast. With single-channel detection, a coupling of the scanning of the wavenumber and the delay allows optimized sensitive spectral acquisition with simultaneous reduction of the nonresonant background, while CCD acquisition allows acquisition of spectra in as little as 50 ms. The sensitivity achieved is sufficient for successful studies of materials like polymer blends, where majority chemical species form structures of interest. Weakly scattering molecules in concentrations in or below the percent range usually are too challenging to detect in this scheme, although exceptions are possible given a suitable sample matrix or

signal amplification due to the involvement of electronic states resonant with the excitation laser light, as was found in first studies for samples of bacteriorhodopsin.[72]

It has to be stated clearly that quantitative analysis and removal of nonresonant background in the MCARS method is only performed *afterwards* by analysing the spectral shapes and fitting to physical models. This in many cases requires a substantial knowledge about the composition of samples, *e. g.* by providing MCARS data on pure components in mixtures. The measured signal itself always contains nonresonant background and shows the complicated behaviour of a squared coherent sum. This is the limitation of the present approach, which uses only spectral shape for achieving spectroscopic function. If the CARS excitation is performed with pulses of even higher functionality, all these issues can be addressed *within the experiment*. The requirement is a precise control over the spectral and temporal shape of the pulses and goes beyond spectral engineering: active shaping and phase management of ultrashort femtosecond laser pulses will be needed. The realization of this concept will be presented in the following chapters of this thesis.

4 Compression and phase management of ultrashort femtosecond pulses in a microscope[‡]

In order to use ultrashort femtosecond pulses in the environment of a microscope, it has to be ensured that they arrive *in situ* at the sample without temporal distortion. From the considerations presented in chapter 2 on pulse broadening and *chirp* due to material dispersion, it is clear that high-performance microscope objectives consisting of many optical elements require dispersion compensation when used in conjunction with the shortest of pulses (Fig. 4.1a). Furthermore, if the exact temporal shape of the laser pulses is to be exploited for spectroscopy, tight phase management is of even greater importance: phase distortions due to dispersion do not simply decrease efficiency (which is detrimental enough), but prevent spectroscopic function.

As introduced in chapter 1, for high excitation intensities in multiphoton microscopy femtosecond lasers are ideally suited due to their enormous ratio *G* of peak versus average intensity [Eq. (2.1)]. However, the shorter fs-pulses are, and thus the more efficient a nonlinear excitation can be, the more they are susceptible to broadening in time due to the dispersion of optical elements. In conventional femtosecond spectroscopy, dispersive optical elements are usually avoided for that reason whenever possible. In microscopy though, this is not easily possible due to the superiority of "conventional" transmissive objectives one does not want to abandon. Therefore, to obtain high peak intensities with as short pulses as possible, the inevitable distortions of the spectral phase have to be compensated for imaging under optimal conditions.[73] Furthermore, some fs-sources, for example inexpensive and compact fibre-based fs-lasers, already emit pulses with a spectral phase far from the *Fourier*-limit case. Only if this can also be accounted for in the compensation of spectral phase distortions, such a nonlinear microscope will reach its full potential.

Typically, the linear chirp of fs-laser pulses in microscopy has been compensated using grating or prism based passive compressor schemes,[74-77] adjusting the compressor to maximize a nonlinear signal from the microscope focus. For even shorter pulses, however, higher order dispersion becomes increasingly important. Additionally, the adjustment of passive compressors is time consuming and the setup rather inflexible. Very flexible compression of arbitrary phase distortions in the context of microscopy can instead be achieved employing femtosecond pulse shaping. This allows very rapid compression, in particular under changing experimental conditions. In addition, the use of a pulse shaper already is a prerequisite to create the arbitrarily shaped pulse sequences needed for advanced microspectroscopy schemes.

[‡] Parts of this chapter have been published in "*Actively Shaped Supercontinuum from a Photonic Crystal Fiber for Nonlinear Coherent Microspectroscopy*" by B. von Vacano, W. Wohlleben and M. Motzkus in Optics Letters **31**, 413-415 (2006), in "*In-situ broadband pulse compression for multiphoton microscopy using a shaper-assisted collinear SPIDER*", by B. von Vacano, T. Buckup and M. Motzkus in Optics Letters, **31** 1154-1156 (2006) and "*Shaper-assisted collinear SPIDER: fast and simple broadband pulse compression in nonlinear microscopy*" by the same authors in Journal of the Optical Society of America B **24**, 1091-1100 (2007).

With the capability to introduce arbitrary phases on an ultrafast laser pulse, pulses can be crafted to precompensate dispersion. This means that a pulse which is to travel through a piece of glass material will be shaped to have the right amount of *negative chirp*, with blue frequency components preceding red ones. After passing through the glass, the different group delays of red and blue parts have vanished due to dispersion, and the pulse is compressed (Fig. 4.1b).

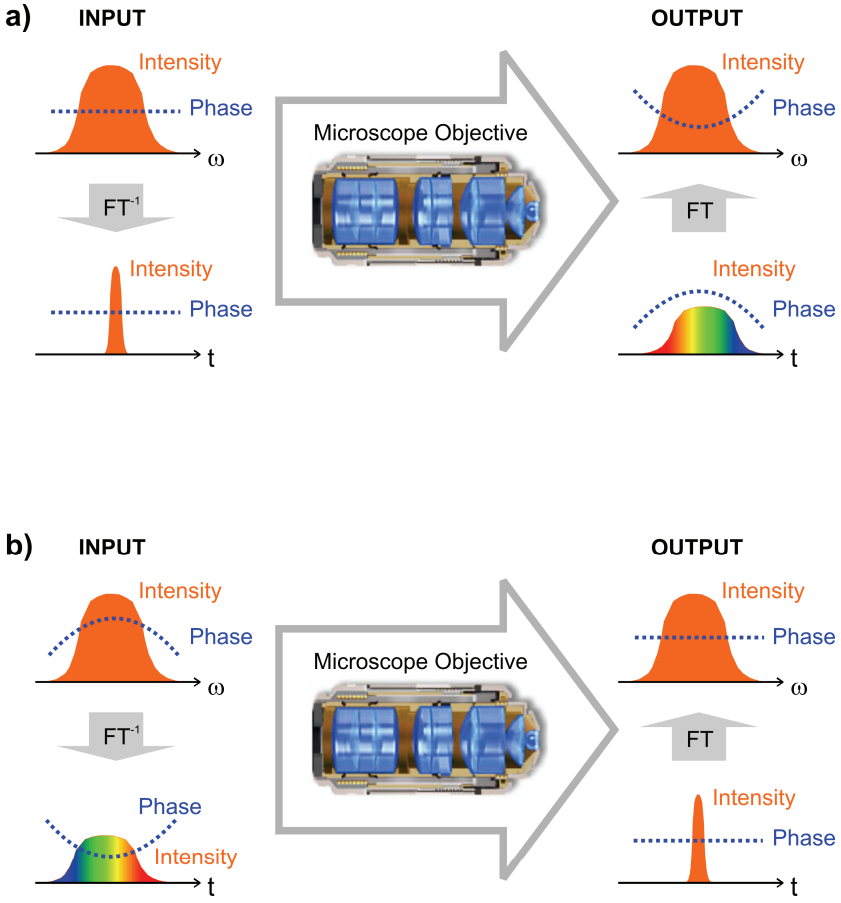

Fig. 4.1: a) Schematic depiction of ultrashort pulse propagation in a microscope objective consisting of a complex lens system (microscope objective graphics adapted from *Nikon, http://www.microscopyu.com*). The input pulse has a flat spectral phase, corresponding to a *Fourier*-limited ultrashort pulse. Due to dispersion, the red frequency components of the pulse propagate faster through the dispersive glass elements, while blue lags behind. This leads to a chirp of the focussed pulse, which manifests itself in a quadratic spectral phase in the frequency domain. **b)** Precompensation of material dispersion in a microscope objective. The input pulse is shaped in such a way, that it has exactly the sign-inverted phase that a transform-limited pulse acquires while passing through the objective. Thus, the pulse becomes *Fourier*-limited again in the focus, where it is needed for the spectroscopic interaction.

Therefore, to correct for phase distortions of the laser source and the additional propagation in a microscope, the appropriate phase to be applied beforehand has to be found. A simple approach is “trial and error”: to use a nonlinear signal or an autocorrelation trace measured at the site of the microscopic sample as feedback in an automated optimization, which is

typically based on a genetic algorithm learning loop.[70, 78, 79] A more sophisticated procedure is to measure the distortion phase and use this information directly to apply the exact compensation phase. Both approaches will be described in the following, but first of all the pulse shaper as the necessary tool will be introduced.

4.1 Short introduction to femtosecond pulse shaping

In principle, femtosecond pulse shaping can be achieved in two different ways: The first possibility is an optical *Fourier* transform performed spatially (from time to frequency domain in a so-called 4*f*-arrangement) using gratings and lenses;[80, 81] the second is the use of an acousto-optical programmable digital filter (AOPDF), which is based on a longitudinal acousto-optic interaction in an anisotropic birefringent crystal.[82] The AOPDF shaper is very compact, robust, but can only be used with fs-oscillators, if some experimental measures are taken to account for the high MHz repetition rates of fs-oscillators.[83] The alternative 4*f* setup, being slightly more complex, offers direct access to the laser pulses in the frequency domain and is compatible with any laser repetition rate, if liquid crystal modulators are used. A schematic view is shown in Fig. 4.2: The colours of the incoming fs-laser beam are diffracted from the first grating in different angles. Placed at the focal distance *f* of the lens (which is usually a focusing mirror in the experiment to avoid dispersion), the dispersed colours are parallelized and focused each at a different position in the *Fourier* plane, at another distance *f* from the lens. On the other side of the *Fourier* plane, the setup is reproduced leading to the characteristic 4*f* setup.

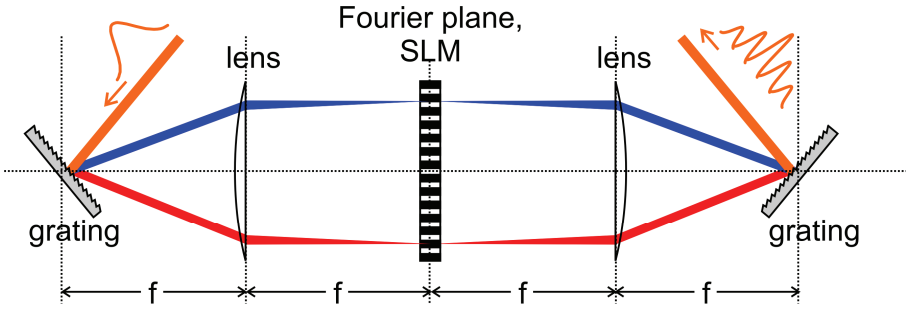

Fig. 4.2: Schematic diagram of a 4*f* femtosecond pulse shaper. An input pulse is split by a grating into its different frequency components, each of which is focussed onto a defined spatial position in the *Fourier* plane of the setup. A mirrored arrangement reverses the transform and reassembles an output pulse. In the *Fourier* plane, a pixilated spatial light modulator (SLM) can be placed, allowing manipulation of the amplitude, phase and/or polarization of each frequency component in order to create arbitrarily shaped ultrashort output pulses.

Pulses are shaped by controlling each frequency component with a spatial light modulator (SLM). By different means, the phase (and therefore the group delay), amplitude and even polarization for each frequency component can be set as desired. The modification of the group delay only requires phase shaping, by applying the integrated $T_g(\omega)$ as $\varphi(\omega)$, introduced in chapter 2.1. In this case of pure phase modulation, the complete bandwidth of the excitation source is maintained. Amplitude shaping on the other hand allows tailoring the spectrum, for example to achieve more complex pulse shapes. Amplitude shaping is

performed by SLM consisting of a double liquid crystal mask array. The double mask is arranged in such a way, that addressing of both displays for each pixel allows to independently phase-shift and rotate polarization. A polarizer at the output port of the shaper thus converts polarization rotation into amplitude modulation. Leaving this polarizer out, the polarization rotation can be used itself *e.g.* to create pulse sequences with alternating polarization on the femtosecond time scale (chapter 5.6.2).[84]

The operation of the shaper in phase and amplitude can be understood as a modulation of the input electric field $\tilde{E}_{in}(\omega)$ with a mask function $\tilde{M}_{SLM}(\omega)$:

$$\tilde{E}_{out}(\omega) = \tilde{E}_{in}(\omega) \cdot \tilde{M}_{SLM}(\omega) = \tilde{E}_{in}(\omega) \cdot \left|\tilde{M}_{SLM}(\omega)\right| \cdot \exp\left[i\varphi_{SLM}(\omega)\right]. \tag{4.1}$$

According to the *Fourier* convolution theorem, this results in the time domain in a convolution of the temporal input field $E_{in}(t)$ with the *Fourier* transform of $\tilde{M}_{SLM}(\omega)$:

$$E_{out}(t) = E_{in}(t) \otimes M_{SLM}(t) = \int_{-\infty}^{+\infty} d\tau \, E_{in}(\tau) \cdot M_{SLM}(t-\tau). \tag{4.2}$$

Eqs. (4.1) and (4.2) completely describe ideal pulse shaping. In reality, though, the shaper is always non-ideal. The consequences have been analyzed in depth in Ref. [85] and in the diploma thesis of *T. Hornung*,[86] which the reader might refer to for a detailed mathematical description of a realistic 4*f* pulse shaper. Also, some further aspects of pulse shaper pixilation have been discussed in a recent article by *Vaughan et al.*[87] Here, only a brief introduction to shaping "artefacts" shall be given to lay a foundation for the later discussion of shaping artefact effects in experiments. In Fig. 4.3, the effects of pixilation and pixel gaps occurring in a real life 4f shaper are summarized. The ideal modulation in this exemplary case is a simple *V*-shaped phase to create two-color double pulses, and amplitude modulation is performed to attenuate the blue part of the spectrum to roughly half the intensity. The corresponding ideal output in the time domain looks as expected. The discretization due to the pixilation of a liquid crystal spatial light modulator has to be introduced by (i) multiplication with a *Dirac* comb function according to the pixel periodicity and (ii) subsequent convolution with the rectangular shape of the pixels, taking into account the small gaps between pixels. This leads to a mask modulation with discrete shaped phases and amplitudes, and unmodulated parts in the gaps, where the incoming spectrum is transmitted without phase and amplitude modulation. In the time domain, pixilation leads to the creation of temporal replica of the desired output pulse shape, which are dampened drastically by multiplication with the *Fourier* transform of the pixel shape. The presence of unshaped gaps leads to the appearance of an additional unshaped pulse replica at time zero.

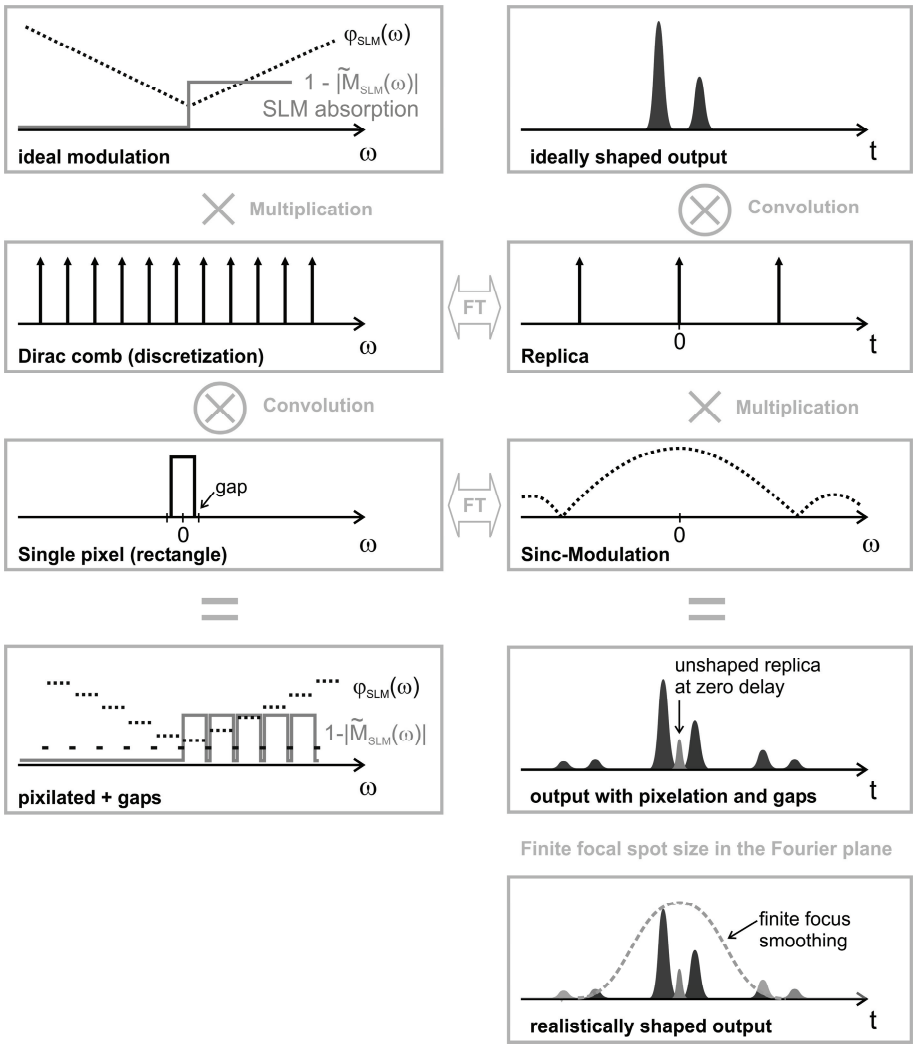

Fig. 4.3: Effects of pixilation in 4*f* femtosecond pulse shaping. The ideal mask modulation in phase $\varphi_{SLM}(\omega)$ and amplitude $\left|\tilde{M}_{SLM}(\omega)\right|$ is rendered discretely by a pixel pattern with inactive gaps in between the pixels. In the time domain, the pixel periodicity leads to replica, which are however significantly dampened due to multiplication with the *Fourier* transform of the pixel shape. The pixel gaps give rise to a small unshaped replica pulse. Due to the finite size of the focal spot size of each color in the *Fourier* plane, additional dampening of replica occurs.

Due to the finite focal spot size of each color in the *Fourier* plane, which for that reason is adjusted to be in the range of the pixel size, the temporal output is multiplied by the *Fourier* transform of the focal profile, which is typically *Gaussian*. This leads to further suppression of replica. From Fig. 4.3 it can also be immediately understood, that the pixilation of the SLM limits the dynamic range of temporal modulations the shaper can perform. The longest pulse structure in time will always be confined to the region defined by the *Fourier* transform of the pixel periodicity. This will be discussed in greater detail in chapter 5.3. If the spectral resolution is poorly chosen with a focal spot size in the *Fourier* plane much larger than the pixel dimensions, this dynamic range is even limited more.

Another artefact occurring in every 4*f*-shaping scheme is space-time coupling.[86, 88] This simply means that a temporal pulse shaping by applying a mask function $\tilde{M}_{SLM}(\omega)$ also

leads to a spatial modulation of the shaper output. As simple example, the effect of a linear spectral phase (which corresponds to a wedge-shaped phase object in the *Fourier* domain - just like a thin glass prism) is demonstrated in Fig. 4.4.

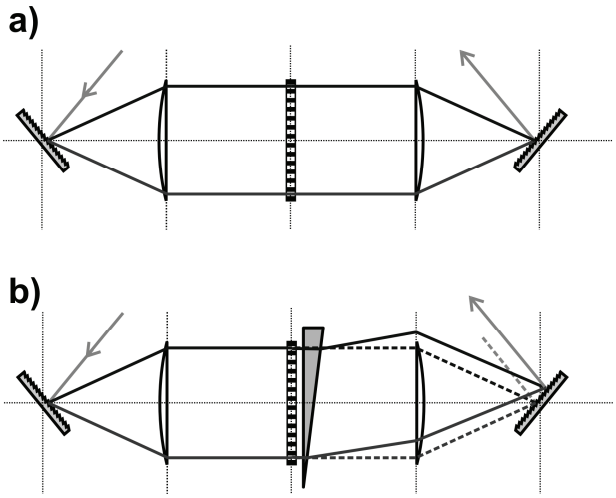

Fig. 4.4: Space-time coupling in 4*f*-pulse shaping. **a)** 4*f*-setup without applied phase function. **b)** Shaper with linear spectral phase modulation, which corresponds to a wedge-shaped phase object (*i.e.* a "glass"wedge). This leads to a spatial displacement of the output beam (solid versus dashed lines), which is proportional to the slope of the spectral phase, or in other words to the temporal delay introduced by the shaping.

4.2 Pulse compression by closed-loop optimization

The compression approach of "trial and error" can be considered an example of closed-loop optimization (Fig. 4.5), which is generally often applied for quantum laser control.[19] Starting from an initial assumption of a correction phase, which might as well be a zero flat SLM phase, a first generation of trial phases (each of them referred to as an "individual") is created randomly based on a suitable parameterization scheme.[70] Like this, each individual is described by a set of coefficients (called "genes"). Each individual of the generation is realized by the pulse shaper and tested in the experiment, *i.e.* the total second harmonic generation signal – which is inversely proportional to the pulse duration – is measured. The best individuals are selected for the next generation, with different mechanisms such as mutation (random change of a single gene in an individual) and recombination (creation of a new individual by combining genes from two parents) introducing new variation. Again, they are fed into the experiment to close the learning loop. In this way, better and better correction phases can be found, given that the parameterization allows well rendering the needed phase function. This application of a closed-loop learning algorithm was indeed one of the earliest implementations of the scheme in the context of ultrafast laser-matter interaction.[78, 79] The advantage is that no knowledge about the phase distortions is needed and only a simple feedback has to be established, the disadvantage is that the optimization is rather time-consuming and requires a well-suited parameterization which has to contain the optimal correction phase.

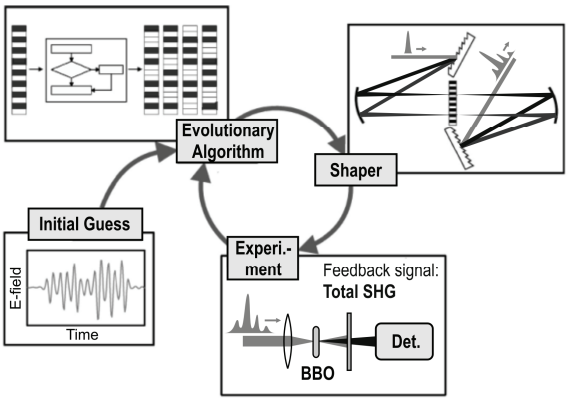

Fig. 4.5: Closed-loop optimization for compression of femtosecond laser pulses without *a priori* knowledge. An initial guess (*e.g.* the uncompressed pulse field) is fed into an evolutionary algorithm, which uses a given parameterization to generate a series of randomized variants of this initial field. Each variant is than realized by a pulse shaper and the resulting nonlinear signal measured. Based on the best trial solutions with the largest feedback signal, a new generation of variants is created, and the loop repeated, ideally until convergence is achieved.

Having said this, the choice of phase parameterization of the optimal learning is important. Classically, one would simply use a Taylor-expansion of the spectral phase, which usually allows expressing typical material dispersion (the quadratic phase in first order) very efficiently [Eq. (2.5)]. If more complex phase patterns arise, as is the case *e. g.* for self-phase modulation in photonic crystal fibers (chapter 2.2.2), non-polynomic phase parameterizations will often perform better. An efficient parameterization is able to render a set of compensation phases with suitable shapes with a minimum of parameters. The more parameters are used, the longer an optimization will take to converge. Therefore, a parameterization based on *Bézier* curves was developed in this thesis. *Bézier* curves allow rendering smooth functions which are "bent" into shape by placing a number of nodes (Fig. 4.6).

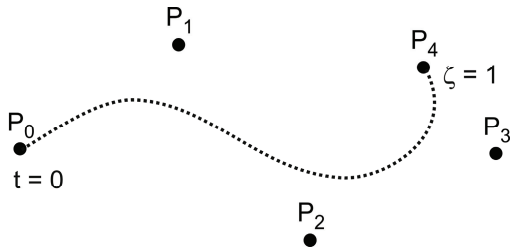

Fig. 4.6: Schematic *Bézier* curve defined by 5 control nodes. It can be seen that the curve starts in the first node (P_0) and ends in the last one (P_4), while the intermediate nodes exert "attractive forces" on the dotted curve itself. Therefore, by placing the nodes the shape of the curve can be altered, while smoothness is always ensured.

A *Bézier*-curve $\vec{C}(\zeta)$ is described as follows

$$\vec{C}(\zeta) = \sum_{i=0}^{n} \vec{P}_i \cdot B_{i,n}(\zeta), \tag{4.3}$$

where $\vec{C}(\zeta)$ is the (vectorial) curve dependent on a single parameter ζ, which describes any position on the curve from its beginning at $\zeta = 0$ to its end $\zeta = 1$. The set of $n + 1$ control nodes is given by the vectors $\vec{P}_i$, and $B_{i,n}(\zeta)$ are the *Bernstein* polynomials:

$$B_{i,n}(\zeta) = \binom{n}{i} \cdot \zeta^i \cdot (1-\zeta)^{n-i}. \tag{4.4}$$

As can be seen in Fig. 4.6, generic *Bézier* curves in a two-dimensional setting (in this case the two axes will be corresponding to phase *vs.* frequency or pixel in order to represent compensation phase functions for the shaper) generally are not unique functions of one of the axes (*e. g.* frequency), as they can include loops. To restrict *Bézier* curves to unique functions in the frequency or pixel axis, the set of nodes $\vec{P}_i$ has to be sorted such that $\vec{P}_i$ have ascending abscissa coordinates. This is shown as an example in Fig. 4.7, where eight nodes have been created with arbitrary ordinate phases and ascending abscissa pixel values. The flexibility of the *Bézier* curve upon variation of the ordinate value of the fourth node is also indicated.

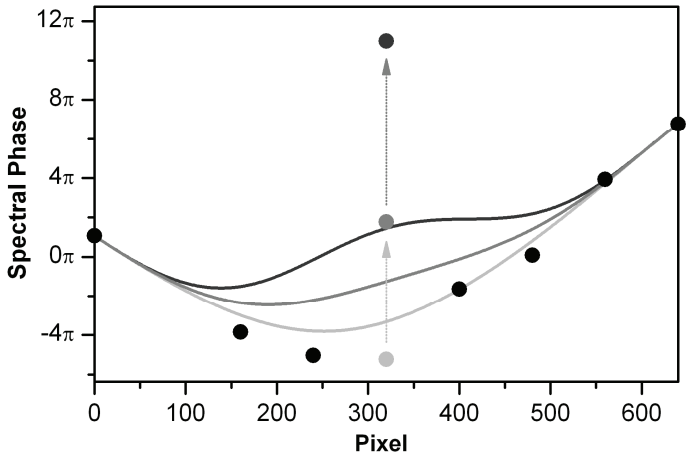

Fig. 4.7: Example of a *Bézier* curve based on nodes with ascending abscissa coordinates, which ensures unique phase functions. The ordinate coordinate of the fourth node has been varied from -4.5π to 11π, demonstrating the flexible "bending" of the curve. Like this, a limited number of parameters allowing generation of a very flexible set of smooth, realistic trial phase functions.

The experimental realization of closed-loop pulse compression (Fig. 4.5) in a multiphoton microscope using *Bézier* phase parametrization only requires the broadband laser source described in chapter 2.2, a pulse shaper, the microscope setup with a nonlinear medium for generating the feedback signal and detection (Fig. 4.8). In this work, second harmonic generation was chosen as feedback signal, which is easily implemented with a small fragment of a nonlinear crystal (BBO, type I) as sample in the microscope. To verify successful compression, a SHG - frequency-resolved optical gating (FROG) setup was added to the experiment, which could be provided with the shaper output by a flipping mirror (FM) alternatively to the microscope. Of course, the FROG measurement does not include the dispersion of the microscope objectives, but only the phase distortion due to dispersion in the PCF and the self-phase modulation processes.

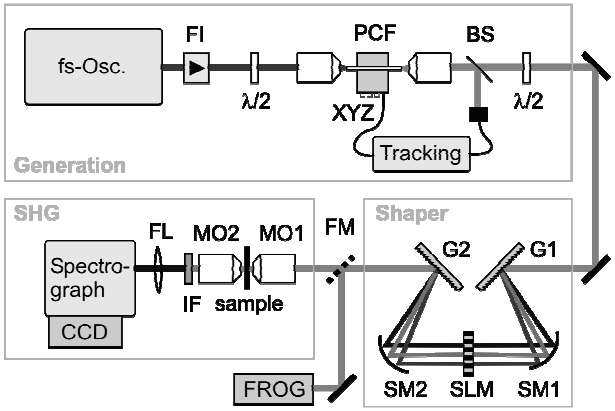

Fig. 4.8: Experimental setup for *in situ* broadband pulse compression using a closed-loop optimization. The setup for broadband laser generation is the same as described in chapter 2.3. Briefly, a standard 100 fs-oscillator is coupled into a photonic crystal fibre (PCF) to generate broadband continuum. This light is then sent through a 4*f* pulse shaper ($f = 200$ mm), consisting of a pair of gratings (G1, G2 with 1200 grooves/mm), two spherical mirrors (SM1, SM2 with $f = 200$ mm) and a 640 pixel double liquid crystal spatial light modulator (SLM). The shaped pulses can be diagnosed either with an external frequency-resolved optical gating (FROG) setup, or second harmonic generation (SHG) can be performed with a crystal *in situ* in the microscope.

Therefore, the first step towards *in situ* compression in the microscope was a closed-loop optimization run on the total SHG signal in the FROG, which allows a direct characterization of the ultrashort pulses before and after performing the optimization. The SHG-FROG method can be understood simply as a spectrally resolved autocorrelation: integrating the FROG trace for each delay, the autocorrelation of the measured pulse is obtained. In the two-dimensional FROG traces, however, the exact shape of the pulse is contained in the symmetric pattern. A suitable reconstruction algorithm can use this pattern to compare it to trial solutions, and thus find the pulse shape which is responsible for creating such a FROG trace.[89, 90]

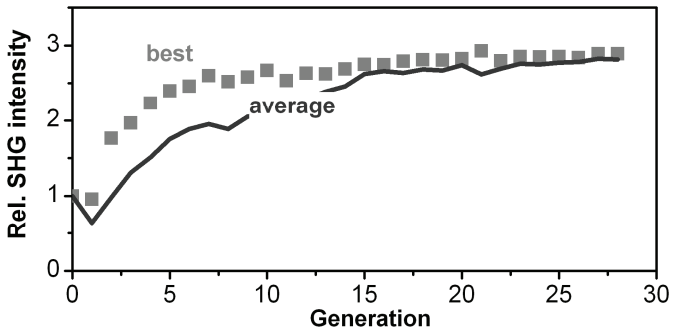

Fig. 4.9: Typical learning curve for a closed-loop pulse compression in situ in a microscope. The trial phase functions for the evolutionary algorithm have been parameterized by flexible *Bézier* curves with 12 nodes. See text for details.

The optimization was parameterized with a *Bézier* curve based on 12 nodes. Convergence of the evolutionary optimization typically and reproducibly occurred after ~30 generations, in about 30 min. A typical learning curve showing the average and best relative SHG intensity for each generation of the optimization can be seen in Fig. 4.9.

With the FROG setup, the uncompressed pulses have been characterized (Fig. 4.10a) and reconstructed (512×512 grid, FROG error 0.0061) to yield the complex spectral phase of the PCF output (Fig. 4.10c, solid curve), which due to additional fibre and experimental dispersion differs from the symmetric spectral phase expected for pure self-phase modulation, seen *e.g.* in Fig. 2.4, chapter 2.2.1. In Fig. 4.10c, the phase on the pulse shaper (dashed curve) shows that no modulation has been applied, hence it is a horizontal line. After optimization, with the optimal trial *Bézier* phase function found (Fig. 4.9) and applied in the shaper (Fig. 4.10d, dashed curve), the FROG trace looks markedly different, exhibiting by far most intensity centred around zero delay. The now reconstructed phase (512×512 grid, FROG error 0.0066, Fig. 4.10d - solid curve) is much flatter and only contains minor remaining "wiggles". Consequently, the optimal phase φ_{corr} found by the evolutionary algorithm directly corresponds to the smoothed, sign-inverted reconstructed phase of the uncompressed pulse (Fig. 4.10c, solid curve).

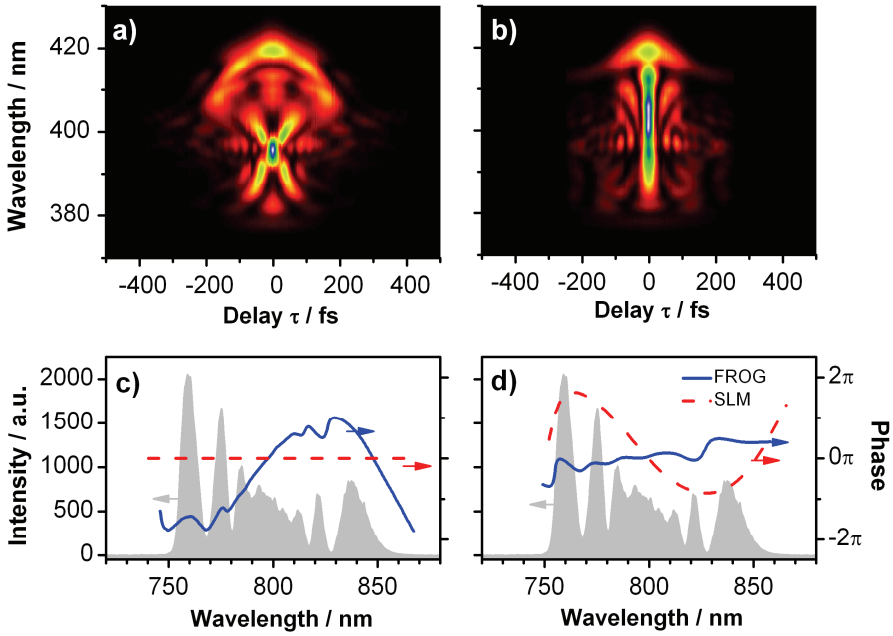

Fig. 4.10: Measurement of evolutionary pulse compression with frequency-resolved optical gating (FROG). The measured traces (a, b) can be reconstructed to yield the pulse spectrum and phase (c, d). Note that in the compressed case (d) the reconstructed phase (solid curve) is much flatter than in the uncompressed case (c), and the applied compensation phase found by the evolutionary algorithm (dashed curve in panel d) closely matches the sign-inverted reconstructed phase of the uncompressed pulse (solid curve in panel c)

In the time domain, the reconstructed compressed pulse has a duration of only 18 fs, which is very close to the *Fourier* limit of ~16 fs. These results prove that the evolutionary

algorithm is capable of compressing the PCF continuum, although so far only in the FROG setup. If the same procedure is followed for a flipped mirror in order to send the shaped laser beam into the microscope, very similar evolutionary optimization of SHG signal can be performed. At this stage, however, the pulses cannot be characterized directly as is possible in the FROG setup. Comparing the compensation phases found in the microscope with the phase φ_{corr} of Fig. 4.10d (dashed curve), the same functional shape is found with a strong additional quadratic term of $\varphi'' = -3800\ fs^2$ to compensate the dispersion of the microscope objective.

At this point, with the FROG pulse characterization available, it can also be shown how, moreover, compressed pulses can be shaped by adding an arbitrary phase modulation on top of the compression phase φ_{corr}. This shall briefly be demonstrated in Fig. 4.11 for a supplementary sinusoidal modulation $\varphi_{mod} = a \times \sin(b\omega + c)$ with $a = 1.23$, $b = 150$ fs and $c = 0$ to yield a shaper phase $\varphi_{SLM} = \varphi_{corr} + \varphi_{mod}$.

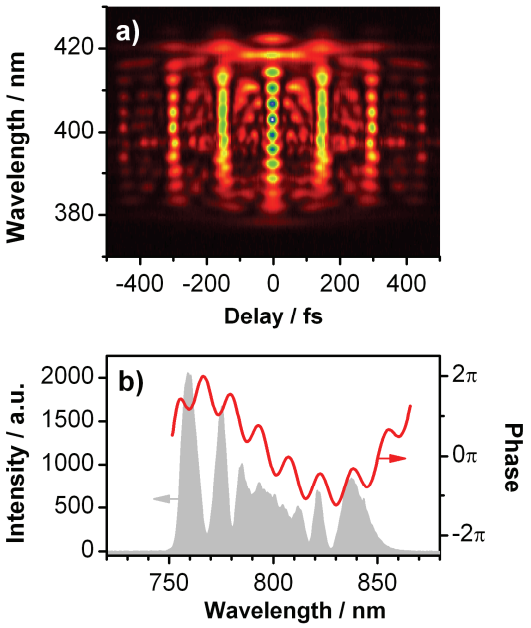

Fig. 4.11: FROG measurement (**a**) and accordingly applied phase φ_{SLM} (**b**) of a compressed PCF continuum with an additional sine modulation, leading to the splitting of the compressed pulse into a multipulse sequence. The intra-pulse distance b was chosen to be 150 fs, and the FROG trace shows the characteristic interferences expected for such pulse shapes.

As can be seen from this example, closed-loop optimization is able to successfully perform *in situ* compression for pulse shaping applications in microscopy. The drawbacks of the very simply implemented method are, however, that it is rather slow (~30 min) and does not reproduce all details of complex phase distortions (see remaining "wiggles" in Fig. 4.10d). This makes a faster, directly knowledge-based compression method attractive: in principle, the retrieved FROG phase (Fig. 4.10c) could be sign-inverted and used for compensation. While this procedure is possible for pulse compression in the FROG device, it will fail in the microscope, as the phase measurement has to be performed *in situ*. This is not possible with

conventional FROG, although FROG variants can also be developed for collinear beam arrangement (see *e. g.* XFROG implementation later in this text).

4.3 Direct phase measurement for compression

There are several schemes which have been applied or have the potential for *in situ* pulse characterization in microscopy. A common requirement is collinear beam geometry of the scheme to apply it with high numerical aperture microscope objectives. One possibility is a collinear variant of FROG, which has been demonstrated under the conditions of microscopy.[91-93] However, as mentioned before, the scanning of the temporal delay during the FROG measurement and necessary iterative reconstruction after the acquisition of the data makes this technique rather slow and prevents a practical use for rapid direct feedback of the retrieved phase for compression. There are other methods also relying on the subsequent scanning of a parameter to measure the spectral phase, which are already based on the presence of a pulse shaper in the experimental setup: One approach is time-domain nonlinear interferometry, where the necessary sequence of pulses with variable delay is generated by pulse shaping.[94] From the obtained interferogram, the spectral phase of the input pulse can be extracted and used for compression. This scheme has not explicitly been demonstrated for microscopy, but should be directly applicable due to its single-beam nature. Another possible approach, equally relying on only a single beam, is the multiphoton intrapulse interference phase scans (MIIPS) technique.[95] Here, the spectral phase of pulses is determined *in situ* by applying subsequently varying reference phase modulations, recording the frequency resolved second harmonic spectrum, and iterating this correction several times until the phase compensation is sufficient. MIIPS has been demonstrated in microscopy.[96]

The techniques mentioned so far are relatively slow and require scanning of at least one parameter. Therefore, they are not capable of a real-time characterization of the spectral phase. This highly desirable capability, though, even for the measurement of very complex phases, is known from spectrally sheared interferometry for direct electric field reconstruction (SPIDER).[97-99] Consequently, a shaper-assisted collinear SPIDER (SAC-SPIDER) was developed as a collinear implementation for the use in microscopy.[17] This novel scheme greatly simplifies the experimental setup by the use of the pulse shaper, and allows precise and very rapid *in situ* total phase control.

4.3.1 "Spectral shear interferometry for direct electric field reconstruction" (SPIDER)

Spectral interferometry techniques are based on the comparison of two mutually coherent beams. However, these techniques are only sensitive to the relative phase between the two sources. To measure the absolute phase of one of the beams, the phase of the other must already be known beforehand. A way out of this tight requirement is to use a self-referencing modification of spectral interferometry, such as the SPIDER method.[97-99] In the SPIDER method, the unknown test pulse is duplicated and both replicas are upconverted by mixing with a strong chirped reference pulse. The two up-converted replicas interfere and from the interferogram the spectral phase of the unknown pulse can be unambiguously retrieved (Fig. 4.12). The self-referencing in the SPIDER method is

achieved by delaying the two replicas against each other by a delay τ before the sum-frequency process. It ensures that each replica will mix with a different single frequency of the chirped reference pulse. The phase reconstruction in the SPIDER method is a straightforward process known from interferometry[100] and has been discussed in several publications in the context of SPIDER.[97, 98, 101]

The interferogram resulting from the two spectrally sheared, delayed replicas is *Fourier*-transformed and the sideband centred at delay τ in the time-domain is filtered out (Fig. 4.12). The filter width was found to be not very critical and independent on the signal-to-noise-ratio.[102] This sideband is then transformed back to the frequency domain with an inverse fast *Fourier* transform (FFT). That way, the phase variation of the unknown test pulse is obtained. The phase can then be directly reconstructed by a concatenation or integration process. The delay τ generates a linear term which can be easily measured in the experiment and needs to be subtracted as will be described in section 4.5.2 (p. 56). If this term is not correctly determined, it will give rise to a quadratic contribution in the reconstructed phase, which cannot be distinguished from such phase terms of unknown pulses.

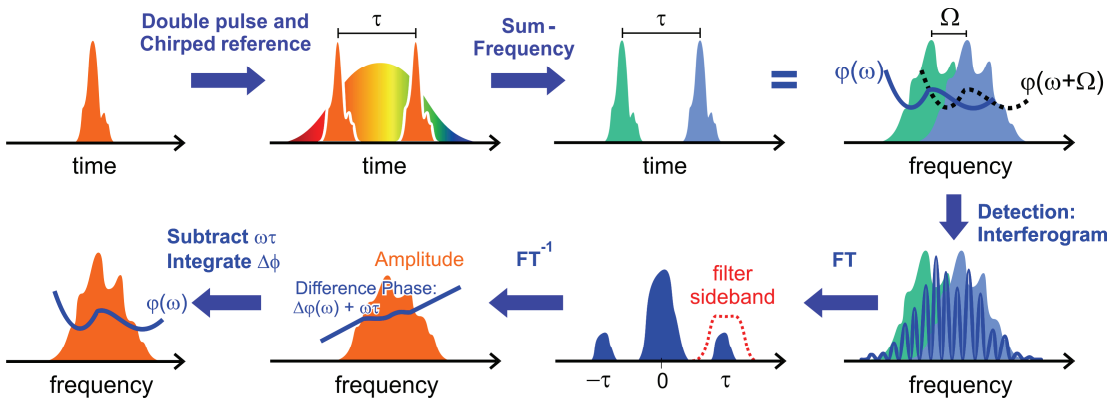

Fig. 4.12: Schematic diagramm explaining SPIDER phase reconstruction. From the pulse to be characterized two identical copies are created and delayed in time by τ. This input pulse doublet is then overlaid with a strongly chirped reference pulse, and sum-frequency mixed. Like this, each copy of the input pulse mixes with a different colour, leading to replicas frequency shifted by the shear Ω and separated by τ in time. These replicas interfere spectrally, yielding an interferogram which contains the phase difference given by Ω. Simple *Fourier* transform of the interference fringes, filtering of one sideband, reverse *Fourier* transform, subtraction of the linear phase term caused by the delay τ and concatenation of the phase with Ω gives the spectral phase of the unknown pulse.

The phase variation in the frequency domain is sampled with a frequency step given by the spectral shear Ω. That means that the choice of the spectral shear Ω can not be arbitrary: for *Gaussian*-shaped pulses, a ratio between the spectral width and the shear of about a factor 4 is enough to reconstruct the phase correctly. Depending on the complexity of the spectra, however, the shear must be chosen to be about 20-25 times smaller than the spectral bandwidth.[102] On the other hand, the frequency shear Ω is dependent on the amount of

delay τ between the replicas and on the group-delay dispersion *GDD* used to generate the chirp of the reference pulse:

$$\Omega = \frac{\tau}{GDD} \tag{4.5}$$

In practice, the amount of delay τ is chosen such that the sideband after the FFT in the phase reconstruction procedure is well separated from the central peak and that the number of fringes in the interferogram can still be resolved with the given spectrometer resolution. The *Whittaker-Kotelnikov-Shannon* sampling theorem states that in order to sample correctly the fringes, there must be at least two data points per fringe. The actual sampling rate required will be somewhat higher because of noise and other possible perturbations. It has been shown that a number of at least 20 fringes is enough to reconstruct the phase correctly.[99] Thus, for a given optimal delay τ the spectral shear Ω is fixed. Additionally, the amount of *GDD* of the reference pulse has to ensure that the instantaneous frequency is approximately constant during the unknown test pulse duration. Of course, even with optimized Ω, τ and *GDD*, the maximum relative phase variation that can be measured with spectral interferometry is still limited by the spectral resolution of the spectrometer.

The SPIDER method has the practical disadvantage that the unknown pulse must be split in two delayed replicas, which adds dispersion. To avoid additional dispersion for the test pulse in an interferometer, a zero additional phase SPIDER has been proposed,[101] where the chirped reference pulse is split into a doublet and mixed with an unmodified input pulse. The ZAP-SPIDER has the advantage that the delay between the up-converted replicas is now independent on the frequency shear. Both can be adjusted separately. However, this modified scheme cannot be implemented in a collinear geometry and is more complex to realize experimentally.

The choice of the nonlinear process for frequency conversion also plays an important role in the SPIDER method and its variants. In this sense, type II phase matched crystals are the best choice for the sum-frequency generation due to their larger phase-matchable bandwidth. Additionally, they are a prerequisite for background-free sum-frequency mixing in collinear beam geometry.

4.3.2 Principles of Shaper-Assisted Collinear SPIDER (SAC-SPIDER)

There is a possibility to construct a completely dispersion-free interferometer for the SPIDER setup: A pulse-shaper, capable of phase- and amplitude modulation, can be used to create double pulses, identical copies of the test pulse, which are then up-converted by mixing with the chirped reference pulse. For experiments which rely on a shaper anyway (for pulse compression or coherent control[19, 30]), this means that there is no need to introduce any other element in the beam path. It is only necessary to program the shaper for SPIDER compression.[17] To create double pulses with a temporal separation τ, the desired pulse-shaping effect in the time domain is a convolution of the input pulse with two *Dirac* delta functions at $t + \tau/2$ and $t - \tau/2$ (Fig. 4.13a):

$$E_{out}(t) = E_{in}(t) \otimes M_{SLM}(t) = \int_{-\infty}^{+\infty} d\tau \, E_{in}(\tau) \left[\delta(t + \frac{\tau}{2}) + \delta(t - \frac{\tau}{2}) \right] \tag{4.6}$$

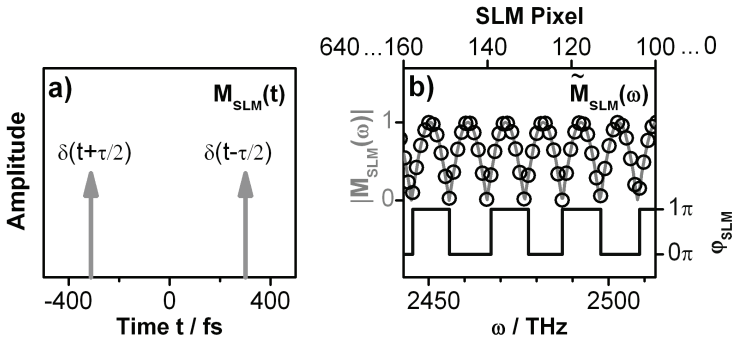

Fig. 4.13: Creation of double pulses with the fs pulse-shaper. **a)** Shaping target $M_{SLM}(t)$ in the time domain for the generation of the desired identical copies of the input pulse with a separation $\tau = 600$ fs in this case. **b)** Corresponding frequency domain modulation $\tilde{M}_{SLM}(\omega)$ with amplitude $\left|\tilde{M}_{SLM}(\omega)\right|$ and phase $\varphi_{SLM}(\omega)$ as realized by the pixilated SLM in the *Fourier*-plane of the 4*f*-pulse shaper. For clarity, only a section of the 640 pixel range is shown. For the given case ($\tau = 600$ fs), it can be seen that each period is rendered by 18 pixels, which is well above the *Nyquist* limit (see text for details).

To achieve such a shaping with a 4*f*-pulse shaper,[81] in the frequency domain the following mask function $\tilde{M}_{SLM}(\omega)$ has to be applied to the input spectrum [Eqs. (4.7) and (4.8)]:

$$\tilde{E}_{out}(\omega) = \tilde{E}_{in}(\omega) \cdot \tilde{M}_{SLM}(\omega) \,, \tag{4.7}$$

where $\tilde{M}_{SLM}(\omega)$ is given by:

$$\tilde{\mathrm{M}}_{\mathrm{SLM}}(\omega) = \mathrm{FT}^{-1}\left\{\delta\left(t+\frac{\tau}{2}\right)+\delta\left(t-\frac{\tau}{2}\right)\right\} = \underbrace{\mathrm{abs}\left(\cos\left(\omega\frac{\tau}{2}\right)\right)}_{Amplitude\ \left|\tilde{M}_{\mathrm{SLM}}(\omega)\right|} \cdot \exp\underbrace{\left[i\arg\left(\cos\left(\omega\frac{\tau}{2}\right)\right)\right]}_{Phase\ \varphi_{\mathrm{SLM}}(\omega)}. \tag{4.8}$$

For a liquid crystal spatial light modulator (SLM), this mask function is rendered as a discrete pattern on the pixels (Fig. 4.13b), modulating the input spectrum in phase and amplitude.

The modification of the period of the mask function in Eq. (4.8), parameter τ, enables the delay between the two replicas to be easily adjusted. Additional phase shaping is possible simply by adding a correction phase $\varphi_{corr}(\omega)$ to $\varphi_{SLM}(\omega)$, leading to a modified mask function $\tilde{M}_{SLM}(\omega)$. The maximum achievable delay τ depends on the number *N* of pixels illuminated by the spectrum and is limited by the *Whittaker-Kotelnikow-Shannon* sampling theorem. To create a clean double pulse, each oscillation of the mask function $\tilde{M}_{SLM}(\omega)$ has to be rendered with at least 4 pixels to ensure that $\tilde{M}_{SLM}(\omega)$ is well defined. This case constitutes the *Nyquist* limit. Hence, one can approximate that

$$\tau < \frac{\pi N}{2\,\Delta\omega}, \tag{4.9}$$

where $\Delta\omega$ is the bandwidth transmitted through *N* pixels.

The second essential requirement of SAC-SPIDER is collinear sum frequency mixing under tight focusing conditions. Such sum-frequency generation using high numerical aperture objectives, however, is rather easily implemented and even shows advantages over more conventional optical setups: Due to the tight-focusing condition, a much broader bandwidth can be phase-matched and the walk-off is strongly minimized.[91, 103]

4.4 Experimental implementation of SAC-SPIDER

The experimental setup is depicted in Fig. 4.14. The primary laser source used in this study is a standard Ti:Sapphire oscillator. It delivers 100 fs pulses with a central wavelength of 795 nm at 80 MHz repetition rate. Of this laser output, 25% are picked off[§] and a linear chirp φ'' of 37000 fs^2 is introduced for SPIDER measurements by a grating stretcher. This provides the intense chirped reference beam for the generation of the spectrally sheared replica. The use of a grating stretcher is by no means necessary or ideal; the introduction of linear chirp can be accomplished much more easily with a simple rod of highly dispersive glass. Finally, the polarization of the reference beam is rotated 90° with a $\lambda/2$ wave plate. The broadband femtosecond pulses to be compressed in this work with SAC-SPIDER stem from nonlinear spectral broadening in a photonic crystal fibre (PCF). This supercontinuum is created by focusing the remaining fundamental laser beam (about 3 nJ pulse energy) into a polarization maintaining PCF (Crystal Fibre, NL-PM 800, 24 mm). The resulting continuum with 1.2 nJ pulse energy is sent into a *4f*-pulse shaper, consisting of two gratings (1200 grooves/mm, G1-2) and two spherical mirrors (f = 200 mm, SM1-2). In the *Fourier* plane, phase and amplitude of each spectral component can be modulated by a dual mask 640 pixel liquid crystal spatial light modulator (SLM) with parallel thin-film polarizers. The shaper configuration transmits a spectral range from 750 – 880 nm, yielding shaped 0.3 nJ pulses.

[§] A 3:1 beamsplitter was chosen to generate the reference beam to maintain a sufficient power level for the creation of the desired supercontinuum spectrum. An optimal choice might be different for other applications; in this case it ensures high enough pulse energies of the compressed test pulses *in situ* for microscopy.

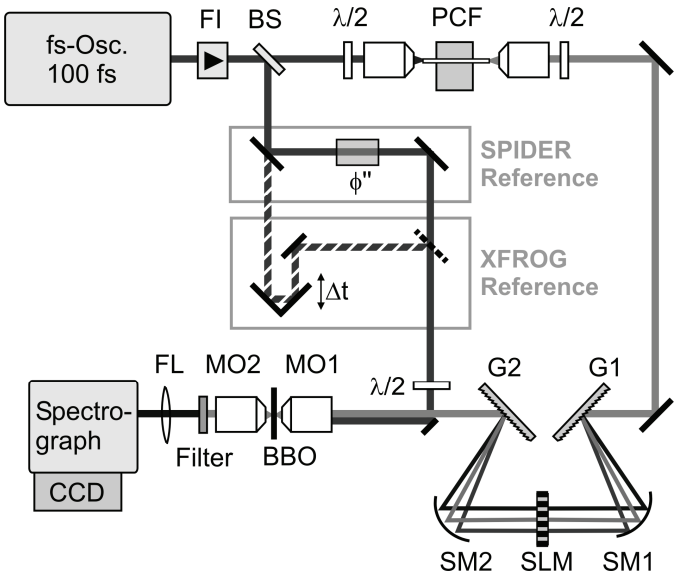

Fig. 4.14: Experimental setup. The fs oscillator output beam is sent through a Faraday isolator (FI) and then split into two parts. 75% of the energy are used to generate supercontinuum in a PCF sent into the fs pulse-shaper (G1-2: Gratings, SM1-2, spherical mirrors, SLM: spatial light modulator with 640 pixels for phase and amplitude modulation). The remaining 25% of oscillator energy are used to provide an orthogonally polarized reference beam, which is chirped (φ") for the SPIDER measurement. Both beams are collinearly superimposed and focused (MO1-2: microscope objectives) into a type II BBO crystal at the position of the sample. The sum-frequency generation is finally analyzed in a spectrograph (FL: focusing lens). The hatched beam indicates an alternative path for *in situ* XFROG measurements, where the reference beam is not chirped, but delayed by a variable time Δ*t*.

After collinearly superimposing the shaper input with the orthogonally polarized reference beam, both are focused with a microscope objective (60x, NA 0.7, MO1) onto a 50 µm BBO (Type II, $\theta = 45°$, $\varphi = 0°$). The generated nonlinear signal, together with unconverted excitation light, is recollimated with a second microscope objective (40x, NA 0.6, MO2). The desired sum frequency signal can finally be extracted by a short-pass filter (*Schott BG 42*), and detected spectrally resolved in a CCD equipped spectrograph ($f = 300$ mm). By not applying the group delay dispersion in the reference arm and introducing a variable delay Δ*t* instead (shown as hatched beam path in Fig. 4.14), the setup can immediately be used as an independent *in situ* cross frequency resolved optical gating (XFROG) device, where the unknown pulse is sampled by the 100 fs oscillator pulses and the resulting SFG spectrum is recorded for each Δ*t*.

4.5 Preparations for SAC SPIDER operation

4.5.1 Creation of pulse doublets

In the present study, a spectrum with a bandwidth $\Delta\omega$ of 400 THz was used, which illuminated approximately $N = 450$ pixels. According to Eq. (4.9), the maximum delay τ is therefore about 1.75 ps, which allows complete coverage of the usual double pulse spacing range found in SPIDER literature. To verify the successful creation of pulse doublets, we have applied mask functions $\tilde{M}_{SLM}(\omega)$ for different delays τ and recorded *in situ* frequency

resolved cross correlations (XFROG). Details of the XFROG measurements are given in section 4.7, where we use this technique to independently verify the SAC-SPIDER results. The experimental XFROG traces are shown in Fig. 4.15. In the top row (Fig. 4.15a), a cross correlation of the unshaped input pulse, which is to be characterized and compressed by SAC-SPIDER, can be seen. In this case, no mask function was applied to the shaper. The trace shown thus corresponds to the unknown pulse $E_{in}(t)$. Double pulses have been created with increasing temporal separations τ (200, 800 and 1600 fs). As can be seen in Fig. 4.15b), for 200 fs the resulting pulse is not a well separated double, because the duration of $E_{in}(t)$ still exceeds τ. Therefore, the replica of $E_{in}(t)$ overlap and yield an interference pattern in the XFROG trace. For $\tau > 800$ fs, the pulses are clearly separated.

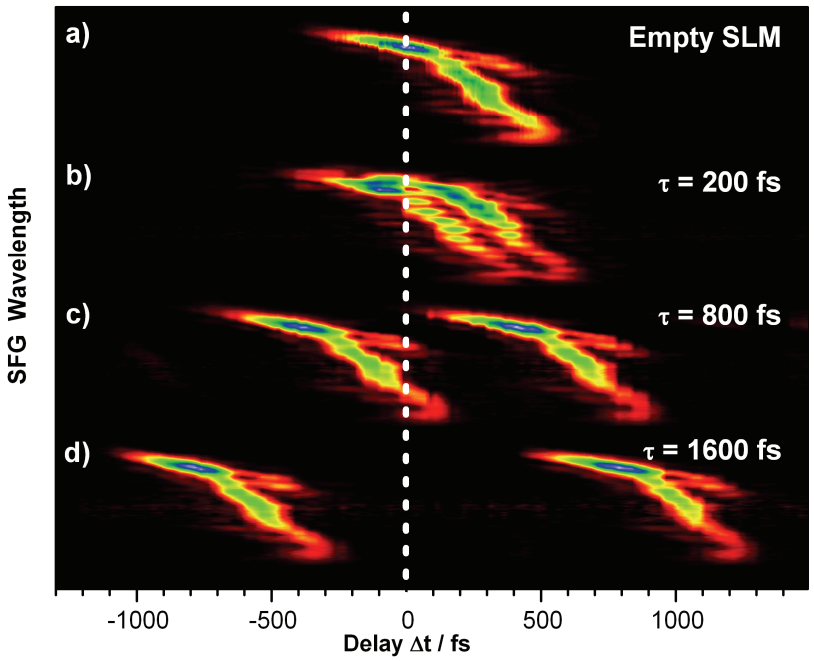

Fig. 4.15: Experimental confirmation of the double pulse shaping by frequency resolved cross correlation (XFROG, for details see section 4.7). Shown are data sets for an **a)** unshaped pulse and doublets with **b)** τ = 200, **c)** 800 and **d)** 1600 fs.

It can be seen that each of the replica, within the experimental noise of the XFROG implementation, exactly matches the unshaped $E_{in}(t)$. Even twice this temporal separation τ = 1600 fs allows the successful creation of double pulses with our pulse shaping approach, as expected from the estimation based on Eq. (4.9).

4.5.2 Calibration procedures

Apart from a carefully calibrated pulse shaper and spectrograph, there are three specific calibration steps that have to be performed for successful operation of the SAC-SPIDER. First, the measured spectral phase $\varphi(\omega)$ is going to be inverted and fed back to the pulse shaper. Therefore, the mapping between the fundamental frequency ω of the pulse to be characterized and the sum-frequency $\omega_{SFG} = \omega + \omega_{ref}$, where ω_{ref} is the effective mixing frequency of the reference pulse, must be known. With the amplitude modulation

capabilities of the pulse shaper, this relation can be very conveniently established, by simply creating a narrow spectral feature from the supercontinuum and measuring its fundamental spectral position ω' and the resulting sum-frequency ω'_{SFG}.

The second calibration requirement is the determination of the spectral shear Ω for the given chirped reference pulse and the temporal separation τ of the test pulse replica. Again, with SAC-SPIDER this can be achieved in a fully automatic scheme without any changes to the setup. Instead of creating a pulse doublet with a SLM mask function, the test pulse is only shifted in time by ± τ/2 using the pulse shaper. This is very easily achieved with a phase-only modulation, introducing the spectral phases $\varphi_{SLM}(\omega) = \pm (\omega-\omega_0)\cdot\tau/2$ one after the other, and recording the respective sum-frequency spectrum of the delayed pulses. As the pulse at - τ/2 overlaps with a different color of the chirped reference pulse than at + τ/2, the spectral shift of the sum-frequency spectrum immediately gives the shear Ω. To exactly determine Ω, it is necessary to have easily distinguishable spectral features, such as the maximum of a smooth *Gaussian* spectrum or a sharp dip or peak. If the spectrum of the unknown pulse does not show such a suited spectral feature, the pulse shaper can always create one by amplitude modulation, making the determination of Ω with SAC-SPIDER very easy and straight-forward.

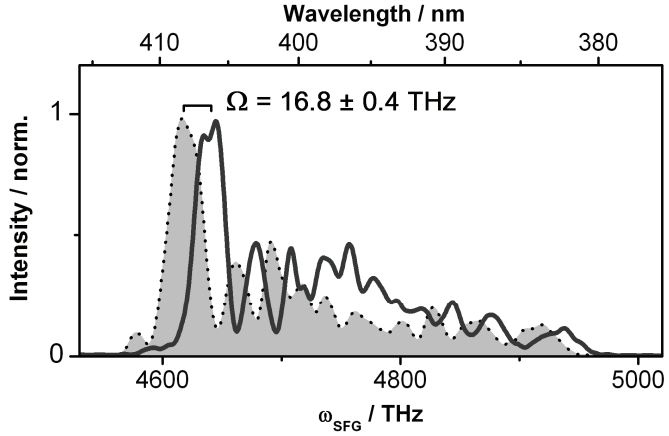

Fig. 4.16: Calibration of the spectral shear with SAC-SPIDER. Shown are two spectra created by sum frequency mixing of a single test pulse replica delayed by the shaper to 300 fs (+τ/2, solid curve) and -300fs (–τ/2, dashed curve and shaded area) respectively, with the chirped reference pulse.

An example of two spectra recorded by sum-frequency mixing of two test pulse replicas at + τ/2 and - τ/2 for τ = 600 f is shown in Fig. 4.16. The test pulse spectrum is well reproduced for both replicas, only showing some minor deviations in the relative intensities due to the mixing with different parts of the chirped reference pulse. Comparing distinct spectral features of the upconverted replicas, the spectral shear Ω is determined as average of 8 different positions yielding Ω = 16.8 ± 0.4 THz.

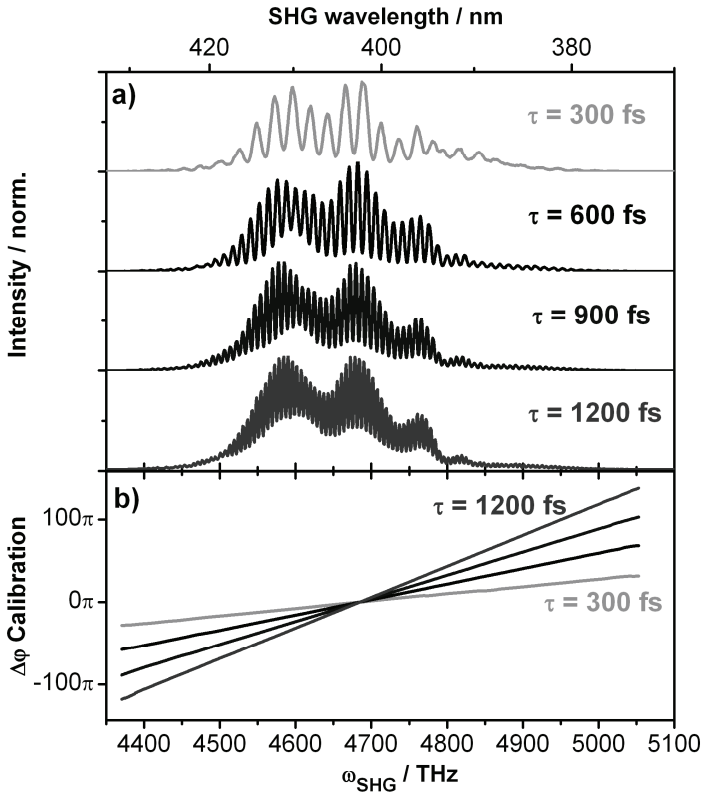

Fig. 4.17: τ-calibration. **a):** SHG-Calibration interferograms for different separations of the test pulse doublet. **b):** Phase differences retrieved from the calibration interferograms corresponding to the linear term introduced by τ (see text for details).

Finally, for the SPIDER measurement of the spectral phase, the temporal separation τ of the double pulses has to be known precisely. As already stated in section 4.5.1 (p. 55), the temporal delay between the interfering pulse doublet is directly proportional to the fundamental frequency of the interference fringes. In the SPIDER phase retrieval, the linear contribution of τ to the phase difference between the test pulse replicas has to be subtracted. As discussed in section 2.1, an incorrect value of τ will, in the SPIDER algorithm, lead to an erroneous quadratic contribution in the recovered phase. Additionally, deviations in the spectrometer calibration are known to lead to systematic errors in the recovered phase.[104] With a simple procedure, already applied in the seminal SPIDER work,[97] these issues can be addressed: It is only necessary to record an interferogram of upconverted replica pulses which are delayed, but not spectrally sheared. Due to the fact that $\Omega = 0$, the interferometric fringes only contain the linear phase term $\omega\tau$ and additional contributions due to residual errors of the spectrometer calibration. This phase difference can now be subtracted from any SPIDER measurement before the final integration step in the algorithm. To obtain the desired interferogram of upconverted, but spectrally not sheared replica, two approaches are viable with SAC-SPIDER. To begin with, due to the collinear nature of SAC-SPIDER it is possible to simply rotate the nonlinear crystal in the microscope focus for type I frequency mixing (both beams polarization parallel to the ordinary-axis) and blocking the reference beam. Thereby, each of the delayed pulse replicas is frequency doubled yielding the desired interferogram with $\Omega = 0$. Such calibration interferograms are shown in Fig. 4.17a) for different values of τ. To obtain the wanted linear phase difference $\omega\tau$, the interferograms are

processed in the SPIDER algorithm as described in section 2.1, without the last concatenation or integration step. This calibration phase is then stored in the SAC-SPIDER software, and subsequently subtracted prior to concatenation from any phase differences in SPIDER measurements with $\Omega \neq 0$. Note, that the mentioned deviations from a perfect linear phase difference $\omega\tau$ due to spectrometer errors are too small to be discernible in Fig. 4.17b), except at the very edges of the SHG spectrum. However, they have to be taken into account and subtracted with the calibration procedure for a precise SPIDER phase measurement.

The SHG procedure described so far is carried out very easily, but can only be used if the second harmonic of the test pulses lies in the same frequency range as the sum-frequency of the test pulse mixed with the reference pulse, which is evaluated for the SPIDER measurement. Additionally, the intensity of the test pulses needs to be high enough to generate enough SHG signal to detect, because in this calibration step they are not mixed with a strong reference beam. If this is not the case, a second approach can always be used, which is based on the same sum-frequency mixing process as the SAC-SPIDER measurement. In this approach, the chirped reference beam is filtered to a very narrow spectral portion, which corresponds to a long (picosecond-) pulse with approximately constant frequency. Now, the test pulse doublet is mixed in the type II nonlinear crystal, yielding two upconverted, but spectrally not shifted replica with $\Omega = 0$. In this procedure, the reference interferogram with $\Omega = 0$ is always created in the same spectral position where the SPIDER measurement is being performed. Furthermore, a strong reference beam can be used if very weak test pulses are to be characterized. The spectral filtering can either be achieved by a very narrow interference bandpass-filter in the reference beam, or conveniently by geometrical filtering in the *Fourier* plane, if the chirp of the reference beam is introduced by a grating stretcher, as is the case in our experimental implementation.

All the calibration steps can easily be completed within a few minutes, without changes to the experimental setup.

4.6 SAC-SPIDER operation

4.6.1 *In situ* Phase Measurement and Pulse Compression

With the SAC-SPIDER apparatus carefully calibrated, it can immediately be used for *in situ* pulse compression. As already mentioned in the description of the experimental setup, the microscopic sample is replaced by a thin slab of a nonlinear crystal (BBO). Therefore, all dispersive elements including the focusing microscope objective are taken into account. It is easily possible to include cover slips and even immersion media, depending on the microscopic application. The unknown test pulse in this study is formed by supercontinuum generation in a PCF. Prior to compression it is stretched in time over more than 450 fs at the site of the nonlinear interaction in the microscope, which can be estimated from the XFROG trace in Fig. 4.15a. To characterize this pulse, the first step is to apply a double-pulse forming mask function $\tilde{M}_{SLM}(\omega)$ (see section 4.5.1, p. 55). The temporal spacing of the double pulse τ has to be chosen appropriately for the given bandwidth, to achieve a set of experimental parameters τ and Ω which fulfil the SPIDER requirements

described in section 4.3.1 (p. 50). Here, τ was chosen to be 600 fs, which gives a calibrated spectral shear of $\Omega = 16.8 \pm 0.4$ THz. This value of Ω is well within the desired range for the bandwidth $\Delta\omega$ of 400 THz. The compression of the test pulse with these parameters is summarized in Fig. 4.18. Sum-frequency mixing of the test pulse doublet with the chirped reference beam in the nonlinear crystal gives the SPIDER interferogram of the uncompressed pulse, as can be seen in Fig. 4.18a) as a thin solid curve. Comparing the frequency shifted interferogram with the independently measured spectrum of the test pulse (Fig. 4.18a, grey shaded area) confirms that all frequency components are upconverted in the SFG process. From the interferogram, it can already be discerned that the fringe spacing is non-uniform. This corresponds to the spectral phase difference of the spectrally sheared test pulse replica being non-zero. Accordingly, the SPIDER algorithm retrieves a spectral phase (Fig. 4.18a, thick solid curve) which is dominated by a quadratic term, but also has complex higher order contributions. This phase measurement is performed with the pulse shaper acting only as dispersionless interferometer, *i.e.* no additional phase $\varphi_{corr}(\omega)$ has been applied and the shaper is used only to generate the replica pulse doublet. $\varphi_{corr}(\omega) = 0$ is depicted in Fig. 4.18a) as squares.

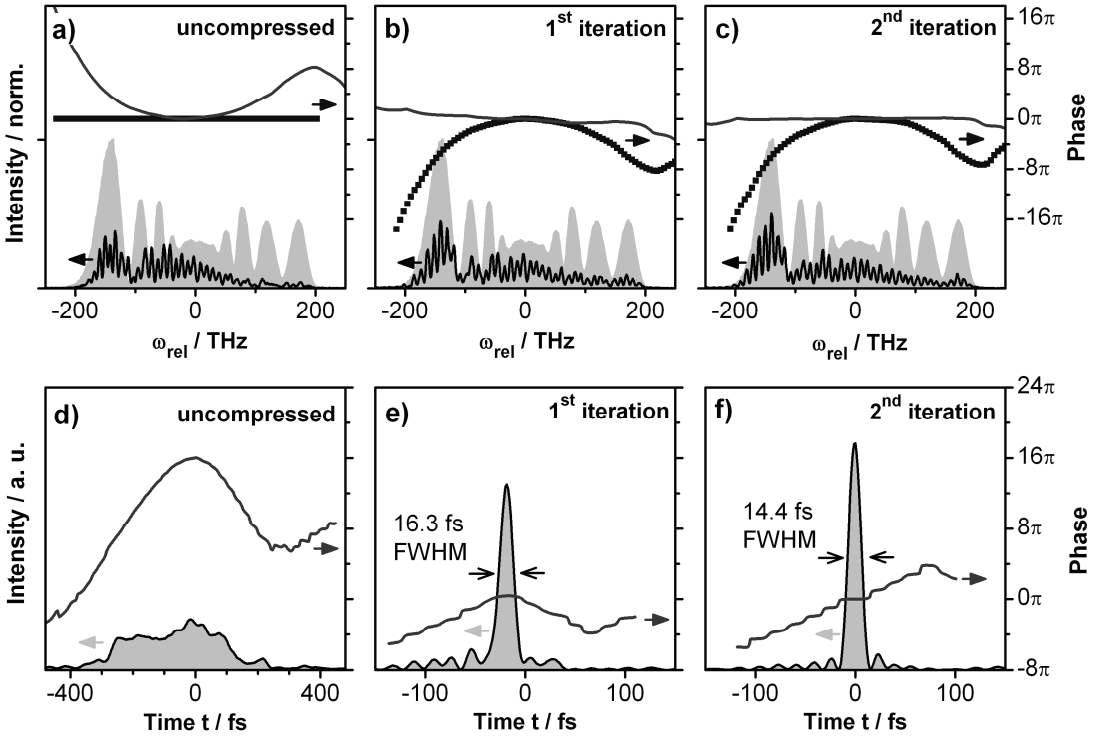

Fig. 4.18: *In situ* pulse compression with SAC-SPIDER. Shown are the pulse spectra, interferograms and phases in the frequency domain (**a**-**c**), and reconstructed temporal pulse profiles and phases (**d**-**f**). From the left to the right, the compression sequence can be followed with the uncompressed case (**a**+**d**), the first (**b**+**e**) and second (**c**+**f**) compression iteration. In panels **a)** to **c)**, the spectral phases are shown as thick solid curves, the shaper correction phase $\varphi_{corr}(\omega)$ as squares, interferograms as thin solid curves and the fundamental pulse spectrum as grey shaded area. All frequency domain data are shown relative to the pulse central frequency $\omega_{rel} = 0$. In panels **d)** to **f)**, the temporal pulse intensity is shown as grey shaded area with a thin contour, the temporal phase as thick solid curve.

This obtained phase information can now directly be used to apply a correction phase $\varphi_{corr}(\omega)$ in the pulse shaper. Evidently, the necessary correction phase is the sign-inverted measured phase of the unknown test pulse. This correction phase is shown in Fig. 4.18b) as squares. By applying the modified mask function $\tilde{M}_{SLM}(\omega)$ containing the correction, the interferogram changes and shows a much more uniform interference fringe pattern (Fig. 6b, thin solid curve). Accordingly, the reconstructed phase (Fig. 4.18b, thick solid curve) is much more flat. Still, there are remaining undulations in the residual phase. This residue can, however, simply be added to $\varphi_{corr}(\omega)$ in an iterative manner. Thus, in the second iteration step (Fig. 4.18c) the interferogram only shows subtle changes. The retrieved phase is now almost perfectly flat, and compression successfully achieved. This is confirmed when considering the reverse *Fourier* transform of the frequency domain data in the time domain to reconstruct the pulse shapes. The uncompressed test pulse (Fig. 4.18d) is stretched in time over more than 450 fs, as expected, and has a mainly quadratic temporal phase in the central part. The first compression step already produces a dramatic effect, as the pulse resulting from the flattened spectral has a temporal duration of only 16.3 fs (FWHM). The second iteration corrects for remaining phase distortions and results in a clean 14.4 fs (FWHM) pulse, which is very close (less than 4%) to the calculated *Fourier* limit of 13.9 fs (FWHM) for this spectrum.

The fact that the first iteration is not yet giving the optimal compression result can have two reasons. First of all, the assumption that the instantaneous frequency remains constant during the length of the test pulse is not very well fulfilled at the beginning. Uncompressed pulses have several hundred femtosecond duration, while the chirped reference pulse ($\varphi'' = 37000\ fs^2$) has about 1.5 ps. Such cases of highly chirped test pulses have very recently been thoroughly investigated,[105] and it was found that only a modified retrieval scheme taking into account a chirp-dependent shear will measure the correct phase without iteration, while the conventional approach based on the constant frequency assumption will generally underestimate the phase. This is the main reason for the remaining residual phase after the first SAC-SPIDER iteration seen in Fig. 4.18b) as thick solid curve. After this first iteration, the pulse is short enough to perfectly fulfill the instantaneous frequency requirement; therefore the measured residual phase is correct and the compression succeeds with the second iteration. A second reason, why iterations can be necessary in SAC-SPIDER, is due to errors in the calibration of Ω. As the measured phase is proportional to Ω^{-1}, a too large shear will underestimate, while a too small Ω will overestimate the measured phase. Iteration, however, makes SAC-SPIDER very robust against even grossly deviating values of Ω, only increasing the number of iterations until the residual phase approaches zero. Based on that it becomes clear that Ω was determined precisely for the experiment in Fig. 4.16, as the first iteration already performs almost all of the compression.

4.6.2 Measurement Time and Retrieval of Complex Phases

The complete compression in Fig. 4.19 was performed very rapidly in less than 2 seconds. The phase measurement itself in SAC-SPIDER is only limited by the acquisition time of the CCD camera and the time needed to perform the SPIDER algorithm. This is a general property of SPIDER techniques and has already been demonstrated for real-time measurements.[99] An iteration step for *in situ* compression takes a little bit longer, as now the limiting factor is the rate at which the pulse shaper can be updated. The unit used in this

study is equipped with a rather slow serial computer interface, which limits the rate at which mask functions $\tilde{M}_{SLM}(\omega)$ can be written on the SLM. For the present configuration, run-time measurements determined that the complete cycle of a SAC-SPIDER measurement, phase inversion and writing of the modified mask function is completed within 780 ms.

The presence of the pulse shaper allows easily evaluating the capabilities of the system to characterize pulses with even more complex pulse shapes. On the basis of the correction phase $\varphi_{corr}(\omega)$, which creates a clean pulse with a flat spectral phase, additional phase modulations $\varphi_{mod}(\omega)$ can be added. This means that the phase of the mask function $\varphi_{SLM}(\omega)$ now consists of the phase modulation necessary for the creation of double pulses, the correction phase $\varphi_{corr}(\omega)$ and $\varphi_{mod}(\omega)$. In Fig. 4.19 some examples for typical phase modulations $\varphi_{mod}(\omega)$ are shown, which are frequently used in coherent control[106]. In Fig. 4.19a), an additional quadratic phase of $\varphi_{mod}(\omega) = 2000\ \mathrm{fs}^2 \cdot (\omega - \omega_0)^2$ (solid curve) was added and successfully retrieved by the SAC-SPIDER (crosses). Similarly, sinusoidal phases of the type $\varphi_{mod}(\omega) = A \cdot \sin(\tau_m \cdot \omega + c)$ were added with amplitude $A = \pi$, modulation frequency $\tau_m = 50$ fs, and a constant phase offset of $c = 0$ (Fig. 4.19b) and $c = \pi/2$ (Fig. 4.19c). In both cases, the oscillating phase is nicely retrieved, and the phase shift between Fig. 4.19b) and Fig. 4.19c) is clearly discernible. Sinusoidal phases are highly relevant for applications in nonlinear microscopy, as they can be used for selective multiphoton imaging[107, 108] and for single-beam coherent anti-*Stokes Raman* scattering microscopy,[17, 109] which allows chemical contrast with a single broadband femtosecond laser and a pulse shaper. Finally, in Fig. 4.19) a phase indent with a "depth" of $0.7\,\pi$ is shown, which is also successfully characterized. Much larger indentation depths, however, can lead to disruptions in the interferograms which cause the SPIDER algorithm to introduce systematic errors in the reconstructed phase.

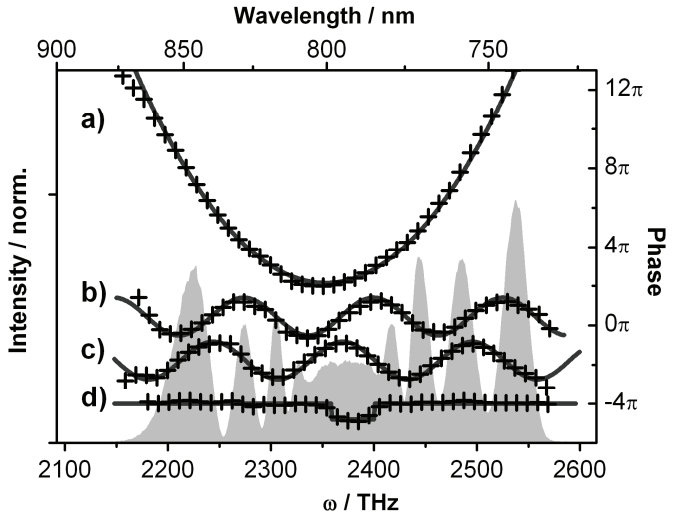

Fig. 4.19: Retrieval of complex phases. In addition to the compressed pulse, arbitrary phase modulations $\varphi_{mod}(\omega)$ were applied: **a):** quadratic phase with 2000 fs², **b)** and **c):** sinusoidal phases with $\pi/2$ phase offset, **d):** rectangular phase indentation. $\varphi_{mod}(\omega)$ is always shown as thick solid curve, and the retrieved SAC-SPIDER phases as crosses. For comparison, the pulse spectrum is indicated as grey shaded area.

Similarly, if the spectrum of the unknown pulse is very much structured and if the spectral intensity drops to zero, the SPIDER phase retrieval loses track of the fringe phase and encounters phase-cycle slip errors, which lead to artificially large linear spectral phases for the spectrum after such a problematic area in the interferogram. This property is common to all SPIDER implementations. SAC-SPIDER, however, allows in some cases mitigating phase-cycle slip problems: Due to the creation of the double pulses with the shaper, the relative offset phase between both replicas can be adjusted independently from their temporal separation. This permits very easy shifting of the interference fringes in the SAC-SPIDER interferogram, which can help to overcome problems in the phase reconstruction. If an interference fringe is placed where there is a sharp dip in the test pulse spectrum, the phase cycle slip can be avoided at this spectral position. Thus, from a series of interferograms recorded with different offset phases, much more robust phase information can be obtained for highly structured pulses.

4.7 Verification by independent XFROG-measurements

To independently verify the phase obtained with the SAC-SPIDER, XFROG measurements[110-112] were performed *in situ*. As reference pulse the 100 fs laser oscillator was used. For this purpose, in the SAC-SPIDER setup (Fig. 4.14, hatched beam path) the reference beam is not chirped as for SPIDER measurements, but can be delayed by Δt using a linear moving stage. Additionally, linear chirp of the reference pulse could be compensated by a pair of gratings. The sum-frequency mixing signal between this reference beam and the beam of the test pulses was detected in the same setup, as described in section 4.4 (p. 54). The 100 fs oscillator as reference pulse which has a much longer duration than the compressed test pulse has to be carefully characterized. This was performed with an *in situ* FROG measurement of the reference pulse under the same experimental conditions, *i.e.* taking in account all optical dispersive elements.

In Fig. 4.20 the characterization of the test pulse with the *in situ* XFROG and SAC-SPIDER methods is shown for the uncompressed (a-c) and compressed (d-f) supercontinuum phase. For both situations, the agreement between the methods is almost perfect: the uncompressed pulse shows a spectral phase with a strong quadratic phase and higher order contributions, which is correctly identified by SAC-SPIDER (Fig. 4.20c, solid curve) and XFROG (Fig. 4.20c, crosses). When the SAC-SPIDER is used to compress the pulse *in situ*, the XFROG also finds a flat spectral phase (Fig. 4.20f, crosses) and confirms the successful compression. The fact that the reference pulse is not *Fourier* transform limited but has some degree of higher order phase distortions can be seen in the experimental XFROG traces in Fig. 8: They are, to some extent, smeared out in time. Note that the precise knowledge of these distortions in the reference pulse nevertheless allows a very accurate reconstruction of the test pulse, as can be seen from the very close match of the experimental (Fig. 4.20 a+d) and retrieved (Fig. 4.20 b+e) XFROG traces. However, the procedure to obtain the test pulse phase *in situ* with XFROG is much more time-consuming (approaching several tens of minutes) and complicated than the original SAC-SPIDER measurement (less than a second).

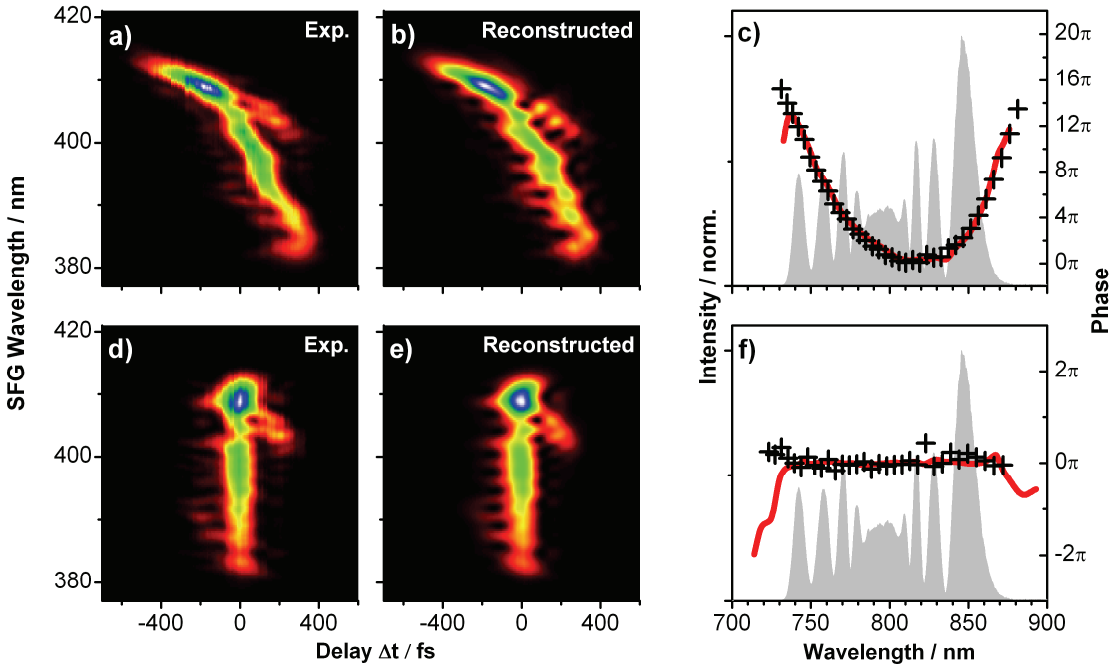

Fig. 4.20: Comparison between SAC-SPIDER and XFROG methods. Both methods retrieved the same phase for uncompressed (a-c) and the compressed supercontinuum pulses (d-f). The experimental XFROG traces (a and d) were reconstructed (b and e, respectively) and the spectral phase was retrieved (crosses in c and f, respectively). The corresponding phases measured with SAC-SPIDER are shown as solid lines and the test pulse spectrum is indicated as grey shaded area. Note that the SAC-SPIDER phase shown in panel c) is obtained after two iterations (compare Fig. 4.18).

4.8 Multiphoton Microscopy Application Examples

As shown in the above sections, SAC-SPIDER is a very useful tool for rapid and precise *in situ* compression even of very complex pulses in a nonlinear microscope. To demonstrate how valuable this precise phase control is for multiphoton microscopy, two-photon fluorescence (TPF) microscopy was performed using the compressed PCF source, and images compared obtained without and with SAC-SPIDER compression. The sample was prepared with a diluted solution of 8 µm monodisperse melamine-formaldehyde-resin microparticles labelled with Rhodamine B (*Kisker Biotech*) in water, which was placed within a 2 × 4 mm recess incised in a 100 µm Teflon spacer on a microscope slide, and sealed with a cover slip. The sample was mounted on a XYZ-closed loop piezo translation stage (*PI Nanocube*), which allows a maximum scanning range of 100 µm in each direction with nm resolution. Placing the focal volume exactly inside a microparticle, the two-photon fluorescence spectrum of the labelling dye Rhodamine B could be recorded: In Fig. 4.21a) the respective spectra can be seen for uncompressed [solid line, hatched in dark grey in Fig. 4.21a), temporal profile Fig. 4.18d)] and compressed pulses [dashed line, hatched in light grey in Fig. 4.21a), for temporal profile see Fig. 4.18f)].

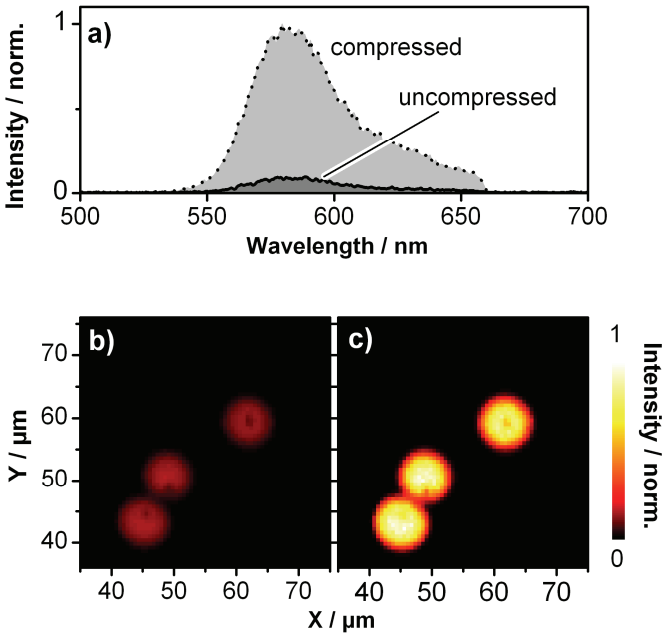

Fig. 4.21: Application example of SAC-SPIDER compressed pulses in two-photon fluorescence microscopy. **a):** Two-photon fluorescence spectra measured in a Rhodamine B labeled polymer particle with uncompressed (solid curve, hatced in dark grey) and compressed (dashed curve, hatched in light grey) pulses. **b+c):** Imaging of fluorescent microparticles with uncompressed (**b**) and compressed (**c**) pulses. The integrated fluorescence intensity is normalized on the same scale.

The integrated intensity of TPF obtained with compressed pulses is more than one order of magnitude larger than for uncompressed pulses. Using the integrated fluorescence signal intensity, imaging of the microparticles could be performed. For each pixel recorded with a step size of 600 nm in *X* and *Y* direction, the shaper first applied an empty mask function for the uncompressed pulses, and then the SAC-SPIDER correction phase for the compressed pulses. In Fig. 4.21b+c, both resulting images are shown on a common normalized intensity scale. As expected, the image obtained with SAC-SPIDER compression has a much higher contrast. Apart from the optimization of the signal level, the SAC-SPIDER would now also immediately allows imprinting additional phase functions - like sine-modulations shown in Fig. 4.19 b+c - to perform selective multiphoton fluorescence microscopy with shaped pulses.[107, 113]

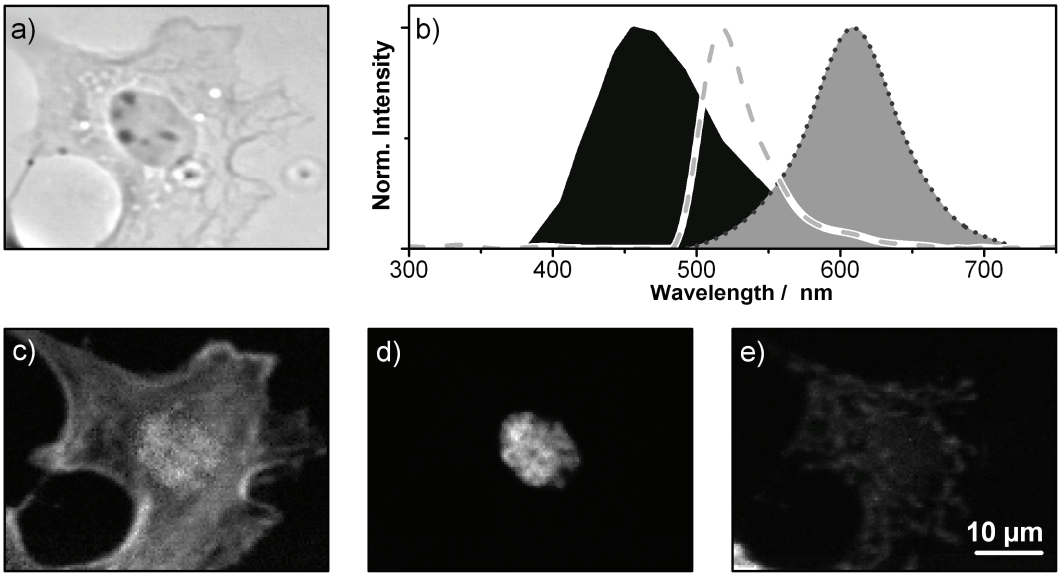

Fig. 4.22: Broadband TPF microspectroscopy, demonstrated on BPAE cells (Invitrogen FluoCells® prepared slide #1) labeled with three different fluorophors. **a)** A conventional phase-contrast image of a cell. **b)** Normalized, smoothed emission spectra of the three dyes, as used for the linear decomposition of the TPF spectrum from each sample position: BODIPY® FL phallacidin (dashed curve), DAPI (solid hatched curve), and MitoTracker® Red (dotted curve). **c)** Resulting partial image, showing the distribution of BODIPY® FL phallacidin and therefore the cytoskeleton. **d)** Partial image of DAPI, revealing the nucleus. **e)** Partial image of MitoTracker® Red signal, highlighting mitochondria. In panel **c)**, small residual crosstalk with the DAPI channel **d)** can be seen, which is due to DAPI having a fluorescence signal in our sample an order of magnitude stronger.

Instead of selective excitation and **single channel** detection, a different approach shall be taken as a real-life TPF microscopy example using the SAC-SPIDER compressed fs-pulses. It relies on simultaneous excitation and **multichannel** spectroscopic detection of the different fluorophors. Image contrast and selectivity is achieved by a decomposition of the microspectroscopy signal for each spatial position into the different contributions from all labeling dyes used.[114-116] The sample used is a commercially available test slide (*Invitrogen FluoCells®*, prepard slide #1, containing labeled bovine pulmonary artery endothelial cells). The conventional optical phase-contrast microscopy image (Fig. 4.22a) shows the cell selected for spectroscopic TPF imaging. Different functional entities of the cell are labeled by different fluorescent dyes, which can all be excited in a two-photon transition within the broad excitation bandwidth provided. The normalized fluorescence spectra of the dyes are shown in Fig. 4.22b, featuring different emission maxima but still strongly overlapping spectra. However, as the fluorescence signal from different dye molecules adds up incoherently in the detector, any TPF microspectroscopy signal will be a linear combination of these spectral profiles of the native dyes [Note that this property of linear signal superposition was not the case in MCARS spectroscopy, where signals and nonresonant interfere and have to be disentangled as described in the previous chapter, section 3.5.2].

Spectral decomposition can be performed in a variety of ways; here the same evolutionary algorithm[70] as in the MCARS image analysis was used to find the partial intensity of each dye spectrum for every spatial position in the sample. This gives images showing the distribution of one specific dye, which allows locating the functional entities labeled (Fig. 4.22c-e). This example again shows how useful broadband excitation combined with spectrally resolved detection can be, if the pulse duration at the sample position can be controlled. Also, again the "multiplex" analysis of spectral profiles performed to discriminate the different dyes is much more powerful than simple single-channel detection at selected emission wavelengths.

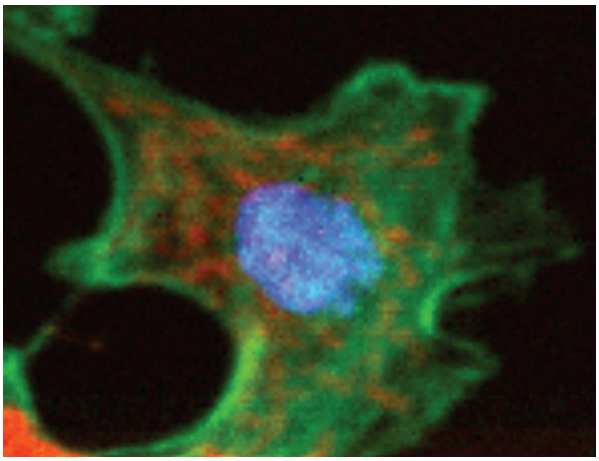

Fig. 4.23: (Color) Composite RGB image of labelled BPAE cells (Invitrogen FluoCells® prepared slide #1) created as overlay of the disentangled fluorescence channels in Fig. 4.22.

These first examples of multiphoton microscopic imaging already show the extreme usefulness of compressed broadband pulses in microscopy and microspectroscopy. The newly developed SAC-SPIDER method permits full *in situ* phase measurement and compression and thus enables high-performance imaging in the unavoidable presence of dispersion and phase distortions. With the incorporation of the pulse shaper, it also lays the foundation for functional multiphoton microspectroscopy using precisely tailored femtosecond pulses and coherent control schemes.

5 Single-beam CARS[**]

With everything in place: broadband laser source, pulse shaper and compressed ultrashort pulses in the microscope, single-beam CARS can be implemented as an exciting application of coherently controlled broadband nonlinear microspectroscopy. In contrast to other multiphoton microscopies such as TPF, SHG or THG, CARS provides spectroscopic, chemically selective information without the need for any labelling dyes (Fig. 5.1).[11, 12, 117] As already shown in chapter 3, this allows studying whole new classes of systems, demonstrated by imaging complex polymer blends using MCARS microscopy[55, 118].

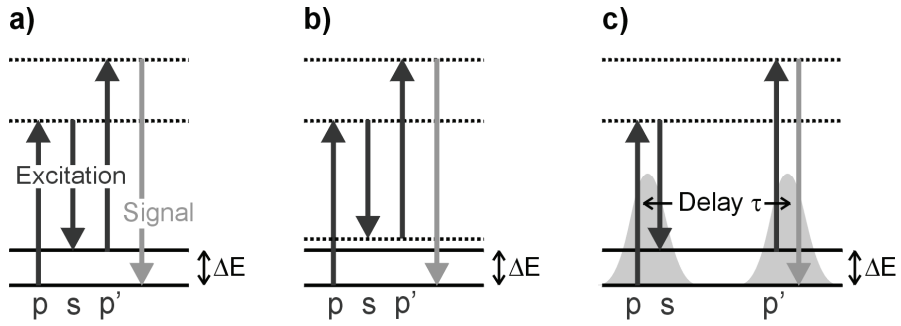

Fig. 5.1: Energy level diagrams of the coherent anti-*Stokes Raman* scattering (CARS) process. **a)** Pump (p), *Stokes* (s) and probe (p') photons generate a blue-shifted signal at the anti-*Stokes* frequency of p'. This process is efficient, due to its resonance with a vibrational level at energy spacing ΔE. **b)** Origin of nonresonant background: The CARS process can also occur via an intermediate virtual state that does not reflect the molecular energy levels. **c)** Principle of time-resolved CARS experiments: Pump and *Stokes* photons from one or two ultrafast laser pulses excite a coherent molecular vibration, which is probed after a time delay τ by a probe pulse.

In the context of the MCARS implementation (3.2), it has become clear that the high demands of CARS on peak intensity and multi-colour synchronized excitation sources are the key technical challenge in promoting CARS for microscopy applications. The robust MCARS scheme presented in chapter 2 was already a huge step towards simplified microspectroscopy. However, there is still room for improvement: (i) the nonresonant background in MCARS has to be removed in a fitting procedure *a posteriori*, (ii) spectral resolution is limited due to the compromise with signal strength and (iii) the setup is rather specialized, being designed only to perform as MCARS microscope without the possibility to simply correlate other nonlinear signals. Additionally, the sensitivity is limited due to the square dependency of any CARS signal on the concentration of scattering molecules. All these issues can be addressed with broadband shaped femtosecond excitation and coherent control, allowing huge simplification of CARS in a single beam, complete suppression of

[**] Sections of this chapter have been published in *„Time-resolving molecular vibration for microanalytics: Single laser beam nonlinear Raman spectroscopy in simulation and experiment"* by B. von Vacano and M. Motzkus, Phys. Chem. Chem. Phys. 10, 681-691 (2008); and *„Time resolved two color single beam CARS employing supercontinuum and femtosecond pulse shaping"* by the same authors, Optics Communications 264, 488-493 (2006).

nonresonant background, very high spectral resolution, flexible software-controlled correlation measurements with other nonlinear signals and the possibility to drastically increase detection sensitivity by intrinsic interferometric detection. The presentation of these developments and findings will be the scope of this chapter.

5.1 CARS in frequency and time domain

CARS is generally considered in the framework of quantum states with discrete energies. Mathematically, in this case the CARS signal field $\tilde{E}_{CARS}(\omega)$ is described in the following way[††]:

$$\tilde{E}_{CARS}(\omega) \propto N \cdot \int_0^\infty d\Omega\, \tilde{E}_{p'}(\omega-\Omega) \cdot \chi^{(3)}_{CARS}(\Omega) \cdot \int_0^\infty d\omega'\, \tilde{E}_s^{\,*}(\omega')\tilde{E}_p(\omega'+\Omega)\,. \tag{5.1}$$

Written like this, it is immediately seen that the last integral over the pump field $\tilde{E}_p(\omega)$ and the *Stokes* field $\tilde{E}_s(\omega)$ can be understood as a frequency filter function with which the frequency-domain susceptibility $\chi^{(3)}_{CARS}(\Omega)$ is multiplied. Therefore, it is highly convenient to explicitly state this "*Raman* excitation probability" as

$$A(\Omega) = \int_0^\infty d\omega'\, \tilde{E}_s^{\,*}(\omega')\tilde{E}_p(\omega'+\Omega)\,. \tag{5.2}$$

$A(\Omega)$ gives the number of frequency pairs connecting two energy levels with a spectral separation of Ω.

As all fields enter as complex quantities in Eq. (5.2), $A(\Omega)$ is highly dependent on the relative phase of the frequency pairs. This directly gives a lever for coherent control, which will be exploited extensively later on. On the other hand, the spectral shape and position of $\tilde{E}_p(\omega)$ and $\tilde{E}_s(\omega)$ determines the vibrational energy range accessible (Fig. 5.2). For a combination of two *cw*-lasers at ω_p and ω_s $A(\Omega)$ would simply peak at $\Omega' = \omega_p - \omega_s$ with a *Dirac* delta function (Fig. 5.2a). Eq. (3.1) is fully sufficient to numerically simulate different CARS implementations. To describe time-domain CARS experiments, the temporal information about the pulses, such as a delay τ of the probe electric field in Fig. 5.1c, enters solely via a linear term in the spectral phase, *e. g.* via $\tilde{E}_{p'}(\omega) = \tilde{E}_{p'}(\omega) \cdot \exp[-i\omega\tau]$ (see 2.1).

[††] In principle, the same expression has already been used in section 3.2, however stated there in a slightly varied form as $S_i(\omega)$ in order to lay the foundation for the spectral decomposition performed in that chapter.

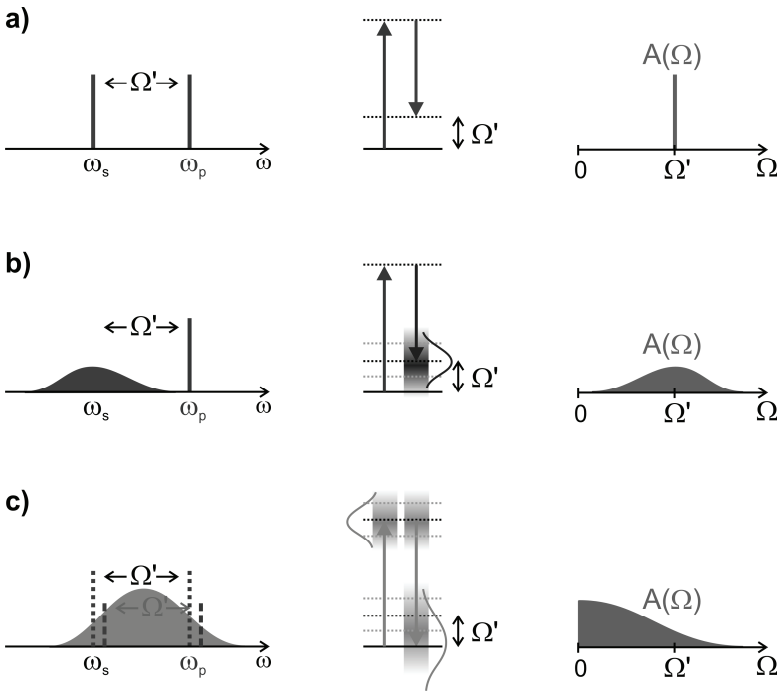

Fig. 5.2: Visualization of the *Raman* population amplitude A(Ω), Eq. (5.2). **a)** Two narrowband lasers at ω_p and ω_s are only able to excite *Raman* transitions at exactly $\Omega' = \omega_p - \omega_s$. **b)** If the *Stokes* laser has a broad bandwidth, as in MCARS, $A(\Omega)$ reflects this extended spectral coverage, again centred at the excitation peak-peak spectral distance Ω'. **c)** If pump and *Stokes* pulses are identical and have a broad spectrum, as in single-beam CARS, there are a number of suitable frequency pairs for each *Raman* energy Ω' within the pulse bandwidth. Naturally, the number of frequency pairs becomes larger as $\Omega \to 0$, thus $A(\Omega)$ peaks at zero.

5.1.1 Frequency-domain CARS

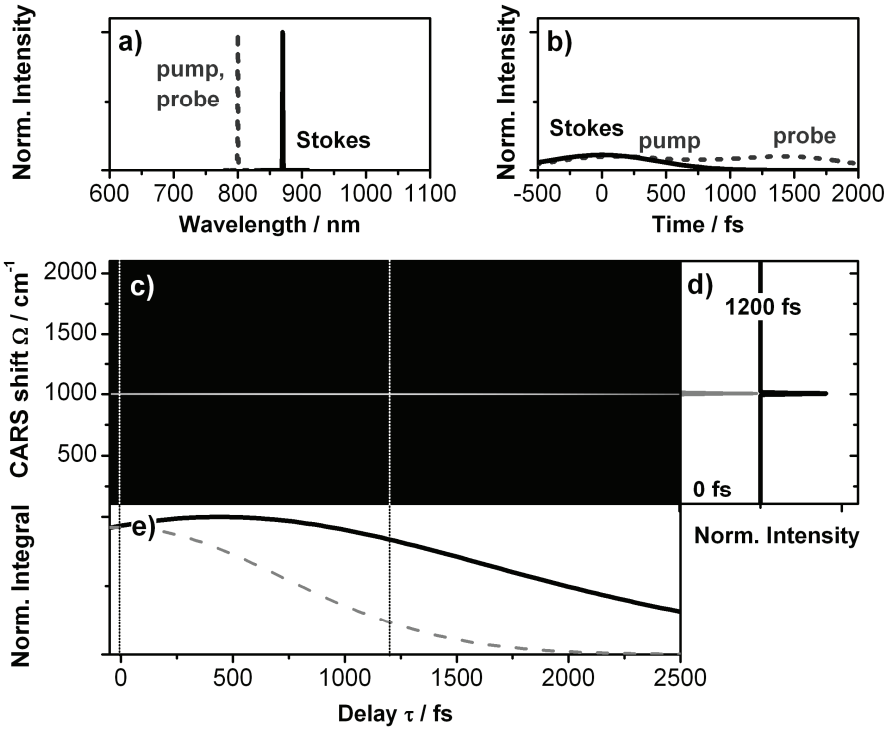

Fig. 5.3: Simulation of ps-CARS. **a)** Pump and probe pulses (dashed curves) are assumed as 1 ps pulses with identical spectra (but delayed by τ), while the *Stokes* pulse (1 ps duration, solid curve) is red-shifted. **b)** Here, the simultaneous arrival of pump and *Stokes*, with a probe delayed exemplarily by 1500 fs is shown. **c)** Time-frequency representation of the CARS signal generated from the pulses for different delays t. A molecular sample has been given with resonances at 500 cm^{-1}, 1000 cm^{-1} and 1100 cm^{-1}. The *Stokes* pulse is tuned on resonance such that $\Omega = \omega_p - \omega_s = 1000\ cm^{-1}$. **d)** Spectral cuts through the 2D representation for delay $\tau = 0$ (all pulses arrive simultaneously, grey hatched curve) and $\tau = 1200$ fs (black curve). It can be seen that in both cases only a spectrally narrow CARS signal is detected, which has already decayed to some degree for $\tau = 1200$ fs. **e)** Spectrally integrated transient.

Due to the nonlinearity of CARS and the consequent requirement of high peak intensities, the just mentioned frequency-domain approach using *cw* lasers is not viable. However, the condition of spectrally narrow frequency-domain excitation still holds for pulsed laser sources, which have a spectral bandwidth in the range of or lower than typical *Raman* line widths, which in the condensed phase are in the order of some wavenumbers. Therefore, the classical CARS microscopy implementation is with two synchronized ps-laser, which often is claimed "ideal" for the given reasons.[11] Pump, *Stokes* and probe pulses arrive simultaneously, with the pump and probe pulse being identical. In principle, also in this clearly frequency-domain based ps-implementation, a delay τ can be introduced between a first pump (arriving simultaneous with the red-shifted *Stokes* pulse), and a subsequent probe (Fig. 5.1c). This case has been simulated using Eq. (3.1) for different delays τ and is summarized in Fig. 5.3.

As the *Stokes* laser is tuned to 870 nm, with pump and probe at 800 nm (Fig. 5.3a), CARS signal is only generated around $\Omega = \omega_p - \omega_s = 1000\ cm^{-1}$. The information obtained for $\tau = 0$, *i. e.* simultaneous arrival of all pulses, is only the magnitude of the blue shifted CARS signal, which merely by its strength allows discriminating nonresonant contributions from a resonant signal. The fact that Ω has been tuned to one of the resonances given in the model (at 500 cm^{-1}, 1000 cm^{-1} and 1100 cm^{-1}) becomes only visible when increasing τ. A purely nonresonant, instantaneous signal will reflect solely the pulses temporal profile (Fig. 5.3e, normalized dashed curve), while a resonant signal lives longer and leads to a slower exponential decay convoluted with the ps-pulse envelopes (Fig. 5.3e, black solid curve - note that the maximum in the CARS transient shifts away from zero due to the convolution). This again demonstrates that ps-CARS does not yield spectroscopic information unless the *Stokes* laser is scanned subsequently. MCARS on the other hand, as laid out in chapter 3, immediately provides spectroscopic information. Therefore, Fig. 5.4 shows an MCARS implementation with a 1.3nm bandwidth spectrally narrow laser (700 fs at 800 nm, dashed curve in Fig. 5.4a) for pump and probe and a broadband *Stokes* (10 fs at 800 nm, solid curve in Fig. 5.4a).

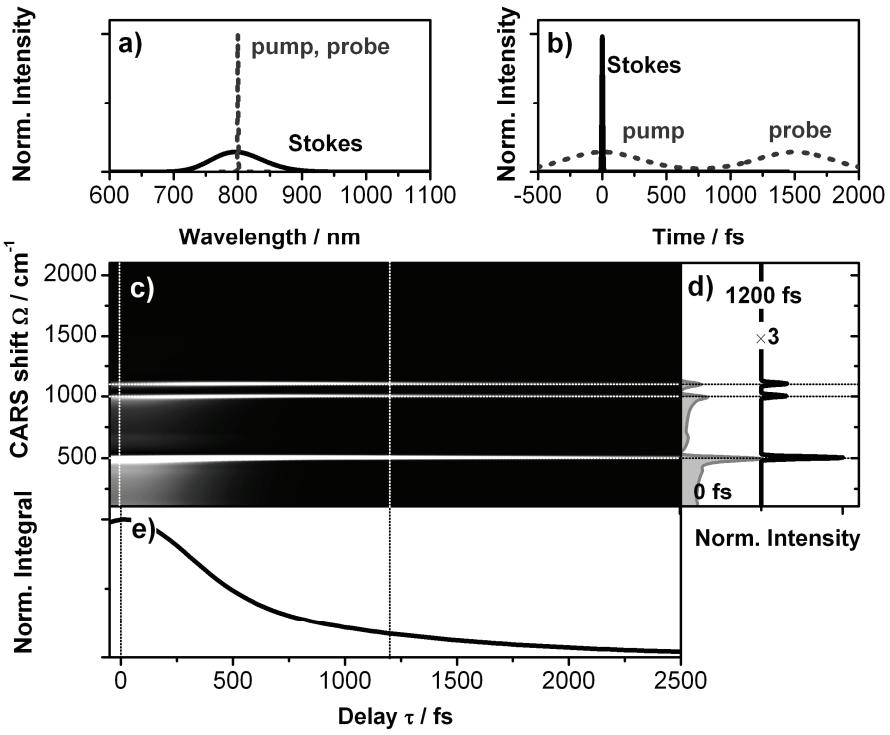

Fig. 5.4: Simulation of MCARS with 700 fs pump and probe (dashed curve) and a 10 fs broadband *Stokes* pulse (solid curve). **a)** Spectra of pump, probe and *Stokes* pulses. **b)** Temporal shape of pump and *Stokes*, and a probe pulse delayed exemplarily by 1500 fs. **c)** Time-frequency representation of the MCARS signal generated. The same sample as before is assumed (resonances at 500 cm^{-1}, 1000 cm^{-1} and 1100 cm^{-1}). **d)** Spectral cuts through the 2D representation for delay $\tau = 0$ (grey hatched curve) and $\tau = 1200$ fs (black curve). **e)** Spectrally integrated transient.

The case realized in chapter 3 is with no delay between pump and probe, as they are both provided by the same laser pulse, therefore τ is always zero. The resulting MCARS spectrum

(Fig. 5.4d, grey hatched curve) shows the molecular resonances with decreasing intensity within the bandwidth of the *Stokes* [entering *via* the shape of $A(\Omega)$, see Fig. 5.2b]. The typical CARS-lineshapes with dips and peaks due to the presence of the pedestal of nonresonant background is clearly visible. If now a separate probe is introduced at a delay, *e. g.* $\tau = 1200$ fs, the instantaneous nonresonant background vanishes completely, while the resonant CARS lines remain. This yields a background-free, yet slightly less intense CARS spectrum (Fig. 5.4, black solid curve -. note that this data has been scaled by a factor of three for better visibility). Such an approach might be viable to improve MCARS microscopy.[‡‡] The spectrally integrated signal for various values of τ does not contain spectroscopic information; it again only shows the coherence decay of the vibration convoluted with the 700 fs probe pulse. All the structure is in the frequency domain, this is why taking a spectrum at any given value of τ (typically $\tau = 0$ due to experimental constraints) is sufficient to obtain the complete information.

[‡‡] However, in practise the "classical" MCARS signal contributions of pump/probe at zero delay, which in collinear beam geometry is always present, and the desired background-free signal of a delayed probe cannot be separated. Using carefully chosen polarization arrangements, only resonant signal can be picked out. It could, however, also be disentangled if a probe pulse at a largely different blue-shifted frequency is chosen, which most conveniently could be obtained by frequency doubling of the narrowband probe.

5.1.2 Hybrid time-frequency CARS

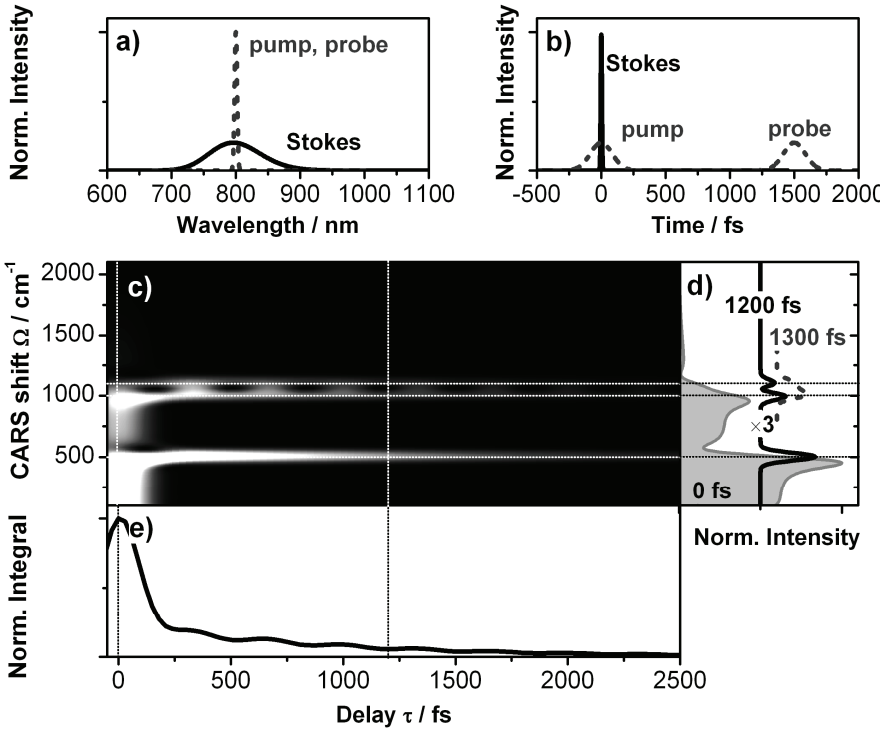

Fig. 5.5: Simulation of MCARS with 200 fs pump and probe (dashed curve) and a 10 fs broadband *Stokes* pulse (solid curve). **a)** Spectra of pump, probe and *Stokes* pulses. **b)** Temporal shape of pump and *Stokes*, and a probe pulse delayed by 1500 fs. **c)** Time-frequency representation of the MCARS signal generated. **d)** Spectral cuts for delays $\tau = 0$ (grey hatched curve), $\tau = 1200$ fs (black solid curve) and $\tau = 1300$ fs (dashed curve). **e)** Spectrally integrated transient.

As already discussed in 3.2, the spectral width of the narrow probe pulse determines the spectral resultion in MCARS. With an assumed *Gaussian* 700 fs pulse in Fig. 5.4, corresponding to a resolution (FWHM) of ~20 cm^{-1}, the two simulated vibrational resonances at 1000 cm^{-1} and 1100 cm^{-1} are well resolved. What happens, if the pump/probe pulses have a broader spectrum and are shorter, *e. g.* 200 fs in Fig. 5.5?

In principle, the time-frequency representation looks similar to the previous case in Fig. 5.4. As expected, the spectral resolution is decreased. Additionally, for the spectral cut at $\tau = 0$ (Fig. 5.5d, grey hatched curve) the ratio of nonresonant background to resonant signal is clearly worse. This fact has been discussed in the literature, and was given as a reason for the allegedly poor performance of femtosecond lasers in CARS microscopy.[11] For larger τ, the nonresonant background is again completely suppressed. The spectral resolution however does not allow a baseline separation of the 1000 cm^{-1} and 1100 cm^{-1} modes any more (Fig. 5.5d, black solid curve). As both resonances overlap in the frequency domain and originate from molecular vibrations of different energy, they give rise to an oscillatory interference in the τ-axis. This beating is clearly present in the spectrally integrated transient (Fig. 5.5e). The information about the precise molecular resonances is therefore not lost, but simply not

contained along the frequency axis anymore, but distributed in both frequency and time domain.[119]

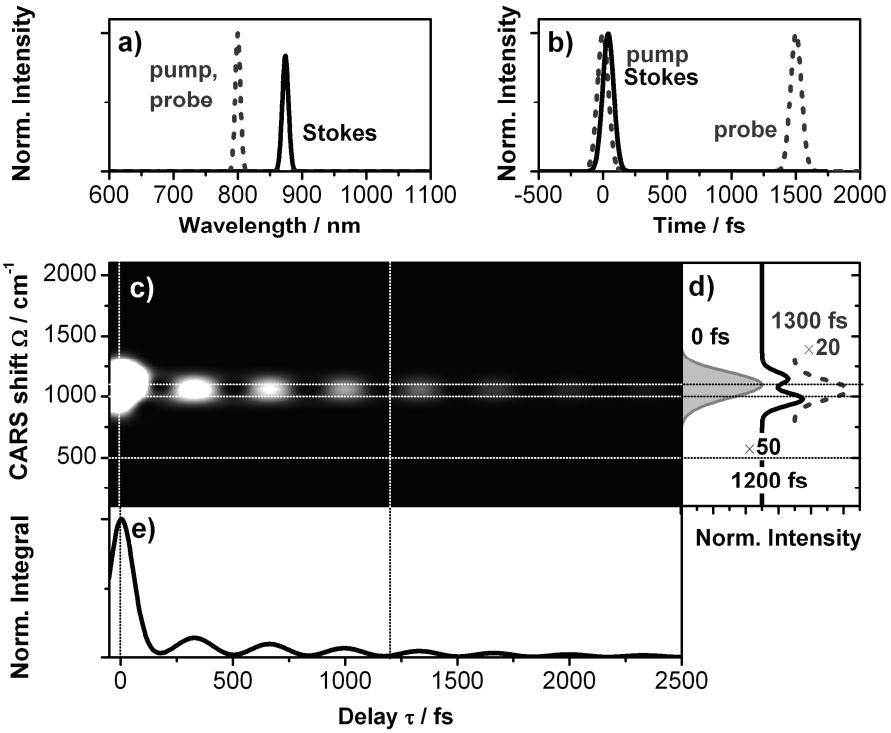

Fig. 5.6: Simulation of fs-CARS with 100 fs pulses, adjusted for *Raman* vibrations around 1000 cm^{-1}. **a)** Spectra of pump, probe (dashed curve) and *Stokes* (solid curve) pulses. **b)** Temporal shape of pump (dashed curve) and *Stokes* (solid curve), and a probe pulse delayed by 1500 fs (dashed curve). **c)** Time-frequency representation of the CARS signal generated. **d)** Spectral cuts through for delay $\tau = 0$ (grey hatched curve), $\tau = 1200$ fs (black solid curve) and $\tau = 1300$ fs (dashed curve). **e)** Integrated transient showing beating with ~330 fs according to the 100 cm^{-1} energy difference between the assumed high-frequency modes of the molecule.

Such an intermediate regime of spectroscopic information in both time and frequency domain is characterized by the typical appearance of beating oscillations in the transients, as already seen in Fig. 5.5e. It is in this regime, that time-resolved femtosecond CARS experiments have usually been carried out.[120-122] The employed femtosecond pulses are not shorter than the vibrational period of molecular oscillations, but spectrally much broader than the *Raman* resonances. Necessarily, like in MCARS, pump and *Stokes* photons thus have to be provided from lasers of different colour to match a *Raman* energy Ω. Based on the same model, such a case has been simulated in Fig. 5.6 with 100 fs pulses at 800 nm (pump and probe photons) and at 870 nm (*Stokes*), corresponding to an average Ω of ~1000 cm^{-1}. In the frequency domain, the CARS signal is washed out, not allowing a clear discrimination of both underlying vibrational modes at 1000 cm^{-1} and 1100 cm^{-1} (Fig.

5.6d).[§§] The time-dependent CARS signal shows decay with the coherence time T_2 of the levels probed overlaid with beating originating from the 100 cm^{-1} energy difference, which is well within the bandwidth of the lasers. The information from the beating alone, however, is not sufficient to determine, which resonances are responsible for its occurrence: Obtaining the complete spectroscopic information about both modes accessed in this regime requires time- and frequency resolved data to be analysed simultaneously.[123-128]

Despite the additional complexity for time-resolved CARS measurements by introducing τ, it offers a huge advantage over a pure frequency-dispersed approach in all regimes: Nonresonant background is suppressed completely. The reason for this is obvious from the scheme in Fig. 5.1b: no more than virtual states are involved in the background generation, which only exist instantaneously during the interaction of the light fields with the molecule. This fact – in the hybrid time-frequency regime only - has already successfully been exploited in CARS microscopy, where background suppression is vital for high-contrast chemical images.[11, 129]

With even shorter ultrafast laser sources, however, vibrations can be excited impulsively. Fully time-resolved CARS does thus not rely on frequency dispersion of the generated signal wave, but on the measurement of the temporal response of the system.[47] In the "impulsive" limit of extremely short laser pulses, this measured response reflects the complete dynamics of the molecule, and therefore shows oscillations at the frequencies of all molecular vibrations (Fig. 5.7).[130]

5.1.3 Impulsive femtosecond CARS

Experimentally, the condition for impulsive measurement of a vibration with energy $\Delta E = \hbar\Omega$ is that laser pulses employed have to be shorter than the vibrational period $T_{vib} = h \cdot \Delta E^{-1} = 2\pi \cdot \Omega^{-1}$, where h is the Planck constant and $\hbar = h \cdot (2\pi)^{-1}$. In the frequency domain this translates into a pulse spectral width which is larger than $\Delta E / h$: within the ultrashort excitation pulse, photon pairs have to be provided allowing a coherent excitation of the vibration (Fig. 5.2c). If probed with an equally short laser pulse after a delay τ (Fig. 5.1c), the molecular vibrations are resolved as intensity modulations of the CARS signal in the transient. The complete spectroscopic information is contained in the time domain (Fig. 5.7e), and washed out along the frequency axis (Fig. 5.7d). Comparing the impulsive transient of Fig. 5.7e with the intermediate beating case of Fig. 5.6e reveals the 330 fs beating as envelope of faster oscillations. These faster oscillations correspond to the average fundamental frequency of the high-wavenumber-resonances. The exact oscillatory shape of transients depends on the properties of the molecule, *i. e.* especially the strength of CARS signal contribution from low-frequency vibrations and librations and on the amount of scattered excitation light. In the simulation in Fig. 5.6, these contributions are stronger than the resonant faster oscillations, as is typical for condensed phase experiments. They are visible as unmodulated offset in the impulsive CARS transients.[119, 131]

[§§] In this case, at τ = 1200 fs, one can still guess that the CARS signal originates from two modes. At some later or earlier delay, however, *e. g.* in a maximum of the beating oscillation at τ = 1300 fs (Fig. 5.5, dashed curve), only a single broad peak would be detected.

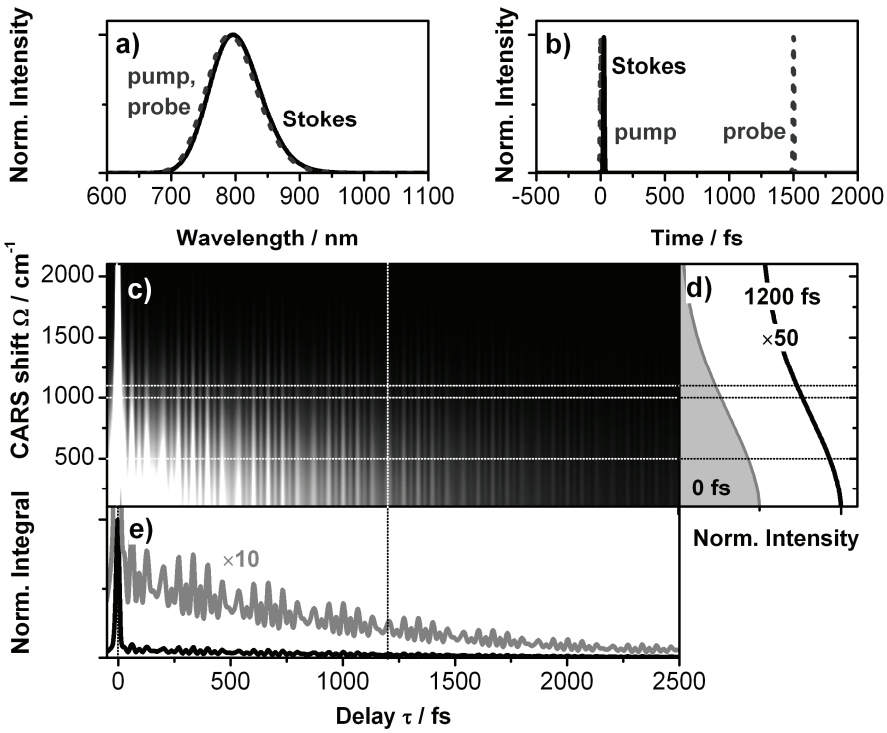

Fig. 5.7: Simulation of impulsive fs-CARS with 10 fs pulses. **a)** Spectra of pump, probe (dashed curve) and *Stokes* (solid curve) pulses, which are all identical and centred at 800 nm. **b)** Temporal shape of pump (dashed curve), *Stokes* (solid curve) and a delayed probe pulse (dashed curve). **c)** Time-frequency representation of the CARS signal. **d)** Spectral cuts through for delay $\tau = 0$ (grey hatched curve) and $\tau = 1200$ fs (black curve) showing no information. **e)** Integrated transient (black) with dominant nonresonant peak at $\tau = 0$ fs and magnified (grey curve).

The impulsive limit of femtosecond CARS (Fig. 5.7e) is much more attractive than hybrid time-frequency-schemes. The reason for this is that the complete molecular information can be obtained from a spectrally integrated detection only in the time domain, which makes impulsive femtosecond CARS a true *Fourier*-transform spectroscopic technique, comparable to modern pulsed nuclear magnetic resonance spectroscopy. Advantages are the simple single-channel detection, an almost arbitrarily high spectral resolution limited only by the length of the acquired delay series, and the possibility to even measure the relative phase between different molecular vibrations due to their acquisition in time domain.[47] Conventionally, impulsive femtosecond CARS is implemented with ultrashort laser pulses which are overlapped in space in a distinct geometrical arrangement to fulfil the phase-matching condition (which can be understood as the conservation of momentum for the photons involved) imposed on any parametric four-wave mixing process.[132] Two of the pulses arrive simultaneously from different directions, acting as pump and *Stokes*, while a third, from yet another direction, is delayed by τ. All the pulses used can, however, stem from the same ultrafast laser source, consequently having identical spectra. In this case, the technique is often also termed time-resolved degenerate four-wave mixing (DFWM) spectroscopy,[133, 134] but operates in exactly the same way. Such experiments have very successfully been used to reveal molecular dynamics of a variety of molecular systems, even of excited electronic states.[135-138] The experiment itself, however, involves a rather complicated setup due to the creation of three pulses, each of them with a controllable time

delay, which then have to be overlaid in the required phase-matching geometry. Recently, it has been shown that a simplification is possible using a two-dimensional spatial light modulator to create all necessary beams.[139] Nevertheless, these approaches are not applicable to microscopic imaging, where the requirement is a collinear beam arrangement. There, phase matching is fulfilled automatically by the tight focussing.[140, 141] For a microscopic time-resolved measurement, pump and *Stokes* photons are thus provided by a first femtosecond pulse $E_1(t)$, which is followed by a second pulse $E_2(t)$ acting as probe (Fig. 5.1c). A direct implementation of impulsive time-resolved CARS with two pulses in collinear geometry has recently successfully been shown by *Ogilvie* et al. using a femtosecond laser and a *Michelson*-type interferometer,[108, 113] which directly allows chemically selective imaging in a microscope. Further simplification and flexibility can be achieved if instead of the interferometer a pulse shaping apparatus is used. In this case, the complete experiment is carried out in a single beam, which will be presented in the following.

5.1.4 Mathematical analysis of impulsive time-resolved CARS

Although all the simulations, including clearly time-domain scenarios like Fig. 5.7, have been performed in the frequency domain according to Eq. (3.1) using an extension of the Lab2 femtosecond laser simulation package[142] created in the course of this thesis, it is much more intuitive to analyse impulsive fs-CARS in a time-domain picture. Mathematically, a time-resolved CARS signal can be described as follows:[130]

$$S_{CARS}(\tau) \approx \int_{-\infty}^{\infty} dt \left|E_2(t)\right|^2 \left| \int_{-\infty}^{\infty} d\Omega \exp[-i\Omega(t+\tau)]\, A(\Omega) \cdot \chi^{(3)}_{CARS}(\Omega) \right|^2 , \tag{5.3}$$

where $S_{CARS}(\tau)$ is the detected signal for a given delay τ and $E_2(t)$ the temporal electric field of the probe pulse. The factor $A(\Omega)$ is already known from Eq. (5.2), but can in impulsive time domain fs-CARS also be interpreted as the *Fourier* transform of the temporal intensity of the first pulse $E_1(t)$ acting as pump and *Stokes*:

$$A(\Omega) \approx \int_{-\infty}^{\infty} dt \exp[i\Omega t] \left|E_1(t)\right|^2 . \tag{5.4}$$

$\chi^{(3)}_{CARS}(\Omega)$ in Eq. (5.3) is the third-order susceptibility responsible for CARS, which can again be expressed (exactly like in chapter 3) by two terms: a constant $\chi^{(3)}_{NR}$ for the nonresonant background and *Lorentzian* lines representing the n vibrational resonances of the molecule at energies $\Delta E_n = \hbar\Omega_n$ with amplitudes f_n and linewidths Γ_n.

$$\chi^{(3)}_{CARS}(\Omega) = \chi^{(3)}_{NR} + \sum_n \frac{f_n}{\Omega_n - \Omega + i\Gamma_n} \tag{5.5}$$

In the purely impulsive limit, which assumes *Dirac* delta pulses $E_1(t) = E_2(t) = \delta(t)$, Eq. (5.3) simplifies to

$$S_{CARS}(\tau) \approx \left| \int_{-\infty}^{\infty} d\Omega \exp[-i\Omega(t+\tau)] \cdot \chi^{(3)}(\Omega) \right|^2 , \tag{5.6}$$

reflecting the fact that the complete molecular information contained in $\chi^{(3)}(\Omega)$ is measured in time domain by $S_{CARS}(\tau)$. In the more realistic case of Eq. (5.3) with finite pulse durations, two effects come into play: First of all, the spectrum of $E_1(t)$ only offers a limited number of photon pairs matching a certain energy difference $\Delta E = \hbar\Omega$. This weighting effect is represented by the multiplication of $\chi^{(3)}(\Omega)$ with $A(\Omega)$. The modulus square of $A(\Omega)$ directly gives the relative number of suitable photon energy pairs, and thus the probability of any mode with frequency Ω to be excited with the laser pulse $E_1(t)$.[143, 144] Secondly, in Eq. (5.3) the response of the molecule in time domain, given by the inverse *Fourier* transform of the product $A(\Omega) \cdot \chi^{(3)}(\Omega)$, is convoluted by the temporal intensity of the probe pulse $E_2(t)$. These relations quantitatively substantiate the necessity of ultrashort pulses for both pulses involved, and allow analyzing the effects of finite pulse bandwidth on the measured CARS data. They are summarized and visualized in Fig. 5.8.

In this example, a molecule is assumed with two vibrational resonances at 800 and 1500 cm^{-1}, and with a low-frequency contribution modelled by the *Fourier* transform of an exponential decay to obtain a simulated CARS signal comparable to typical experiments. In the first column (panels a,d and g) laser pulses E_1 and E_2 are depicted for a delay τ of 300 fs and three different situations. In the case of a purely impulsive excitation with infinitely short pulses (Fig. 5.8a), as was assumed for Eq. (5.6), the excitation probability $A(\Omega)$ is constant for all vibrational energies (Fig. 5.8b, dashed curve). Thus, the product $R(\Omega) = A(\Omega) \cdot \chi^{(3)}(\Omega)$ (Fig. 5.8b, grey solid and black dotted curves) reflects all molecular information from $\chi^{(3)}(\Omega)$ without modification. (Fig. 5.8b) The time-domain response of the molecule is given by the inverse *Fourier* transform of this product according to eq. (1), and convolution with E_2 is not necessary under the given assumption of an ideally short E_2. The signal S_{CARS} resulting in this case is shown in Fig. 5.8c: One can discern distinct modulations and a beating pattern from both vibrational modes. The instantaneous nonresonant background from $\chi^{(3)}_{NR}$ only shows up at $\tau = 0$, directly representing the *Dirac*-delta temporal profiles of the pulses E_1 and E_2.

Consider now the case of an excitation pulse E_1 with a finite bandwidth, while the probing is still performed with an ideally short pulse E_2 (Fig. 5.8d). In this simulation, a *Gaussian* spectrum of E_1 with a full width at half maximum (FWHM) of 750 cm^{-1} has been assumed corresponding to laser pulses with 20 fs duration. The finite bandwidth now allows only a limited number of photon pairs with energy differences $\Delta E = \hbar\Omega$. This fact is rendered in the decline of $A(\Omega)$ (Fig. 5.8e, dashed curve). Therefore, the molecular vibrational spectrum contained in $\chi^{(3)}(\Omega)$ is equally declining for larger Ω in the product $R(\Omega) = A(\Omega) \cdot \chi^{(3)}(\Omega)$ (Fig. 5.8e, grey solid and black dotted curves). As the probing is performed with an ideal pulse E_2, the CARS signal S_{CARS} is directly obtained from the squared inverse *Fourier* transform of $R(\Omega)$. The effect of the different weighting of the two assumed vibrational modes at 800 and 1500cm^{-1} due to $A(\Omega)$ leads to a signal S_{CARS} in Fig. 5.8f which clearly differs from Fig. 5.8c: The high-frequency oscillation corresponding to the 1500 cm^{-1} mode is only very weakly recognizable. Finally, the effect of a probe pulse E_2 with a finite temporal duration of equally 20 fs can be shown (Fig. 5.8g-i): The molecular response (Fig. 5.8h) does not differ to the previous case, only the signal is washed out by the convolution with the temporal intensity profile of E_2. This leads to diminished contrast of the oscillations, and to a complete vanishing of signatures from the fast oscillations of the 1500 cm^{-1} mode. The instantaneous nonresonant background due to $\chi^{(3)}_{NR}$ can be seen in Fig. 5.8i as a peak

around delay $\tau = 0$, whose shape is determined by a third-order cross-correlation of the pulses E_1 and E_2. This said, it is clear that the nonresonant background can serve as an independent measure of the instrumental temporal resolution achieved in a time-resolved CARS experiment.

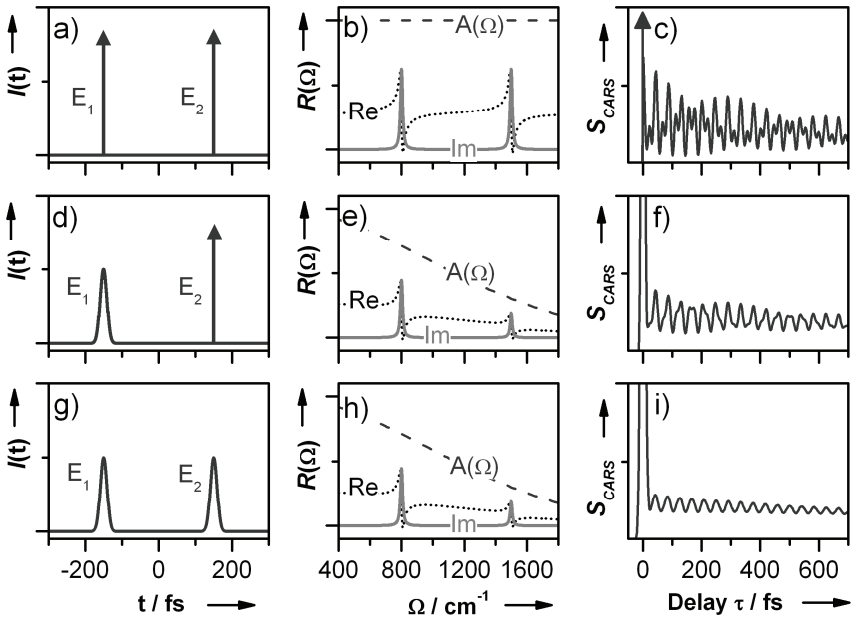

Fig. 5.8: Simulation of time-resolved CARS for two vibrational resonances at 800 cm^{-1} and 1600 cm^{-1} in the perfect impulsive limit **(a-c)**, in a case of finite bandwidth excitation and ideal probing **(d-f)** and finally for a realistic situation with 20 fs pulses for excitation and probing **(g-i)**. The second column **(b, e, h)** always shows $A(\Omega)$, calculated from eq. (2), as dashed line and the respective molecular frequency domain response $R(\Omega)$ as real (dotted curve) and imaginary part (grey solid curve). $R(\Omega)$ is given by the product of $A(\Omega)$ and $\chi^{(3)}(\Omega)$ according to Eqs. (5.4) and (5.5). The last column **(c, f, i)** finally shows the simulated time-resolved CARS signal, obtained from the squared inverse *Fourier* transform of $R(\Omega)$ convoluted by the temporal profile of the probe pulse E_2. See text and Eq. (5.3) for details.

5.2 Schemes for time-resolved single-beam CARS

A single-beam implementation of CARS allows a robust, very simple and compact setup (Fig. 5.9): As introduced in chapter 1, a broadband femtosecond laser source is combined with a pulse shaper to provide the optical excitation. The experiment itself is conducted in a microscope, with tight focusing guaranteeing phase-matching and high enough peak intensities for the nonlinear CARS process, as well as immediately allowing three-dimensional imaging with chemical contrast. Conventionally, the pulse shaper is used to block the blue wing of the excitation pulses to detect the blue-shifted CARS signal in that spectral region, although interferometric detection is also possible (see section 6, p. 115).[113, 145]

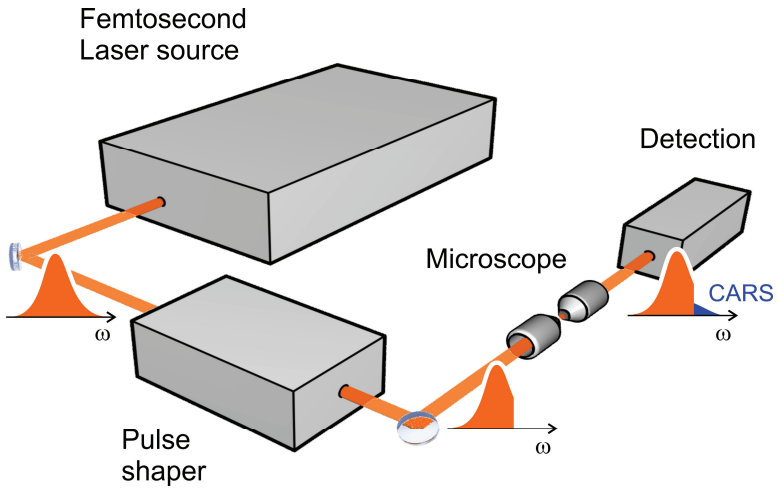

Fig. 5.9: Schematic drawing of a single-beam CARS experiment, as already shown in chapter 1. Time-resolved vibrational spectroscopy is performed by creating computer-controlled pulse sequences with the shaper, and detecting the respective blue-shifted CARS signal.

These features are common to all single-beam CARS schemes, be they operating in time- or frequency domain. Shaping the femtosecond laser beam is always necessary: Otherwise, the CARS signal cannot be spectrally resolved and is dominated by nonresonant background generated for all combinations of photon energies within the spectrum of the excitation pulses. Using the pulse shaper, the excitation light field is therefore tailored in such a way that either spectral resolution is restored by creating a narrowband probe,[143, 146-148] or time-resolved measurements are possible due to the creation of a controlled pulse sequence (Fig. 5.10), followed by *Fourier*-transformation of the recorded transient data.[17, 62, 109, 143, 144] There are several viable approaches, some of which have been newly developed in this thesis, which will be examined extensively, will successfully be applied to different spectroscopic problems and compared in the following. The seminal single-beam CARS approach by *Dudovich, Oron and Silberberg*[109, 143] uses a multipulse sequence created by the pulse shaper (Fig. 5.10a). *Fourier*-transform CARS can be implemented directly by shaping identical double pulses (Fig. 5.10a, see also chapter 4.3.2). To remove ambiguities, in this thesis a novel scheme was developed, which uses defined two-color double pulses (Fig. 5.10c), allowing additional polarization shaping and coherent control of the excitation (Fig. 5.10d).

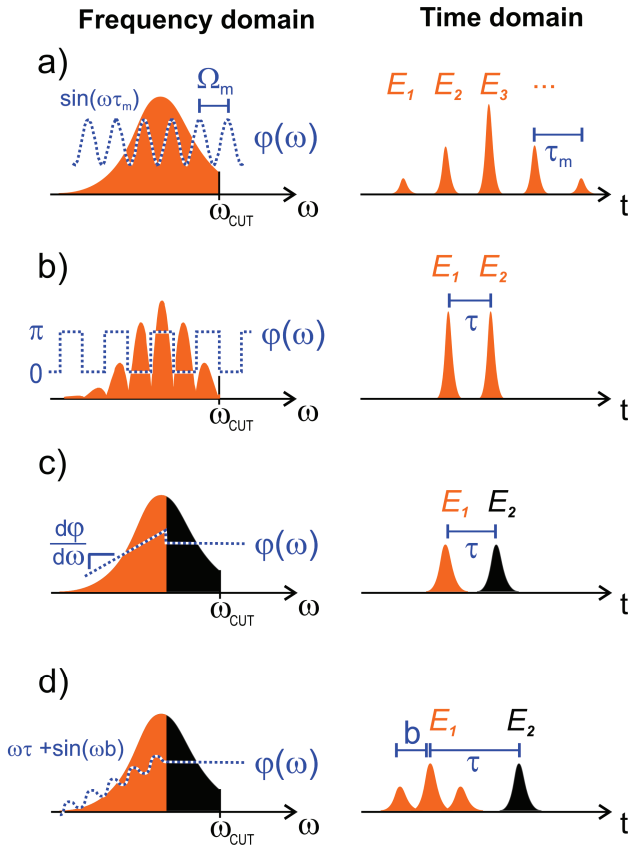

Fig. 5.10: Single-beam CARS schemes in time domain. **a)** Multipulse method, where a sine modulation of the spectral phase $\varphi(\omega)$ with a period Ω_m leads to a splitting of the pulse train into a multipulse sequence with sub-pulse separations $\tau_m = 1 / \Omega_m$. **b)** Identical double pulses avoid ambiguities of the multipulse method. **c)** Further improvement is possible assigning the role of distinguishable pulses by creating them from different spectral parts of the input pulse. This is done by applying a linear phase $\varphi(\omega)$ for one part, leading to a group delay $\tau = GD(\omega) = d\varphi/d\omega$. For conventional single-beam CARS measurements, the blue wing of the excitation spectrum is blocked for $\omega > \omega_{cut}$ to detect the much weaker, blue-shifted CARS signal in this spectral region. **d)** Even more complex pulse sequences can be created, *e. g.* with a multipulse sequence for selective excitation (sinusoidal phase) and a time-delayed probe.

For the simulations in Fig. 5.3 to Fig. 5.8, it was assumed that the role of the pulses $E_1(t)$ as pump and *Stokes* and $E_2(t)$ as probe is defined. This is the case in a setup where phase-matching is fulfilled by irradiating the sample with beams from different directions, in which case the respective wave vectors select exactly the wanted process. In a collinear scheme, this difference is not given, and pulses irradiated with the same spectrum are indistinguishable. Furthermore, in the same direction CARS signal is also being generated from each pulse alone, independent of delay τ.[62] The complete single-beam signal is then given by the interference of signal contributions from different combinations of E_1, E_2 taking the place of either pump and *Stokes*, or probe, or both pulses in Eq. (5.3). Additionally, only the blue wing of the generated signal is evaluated to be able to discriminate it against the much stronger excitation light. Therefore, a simulation of single-beam CARS must go beyond Eqs. (3.1) and (5.3) and take into account these effects. To study the consequences and compare different approaches for time-resolved single-beam CARS, numerical simulations have been performed again based on the same extension

created for the simulation package Lab2.[142] The molecular model system entering as $\chi^{(3)}(\Omega)$ has been chosen to be the same as in Fig. 5.8, while a shaped 10 fs pulse with a FWHM of 1500 cm^{-1} has been assumed for the excitation, with the blue wing of the spectrum clipped.

5.2.1 Multipulse excitation

As briefly mentioned before, the first single-beam CARS implementation by *Dudovich et al.*,[109, 143] used multipulse sequences. The shaping applied was a sinusoidal phase of the form

$$\varphi(\omega) = a \cdot \sin(\omega\tau_m + c), \tag{5.7}$$

where a is a phase amplitude factor which determines the depth, τ_m the frequency and c the phase of the modulation.

The most important notion is that the periodicity given by τ_m in the spectral phase leads to a temporal splitting of the input pulse into a multipulse sequence with exactly this temporal separation (Fig. 5.10a, Fig. 5.11). The resulting temporal field can be calculated analytically[35] as

$$E_{out}(t) = \sum_{n=-\infty}^{\infty} J_n(a) \cdot E_{in}(t - n \cdot \tau_m) \cdot \exp[-i \cdot n \cdot c], \tag{5.8}$$

where $E_{out}(t)$ ist the shaped pulse sequence, J_n(a) the *Bessel* function of the first kind and n-th order and $E_{in}(t)$ the unshaped input pulse shape. Eq. (5.8) confirms that the multipulse sequence consists of copies of the input pulse, shifted in time by $n \cdot \tau_m$, amplitude weighted by the *Bessel* function and equipped with an individual phase determined by c. The effects of a and c on the shape of the multipulse sequence are summarized in Fig. 5.11.

The possibility to use such shaped multipulses to control *Raman* transitions and thus the selective population of vibrational levels was first demonstrated by *Weiner et al.*[27] in 1990. For single-beam CARS, the very same idea applies for the excitation: τ_m controls the shape of the *Raman* excitation probability $A(\Omega)$ [Eqs. (5.2) and (5.4)], which can thus be tuned to certain vibrational energies. As stated before, and within the frequency domain framework of pathway-interference [Eq. (5.2)], $A(\Omega)$ can be interpreted as the sum of all frequency pairs within the excitation pulse having a frequency spacing of Ω, thus capable of populating *Raman* levels with this energy separation. For the further discussion, the frequency representation of $A(\Omega)$ shall be stated explicitly once again:

$$A(\Omega) = \int_0^{\infty} d\omega' \, \tilde{E}_s^*(\omega') \tilde{E}_p(\omega' + \Omega), \tag{5.2), (5.9}$$

where $\tilde{E}_s(\omega) = \tilde{E}_p(\omega) = \tilde{E}(\omega)$ in single-beam CARS.

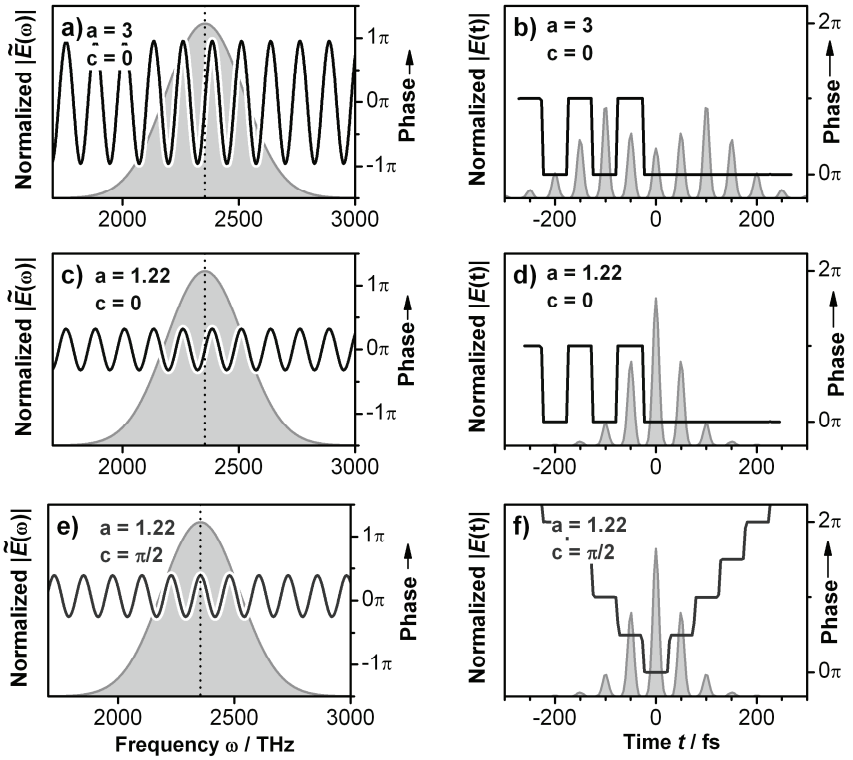

Fig. 5.11: Multipulse shaping with sinusoidal phases, showing the influence of the modulation amplitude *a* and the phase *c*. In all cases, the sub-pulse temporal spacing τ_m was set 50 fs. The input field $E_{in}(t)$ is a 10 fs *Gaussian* transform limited pulse. **a)** Strong modulation with $a = 3$ leads to a splitting of the input pulse into a temporally very long sequence. Note that the temporal intensity maximum is not at time zero. **b)** Multipulse for a modulation *a* of 1.22, which will show the best selectivity in coherent control of molecular motion. For $c = 0$ (pure sine phase), phase jumps of π occur in the pulse sequence between one half of the sequence. **c)** For $c = \pi/2$ (pure cosine phase) jumps of $\pi/2$ occur between all subpulses.

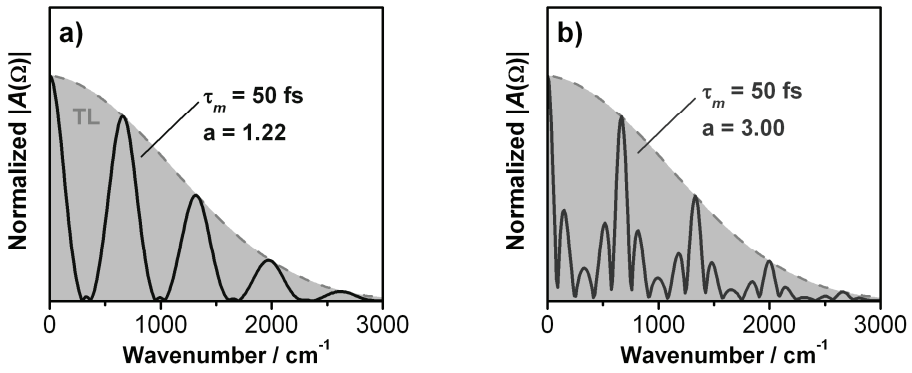

Fig. 5.12: Comparison of *Raman* population amplitude $A(\Omega)$ for different values of the sinusoidal modulation amplitude *a*: **a)** $a = 1.22$ and **b)** $a = 3$. It can be seen that although larger *a* create narrower and thus more "selective" filtering in Ω, the contrast is largely diminished. Therefore, generally $a = 1.22$ is the optimal choice for multipulse coherent control of *Raman*-type transitions.

The behaviour of $A(\Omega)$ for a *Gaussian* excitation spectrum is shown in Fig. 5.12 for the *Fourier* transform limited case (FL, see also Fig. 5.2) and two different spectral phase functions $\varphi(\omega)$ with sine modulation amplitudes $a = 1.22$ (Fig. 5.12a) and $a = 3$ (Fig. 5.12a): *Fourier* transform limited excitation (grey dashed curve) and sinusoidal modulation with frequency $\tau_m = 50$ fs and correspondingly a period $\Omega_m = 2\pi / \tau_m \sim 660$ cm^{-1} (thick solid curves).

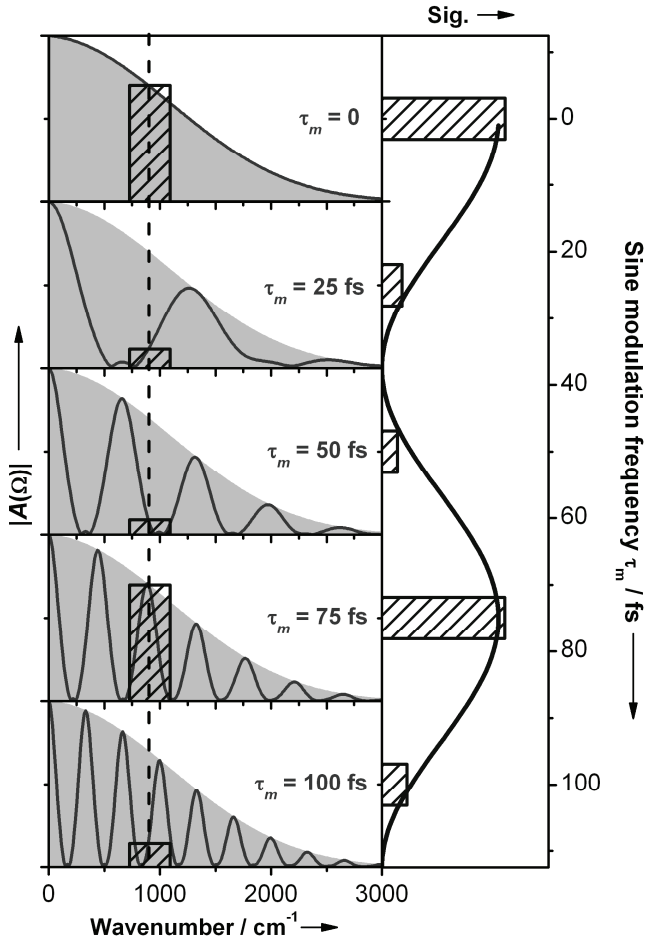

Fig. 5.13: Single-beam CARS spectroscopy with multipulse sequences created by a sinusoidal spectral phase modulation. It can be seen that for $\tau_m > 0$ only certain wavenumbers Ω can be excited in a *Raman*-type process, reaching again the same value as an unmodulated, transform-limited pulse ($\tau_m = 0$, grey hatched curve). To perform spectroscopy, τ_m is scanned and the resulting CARS signal spectrally integrated and recorded. For a given vibrational level in the molecule - here, a resonance at $\Omega_R = 900$ cm^{-1} is assumed - this results in $A(\Omega)$ alternating between maxima (for $\tau_m = 0$ and $\tau_m = 75$ fs) and minima (25 fs < τ_m < 50 fs). The integrated signal therefore shows an oscillation in τ_m, which has a period of ~75 fs. This is exactly the vibrational period of the given ~900 cm^{-1} mode and hence substantiates that the wanted vibrational spectrum can directly be obtained from the *Fourier* transform of the τ_m-scan.

If $\tilde{E}^*(\omega')$ and $\tilde{E}(\omega'+\Omega)$ have a constant phase relation in Eq. (5.9) for each frequency ω', they add up constructively, as it is always the case for *Fourier*-transform limited excitation pulses with $\varphi(\omega) = const$. However, when the spectral phase $\varphi(\omega)$ is modulated periodically with a period Ω_m, meaning that $\varphi(\omega) = \varphi(\omega + \Omega_m)$, constructive interference occurs only for Ω =

$N \times \Omega_m$ (N being an integer number). In this case, $A(\Omega)$ reaches the value of the transform limited case. Otherwise, the varying phase between different frequency pairs with spacing Ω leads to destructive interference, meaning that such *Raman* levels cannot effectively be populated any more (see Fig. 5.12). This mechanism thus allows discriminating different resonant *Raman* levels in the CARS process and is the key to restoring spectral resolution: The created population of an excited level is probed by the same pulse, leading to a broad blue-shifted signal spectrum, whose integrated intensity depends on $A(\Omega)$. For single-beam CARS spectroscopy, signal is recorded for each value of τ_m. This is demonstrated schematically in Fig. 5.13.

A more detailed analysis[14] reveals, that periodic phase modulation of the excitation pulse is at the same time capable of effectively suppressing the nonresonant background, which is maximized for the transform-limited case.

In the time-domain, the whole scheme can be understood in terms of the excitation pulse being split into a pulse train with subpulses separated by τ_m, which is caused by the periodic modulation of the spectral phase. The very effective background suppression can in this framework be explained as follows: The excitation energy in a multipulse is distributed over a series of subpulses, in contrast to a single transform-limited pulse. As the nonresonant background signal is a third-order nonlinear and instantaneous material response, a single pulse containing the complete energy will create a signal 25 times stronger than assumed five pulses with each a fifth of the energy. Varying τ_m for spectroscopy means synchronizing the temporal spacing of the sub-pulses with the nuclear motion in a vibrating molecule. In a time-domain description, this is very much reminiscent of impulsive fs-CARS introduced in section 5.1.3 (p. 77) for just two pulses. The presence of a larger number of subpulses in the sequence is responsible for ambiguities arising in the multipulse spectroscopy method. To understand this, the time-domain CARS description of Eq. (5.3) shall be used again:

$$S_{CARS}(\tau) \approx \int_{-\infty}^{\infty} dt \left|E_2(t)\right|^2 \left| \int_{-\infty}^{\infty} d\Omega \exp[-i\Omega(t+\tau)]\, A(\Omega) \cdot \chi^{(3)}_{CARS}(\Omega) \right|^2, \qquad (5.3), (5.10)$$

The second part of Eq. (5.10), stated as a *Fourier* transform in Ω, was very convenient earlier to understand the influence of the *Raman* excitation probability $A(\Omega)$ and limited bandwidth. However, this led to the first interacting field $E_1(t)$ vanishing in $A(\Omega)$. For now, the Ω-dependent part of (5.10) shall be formulated in the time domain. Also, the squared modulus of Eq. (5.10) is not appropriate when signal contributions from different multipulses are to be discussed, as one has to deal with coherent signals, which are linear in the field but not in the intensity. Therefore, the polarization P_{CARS} as source term of the CARS field will be used. The *Fourier* transform of the product of $A(\Omega)$ and $\chi^{(3)}_{CARS}(\Omega)$ in (5.10) therefore becomes a convolution of their respective *Fourier* transforms $|E_1(t')|^2$ and $R(t')$, yielding:

$$P_{CARS}\{E_1, E_1, E_2\}(t,\tau) = -E_2(t) \int_0^{\infty} dt' \left|E_1(t+\tau-t')\right|^2 \cdot R(t'). \qquad (5.11)$$

Eq. (5.11) assumes CARS signal generation from two optical pulses. The curly brackets are used to indicate the role of the pulses: $E_1(t)$ acts as pump and *Stokes* and $E_2(t)$ as delayed probe. $R(t')$, as *Fourier* transform of $\chi^{(3)}_{CARS}(\Omega)$ is the molecular response function,[130]

which contains the entire molecular dynamics. If no contributions from other combinations of $E_1(t)$ and $E_2(t)$ play a role, integrating and calculating the squared modulus of Eq. (5.11) yields the signal

$$S\{E_1,E_1,E_2\}(\tau) \propto \int_{-\infty}^{\infty} dt \left| P_{CARS}\{E_1,E_1,E_2\}(t,\tau)\right|^2, \tag{5.12}$$

which is mathematically identical to Eq. (5.10), but having introduced a notation explicitly stating the involvement of the different electric fields. For a situation with interfering contributions of electric fields, and only considering cases with τ significantly larger than the duration of the longest pulse involved, the total signal contains interference of all possible polarizations:

$$S_{total}(\tau) \propto \int_{-\infty}^{\infty} dt \left| \sum\sum_{i\neq j} P_{CARS}\{E_i,E_i,E_j\}(t,\tau)\right|^2 . \tag{5.13}$$

Let us now consider single-beam CARS with periodic phase modulation: A compressed input pulse (Fig. 5.10a) is split into a train of sub-pulses E_1, E_2, … (Fig. 5.10b). Every single sub-pulse can act as pump, *Stokes* and probe. Because of the collinear excitation geometry, the single-beam CARS signal originates from components $P_{CARS}\{E_1,E_1,E_1\}(t,\tau)$, $P_{CARS}\{E_2,E_2,E_2\}(t,\tau)$, … generated by each pulse alone, together with the normal time-resolved signal field, where a first pulse excites a coherent vibration which is then probed by a pulse delayed by τ: $P_{CARS}\{E_1,E_1,E_2\}(t,\tau)$, $P_{CARS}\{E_2,E_2,E_3\}(t,\tau)$, … However, as the role of the sub-pulses is not defined, there are also contributions such as $P_{CARS}\{E_1,E_1,E_3\}(t,\tau)$, which correspond to a conventional time-resolved signal at 2τ. This is why ambiguity arises in multipulse single-beam CARS data. For a demonstration, multipulse single-beam CARS has been simulated in Fig. 5.14 for the molecular system with two resonances at 800 cm^{-1} and 1500 cm^{-1} already used in Fig. 5.8.

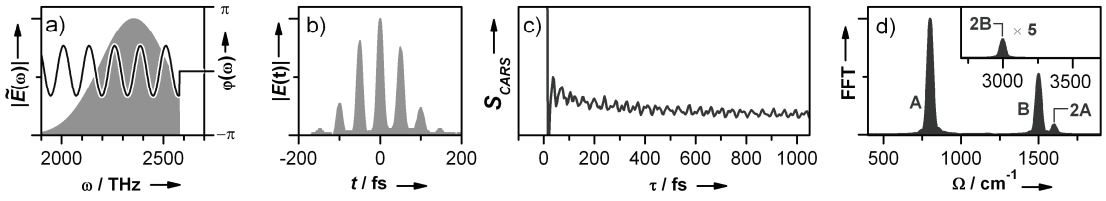

Fig. 5.14: Simulation for multipulse single-beam CARS: **a)** Sinusoidal phase with τ_m = 50 fs and **b)** resulting temporal multipulse structure. **c)** Simulated single-beam CARS τ_m-scan, together with **d)** the corresponding *Fourier* spectrum. Basis of these numerical simulations is again the same $\chi^{(3)}_{CARS}$ as in the data of Fig. 5.8. Note the ambiguities arising in the *Fourier* spectrum for mode *A* (800 cm^{-1}) at *2A* (1600 cm^{-1}) and mode *B* (1500 cm^{-1}) at *2B* (3000 cm^{-1}).

As expected from Fig. 5.13, the single-beam CARS signal (Fig. 5.14c) shows oscillations and a beating pattern, which is expected as both vibrational modes can be excited by the 10 fs pulse used in the simulation. However, the ambiguities due to the multipulse contributions discussed in the last paragraph are clearly visible in its *Fourier* spectrum (Fig. 5.14d): While the two vibrational modes appear as expected, with the 1500 cm^{-1} ("B") being weaker than

the 800 cm^{-1} one ("A") due to less available excitation frequency pairs, higher harmonics of both modes are present. While the resulting additional peak at 3000 cm^{-1} (Fig. 5.14d, inset, "2B") can immediately be discarded as artefact due to the limited available excitation bandwidth, the 1600 cm^{-1} peak ("2A") cannot be discriminated against a true molecular vibrational level at this spectral position. To prevent erroneous interpretation in multipulse single-beam CARS, the modes which can be excited by the pulse train bandwidth and are detected thus have to be restricted to one octave of wavenumbers.[143] Thus higher harmonics can always be excluded. Therefore, excitation and detection have to be carefully matched to a certain range of wavenumbers. While this is acceptable for a limited analysis of the fingerprint spectral region (*e. g.* 600 – 1200 cm^{-1}) it becomes utterly impractical for low frequency vibrations (only small ranges such as 50 cm^{-1} – 100 cm^{-1}, 100 cm^{-1} – 200 cm^{-1}, … can be detected in one run of the experiment). Suitable "sculpting" of the excitation spectrum allows easier handling of multiple runs and thus successfully studying low-frequency vibrations,[16] but still requires several runs and adjustments.

To overcome these limitations, a new scheme was developed in the course of this thesis which directly and unambiguously implements impulsive time-resolved CARS. A pulse sequence with only two distinct pulses $E_1(t)$ and $E_2(t)$ is generated, which will be described in the following sections.

5.2.2 Excitation with identical double pulses

The most direct approach to single-beam time resolved vibrational spectroscopy is an implementation of the FT-CARS scheme by *Ogilvie* et al.,[108] with the creation of a doublet of identical copies of the input pulse by the shaper (Fig. 5.10b, Fig. 5.15a-d). This is achieved by a simultaneous phase and amplitude modulation of the input spectrum (Fig. 5.15a).[62] In this case, as in the case of multipulse shaping (previous section 5.2.1, p. 84) the complete bandwidth of the ultrafast laser source can be used for combinations of pump and *Stokes* photons, thus the widest range of vibrational energies becomes accessible within the envelope of $A(\Omega)$. It can also be seen in Fig. 5.15c that due to the two pulses being indistinguishable, the transient CARS signal S_{CARS} measured is symmetric with respect to τ. A disadvantage of the scheme is the inherent interference of the mostly instantaneous nonresonant signals generated by each of the pulses alone. As long as they are not well separated in time for large enough τ, very complex oscillations arise in the spectrally integrated transient CARS signal, which do not reflect molecular properties. This can be seen in Fig. 5.15d for $\tau < \sim 200$ fs. These unwanted contributions can be windowed out before *Fourier* transforming, by neglecting data for $\tau < \tau_{cut}$. In the simulation, two cases are shown in Fig. 5.15c. In the first case, only the nonresonant signal around $\tau = 0$ is windowed out by chosing a $\tau_{cut} = 30$ fs (Fig. 5.15c, grey arrow).

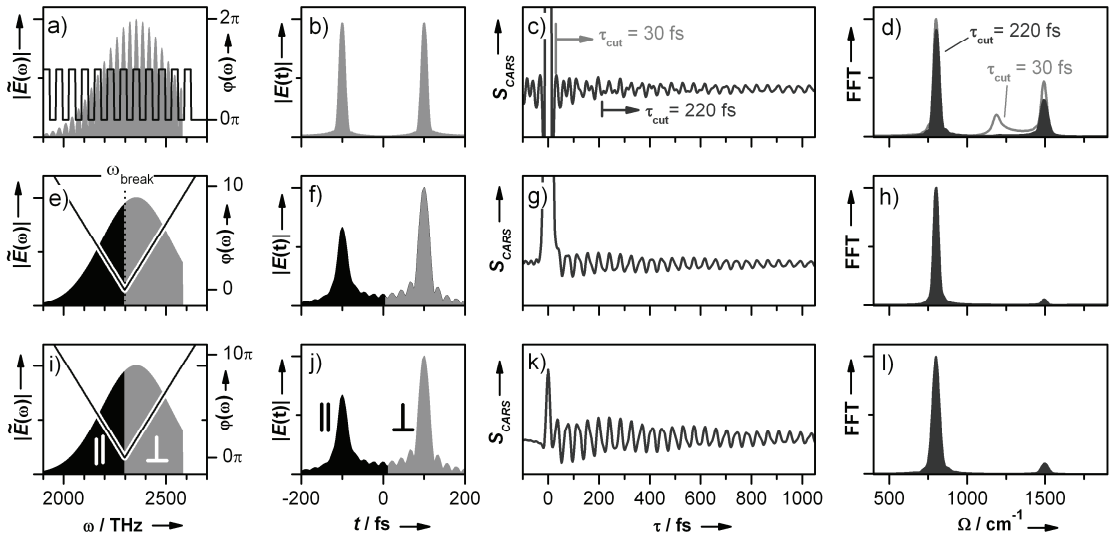

Fig. 5.15: Simulations for different pulse sequences for femtosecond time-resolved single-beam CARS: **a-d)** sequence of identical double pulses, **e)-h)** two-color double pulses and **i)-l)** two-color double pulses with orthogonal polarization. In the first column of panels **a)**, **e)** and **i)** the spectrum together with the spectral phase modulation as created by the pulse shaper is shown. The second column **b)**, **f)** and **j)** depicts the corresponding temporal electric field of the pulse sequence. In the third column **c)**, **g)** and **k)**, simulated CARS transients are shown for each case, together with the corresponding *Fourier* spectra in the forth column **d)**, **h)** and **l)**. Basis of these numerical simulations is again the same $\chi^{(3)}_{CARS}$ as in the data of Fig. 5.8.

The mentioned interferences in the transient signal now show up as artefact peaks in the *Fourier* transform (Fig. 5.15d, grey curve), obscuring the true molecular vibrational spectrum. Only for a larger $\tau_{cut} = 220$ fs (Fig. 5.15c, arrow), interference effects are suppressed and a clean *Fourier* spectrum is obtained (Fig. 5.15d, hatched solid curve). The necessary cut-off delay τ_{cut} strongly depends on the pulse shape: if the pulses employed exhibit pre- and afterpulses, as is the case for more realistic spectra of many ultrashort fs-sources which do not follow a smooth *Gaussian* envelope, τ_{cut} often has to be chosen such that unnecessary loss of spectroscopic information occurs. Also, in this scheme, the transient CARS signal is always detected on top of a massive signal offset, which is subtracted in data analysis prior to the *Fourier* transform.[144]

5.2.3 Excitation with two-color double pulses

These shortcomings can be mitigated if a sequence of double pulses with different color is generated (Fig. 5.15e-h).[62] In this case, due to their separated spectra, the role of the two pulses (E_1 acting as pump and *Stokes*, E_2 as probe) is clearly defined. This advantage comes at the cost of reduced coverage of vibrational energies and thus a more narrow $A(\Omega)$: Two-color double pulses are created by a pure phase-modulation with the shaper (Fig. 5.15e). Applying a phase linear in the optical frequency with different slopes in two spectral regions, the blue spectral half of the excitation pulse with $\omega > \omega_{break}$ is delayed in time, while the red part with $\omega < \omega_{break}$ is advanced (Fig. 5.15f).[149] In this scheme, only half of the spectrum can be used for the impulsive excitation of a vibration with suitable photon pairs

from the first pulse. The frequency shift of the second pulse (E_2) leads to CARS emission, shifted yet further to the blue into a spectral region where no unwanted four-wave mixing signal of the first pulse (E_1) alone can occur. Therefore, disturbing interference effects are highly reduced. Only directly around $\tau = 0$ certain contributions remain because of photons from both sub-pulses taking part in four-wave mixing processes other than the desired CARS, giving rise to a strong peak corresponding to the nonresonant background (Fig. 5.15g). *Fourier*-transforming the data after windowing out only this peak gives the vibrational spectrum shown in Fig. 5.15h. Note the effect of the reduced effective excitation bandwidth, as now the vibrational mode at 1500 cm^{-1} is only barely visible. For this scheme, the question of the optimal choice of the spectral division in the two time-delayed pulses arises. From the considerations in the discussion of Fig. 2 one can assume that a symmetrical partitioning of the bandwidth should be optimal. To test this assumption, the time-resolved single-beam CARS signal has been simulated in this scheme for different values of ω_{break} (Fig. 5.16). In each case, the transient has been evaluated for $\tau > 30$ fs. It can be seen in Fig. 5a that the two molecular vibrations at 800 cm^{-1} and 1500 cm^{-1} are clearly visible only for a more or less symmetric partitioning with ω_{break} near 12200 cm^{-1}. This becomes especially clear in Fig. 5.16b where the *Fourier* amplitude at 800 cm^{-1} (open circles) and 1500 cm^{-1} (filled circles) is plotted versus ω_{break}. It can also be discerned that for a highly unsymmetrical partitioning additional *Fourier* components arise, which are again due to optical interferences, as in the case of the identical double pulses when evaluating the given time window $\tau > 30$ fs. This is particularly the case, if the bandwidth of the red-shifted pump/*Stokes* pulse E_1 largely exceeds the width of the probe E_2, as now signal generated from E_1 alone can be detected on the blue side of E_2 and can interfere with the wanted CARS signal. This manifests itself in the strong artefact features visible for $\omega_{break} > 12750$ cm^{-1} in Fig. 5.16a.

A further increase of signal contrast, suppression of the strong nonresonant peak at $\tau = 0$ and complete removal of optical interference effects can be achieved if another important advantage of two-color single-beam CARS comes into play: both pulses, in addition to the timed sequence, can be independently modified in phase, amplitude and/or polarization. The latter is especially attractive, can be easily achieved with pulse shapers currently used,[84] and introduces an additional degree of flexibility for single-beam CARS:[147, 148] In the case of the time-resolved scheme, practically background-free transient measurements become possible.[***] To achieve this, the polarization of the probe pulse is rotated by 90° in the pulse shaper (designated with the symbols ∥ and ⊥ in Fig. 5.15i), and CARS signal is only detected in this direction of the probe polarization (⊥). This procedure removes all remaining signal contributions from unwanted four-wave-mixing processes between the two pulses E_1 and E_2, and drastically reduces the nonresonant peak at $\tau = 0$ (Fig. 5.15k). Experimental results obtained with this novel combined approach of polarization pulse shaping and time-resolved single-beam CARS measurements will be presented later in this chapter.

[***] It has to be noted, though, that with crossed polarizations a different tensor element of $\chi^{(3)}$ is probed, namely $\chi^{(3)}_{1100}$ instead of $\chi^{(3)}_{1111}$ in the usual nomenclature. The information contained about the molecule is, however, the same for the experiments presented here.

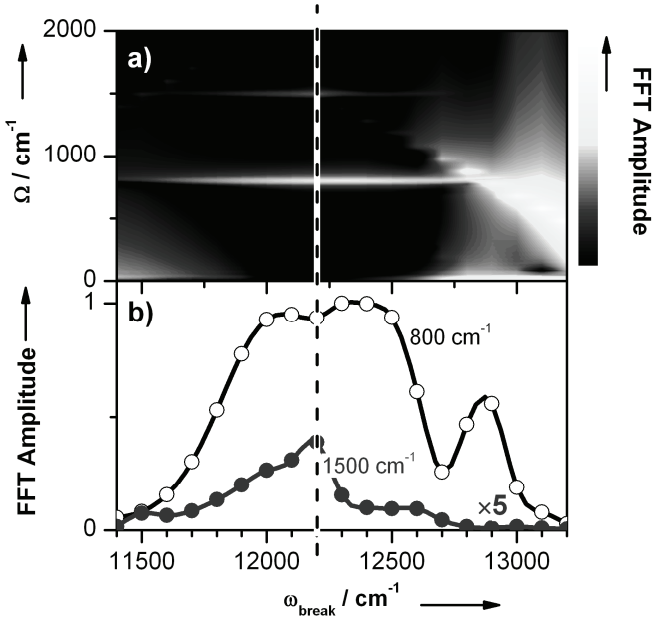

Fig. 5.16: Influence of the spectral position ω_{break} of the break point for the linear phase functions applied to create two-color double pulses (see Fig. 5.15e). Only for a symmetric division of the spectrum into two time-delayed pulses E_1 and E_2 clean *Fourier* spectra are obtained at the best visibility of both vibrations at 800 cm^{-1} and 1500 cm^{-1}. **a)** Intensity map of the *Fourier* amplitude at different wavenumbers Ω for different ω_{break}. **b)** Integrated peak area for the 800 cm^{-1} (open circles) and 1500 cm^{-1} (filled circles) modes, clearly showing a maximum for both vibrations around ω_{break} = 12200 cm^{-1} (indicated by the dashed vertical line). This data has been normalized to the maximum of the 800 cm^{-1} mode, the data for 1500 cm^{-1} has been enlarged by a factor of five for better visibility.

5.3 Potential pulse shaping artefacts

In the typical 4*f*-pulse shaping schemes using LCD-SLM, modulation of the laser spectrum is performed on the basis of single pixels which can electronically be set to a certain phase retardation, amplitude or polarization rotation.[80, 81, 84] The nature of pixilation has an important consequence on the shaping of pulse trains in time-resolved single-beam CARS: The number of available pixels limits the maximum temporal extension any pulse sequence generated can have. Therefore, a time-resolved measurement is limited to a maximum delay τ_{max} defined by the SLM resolution. From the *Fourier* transform nature of 4*f*-pulse shaping, τ_{max} can be estimated as the inverse frequency sampling $\Delta\Omega$ of the phase:

$$\tau_{\max} \approx \frac{1}{\Delta\Omega} = \frac{N}{\Delta\omega_{pulse}} = \frac{N}{2\pi \cdot f} \cdot \Delta t_{pulse} \tag{5.14}$$

where the pixel frequency pitch $\Delta\Omega$ can be expressed by the pulse bandwidth $\Delta\omega_{pulse}$ divided by the number of pixels N available. As a result, the maximum delay τ_{max} for a pulse sequence is the product of the input pulse duration Δt_{pulse} and the number of pixels N divided by the time-bandwidth factor f. As the spectral resolution in any *Fourier*-transform spectroscopy is defined by the inverse length of the time series measured, τ_{max}^{-1} and thus, according to eq. 3, $\Delta\Omega$ directly translates into the spectral resolution. This result is of course obvious in single-beam CARS schemes in the frequency domain, where the narrowest

spectral feature creatable is with one pixel. These considerations have an important consequence: For high-resolution spectroscopy, SLM with high pixel numbers[80] are a prerogative.

An artefact occurring in any 4*f*-pulse shaping schemes is space-time coupling,[88] which has briefly been addressed in chapter 4.1 This phenomenon manifests itself in the fact that shifting a part of the input spectrum in time with the pulse shaper also leads to some spatial shifting. In a single-beam experiment, the aperture of the microscope only selects the central parts of the beam, so that space-time coupling leads to a certain decrease in intensity for pulse sequences with a large value of τ. This effect can, however, rather easily be accounted for by normalizing the experimental data respectively. Another effect of pixilated pulse shaping devices is the occurrence of spurious pulse replica.[87] However, if the shaping is kept well within the limits imposed by eq. 5, the intensity in the artefact replica pulses is low enough to neglect their participation in the nonlinear CARS process. This may not always be completely possible in schemes using interferometric detection,[113, 145] although in these cases suitable phase cycling strategies should allow mitigating unwanted effects.

5.4 Experimental implementation

The setup is identical to the one used in the previous chapters. It again consists of the four building blocks sketched in Fig. 5.9. A schematic is shown in Fig. 5.17. Briefly, the broadband femtosecond laser pulses employed in this study stem from a photonic crystal fiber (PCF, see chapter 2.2.2), pumped by 3 nJ pulses of a standard 100 fs laser oscillator at 795 nm and 80 MHz repetition rate. The PCF (type NL-PM-800, *Crystal Fiber A/S*) is polarization maintaining, and has a zero-dispersion wavelength at 800 nm. The length is only 23 mm, and a coupling efficiency of about 50% is achieved. The pulse shaper used (see chapter 4.1) is based on a 640 pixel dual-layer liquid crystal spatial light modulator (SLM), using 1200 grooves/mm gratings and spherical mirrors with a focal length f = 200 mm.

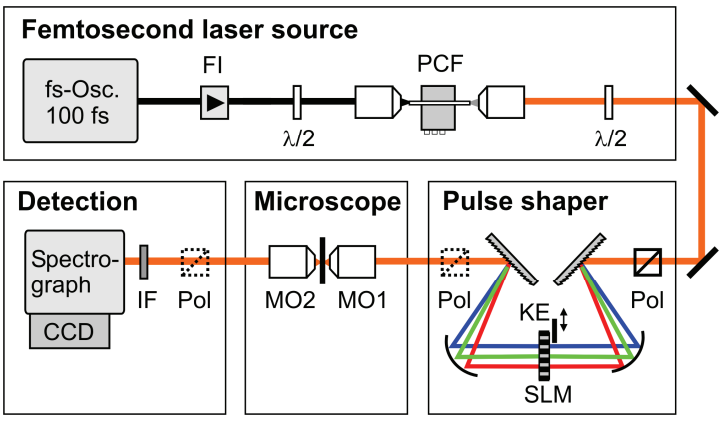

Fig. 5.17: Experimental setup, consisting of a photonic crystal fiber (PCF) based broadband femtosecond laser source, a 4*f* pulse shaper and a microscope setup with detection.

If the dual-layer SLM is used for amplitude shaping, a pair of polarizers is integrated at the input and output port of the shaper. For polarization shaping, the output polarizer is removed and placed in the detection unit. In the *Fourier*-plane of the shaper, a knife-edge

(KE) can be inserted to block the blue part of the excitation spectrum. The microscope assembly uses a 60x microscope objective (MO1, NA 1.2) for focusing and a 40x objective (MO2, NA 0.6) with a long working distance of 4 mm for collecting the CARS signal created in forward direction. Detection is accomplished by a charge coupled device (CCD) camera mounted on a spectrograph, which integrates the blue-shifted CARS signal. To reject the excitation light, a short-pass interference filter is used (passing $\lambda < 760$ nm). In the case of experimental schemes relying on polarization shaping, additionally a polarizer is placed in front of the detection unit. Prior to all experiments, the PCF output pulses were compressed *in situ* in the microscope to fully compensate for its distorted spectral phase and temporal broadening due to dispersion in the microscope using shaper-assisted collinear spectral shear interferometry for direct electric field reconstruction (SAC-SPIDER, see chapter 4.3).[150] Shaped pulse sequences extending in time over several hundreds of femtoseconds and featuring discontinuities in the time-frequency representation (like Fig. 5.18d) need to be characterized using the much slower and more inconvenient cross-frequency resolved optical gating (XFROG, see chapter 4.7) method, which was also be implemented *in situ* in the microscope.[150]

5.4.1 Pulse shaping and *in situ* confirmation

As explained earlier in great detail, the success of any single-beam CARS measurement crucially depends on well compressed and femtosecond pulses shaped with very high fidelity in the focus of the microscope. In the context of discussing *in situ* compression of fs-pulses in the microscope, Fig. 4.19 (section 4.6.2) already gave an example of a compressed and shaped multipulse originating from a sinusoidal spectral phase. In Fig. 5.18, XFROG traces are shown for the compressed pulse of a photonic crystal fibre continuum (Fig. 5.18a) and a sequence of a two-colour double pulse generated by pulse shaping (Fig. 5.18d). From the data of the compressed pulse, the temporal intensity profile can be reconstructed, showing a clean pulse with a duration of 14.5 fs FWHM (Fig. 5.18b). From this, the excitation probability $A(\Omega)$ is immediately computed according to Eq. (5.2), showing that this laser source offers enough bandwidth to cover vibrational modes up to ~1500 cm^{-1}, if the full spectrum is used as $E_1(t)$ in a single-beam CARS scheme with multipulses (Fig. 5.10a) or identical double pulses (Fig. 5.10b). Employing only half of the excitation spectrum in a two-colour double pulse scheme (Fig. 5.10c, d) results in $A(\Omega)$ dropping to zero at already ~800 cm^{-1} due to the unavailability of frequency pairs with a larger difference Ω in $E_1(t)$.

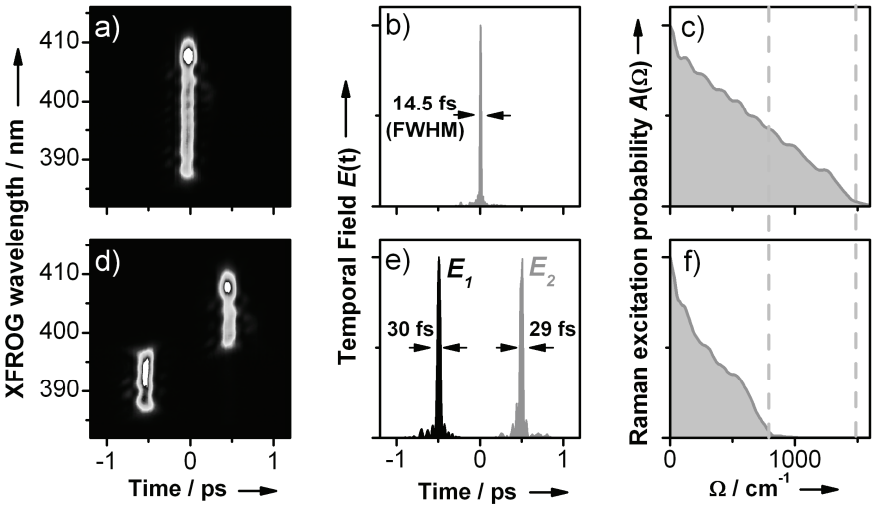

Fig. 5.18: Experimentally realized ultrashort pulses and pulse sequences for single-beam CARS. A time-frequency representation is measured by cross-frequency resolved optical gating (XFROG), yielding maps of pulse frequency versus time (a, d). From this data, the exact temporal field amplitude (b, e) can be reconstructed, and the *Raman* population amplitude $A(\Omega)$ be calculated according to eq. 2. In the first row (a-c), a single compressed pulse is shown, while in the bottom row (d-f) a two-color double pulse sequence with a temporal spacing $\tau = 1$ ps can be seen.

5.4.2 Acquiring and processing the time-resolved data

With the capability to create all wanted pulse sequences in the microscope focus, time-resolved single-beam CARS data can be acquired using one of the schemes presented earlier. All that is needed is to detect the blue shifted CARS signal as a function of the multipulse modulation τ_m or the delay τ respectively, which is introduced in the pulse sequence by computer control of the pulse shaper. So far, the blue wing of the excitation spectrum is always blocked, and only CARS signal is detected in this spectral region after suitable filtering. To demonstrate data acquisition and processing, first a time-resolved single-beam CARS transient obtained with the two-color double pulse method for the sample Diiodomethane (CH_2I_2) shall be considered, and summarized in Fig. 5.19. CH_2I_2 features one strong resonance at 480 cm^{-1} in the accessible range. The measured raw data is an oscillatory signal on top of a slowly varying background (Fig. 5.19a, grey solid curve).

The background is simply due to mostly nonresonant CARS signal generated by the probe $E_2(t)$ alone, as discussed earlier. This contribution is however expected to remain constant and independent of τ, as simulated in Fig. 5.15. In the experiment, the curve shows a decline of the background for larger values of τ, and a concomitant decrease of the oscillation amplitude: this is due to the decreasing excitation intensity because of the space-time-coupling effect of the 4*f*-pulse shaper. For increasing values of τ, steeper and steeper phase functions φ_{SLM} have to be applied. As any phase function needs to be wrapped to fit into the phase interval $[0, 2\pi]$, an increasing number of phase jumps occurs in the *Fourier* plane, leading to more diffraction. Examples of experimentally realized wrapped phase functions are shown for $\tau = 200$ fs and $\tau = 3000$ fs in Fig. 5.19a (top row of insets, open squares). While for $\tau = 200$ fs a smooth modulation with only a few phase jumps in φ_{SLM} is realized,

τ = 3000 fs shows very pronounced phase jumps occurring every fourth pixel. This leads to intensity attenuation, although only a pure phase modulation is performed. Experimentally, the decline in the excitation intensity I_{Exc} due to the shaping can very easily be measured as a function of τ, showing a monotonous attenuation to below 50% when approaching the limit of pixilation of the SLM (Fig. 5.19a, filled squares). For the shaper used, this limit of τ_{max} is about 3700 fs [see Eq. (5.14)]. Using $I_{Exc}(\tau)$, the raw transient CARS data can immediately be corrected for these intensity effects by normalizing the transient with $I_{Exc}(\tau)^3$, according to the well-known intensity dependence of CARS. The result is shown in Fig. 7a as black solid curve. The thus corrected data now shows the theoretically expected modulation on top of a constant offset.

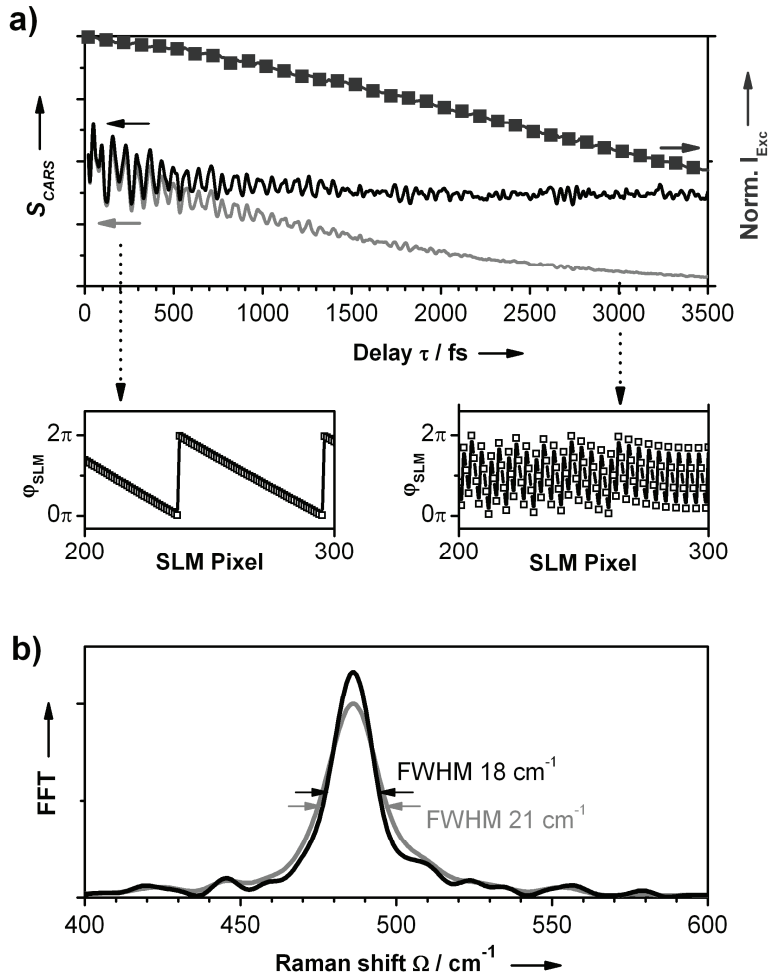

Fig. 5.19: Time-resolved single-beam CARS correction for unintended intensity modulation effects (due to space-time coupling and diffraction in the pulse shaper). **a)** Measured raw transient CARS data (grey solid curve), excitation intensity (filled squares) and corrected CARS transient (black curve). Additionally, experimental phase patterns for two delays τ at 200 fs and 3000 fs, demonstrating the effect of phase jumps and pixilation, are shown as insets in the top row. **b)** Resulting *Fourier* spectra for the transient without (grey curve) and with (black curve) intensity correction. In both cases, the offset of the transient has been subtracted prior to *Fourier* transforming.

Of most importance for spectroscopic applications is the effect of this operation on the *Fourier* spectrum, shown in Fig. 7b. In both cases, for the raw and corrected transient data, the constant or slowly decaying offset was subtracted prior to the *Fourier* transform. Additionally, the *Fourier* transform procedure includes weak apodization and zerofilling, as described in detail in an earlier publication.[144] The resulting *Fourier* spectra for the uncorrected (grey curve) and corrected (black curve) CARS transients are very similar and show the 485 cm^{-1} vibrational mode of CH_2I_2. The peak is, however, slightly narrower in the case of the corrected data (18 cm^{-1} FWHM) as compared to the uncorrected case (21 cm^{-1} FWHM). This is readily expected, as the uncorrected data can simply be understood as subjected to an additional apodization with $I_{Exc}(\tau)^3$, smoothing out side maxima in the *Fourier* spectrum at the cost of slightly reduced spectral resolution. This demonstrates that effects of non-ideal shaping in the experiment are only marginally detrimental for single-beam CARS spectroscopy, while they can be easily corrected for. It has to be noted, though, that the correction procedure can introduce unwanted noise in the *Fourier* spectrum, if the time domain data does not have a sufficiently high signal to noise ratio. In such cases it is much better to proceed without the gain in spectral resolution and not apply the $I_{Exc}(\tau)^3$-correction.

5.5 Results and discussion of multipulse single-beam CARS

With all the technical prerequisites in place and theoretical foundations laid, the applicability of single-beam CARS using shaped supercontinuum and multipulse sequences shall be demonstrated. The first application is spectroscopy of neat samples, the second one a demonstration of the chemical identification of microcrystals as a model approach for "white powder" threat assessment.

5.5.1 Spectroscopy of neat samples in the condensed phase

Employing compressed fs-pulses in the microscope, a blue-shifted CARS signal ranging from 760 to below 705 nm can be detected from the first sample Toluene. For $\tau_m = 0$ fs, this signal is dominated by instantaneous nonresonant background. However, with increasing τ_m the compressed pulse is slowly split into subpulses and the nonresonant signal rapidly decreases, finally approaching a much lower constant value for well separated subpulses. This can be seen in the first 60 fs of Fig. 5.20a (shaded area). This initial decay is therefore a measure for the pulse duration. This experiment has been carried out with pulses compressed in the closed-loop optimization approach described in chapter 4.2, where the reconstructed phase of the pulses has also been shown (Fig. 4.10) For another independent proof of the sub-20 fs pulses *in situ* in the microscope, the nonresonant CARS signal is simulated (inset of Fig. 5.20a, gray solid line) using the earlier characterized pulses and excellent agreement found with the experimental data (circles). *Fourier* transform for $\tau_m >$ 100 fs yields the single-beam CARS spectrum of Toluene (figure 3b). For the present configuration, modes between 500 and 1000 cm^{-1} can unambiguously be assigned. Clearly, the three strongest Toluene modes in the fingerprint region at 521, 786 and 1000 cm^{-1} (indicated as gray bars at the bottom) are well resolved (linewidths < 30cm^{-1}).

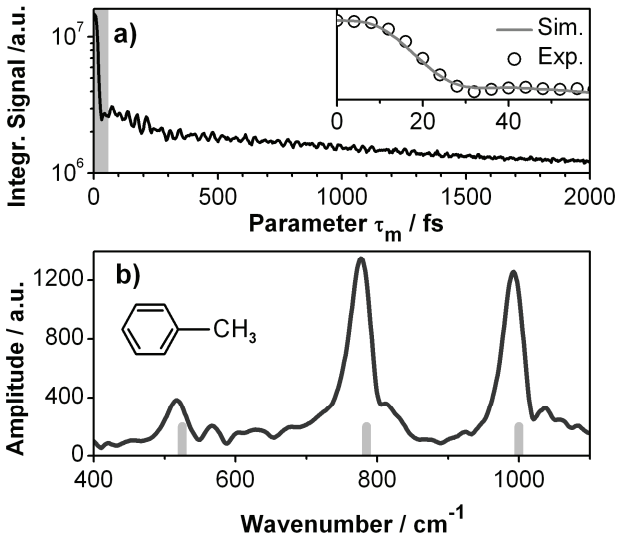

Fig. 5.20: Single-beam CARS results on Toluene. **a)** τ_m-scan data with oscillations. Inset: Zoom into the decay of nonresonant signal (shaded area), with experimental data (circles) and simulation (grey solid line). **b)** Corresponding *Fourier* spectrum. Literature positions of the three strongest fingerprint-modes are indicated as gray bars.

Note that the experimental conditions were chosen such that a unique octave of wavenumbers between ~520 cm^{-1} and 1040 cm^{-1} was ensured to avoid ambiguous peaks (see section 5.2.1, p. 84). In the following examples the slowly varying decay has already been subtracted from the τ_m-scan data. Also, not in all cases the "uniqueness-condition" of one octave of wavenumbers is fulfilled, which is commented upon in the figure caption.

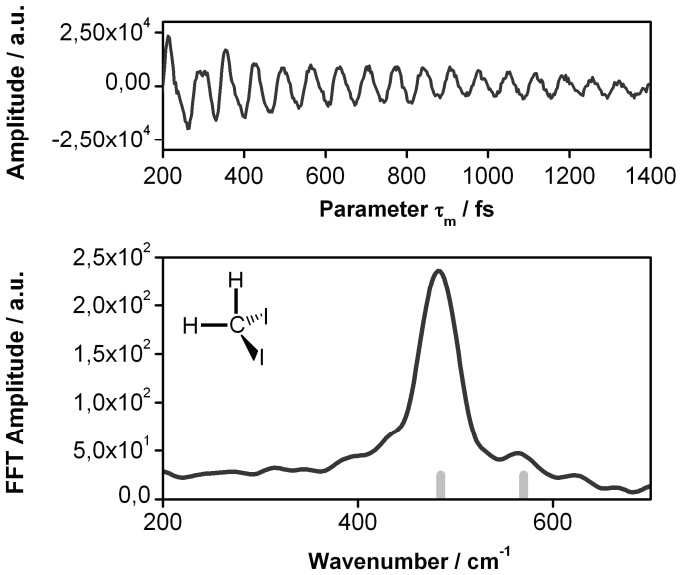

Fig. 5.21: Multipulse single-beam CARS spectrum of Diiodomethane (CH_2I_2). Shown are the τ_m-scan data in the upper panel and the *Fourier* spectrum in the lower panel (solid curve), together with an indication of the strongest *Raman* mode positions from literature (grey bars). For this molecule, only one strong vibration can be detected at 480 cm^{-1} (with a weak shoulder at ~560 cm^{-1}) in the given range of 350 cm^{-1} – 700 cm^{-1}.

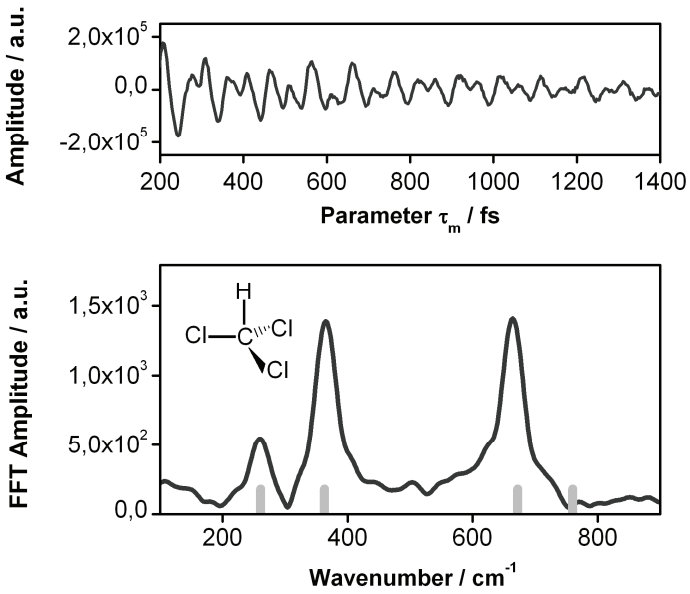

Fig. 5.22: Multipulse single-beam CARS spectrum of Chloroform ($CHCl_3$). Shown are the τ_m-scan data in the upper panel and the *Fourier* spectrum in the lower panel (solid curve) and the strongest *Raman* mode positions from literature (grey bars). Note that this spectrum exceeds one octave of wavenumbers, meaning that ambiguities and additional peaks have to be carefully considered in the spectral interpretation. The harmonic of the lowest visible mode gives rise to the small peak at ~500 cm^{-1}, while the spurious signal of the 380 cm-1 mode vanishes in the blue shoulder of the 660 cm^{-1} vibration.

As examples of typical liquid phase samples of Halomethanes, which exhibit both strong *Raman* scattering cross-sections and a series of distinct vibrational modes down to low wavenumbers, the single-beam CARS spectra of Diiodomethane (CH_2I_2) and Chloroform ($CHCl_3$) are shown in Fig. 5.21 and Fig. 5.22. It is worth mentioning that although a larger volume was used to provide the samples in the cuvette formed by a microscope slide, a ~150µm Teflon spacer and a standard microscopy coverslip, the molecules contributing to the single-beam signal stem only from the focal region, which can be estimated to be smaller than $(1\mu m)^3$, equivalent to 10^{-16} litres or 100 attolitres!

Other examples studied are solid crystals, which typically have been employed as microcrystalline powders (as purchased). Powders are of course highly scattering samples, but placing the focus directly on a microcrystal usually allows transmission-type single-beam CARS measurements with good signal collection efficiency. In the case of 1,4-Bromoiodobenzene (Fig. 5.23), a crystalline solid at room temperature, clear single-beam CARS signal could be detected from the laser focus placed inside a small crystallite (upper panel). The *Fourier* spectrum shows distinct vibrations expected for this molecule (lower panel) at 180 cm^{-1}, around 700 cm^{-1} (690 cm^{-1}) and the typical aromatic ring breathing mode above 1000 cm^{-1}. Again, this range of detected wavenumbers calls to attention the ambiguity issue of multipulse single-beam CARS. In this case, higher harmonics of the 180 cm^{-1} vibration can be expected at 360 cm^{-1}, 540 cm^{-1}, 720 cm^{-1} and so on. With the spectral resolution of better than 30 cm^{-1} achieved at the given length of the τ_m-scans, the strong peak at 690 cm^{-1} can clearly be distinguished from the forth harmonic of the 180 cm^{-1} mode, which has to be hidden under its blue shoulder. Around 540 cm^{-1} there is a spectral feature,

however it is not very pronounced and within the relatively high noise floor. This example shows again, that spectroscopy outside the octave limitation is possible, but requires careful analysis.

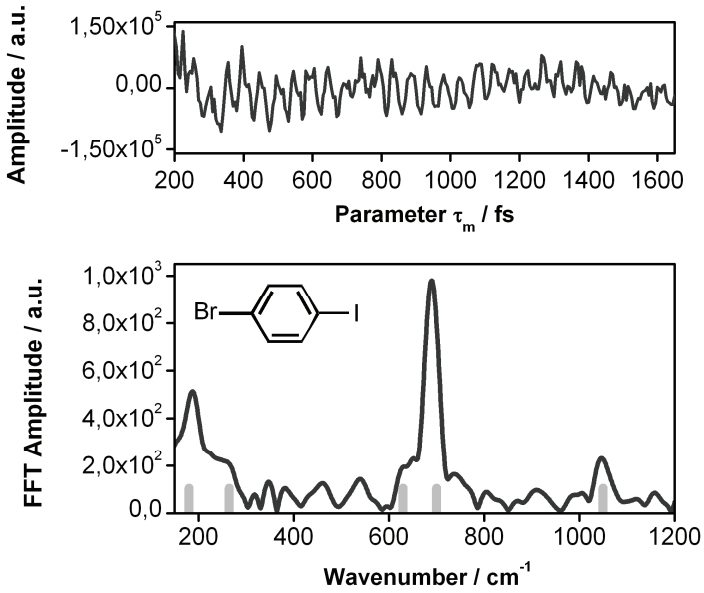

Fig. 5.23: Multipulse single-beam CARS spectrum of 1,4-Bromoiodobenzene (*para*-Bromoiodobenzene). Shown are the τ_m-scan data in the upper panel and the *Fourier* spectrum in the lower panel (solid curve), together with an indication of the strongest *Raman* mode positions from literature (grey bars). Note that this spectrum also exceeds one octave of wavenumbers, meaning that ambiguities and additional peaks have to be carefully considered in the interpretation. Especially the presence of detected low-frequency modes around 180 cm^{-1} inevitably contributes to a rugged "baseline" in the spectrum. Still, the strongest spectral features at 180 cm^{-1}, 690 cm^{-1} and above 1000 cm^{-1} are clearly discernible.

Another example of both a solid sample and an ambiguous measurement range is Benzoic acid (Fig. 5.24). The very rich spectral structure expected in the range between 200 cm^{-1} and 1200 cm^{-1} can be found in the single-beam CARS *Fourier* spectrum. It consists of resonances at 180 cm^{-1} ("A"), 420 cm^{-1} ("B"), 600 cm^{-1} ("C"), 790 cm^{-1} ("D"), and 996 cm^{-1} ("E"). Using this nomenclature, spurious peaks have been assigned in Fig. 5.24. For an unknown substance, and with careless analysis, one might *e. g.* be tempted to assign the blue shoulder of mode "D" to a molecular vibration, however it is much more likely the second harmonic of mode "B" ("2B"). These ambiguities cannot be resolved with the multipulse method, only avoided if the experiment is carried out with a restricted spectral excitation coverage and matching detection window.

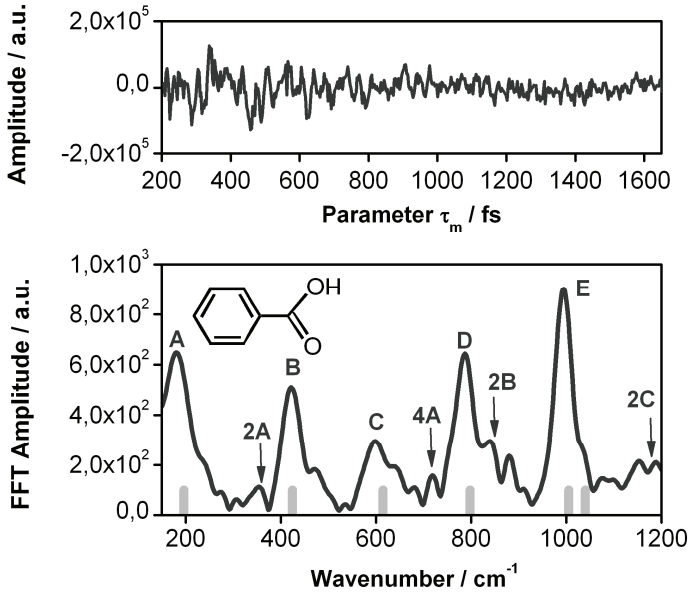

Fig. 5.24: Multipulse single-beam CARS spectrum of Benzoic acid. Shown are the τ_m-scan data in the upper panel and the *Fourier* spectrum in the lower panel (solid curve), together with an indication of the strongest *Raman* mode positions from literature (grey bars). Note that this spectrum exceeds one octave of wavenumbers, meaning that ambiguities and additional peaks have to be carefully considered in the interpretation. See text for details.

5.5.2 Application to white powder identification and threat assessment

As further application example of multipulse single-beam CARS microspectroscopy, a powder sample consisting of a mixture of potassium benzoate (KBenzoate) and the calcium salt of dipicolinic acid (CaDPA) was studied. While KBenzoate is a common food preservative, CaDPA is known as a marker molecule found in anthrax spores. Therefore, the rapid selective detection of CaDPA[151] and discrimination against other harmless compounds (like KBenzoate, for example) can be an important step to improve the assessment of "white powder" threats. With microspectroscopy, single microcrystals in the powder (or, in the case of a real biological agent, single bacterial spores) can be identified. Under a normal light microscope, KBenzoate and CaDPA look alike (Fig. 5.25a).

Using the shaped broadband femtosecond laser beam a single crystal can be studied. The chemical constitution of KBenzoate and CaDPA is very similar (Fig. 5.25b), both featuring an aromatic ring with carboxylate functions. The vibrational spectra are, however markedly different (Fig. 5.25c). While both compounds expectedly feature an aromatic ring breathing vibration around 1000 cm^{-1}, yet in the case of CaDPA at slightly lower wavenumbers, the other fingerprint vibrational bands at 750 cm^{-1} and 820 cm^{-1}, respectively, allow a clear distinction. As the time delay τ (or a corresponding temporal spacing in the multipulse approach) has to be scanned to obtain spectra like Fig. 5.25c, presently the acquisition time for one spectrum is in the range of minutes. This can, however, drastically be sped up using faster pulse shaping apparatuses und somewhat higher laser pulse energies to increase the signal level. With technology available today, spectral acquisition is likely to be cut down to tens of seconds. However, if a certain known molecule has to be detected, a different and

faster approach can be pursued, recording the CARS signal only for a small number of specifically designed pulse shapes. This is especially attractive for chemical imaging, where each pixel of an image should be recorded in as little time as possible. For a chemical imaging example using a two-pulse scheme, such a procedure will be demonstrated later on.

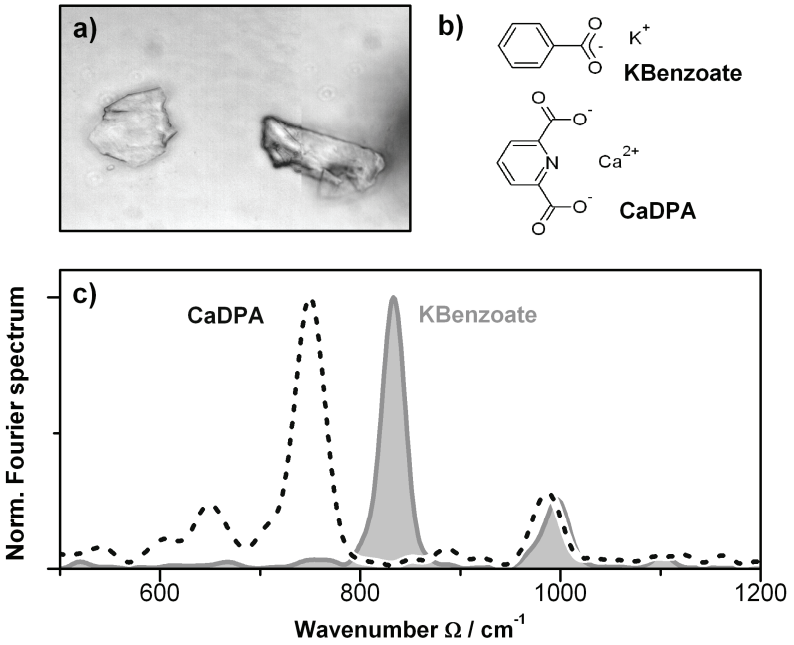

Fig. 5.25: a) Light microscopy transmission image (merged from two acquired camera frames) showing typical ~6 µm sized crystalites of a powder mixture prepared from potassium benzoate (KBenzoate) and the calcium salt of dipicolinic acid (CaDPA). **b)** Chemical structures of the two compounds. **c)** Single-beam CARS microspectroscopy performed on two microcrystals. These results have been obtained with an earlier version of the microscope setup, which did not yet allow simultaneous acquisition of light microscopy transmission images and CARS microspectroscopy. Therefore, different crystalites than shown in panel **a)** have been measured. However, the clear differences in the spectral signature directly allow chemical identification of a microcrystal in the laser focus.

5.6 Results and discussion of unambiguous single-beam CARS using double pulses

In the previous section successful microspectroscopy was presented using multipulse sequences for single-beam CARS. As already elaborated in the theoretical analysis, this method – despite its robustness and simple implementation – has certain drawbacks, especially the limitation due to ambiguities in spectra ranging over more than one octave of wavenumbers. In section 5.2.2 (p. 89) it has already been shown in simulations that the use of just two defined pulses for unambiguous "pump"-"probe" time-resolved measurements is a solution to this problem. Here, experimental findings of different two-pulse single-beam CARS schemes will be presented, compared and discussed.

5.6.1 Comparison of pulse sequences

For a demonstration of the flexibility of single-beam CARS to immediately implement different unambiguous time-resolved spectroscopy schemes, Toluene was again studied with only the computer controlled generation of two-pulse sequences changed to realize the cases presented in Fig. 5.15. In one of them, the aforementioned scheme with two identical double pulses (Fig. 5.15a-d) was used, in the other two-color double pulses (Fig. 5.15e-h) were applied. The results are shown in Fig. 5.26. From the oscillations of the CARS-signal S_{CARS} it can immediately be seen that in the case of identical double pulses (Fig. 5.26a) an additional faster oscillation is resolved compared to the case of two-color double pulses (Fig. 5.26c). This is reflected in the respective *Fourier* spectra: for identical double pulses, the direct transform of the oscillation in Fig. 5.26a yields the expected Toluene vibrational resonances at 520 cm^{-1}, 790 cm^{-1}, 1000 cm^{-1} and 1200 cm^{-1} (Fig. 5.26b, black solid curve). The relative intensities, however, are not directly reflecting the molecular properties, but are weighted with $|A(\Omega)|^2$ and the additional convolution of the probe pulse E_2, as has been discussed for Fig. 5.7.

The effect of $|A(\Omega)|^2$, which is plotted in Fig. 5.26b as thick dashed curve, can be corrected for by using it to normalize the *Fourier* spectrum obtained. In a similar way, deconvolution with $|E_2(t)|^2$ is also easily performed by dividing the resulting spectrum with the *Fourier* transform of $|E_2(t)|^2$, which is again $|A(\Omega)|$, as $E_1(t)$ and $E_2(t)$ have identical temporal profiles. The resulting corrected spectrum is shown as grey hatched curve. Like all deconvolutions, this procedure is only applicable within reasonable limits: experimental noise is augmented infinitely, where $|A(\Omega)|$ drops to zero. This effect can be seen very clearly in the case of the *Fourier* spectrum of the two-colour double pulse measurement (Fig. 5.26d). The vibrational mode at 790 cm^{-1}, although still the dominating feature, is at the limit of the accessible range given by the *Raman* population probability $|A(\Omega)|^2$ (thick dashed curve), which has declined to below 10 % at this spectral position. Measurement is still possible with a sufficiently high signal-to-noise ratio. The *Fourier*-transformed raw data (black solid curve) in this case shows the 520 cm^{-1} mode at roughly half the intensity of the 790 cm^{-1} mode, which changes dramatically if the spectrum is normalized with $|A(\Omega)|^2$ and deconvolved with $|E_2(t)|^2$ (grey hatched curve). Now, the 520 cm^{-1} mode has an intensity of only about 5% of the 790 cm^{-1} mode, perfectly matching the ratio obtained in Fig. 8b for the alternative measurement scheme. Note that the deconvolution procedure in this case amplifies noise in such a way that a peak arises in Fig. 5.26d (marked with an asterisk),

which could be mistaken as a vibrational resonance. This again proves the need to restrict deconvolution to reasonable limits only.

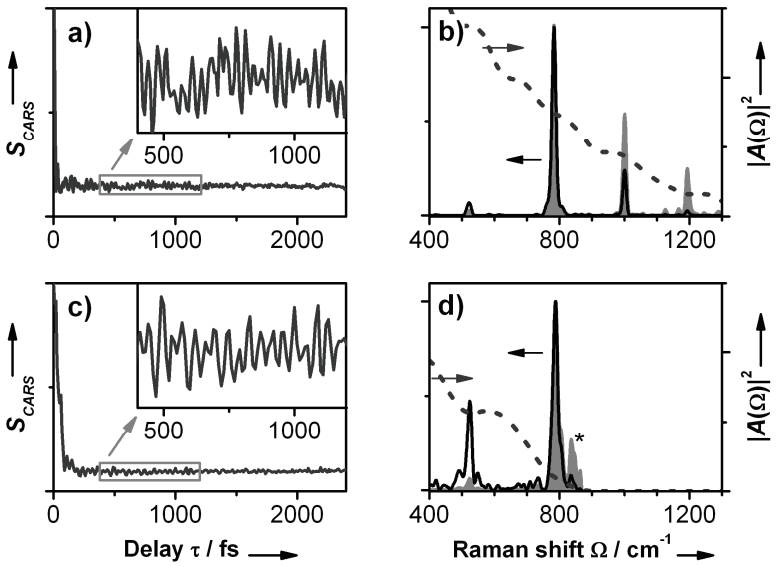

Fig. 5.26: Time-resolved single beam CARS spectroscopy on Toluene, using either identical double pulses (a, b) or two-color double pulses (c, d). Shown is always the transient data for $\tau < 2.5$ ps (a, c), with an inset to better visualize the fast oscillations of the CARS signal S_{CARS}, as well as the corresponding *Fourier* spectra (b, d). In the *Fourier* spectra, normalized data without deconvolution of the limited experimental temporal resolution is shown as black solid curve, while the deconvoluted data is shown as grey hatched curve. The *Raman* excitation probability $|A(\Omega)|^2$, which is decisive for the deconvolution, is shown as thick dashed curve. See text for details

Taken together, Fig. 5.26 shows that – within the expected physical limits – both pulse shaping strategies can provide the same spectroscopic information. From the experimental point of view, both schemes are immediately realized by software control only. Although identical double pulses offers the complete laser bandwidth, it was found that this scheme requires a careful choice of measurement parameters such as sufficient averaging and evaluating the transient data only outside the window affected by interference effects. The two-colour double pulse scheme on the other hand proves more robust in day-to-day measurements, as the signal offset signal is significantly lower and at the same time not affected by interference. The fact that Fig. 5.26d shows a reduced signal-to-noise ratio compared to Fig. 5.26b is mainly due to the fact that this data was acquired about 10 times faster, with about 200 ms acquisition time per data point. Acquisition will, however, be drastically sped up in both cases if higher excitation intensities I_{Exc} are used, as the signal strength scales with the third power of I_{Exc}. Additionally, the two-color double pulse scheme immediately allows full independent control with the shaper over the two sub-pulses, which have clearly defined roles as $E_1(t)$ and $E_2(t)$.

5.6.2 Time-resolved single-beam CARS with polarization control

If both sub-pulses E_1(t) and E_2(t) in the two-color double pulse scheme are created in orthogonal polarization states, the transient CARS data is dominated by the wanted oscillations due to the molecular vibrations. This allows measurements without background interferences and with a very high signal-to-noise ratio. For a demonstration, the molecule Bromotrichloromethane ($CBrCl_3$) has been studied under identical conditions of two-color double pulses, with the only change being in their polarization. In one case, E_1(t) and E_2(t) were polarized parallel to each other and the CARS signal was also detected in this polarization direction. This is shown in Fig. 5.27a.

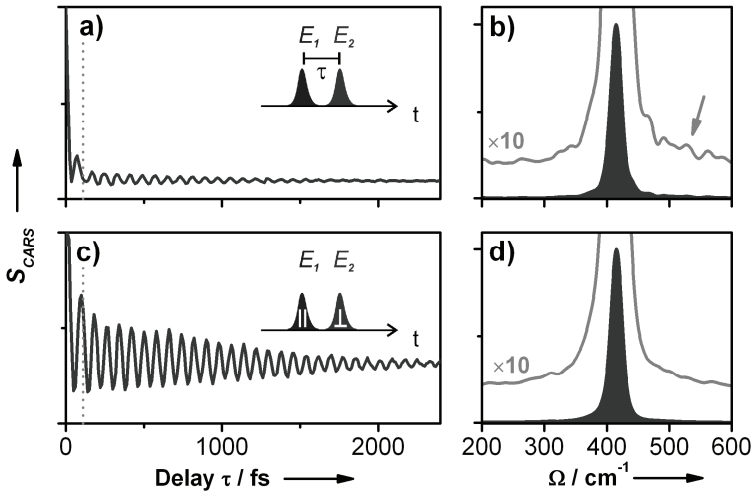

Fig. 5.27: Polarization control of time-resolved single beam CARS, demonstrated for Bromotrichloromethane ($CBrCl_3$). Identical conditions were used, with the only difference being the relative polarization of E_1(t) and E_2(t). In the first case, parallel polarisations for both pulses are used (a, b), while they are orthogonal in the other case (c, d). In both cases, the transient CARS data (a, c) is shown together with the respective *Fourier* transform (b, d). Note the excellent visibility of oscillations and the practical absence of a strong nonresonant peak at delay time zero for the orthogonal polarization case (c), reflected also in a superior signal-to-noise ratio in the *Fourier* spectrum (d).

As expected from the simulation (Fig. 5.27e-h), the transient is dominated by a strong signal around $\tau = 0$ due to nonresonant four-wave mixing background, which is drastically diminished as τ becomes much larger than the pulse duration of E_1(t) and E_2(t). *Fourier* transforming this CARS transient for $\tau > 110$ fs (indicated by the dotted grey vertical line) windows out this nonresonant contribution and readily shows the origin of the oscillatory pattern being due to the dominant vibrational mode of $CBrCl_3$ at 420 cm^{-1} (Fig. 5.27b). A closer look at the *Fourier*-transform data (grey curve in Fig. 5.27b) gives an impression of the experimental noise, with spurious peaks at a ~3 % level of the maximum at 420 cm^{-1} (indicated by the grey arrow in Fig. 5.27b).If in the other case the probe pulse $E_2(t)$ is polarized perpendicular to the pump/*Stokes*-pulse $E_1(t)$, the transient CARS data (Fig. 5.27c) looks markedly different. The transient now consists almost purely of vibrational modulation. The *Fourier* transform (Fig. 5.27d) reveals a vibrational spectrum almost identical to the case of parallel polarized pulses, however the signal-to-noise ratio is

significantly better, as can be seen from the magnified *Fourier* spectrum (grey solid curve), and spurious noise peaks are smaller than 0.3%. The reason for this improvement is attributed to the aforementioned avoiding of additional four-wave mixing interference in the transients, which can be caused by temporal side lobes, pulse replica from shaping artefacts or interferences with residual signal of $E_1(t)$, depending on the choice of ω_{break}.

For a demonstration of microspectroscopy applications of this novel scheme, a series of Halomethanes was chosen, namely Bromotrichloromethane ($CBrCl_3$), Chloroform ($CHCl_3$) and Bromoform ($CHBr_3$). All these compounds have characteristic vibrational resonances in the accessible range up to 800 cm^{-1}. Additionally, a mixture of those three components was prepared, to show the ability to spectrally discriminate them and analyse complex mixtures in the focus of the microscope. The experimental results are summarized in Fig. 5.28.

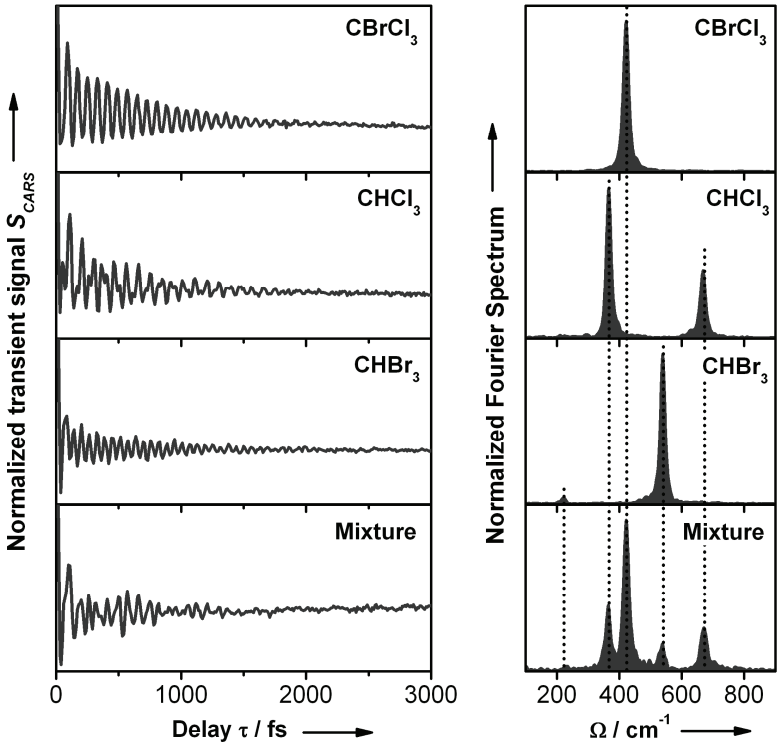

Fig. 5.28: Time-resolved single-beam CARS microspectroscopy of different halomethane molecules and a mixture thereof. In the left column, the CARS transients are depicted, while in the right column the respective *Fourier* spectra can be seen. In the *Fourier* spectra, dotted vertical lines have been added to help assigning the vibrational resonances found in the mixture.

In the left column of Fig. 5.28 the CARS transients can be seen, while the right column shows the respective *Fourier* spectra. For $CBrCl_3$, the transient shows only a single distinct vibration, which corresponds to its 420 cm^{-1} mode. In the case of $CHCl_3$, a beating pattern can be seen in the transient, corresponding to the two vibrations at 366 cm^{-1} and 670 cm^{-1}. In the case of the heavier homologue $CHBr_3$, an inspection of the transient by eye does not indicate a corresponding beating pattern. However, the *Fourier* transform clearly shows a vibrational mode at 222 cm^{-1} in addition to the dominating feature at 540 cm^{-1}. The fact that the 222 cm^{-1} mode only shows up relatively weak is due to the fact that in this experimental

configuration the spectral filtering of the CARS signal was not optimized for the detection of low-frequency vibrational modes.[16] The mixture from all three components (prepared in a volume ratio of 2:5:1 of $CBrCl_3$:$CHCl_3$:$CHBr_3$) shows a very complex transient. As expected, *Fourier* transform reveals all vibrational features, which can very easily be assigned (dotted vertical lines in Fig. 5.28). The spectral resolution achieved is about 25 cm^{-1}, which allows clearly separating the signals around 400 cm^{-1} originating from $CBrCl_3$ and $CHCl_3$.

5.6.3 Chemical imaging example

For a proof-of-principle demonstration of chemical imaging using time-resolved single-beam CARS, the glass-liquid interface of the sample cell was imaged in a lateral and the axial direction (Fig. 5.29) by scanning the sample with a piezo stage. First, CARS transients have been recorded for both regions, namely the $CHCl_3$ liquid phase and the glass cover slip sealing the sample cell (Fig. 5.29a): For $CHCl_3$ (solid curve), the expected oscillations are seen, while the glass transient (dashed grey curve) remains constant for delays $\tau > 120$ fs. If the pulses $E_1(t)$ and $E_2(t)$ arrive simultaneously at the sample at $\tau = 0$, in both cases an elevated detected signal level S_{CARS} can be seen which is mainly due to nonresonant CARS processes. This information alone can be used for imaging, but due to its nonresonant origin does not reveal any chemical information.

A microscopic image of the glass-$CHCl_3$-interface based on the signal S_{CARS} at delay $\tau = 0$ can be seen in Fig. 5.29b. There is only marginal contrast between the two layers, originating from the different level of nonresonant signal generated in the respective materials. Note that this contrast could vanish completely for different samples, or even invert if the nonresonant glass signal is stronger than that of the sample.

Therefore, such images are not useful for chemical mapping. If, on the other hand, the information in the oscillations of $S_{CARS}(\tau)$ is used for constructing the image, high contrast chemical maps can be obtained, which selectively show only the presence of one chemical compound. As an example, a signal has been mapped calculated from the oscillation amplitude of the $CHCl_3$-transient measured from four distinct points at τ_1, τ_2, τ_3 and τ_4 (indicated as dotted vertical lines in Fig. 5.29a) as $|S_{CARS}(\tau_1) - S_{CARS}(\tau_2) + S_{CARS}(\tau_3) - S_{CARS}(\tau_4)|$. This simple procedure allows rapid acquisition of the image, as only four pulse sequences have to be applied and measured for each pixel. Acquiring each pulse sequence is performed in about 200 ms, keeping the measurement time of the complete image low. Alternatively, complete transients can be recorded and *Fourier*-transformed for each spatial position, but this of course leads to slower acquisition times per pixel. As already mentioned earlier, using somewhat higher laser pulse energies and faster spatial light modulating schemes[152, 153] will generally drastically speed up time-resolved single-beam CARS measurements. Nonetheless, the present implementation already demonstrates very useful chemical imaging, as can be seen by the excellent contrast achieved in Fig. 5.29c.

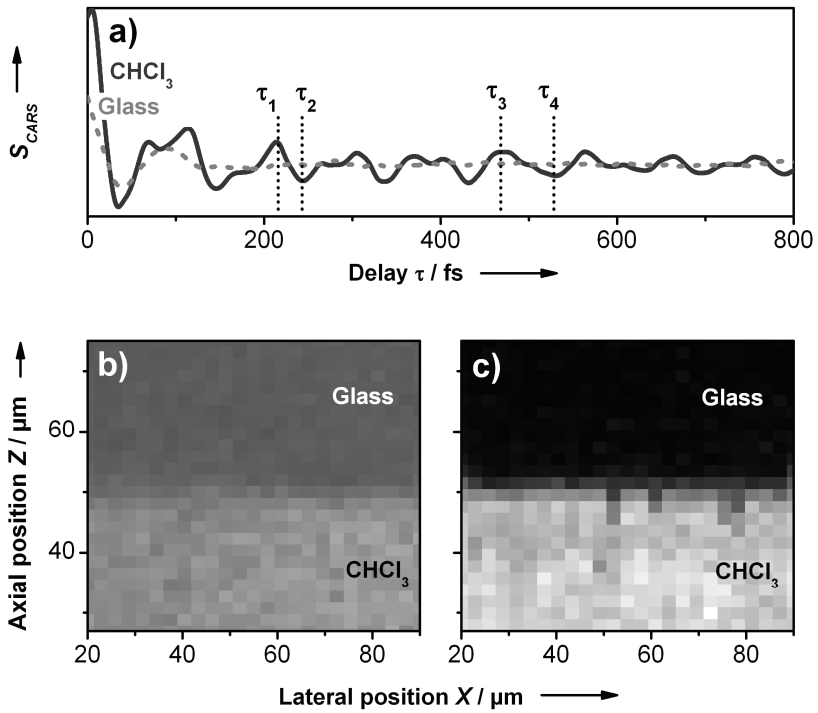

Fig. 5.29: Microscopic imaging example, in which chemical contrast is obtained from the time-resolved CARS signal. **a)** Measured CARS transients for Chloroform ($CHCl_3$, solid curve) and a glass substrate (grey dashed curve). Selected delays τ_1 - τ_4 are indicated with dotted vertical lines, which are used for a chemically selective image of only $CHCl_3$. **b)** CARS image of a Glass/$CHCl_3$ interface. The dissatisfactory contrast is based only on the CARS signal $S_{CARS}(\tau)$ at zero delay $\tau = 0$. **c)** High contrast chemically selective CARS image of the same sample, now based on the amplitude of the characteristic $CHCl_3$ oscillations measured at delays $\tau_1 - \tau_4$. The images were taken at identical scanning steps of $\Delta X = \Delta Z = 2$ µm. in both panels **b)** and **c)**, the grey scale was normalized with white reflecting the maximum, and black zero signal.

5.7 Single-beam Raman control[†††]

Going beyond simple pump-probe time-resolved measurements, shaped "functional" femtosecond pulses can do even more. Here, for example, a single beam of shaped femtosecond pulses will be used to coherently control the *Raman* excitation and to simultaneously observe the resulting vibrations of molecules in a mixture resolved in time. As was shown already earlier in this chapter, molecular vibrations can be measured directly in time-resolved CARS. It has also been shown that shaped laser pulses can selectively excite distinct vibrational modes and thus control the motion of molecules (see section 5.2.1, p. 84).[27, 154-157] As described there, these unique possibilities of coherent control are utilized directly for multipulse single-beam CARS. [16, 17, 109, 148, 158] Both approaches can be combined using the unique capabilities of the pulse shaper.

A first application of these novel tools for the control of vibrational *Raman* wave-packets has been published recently by *Polack et al.*[159], where they restricted their study to a frequency domain measurement of a simple one-component sample. In the course of this thesis, a new method for direct and intuitive time-domain observation and control of molecular vibrations was developed. For a demonstration, a mixture of molecules in the condensed phase will be subjected to a single beam of shaped femtosecond laser pulses, which selectively excites only defined molecular vibrations. The pulse shaper generates not only a tailored pulse sequence for coherently controlled CARS excitation, but also a time-delayed probe pulse at a different colour and polarization, allowing the simultaneous observation of the induced vibrations in a pump-probe scheme. The pump-probe type sequence is directly based on the two-colour double pulse method (section 5.2.3, p. 90), with a red-shifted *Raman* population pulse $E_1(t)$ and a blue-shifted probe pulse $E_2(t)$, each with a duration given by the *Fourier* transform of its partial spectrum and delayed with respect to each other.

By an additional modulation on top of the linear phase for the "population" pulse $E_1(t)$ (Fig. 5.10, Fig. 5.30a), the *Raman* process can be coherently controlled. The most successful approach to this end is the generation of a multipulse sequence for $E_1(t)$, which is achieved by a sine modulation of its spectral phase $\varphi_1(\omega) = a \cdot sin(b \cdot \omega)$. Based on the knowledge established in section 5.2.1 (p. 84), it is clear that this modulation creates a sequence of pulses at a uniform temporal spacing of b. It has also been shown that such a multipulse selectively excites only molecular vibrations fulfilling the condition $b = n \times T_{vib}$, with n being an integer number and T_{vib} the respective vibrational period.[16, 27, 143, 155]

The successful experimental creation of this complex pulse sequence together with a delayed probe $E_2(t)$ at the site of the sample is verified by *in situ* XFROG[150] (chapter 4.7), which is shown in Fig. 5.30b. For the example in Fig. 5.30, the delay τ between $E_1(t)$ and $E_2(t)$ of 1300 fs is created by a V-shaped linear phase, with an additional sine modulation of the spectral phase of $E_1(t)$ with $a = 1.22$ and $b = 420$ fs. The resulting pulses as detected by

[†††] This section has been published as "*Molecular discrimination of a mixture with single-beam Raman control*" by B. von Vacano and M. Motzkus in Journal of Chemical Physics, 127, 144514 (2007).

XFROG (Fig. 5.30b) and simple integrated cross-correlation (XC, Fig. 5.30c) confirm the perfect experimental realization of the desired pulse sequence.

As described in section 5.2.3 (p. 90), the delay τ between the "population" pulse $E_1(t)$ and the orthogonally polarized probe pulse $E_2(t)$ is varied and the blue-shifted CARS is detected. In this way, CARS transients are obtained from the sample mixture of $CHCl_3$ and $CBrCl_3$ for differently shaped "population" pulses $E_1(t)$. For $b = 0$, a transform-limited E_1(t) is obtained, and the CARS transient shows oscillations from all molecular vibrations accessible within its bandwidth (Fig. 5.30d, black solid curve). If b is chosen differently, certain oscillatory components of the transients can be suppressed, which is equivalent to the selective excitation of molecular vibrations. [155] With $b = 45$ fs, for example, the CARS transient shows the fast oscillation as the dominant feature (Fig. 5.30d, grey curve), which is only slightly visible as one component in the case of transform-limited excitation (black solid curve).

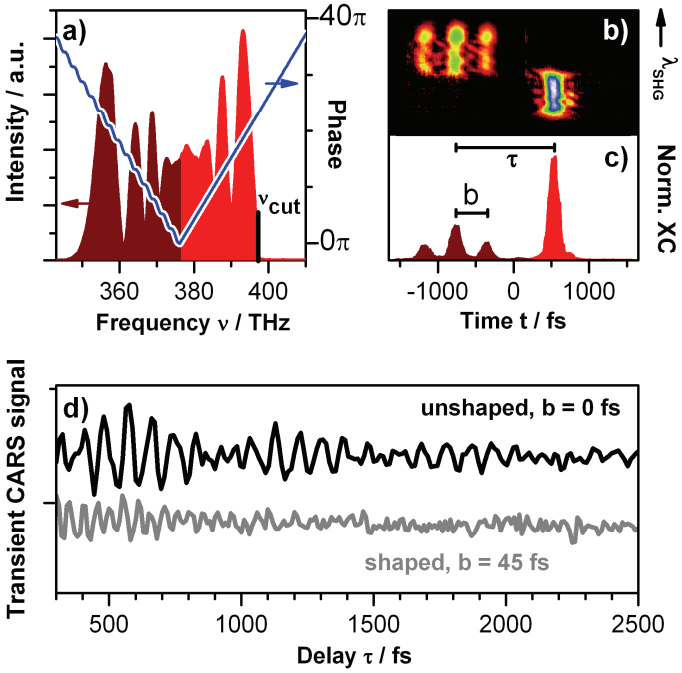

Fig. 5.30: a) Spectrum and spectral phase of the shaped excitation pulses, with the red part at lower freqencies acting as pump and *Stokes*, and the blue part as time-delayed probe. The spectral phase shown creates a temporal separation of the two spectra of 1300 fs, and an additional multipulse modulation on the pump/*Stokes* pulse with a temporal spacing of 420 fs. **b)** A frequency resolved cross-correlation and **c)** the integrated cross-correlation (XC) measured in situ confirm the successful delivery of the desired pulse shape. **d)** Measured CARS transients for the sample mixture ($CHCl_3$ and $CBrCl_3$) with unshaped (black curve) und shaped (grey curve) pulses show direct control over the molecular oscillations.

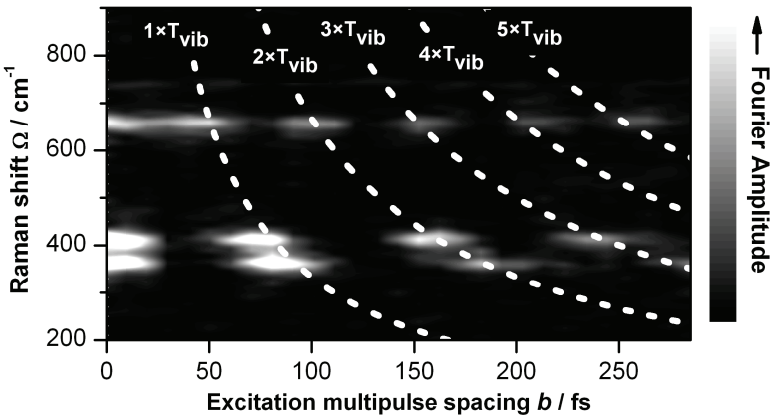

Fig. 5.31: *Fourier* spectra plotted for each multipulse separation b as intensity map. It can be seen that the modes appear only as bright "islands" if b matches an integer multiple of their vibrational period.

An exact analysis of the molecular vibrations involved is possible when *Fourier*-transforming the time-domain CARS data. Windowing out non-resonant signal contributions around zero delay τ, background free spectra are obtained with a spectral resolution of roughly 25 cm^{-1} given by the inverse length of the transient. Transients recorded for different values of b ranging from zero to 290 fs in steps of 10 fs have been *Fourier* transformed and the resulting CARS spectra plotted for each b in Fig. 5.31 as an intensity map. For $b = 0$, the unmodified single-beam CARS spectrum of the $CHCl_3/CBrCl_3$-mixture can be seen, which is also shown separately in the topmost panel of Fig. 5.32. The expected vibrational modes of $CHCl_3$ at 366 cm^{-1} and ~670 cm^{-1} (marked with "*" in Fig. 5.32) are immediately obtained, as well as the dominant mode of $CBrCl_3$ at ~420 cm^{-1} (marked "∇"). For a variation of b, the intensity of each of the vibrational modes modulates, as can be seen in the formation of bright "islands" in Fig. 5.31. From the requirement of b being an integer multiple of T_{vib}, it is straightforward to deduce where any vibrational mode at a wavenumber Ω would show up in Fig. 5.31, the condition being $\Omega(b) = (c \times T_{vib})^{-1} = n\,(c \times b)^{-1}$. This relation is indicated in Fig. 5.31 with dashed white curves for $n \times T_{vib}$, with n ranging from 1 to 5. Very clearly, the "islands" of the experimentally obtained *Fourier* spectra of the $CBrCl_3/CHCl_3$-mixture for different values of b in Fig. 5.31 perfectly lie on these expected curves.

From Fig. 5.31 optimal values of b are directly obtained for the exclusive excitation of each vibrational mode observed simply by finding a suitable vertical cross-section of Fig. 5.31. For the 660 cm^{-1} mode of $CHCl_3$, for example, $b = 45$ fs can be chosen, corresponding to a multipulse spacing b of roughly one vibrational period T_{vib}. A respective *Fourier* spectrum for $b = 45$ fs is shown in Fig. 5.32, revealing the exclusive excitation of the desired vibration. For the spectrally more close vibrations of $CBrCl_3$ at ~420 cm^{-1} and $CHCl_3$ at 366 cm^{-1} discrimination is not perfectly possible with b values corresponding to one respective T_{vib} of either vibration, as they are too similar (79 fs and 91 fs, respectively). However, for larger n, $n \approx 3$ in the case of $CBrCl_3$ (~240 fs) and $n \approx 2$ for $CHCl_3$ (~180 fs), a perfect discrimination is achieved, as can again be seen in the respective spectra in Fig. 5.32.

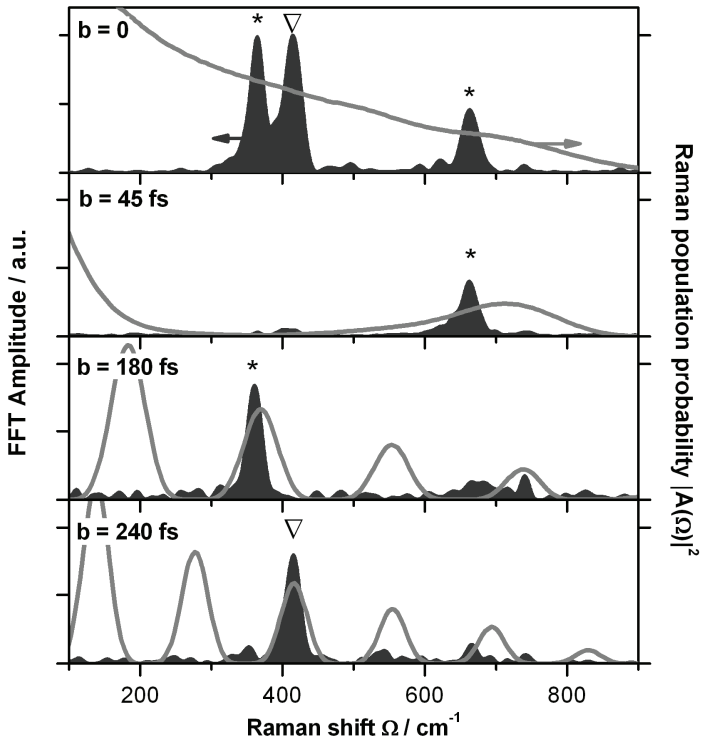

Fig. 5.32: Control results for molecular vibrations selectively excited in a binary mixture of $CHCl_3$ and $CBrCl_3$ with time-resolved single-beam CARS. A suitable multipulse spacing *b* achieves full selectivity and control over all the accessible modes of $CHBr_3$ (marked "∇") and $CHCl_3$ (marked "*").

A detailed analysis of the coherent control effect of this multipulse-shaping of the pulse $E_1(t)$ is again based on the *Raman* excitation probability $|A(\Omega)|^2$ which enters as modulus square [see also Eq. (5.2)]:

$$\left|A(\Omega)\right|^2 = \left|\int_0^\infty d\omega\, \tilde{E}_1^*(\omega-\Omega)\,\tilde{E}_1(\omega)\right|^2, \tag{5.15}$$

where $\tilde{E}_1(\omega)$ is the representation of the electric field of the pulse $E_1(t)$ in the frequency domain. This expression simply corresponds to the sum over all possible pathways leading to a target *Raman* state, given by the availability and relative phase of photon pairs with an energy separation corresponding to Ω. This is a classic example of a Brumer-Shapiro[160] type coherent control scheme. For all the multipulse temporal spacings *b* used in Fig. 5.32, the respective *Raman* population probabilities $|A(\Omega)|^2$ are plotted as grey curves, very clearly demonstrating the spectral filtering effect of the multipulse excitation. In each case, the data have carefully been corrected for constant excitation energy. The clear results show again that the control of molecular vibration through a CARS process with shaped laser pulses is very effective and fully modelled analytically in the perturbative regime, if no electronic resonances are involved. This also means that the coherent control of vibrations yields very high selectivity of the excitation, but cannot exceed the absolute population of a mode achieved with the same *Fourier*-limited excitation pulse. [155]

The results obtained show the successful application of a single-beam experiment to time-domain observation and control of molecular vibration. The CARS process is successfully

exploited in a novel scheme relying on delayed two-color double pulses created from a broadband laser source by pulse shaping. Due to the unambiguous function of each pulse in this approach, the first pulse $E_1(t)$, acting to populate a *Raman* level, could be modulated to yield a multipulse excitation sequence. The excited molecular vibration can immediately be monitored in time with the second, delayed probe pulse $E_2(t)$. This was demonstrated successfully on the control of individual molecular vibrations of a binary mixture of molecules in solution, proving that individual modes of each of the components can be addressed. This very flexible, robust technique should allow the systematic study of the coherent control of vibrational dynamics, and pave the way for simple implementations of novel, highly specific chemical analytics, rapid detection schemes for bacterial spores and enhanced contrast in microscopy based on CARS.

5.8 Present Limitations and Perspectives

The results achieved so far already point to the high potential of nonlinear vibrational spectroscopy performed with a single beam of femtosecond laser pulses. Compared to conventional ultrafast spectroscopy experiments, huge simplification is achieved. So far, however, the point can be made that similar results are also obtained *e. g.* with conventional state-of the art *Raman* detection. Yet, this objection neglects the fact that nonlinear single-beam spectroscopy will be capable to outperform in several respects: If the fs-laser pulse and energy is increased by only one order of magnitude, as is already possible e.g. with long cavity or cavity dumped fs oscillators, the signal will be a thousand times stronger and exceed typical *Raman* signals easily. Additionally, the time to acquire spectra is limited by the rate at which different pulse shapes can be applied, which is only ~3 Hz with the pulse shaper used here due to its slow serial interfacing with the computer. Using most recent liquid crystal SLM this rate can be as high as 60 Hz, while advanced shaping strategies[152, 153] or acousto-optical programmable digital filter (AOPDF)[‡‡‡] pulse shapers[82] already operate in the kHz regime, making high-resolution acquisition of *Fourier* spectra possible within fractions of a second. With such pulse shapers, also the effective "pixel number" can be increased by at least a factor of two[161, 162], leading to the same improvement in spectral resolution. Additionally, the technique allows completely novel approaches, such as coherent optical processing of molecular signals to improve specificity[163], multidimensional spectroscopy, simultaneous acquisition of different nonlinear signals, and others. On the experimental side, compact ultrafast all-fibre laser sources and monolithic pulse shapers like the AOPDF should lead to a drastic further increase in robustness and applicability. Thinking of microscopic imaging, the superiority of nonlinear spectroscopy such as CARS in terms of acquisition speed and three-dimensional resolution is already exploited.

Another issue is the mentioned quadratic dependency of CARS on the concentration of *Raman* scatterers. Using pulse-shaping and the single-beam approach, it will be shown in

[‡‡‡] AOPDF pulse shapers have been claimed not to operate in conjunction with high-repetition rate fs-oscillators. Experiments can, however, be adapted to ensure smooth operation even under these circumstances, *e.g.* by using triggered data acquisition.

the next chapter that interferometric detection easily introduced in this framework drastically increases sensitivity and thus means a huge step towards wider spread applications of CARS.

6 Sensitive single-beam heterodyne CARS detection and adaptation to a compact fiber laser source[§§§]

In the discussion of MCARS in chapter 3 and in the applications of single-beam CARS in the previous chapter it was mentioned that due to the coherent nature of CARS, the signal generated by frequencies ω_p (pump) and ω_s (red-shifted *Stokes*) at $\omega_{CARS} = 2\omega_p - \omega_s$ (anti-*Stokes*) scales quadratically with the number of scattering molecules in the excitation volume[132]. While this is beneficial for samples with a high concentration of an analyte (majority species), *e.g.* for lipid droplets in living cells[164], it turns into a huge disadvantage at lower concentrations. Also, the signal of different sample constitutents interferes which makes quantitative analysis more difficult, as can be seen from the extensive fitting procedure needed to quantify MCARS chemical images in chapter 3. This is all because CARS is normally detected as light intensity, meaning that only the squared modulus of the signal electric field is seen, while phase information is lost. The CARS signal electric field itself is linear in the concentration and in a multicomponent mixture is simply a linear superposition of the CARS signal fields of all components. If one succeeds in measuring the field instead of the intensity of the CARS signal, higher sensitivity and straight-forward disentanglement of mixtures is possible in analytics. Detecting an optical field requires, however, interferometric schemes, as no detector is fast enough to resolve the oscillations of the optical waves. Interferometry on the other hand poses high requirements on an optical setup and usually complicates it considerably.

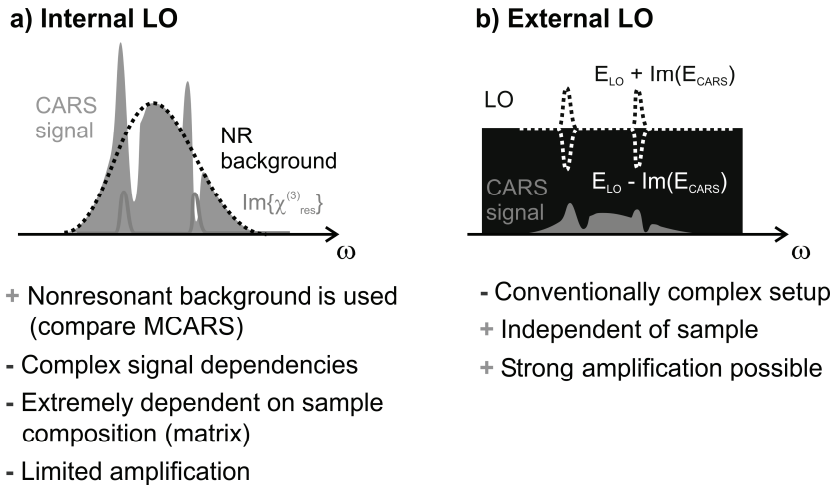

Fig. 6.1: Comparison of **a)** internal and **b)** external local oscillator (LO) for interferometric CARS measurements. See text for details. An internal LO is implicitly also used in some cases in MCARS (see chapter 3), if weak resonant signals interfere with a strong nonresonant background.

[§§§] Parts of this section have been published as "*Highly sensitive single-beam heterodyne coherent anti-Stokes Raman scattering (CARS)*" by B. von Vacano, T. Buckup and M. Motzkus in Optics Letters, 31 , 2495-2497 (2006) and "*Microanalytical nonlinear single-beam spectroscopy combining an unamplified femtosecond fibre laser, pulse shaping and interferometry*" by B. von Vacano, J. Rehbinder, T. Buckup and M. Motzkus (submitted).

Here, in the context of single-beam CARS, which relies on the extreme flexibility of pulse shaping, it will be shown that interferometric detection can be introduced in a novel, simple experimental extension of the technique: The optical fields driving the CARS process and the local oscillator used for heterodyning are derived from the same single beam of ultrashort laser pulses by pulse-shaping. This dramatically increases the sensitivity of chemically selective detection at microscopic resolution, while maintaining the simplicity of the single-beam setup.

Linearization of CARS signal for sensitive detection and mitigating unwanted nonresonant background by interfering the coherent CARS signal with an auxiliary local oscillator (LO) field at ω_{CARS} has therefore been at the focus of attention for some time and has been successfully implemented in CARS microscopy as heterodyne or interferometric detection.[165-169] Common to all approaches using an external local oscillator (Fig. 6.1b and Fig. 6.2a) is a relatively complex experimental setup, consisting of different optical beams to generate the excitation frequencies ω_p, ω_s and the LO, which then have to be overlaid with interferometric stability.

As has been described in the previous chapter, single-beam CARS has been developed to simplify microscopy.[13, 16, 148] Conventionally, the blue part of the excitation spectrum is blocked to permit "non-interferometric" (homodyne) detection of the blue shifted CARS signal, which is orders of magnitudes weaker. Recently, interferometric detection has also been introduced in single-beam CARS: Spectrally resolved CARS signal and nonresonant background serving as LO ("internal" LO, see Fig. 6.1a) are generated in the sample by a phase- and polarization-shaped pulse in orthogonal polarization directions, and brought to interference.[148] This scheme, however, is susceptible to depolarization, which can occur by scattering in realistic microscopic samples, and the intensity of the LO, and thus amplification, is limited by the properties of the sample.

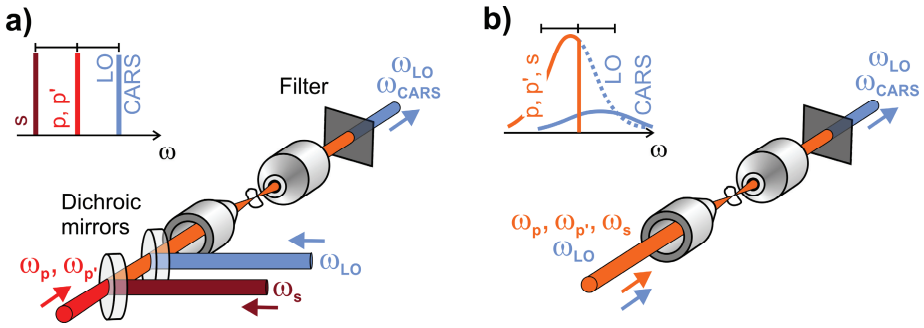

Fig. 6.2: Schematic comparison of interferometric CARS schemes using an external LO. **a)** Conventional approach, **b)** Single-beam approach. (p: pump, p': probe, s: *Stokes*)

6.1 Principles of single-beam heterodyne CARS

Contrary to this, the novel, simplified approach to single-beam heterodyne CARS works as follows (Fig. 6.2b): Instead of blocking the blue part of the broadband excitation spectrum for frequencies $\omega > \omega_{cut}$ in the pulse shaper, it is used as strong, coherent and fully phase-controlled LO field $E_{LO}(\omega)$. Hence, sensitive heterodyne CARS detection can be realized based on only a single beam throughout the entire experiment offering intrinsic

interferometric stability - due to the generation of the LO by pulse shaping.[139] Like described in section 5.2.1 (p. 84), the CARS signal $E_{CARS}(\omega)$ is generated in the sample by all possible combinations of frequencies ω_p, ω_s within the bandwidth of the excitation pulse. As seen before, it can be described by Eq. (3.1), which shall be restated here in a slightly streamlined way as Eq. (6.1) for easier reference. N denotes the number of scattering molecules, $\chi^{(3)}_{CARS}$ the respective third-order susceptibility and $E(\omega)$ the field of the exciting broadband pulse.

$$E_{CARS}(\omega) \propto N \cdot \int_0^\infty d\Omega \int_0^\infty d\omega' \, \chi^{(3)}_{CARS} \, E(\omega-\Omega) E^*(\omega') E(\omega'+\Omega) \tag{6.1}$$

$E_{CARS}(\omega)$ has a defined phase relationship with respect to $E(\omega)$, and the homodyne detected intensity $I_{CARS}(\omega) \propto \left|E_{CARS}(\omega)\right|^2$ scales quadratically with the number N of scattering molecules. Mixing $E_{CARS}(\omega)$ with $E_{LO}(\omega)$ in a square-law detector yields the signal $S(\omega)$:

$$S(\omega) = I_{CARS}(\omega) + \underbrace{2\sqrt{I_{CARS}(\omega)}\sqrt{I_{LO}(\omega)} \times \cos\left[\varphi_{LO}(\omega)\right]}_{S^{(Het)}(\omega)} + I_{LO}(\omega) \tag{6.2}$$

where I_{CARS} and I_{LO} are the homodyne intensities of the CARS signal and the LO respectively, and $S_{(Het)}$, is the heterodyne interference term. From Eq. (6.1) and Eq. (6.2) it becomes clear that (i) $S^{(Het)}$ scales linearly with N and thus with the concentration of *Raman* scatterers, (ii) a huge amplification of the detected signal can be achieved when $I_{LO} >> I_{CARS}$ and (iii) the spectral phase of the LO $\varphi_{LO}(\omega)$ has to be chosen appropriately to ensure maximum amplification. Due to the convolution in Eq. (6.1), the spectral phase of $E_{CARS}(\omega)$ is smooth and varying only slowly in ω.

6.2 Implementation and Experiments

The experimental realization of single-beam heterodyne CARS is based on the usual setup, but for a first demonstration of the principle implemented without the PCF pulse broadening scheme. It is shown in Fig. 6.3; schematic pulse spectra for different positions along the beam in the experiment are indicated as I), II), and III). 100 fs pulses (0.25 nJ) from a Ti:Sapphire oscillator at 795 nm [Fig. 6.3, spectrum I)] are sent into a 4*f* femtosecond pulse shaper (f = 300 mm, G1, G2 gratings with 1800 grooves/mm). In the *Fourier* plane, a liquid crystal spatial light modulator (SLM, 640 pixels) is placed allowing the modulation of the spectral phase of the pulse. Two spectral parts have to be discriminated: The excitation part at frequencies $\omega < \omega_{cut}$ is mechanically chopped (CH) at 700 Hz, whereas the LO part at frequencies $\omega > \omega_{cut}$ is attenuated by a neutral density filter (ND), typically to 5%. This attenuation ensures, due to the nonlinear intensity dependence of I_{CARS}, that the LO part of the spectrum does not significantly generate CARS signal. The thus modified excitation pulses [Fig. 6.3, spectrum II)] are focused into the sample with a microscope objective [60x, numerical aperture (NA) 0.7, MO1] and recollimated (40x, NA 0.6, MO2). An interference bandpass filter selects the weak blue-shifted CARS signal together with the strong LO [Fig. 6.3, spectrum III)]. The filtered signal is detected with photomultiplier and lock-in amplification at the chopping frequency.

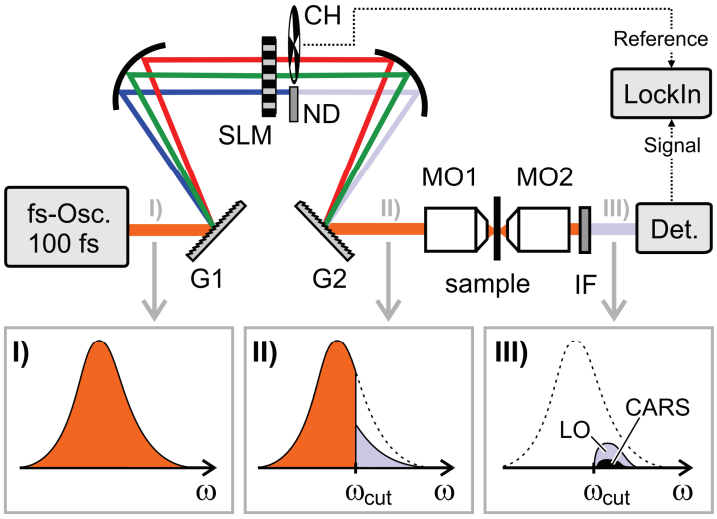

Fig. 6.3: Experimental setup and schematic spectra along the beam path [I), II) and III)]. Excitation pulses [see I)] are sent into a 4*f*-pulse shaper (*f* = 300 mm, G1, G2 gratings 1800 grooves/mm, SLM: spatial light modulator), where the blue part is attenuated (ND: neutral density filter) and the red part chopped (CH: mechanical chopper) [see II)]. They are focused into the sample and recollimated (MO1, MO2: microscope objectives), spectrally filtered (IF: Interference bandpass filter) [see III)] and detected.

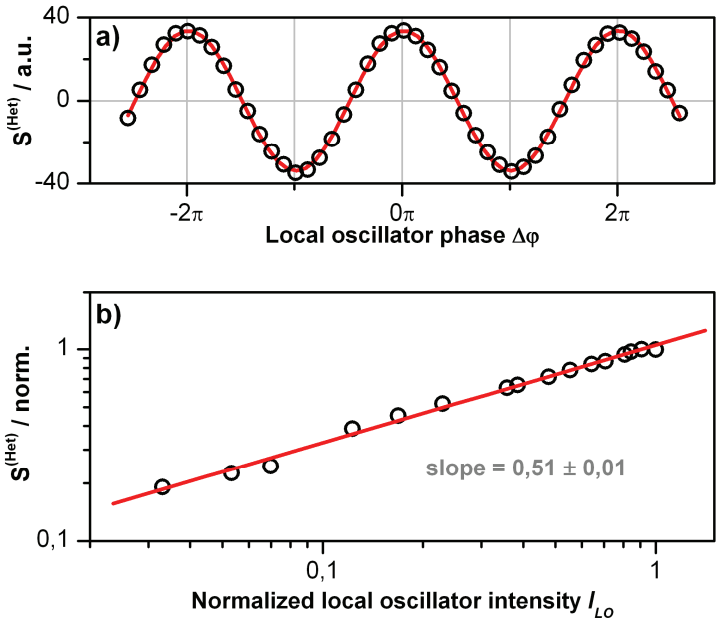

Fig. 6.4: a) Dependence of heterodyne signal $S^{(Het)}$ on LO phase φ_{LO}. Measured data shown as open circles, cosine fit as grey solid line. **b)** Intensity dependence of $S^{(Het)}$; data points for different values of I_{LO} are shown as open circles, a linear fit as grey solid line.

Prior to single-beam heterodyne CARS experiments, the dispersion of all optical elements in the beam path was corrected by the pulse shaper. Additionally, the spectral phase $\varphi_{LO}(\omega)$ of the LO was optimized in an evolutionary closed-loop scheme[70] to yield a maximum of the spectrally integrated heterodyne signal $S^{(Het)}$ at $\varphi_{LO}(\omega) = 0$. Therefore, a best "average" phase was found matching the CARS signal and the LO for constructive interference. The signal detected with this lock-in technique contains $S^{(Het)}$ in addition to a small homodyne

contribution of I_{CARS}. By simply blocking the LO in the shaper and measuring only I_{CARS}, for the prototypical sample $CHBr_3$ (Bromoform) an amplification factor of $S^{(Het)}$ / I_{CARS} of about 5400 was found.

To verify the nature of the heterodyne signal described by Eq. (6.2), $S^{(Het)}$ was recorded for unshaped excitation pulses as a function of a constant phase offset of the local oscillator $\varphi_{LO}(\omega)$: Fig. 6.4a) shows a perfect agreement of the measured data (open circles) with a cosine fit (grey, solid curve). This successfully proves full control over the phase of the LO by the pulse shaper. Similarly, the intensity dependence of $S^{(Het)}$ was examined by using a variable neutral density filter in the LO side of the *Fourier* plane. A linear fit (grey, solid curve) of the measured data (open circles) in double-logarithmic scale is shown in Fig. 6.4b), yielding a slope of 0.51±0.01 in exact agreement with the square root dependence in Eq. (6.2).

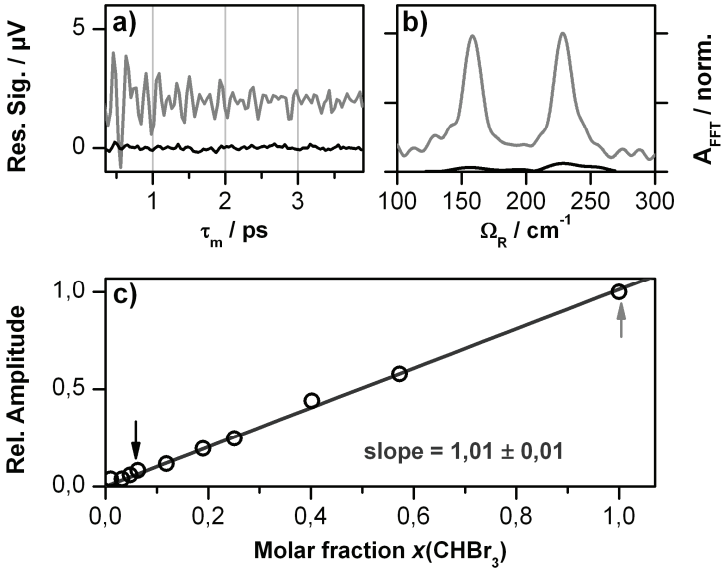

Fig. 6.5: a) τ_m-scans of $CHBr_3$ at molar fractions of 1 (grey solid curve) and 0.06 (black solid curve). The black curve is magnified by a factor of 2, and the grey curve is offset for clarity. **b)** *Fourier* transform of these τ_m-scans. Again, the black curve for $x(CHBr_3) = 0.06$ is magnified by a factor of 2. **c)** The relative amplitudes of the resonant CARS signal obtained from τ_m-scans plotted versus $x(CHBr_3)$ (open circles). A linear fit through the origin is also shown (grey solid line). Arrows indicate the data points corresponding to the traces in a) and b).

Having confirmed successful heterodyne detection of the CARS signal for excitation pulses with a flat spectral phase, pulses with periodic phase modulation are employed to obtain the complete spectroscopic characterization of the molecular sample (see section 5.2.1 on multipulse single-beam CARS, p. 84): For $E(\omega)$, a spectral phase of $\varphi(\omega) \propto \sin(\tau_m\omega)$ leads in the time domain to a splitting of the excitation pulse into subpulses with temporal separation τ_m. For $\tau_m = 0$, *i.e.* flat spectral phase, the CARS signal is dominated by the instantaneous nonresonant contribution. For $\tau_m > 0$, this nonresonant background rapidly decreases and finally reaches a constant level independent of τ_m for well separated subpulses. The resonant CARS signal, however, leads to oscillations of the signal which encode the

molecular vibrations. Hence, evaluating τ_m-scans of $S^{(Het)}$ allows substracting the nonresonant background as a constant offset and recovering the purely resonant CARS spectrum by *Fourier* transform of the oscillations.[16] An experimental τ_m-scan of pure $CHBr_3$ is shown in Fig. 6.5a) for 0.35 ps < τ_m < 3.9 ps as grey solid curve. As expected, the *Fourier* transform of this data yields the two *Raman* modes of this molecule excitable with 100 fs pulses,[16] at 155 cm^{-1} and 222 cm^{-1}. To study the concentration dependence of the molecule-specific resonant CARS signal, similar τ_m-scans were recorded for a number of samples with $CHBr_3$ diluted in EtOH (Ethanol), ranging from a molar fraction $x(CHBr_3)$ of 0.01 to 1.

Note that EtOH does not have any vibrational resonances in the accessible spectral range up to ~350 cm^{-1} and only contributes to the nonresonant background. Even at the lowest concentration of $x(CHBr_3) = 0.01$ used in this study, corresponding to estimated 14 attomole (8×10^6 molecules) in the exciation volume of approx. 80 aL, the characteristic oscillations are found in the τ_m-scan. As an example, the τ_m-scan [Fig. 6.5a), black solid curve] and its *Fourier* transform [Fig. 6.5b), black solid curve] of a sample with $x(CHBr_3) = 0.06$ are shown. Hence, the relative amplitude of the resonant CARS signal can be plotted versus the molar fraction $x(CHBr_3)$, as shown in Fig. 6.5b), exhibiting a nearly perfect line through the origin with a slope of 1.01±0.01. This confirms linear concentration dependence, as expected from Eq.(6.2).

Possible applications of single-beam heterodyne CARS go beyond the multipulse-method employed here. Using the blue part of the excitation spectrum as external LO with full phase control should be directly applicable to any single-beam CARS scheme reported so far. For further simplification, a phase- and amplitude SLM could be used allowing very convenient control of the attenuation of the LO. The range of accessible *Raman* modes can be drastically increased by employing compressed supercontinuum (SC) from a microstructured fibre for single-beam CARS spectroscopy, as has been demonstrated the previous chapter.[17] By means of full control over the spectral phase, SC will also be able to act as external LO for heterodyne CARS microscopy, which is not easy to achieve otherwise.[169] There are several levers for further improvement: Sensitivity will be drastically improved, if the interferometry is carefully optimized with respect to the noise of the LO, the CARS signal and the detector.[170] Furthermore, the same advances concerning measurement speed apply as discussed in chapter 5.8.

6.3 Fiber laser single-beam CARS with interferometric detection

Recently, laser research has seen rapid advances of fibre technology, leading to powerful amplified systems and also to compact and robust ultrafast fibre lasers.[38, 39, 171, 172] Especially unamplified diode-pumped fs-fibre laser oscillators are now available commercially at considerably lower costs than conventional ultrafast laser systems, boasting very small footprints, turn-key operation and no necessity for water cooling. Additionally, due to the pump diodes stemming from established telecommunication applications, operating costs are low and reliability is high. Fibre lasers can thus pave the way for applications of ultrafast nonlinear spectroscopy outside the laser lab. To achieve this, the laser source has to be matched with an equally simple and robust measurement setup. The such achieved inherent experimental simplicity in fact could push real-life applications of

nonlinear spectroscopy,[173] be it chemically selective microscopic imaging[11], threat detection[151] or in other areas.[174]

In this section, the potential of fs-fibre lasers for single-beam CARS spectroscopy is explored. CARS with a fibre laser has been demonstrated in an elegant setup combining fs and ps-pulses[175], but the feasibility of a potentially much simpler single-beam scheme remains to be shown. A general challenge is the intensity dependence of the CARS signal to the power of three. Therefore, a usual single-beam CARS approach (see previous chapter 5) will struggle with very weak signals due to the markedly lower pulse energies in the pJ range of typical unamplified fs fibre lasers compared to conventional Ti:Sapphire based sources. However, with interferometric (heterodyne) detection, introduced in single-beam CARS, signal amplification of several orders of magnitude is possible, as shown in the previous section. Based on this, here a fibre laser implementation is presented, introducing further experimental simplifications and a robust spectroscopy scheme adapted to the fibre laser source. In this context, control of the signal generation and interferometric detection with the pulse shaper is explored, optimizing the weak signal detection. Finally, these capabilities are used for an exemplary chemical monitoring application in a microfluidic capillary flow cell.

6.3.1 Simulation of fibre laser single-beam CARS

For the following discussion, the CARS signal generation and interferometric detection shall for clarity again be stated in the frequency domain. Accordingly, using Eq. (3.1), a single-beam CARS signal is described by

$$E_{CARS}(\omega) \propto \int_0^\infty d\Omega \int_0^\infty d\omega' \, \chi^{(3)}_{CARS} \tilde{E}(\omega-\Omega)\tilde{E}^*(\omega')\tilde{E}(\omega'+\Omega), \tag{6.3}$$

where $\chi^{(3)}_{CARS}$ is the respective nonlinear susceptibility and $\tilde{E}(\omega)$ the spectrum of the broadband shaped excitation laser. To achieve spectroscopic resolution, the multipulse single-beam CARS scheme can be used, applying the sinusoidal spectral phase $\phi(\omega) = a \times \sin(\tau_m \times \omega + c)$ well known by now. In the previous section, the blue wing of $E(\omega)$ was attenuated to a few percent to ensure that it will only serve as LO for linear interferometry, and not participate in the nonlinear signal generation. Here, in the context of fibre laser application, a maximum of $E(\omega)$ is to be used in order to achieve the strongest interferometric signal $S^{Het}(\omega)$ possible [compare Eq. (6.2)]:

$$S^{Het}(\omega) = \left|\tilde{E}_{CARS}(\omega)\right| \cdot \left|\tilde{E}(\omega)\right| \cdot \cos\Delta\varphi(\omega) \tag{6.4}$$

As can be seen again from Eq. (6.4), the relative phase $\Delta\varphi(\omega)$ between excitation and simultaneous LO field $\tilde{E}(\omega)$ and signal $\tilde{E}_{CARS}(\omega)$ has to be zero. If now, in contrast to the situation in the previous section 6.3, the blue wing of $\tilde{E}(\omega)$ serving as LO is not attenuated, it will participate in the signal generation, in the best case generating a stronger CARS signal at the cost not being as easily disentangled due to its signal contribution. Under these circumstances, the pulse shaping strategy for single-beam heterodyne CARS spectroscopy has to be robust against additional modulations and interferences that will arise from this fact. With the great flexibility and full control of the LO interferometry offered by the pulse shaper, an appropriate scheme has been devised, which is simulated and summarized in Fig.

6.6. As always, simulations have been performed with the CARS extension for the Lab2-package.[176]

In Fig. 6.6a, the excitation spectrum $\tilde{E}(\omega)$ (grey shaded area) can be seen, with a sinusoidal phase applied for the red part of the spectrum, and a constant phase ϕ_{LO} in the interval $[-\pi, \pi]$ for the blue part acting as LO (dashed black curve). The signal $\tilde{E}_{CARS}(\omega)$ resulting according to Eq. (6.3) (solid black curve) is broadened compared to $\tilde{E}(\omega)$, as expected in the blue wing for CARS. Note, that $\tilde{E}_{CARS}(\omega)$ is not shown on the same scale as $\tilde{E}(\omega)$, because in the experiment it is several orders of magnitude smaller. For sensitive detection, here also a lock-in amplifier will be used: To introduce the necessary modulation in $\tilde{E}_{CARS}(\omega)$ and hence also in the interferometrically detected signal $S^{Het}(\omega)$,the red part of the excitation spectrum (Fig. 6.6b, grey shaded area) is periodically blocked. This leads to a weaker and narrower signal $\tilde{E}_{CARS}(\omega)$ (black solid line). What will be detected by the lock-in amplifier, the signal called $L(\omega)$, is the difference of the respective interferometric signals:

$$L(\omega) = S_{ON}^{Het}(\omega) - S_{OFF}^{Het}(\omega) \tag{6.5}$$

with the subscripts "ON" (Fig. 6.6a) and "OFF" (Fig. 6.6b) referring to the presence or absence of the red spectral wing of $\tilde{E}(\omega)$. The Lock-in signal $L(\omega)$ will depend on the phase difference $\Delta\varphi(\omega)$, as follows from Eq. (6.4). $E_{CARS}(\omega)$, and will in general show a modulated phase depending on $\chi^{(3)}_{\mathrm{CARS}}$ and the excitation pulse modulation.

This modulation is in general, however, not very strong. Therefore, an optimal "average" phase function can be found for the LO minimizing the phase difference for every multipulse temporal spacing, but not completely avoiding destructive interferences. This approach has been pursued in section 6.1. The DQSI procedure described in this section is always applicable without prior optimization, very robust, and maximizes the signal. In the case simulated here, assuming full integration, DQSI achieves a signal improvement of a factor ~4.

To always detect the ideal case of $\Delta\varphi(\omega) = 0$ for each ω, double quadrature spectral interferometry (DQSI)[177] is performed. As the constant LO phase ϕ_{LO} can be easily scanned with the pulse shaper, a a ϕ_{LO} will be found for each ω maximizing $L(\omega)$. In Fig. 6.6c, simulated $L(\omega)$ can be seen for $\phi_{LO} = 0$, $\pi/2$, π and $3\pi/2$. Although the variation of ϕ_{LO} in $E(\omega)$ will also modulate $E_{CARS}(\omega)$ to a certain degree, the simulation shows the expected periodic dependency of $L(\omega)$ for each ω and confirms that DQSI is applicable:

$$|L(\omega)| = \left(\left[L_{(\phi_{LO}=0)}(\omega) - L_{(\phi_{LO}=\pi)}(\omega) \right]^2 + \left[L_{(\phi_{LO}=\pi/2)}(\omega) - L_{(\phi_{LO}=3\pi/2)}(\omega) \right]^2 \right)^{1/2}, \tag{6.6}$$

the subscripts referring to the LO phase ϕ_{LO} at which the respective $L(\omega)$ value has been measured. The DQSI modulus of $L(\omega)$, determined via Eq. (6.6), is the desired interferometric single-beam CARS signal always measured at maximum constructive interference, and is shown in Fig. 6.6d.

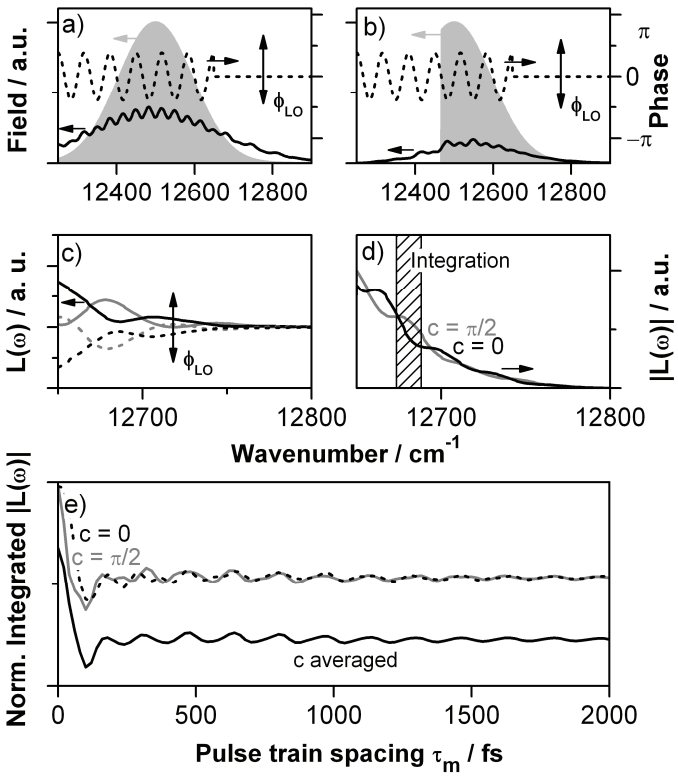

Fig. 6.6: Simulation of single-beam heterodyne CARS with lock-in and DQSI[177] detection. **a)** Full laser spectrum (grey shaded area) with a spectral phase containing a sinusoidal part for excitation and a constant phase offset ϕ_{LO} for interferometry and simulated CARS signal (black solid curve, shown on an arbitrary, magnified scale). **b)** The same simulation for a laser spectrum (grey shaded area) blocked in the red part. Performing this blocking periodically allows lock-in detection of the interferometric signal. **c)** Lock-in detected interferometric signal $L(\omega)$ for different LO phases ϕ_{LO}. **d)** Magnitude of $L(\omega)$ as detected by DQSI from the curves in panel **c)**, for two different c-parameters of the sinusoidal excitation phase. **e)** τ_m-transients from partial integration of $|L(\omega)|$ in the area shaded in panel **d)**. It can be seen that averaging $c = 0$ and $c = \pi/2$ avoids artefact oscillations in the transient.

Integrating this signal for different multipulse separations τ_m yields the desired single-beam CARS transients, as known from the non-interferometric experiments described in section 5.2.1 (p. 84). Due to excitation with the sinusoidal phase function $\phi(\omega) = a \times \sin(\tau_m \times \omega + c)$, the CARS signal $E_{CARS}(\omega)$ and thus also $|L(\omega)|$ shows a slight oscillatory modulation of its magnitude dependent on τ_m and c. This can be seen in Fig. 6.6d, which shows $|L(\omega)|$ for the cases of $c = 0$ (black curve) and $c = \pi/2$ (grey curve). In a full integration of the signal for all ω, these oscillations cancel out. If however only a part of $|L(\omega)|$ is integrated, this optical modulation will result in artefact oscillations in the τ_m-transients. This is demonstrated for integration of a rather narrow spectral band of $|L(\omega)|$ (shaded area in Fig. 6.6d) showing τ_m-transients in Fig. 6.6e. Clearly, the data for $c = 0$ (black dashed curve) and $c = \pi/2$ (grey curve) differ by an artefact oscillation on top of the expected molecular signature. Averaging the two cases of $c = 0$ and $c = \pi/2$ cancels out the spectral modulation of $|L(\omega)|$ and allows obtaining the wanted artefact-free τ_m-transient (Fig. 6.6e, black solid curve).

6.3.2 Experiment and Results

The experimental setup, shown in Fig. 6.7, has been adapted in several aspects compared to section 6.2 in order to cut costs and achieve further simplification. Naturally, the laser source in this study is markedly different, being a directly diode-pumped Er^{3+}-fibre laser (*MenloSystems*, pre-series model TC780, frequency doubled to 780 nm, 120 fs, typically 300 pJ), which is very compact and requires only passive cooling. The local oscillator part of the excitation spectrum is not attenuated, but fully used. A standard 4*f*-pulse shaper (f = 300mm, 1800 grooves/mm gratings, 640 pixel phase-only spatial light modulator) is employed with a transmission of roughly 40%, resulting in an effective excitation pulse energy of <120 pJ at the sample.

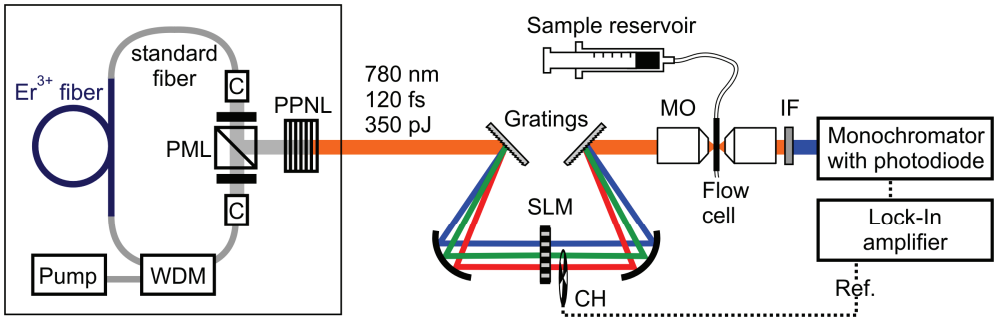

Fig. 6.7: Experimental setup. Laser source is a commercial polarization mode-locked (PML) Er^{3+}-fs-fibre laser, frequency-doubled with a periodically poled lithium niobate crystal (PPNL). "C" signifies collimator packages. The laser output is sent through a 4f-pulse shaper with a liquid crystal spatial light modulator (SLM). The red part of the spectrum is chopped (CH) for lock-in detection. CARS spectroscopy is performed in a flow cell; the signal is detected after an interference bandpass filter (IF) and a monochromator with a photodiode.

For a demonstration of a chemical sensing application a capillary flow sample cell has been chosen with a square inner cross-section of 100 × 100 µm (*Polymicro Technologies*). The capillary coating has been removed to form a transparent detection window. Focusing into the capillary is performed with inexpensive aspheric lenses (f = 4.5 mm at NA = 0.55, and f = 8 mm at NA = 0.5 for signal collection). To keep the setup as simple and robust as possible, the photomultiplier of section 6.2 has been replaced with a photodiode (*New Focus* photoreceiver type 2011). Stray excitation light is rejected by a band pass interference filter (*Andover*), transmitting a rectangular band of 10 nm spectral width centred at 770 nm. Detection is performed with a lock-in amplifier synchronized with the chopper placed in the *Fourier* plane of the pulse shaper, periodically blocking excitation wavelengths $\lambda > 781$ nm. Phase functions applied correct experimental dispersion, with an added excitation phase $\phi(\omega) = a \times \sin(\tau_m \times \omega + c)$ for $\lambda > 778$ nm and a constant phase ϕ_{LO} for $\lambda < 778$ nm.

The verification of interferometric CARS signal is performed with a prototypical sample of diiodomethane (CH_2I_2), which features a distinct *Raman* mode at 120 cm^{-1} easily accessible with the given laser bandwidth of up to 350 cm^{-1}.[16] The signal $L(\lambda)$ detected in the blue wing at 773 nm proves (i) dependent on the sample being placed in the focus, (ii) having a quadratic intensity dependence on the excitation laser, as expected from Eq. (6.3) and (6.4),

and (iii) varying with the LO phase ϕ_{LO} according to Eq. (6.4) (Fig. 6.8a). Measuring $L(\lambda)$ for different values of ϕ_{LO} in a DQSI scheme for a set sinusoidal excitation phase ($a = 1.22$, $\tau_m = 500$ fs, $c = 0$) thus reproduces the behaviour expected from Fig. 6.6c, and is shown in Fig. 6.8a. The resulting DQSI amplitude $|L(\lambda)|$, calculated according to Eq. (6.6), can be seen in Fig. 6.8b for the two cases of the excitation phase parameter $c = 0$ and $c = \pi/2$. As expected from the simulation (Fig. 6.6d), artefact modulations dependent on c arise. The total shape of $|L(\lambda)|$ is more complex than in the simulation, mainly due to the presence of the interference band pass filter.

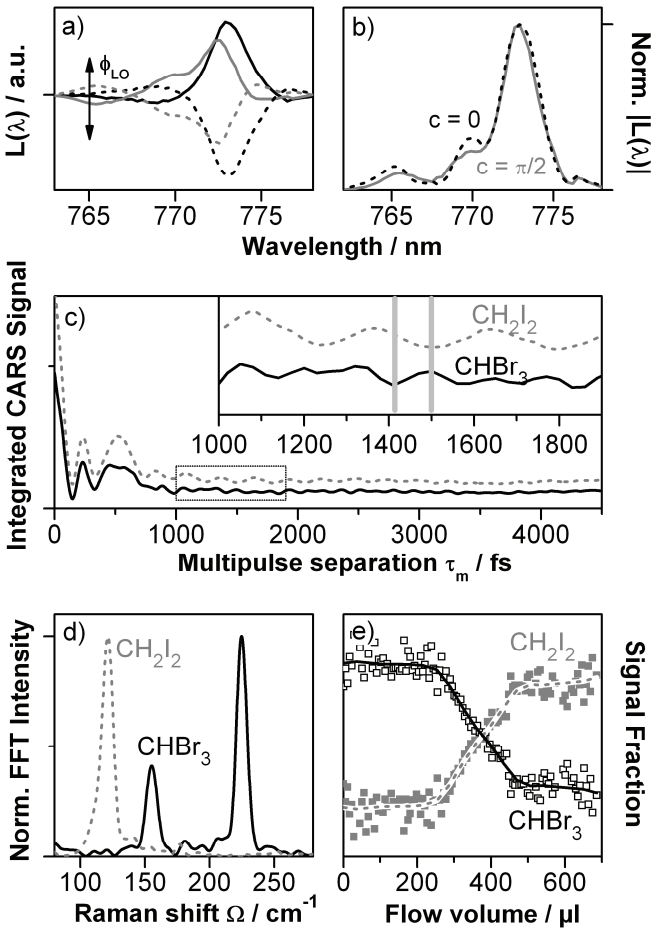

Fig. 6.8: Experimental results of single-beam heterodyne CARS spectroscopy performed with an unamplified femtosecond fibre laser. **a)** Spectrally resolved lock-in signal showing the expected dependency on the LO phase (black solid line $\phi_{LO} = 0$, grey solid line $\phi_{LO} = \pi/2$, black dashed line $\phi_{LO} = \pi$, grey dashed line $\phi_{LO} = 3\pi/2$). **b)** DQSI amplitude for excitation phase parameters $\tau_m = 500$ fs and $c = 0$ (black dashed curve) and $c = \pi/2$ (grey solid curve), showing artefact oscillations. **c)** τ_m-scans for CH_2I_2 (grey dashed curve) and $CHBr_3$ (black solid curve). The inset shows a magnified region from $\tau_m = 1000$ fs to 1900 fs, as indicated by the dotted box. **d)** Resulting *Fourier* intensity spectra of the τ_m-scans for CH_2I_2 (grey dashed curve) and $CHBr_3$ (black solid curve). **e)** Detection of a chemical concentration gradient in a microfluidic capillary, showing the full exchange of $CHBr_3$ (signal fraction shown as open squares and averaged black solid curve) to CH_2I_2 (filled grey squares and averaged grey dashed curve).

To perform spectroscopy, $|L(\lambda)|$ was detected at $\lambda = 773$ nm for varying multipulse separations τ_m, with an increased slit width at the monochromator allowing spectral integration of about 2 nm. Additionally, $|L(\lambda)|$ was averaged for $c = [0, \pi/2]$. In the case of diiodomethane (CH_2I_2), the characteristic signal modulation with a period of roughly 280 fs expected for a single vibrational resonance at 120 cm^{-1} is found (Fig. 6.8c, dashed curve), whereas bromoform ($CHBr_3$) reveals a more complex oscillatory pattern (Fig. 6.8c, black solid curve) corresponding to its two accessible vibrational modes at 155 cm^{-1} and 222 cm^{-1}. It can also be discerned that CH_2I_2 generally shows signal about a factor of two stronger due to its higher *Raman* scattering cross-section and elevated nonresonant CARS background. *Fourier* transform of the τ_m-scan data of Fig. 6.8c directly shows well separated spectra of both halomethanes (Fig. 6.8d), achieving a spectral resolution of better than 10 cm^{-1}.

The ability to perform chemically selective nonlinear spectroscopy with shaped laser pulses from the simplified fibre-laser setup allows a demonstration of a chemical sensing application. Using the capillary flow cell, a concentration gradient can be created by exchanging the syringe constituting the sample reservoir (Fig. 6.7) from one containing $CHBr_3$ to one with CH_2I_2 carefully avoiding air bubbles. Thus, a chemical flow is obtained automatically by transporting this concentration gradient through the system with an automated syringe pump. The capability of the fibre laser CARS microspectroscopy setup now allows monitoring this flow in the microfluidic capillary and detecting the concentration gradient. In order to achieve this, a sequence of shaped pulses optimized to create a maximum signal $|L(\lambda)|$ for one chemical constituent, while minimizing it for the other, is applied. Suitable values of τ_m to create such a sequence are directly read from the data in Fig. 6.8c, shown for $\tau_m = 1410$ fs (minimum for CH_2I_2 and near maximum for $CHBr_3$) and 1500 fs (minimum for CH_2I_2 and maximum for $CHBr_3$) as thick grey vertical lines. Like this, DQSI signal intensities for both τ_m values are determined each ~60 s, while the liquid in the capillary is moved at a rate of 400 µl/h. For an evaluation, each signal is divided by the sum of both signals to display the signal fraction, which is not affected by the concomitant change in the signal offset due to the differing nonresonant background of CH_2I_2 and $CHBr_3$, and is shown in Fig. 6.8e. It can be clearly seen that the signal corresponding to $CHBr_3$ (black) drops at a dispensed volume of ~300 µl, while at the same time the CH_2I_2 (grey) signal rises, subsequently leading to a full exchange after passing the diffusion zone at ~500 µl.

Currently, the need for averaging for a sufficient signal-to-noise ratio and the relatively slow up update rate of the pulse shaper (to apply all the necessary pulse shapes, including 4 LO phase variations at each τ_m for DQSI doubled by c phase averaging) restrict measurement times to several tens of seconds. Therefore, full spectroscopic transients like in Fig. 6.8c presently still require about 60 min. As already discussed in section 5.8 in the previous chapter, using faster pulse shaping schemes,[82, 153] improving laser pulse energy, bandwidth and stability as well as optimizing measurement electronics should allow acceleration of up to two orders of magnitude. Still, this first demonstration already shows the great potential of simplified fibre-laser based schemes for nonlinear spectroscopy in analytics and sensing applications.

7 Summary and Outlook

This work presented a novel, unified approach to **nonlinear spectroscopy** performed in the focus of a microscope. Combining a single sub-15 fs broadband femtosecond laser beam with pulse shaping and microscopy, it offers unprecedented spectroscopic flexibility. The first prerequisite is the availability of such short femtosecond pulses and broad coherent spectra, which was solved by devolping a new light source based on a standard 100 fs oscillator and a **photonic crystal fibre** (PCF, 2.2.2) for spectral broadening. The pulse shaper, later used for coherent control, is at the same time the key building block for this light source, as only its powerful phase management capabilities allow taming the fibre output.

If, in a first step, the photonic crystal fibre output is not compressed to ultrashort pulses, it can still be used as highly flexible frequency converter. This already allowed implementation of a robust setup for chemically selective multiplex coherent anti-*Stokes Raman* scattering (**MCARS**) microscopy employing only a single laser. While this approach had been described before, here it was implemented in a further optimized way. In earlier reports, broadband MCARS lacked energy efficiency and robustness, which was both realized here utilizing a careful combination of passive interferometric filters. Also, in contrast to earlier literature reports of broadband MCARS which always struggle with nonresonant background and interference of signals in mixtures, the broadband multiplex spectra acquired were analysed quantitatively using a physical model and evolutionary algorithm fitting. These developments allowed imaging and quantitative chemical mapping of polymer samples, such as ternary blends.

While MCARS already substantially drew upon broadband excitation, the functionality of the laser radiation used was limited to its spectral shape. Only by using the **pulse shaper** (4.1) and **coherent control** (chapter 1), the full potential of broadband femtosecond excitation can be unleashed. The pulse shaper was shown not only to be capable of compressing the broadband PCF output, but also to be able to completely compensate for all dispersion effects which are inevitable in a high-performance optical microscope. In order to achieve this, however, the precise nature of the distortions has to be known. As there was no method available capable of a rapid, real-time phase characterization of the sub-15 fs pulses used, a new scheme had to be developed providing the necessary capabilities. In order to achieve this, a novel variant of **SPIDER pulse characterization** (4.3) was conceived for the needs of collinear beam arrangement in microscopy and integrated into the existing pulse shaper. Thorough characterization of the novel technique proved its excellent aptitude in the given conditions, delivering precisely shaped pulses *in situ* (compressed in less than 800 ms) for coherently controlled spectroscopy.

Coherent control aims at manipulating the outcome of a light-matter-interaction by controlling the light field. In the context of nonlinear spectroscopy, the phase of the femtosecond laser pulses used can be tailored in such a way, that out of the entangled contributions of all possible signals only the desired one is selected. As phase control is performed by the computerized **pulse shaper**, this scheme is very flexible and allows performing all different kinds of microspectroscopy with software-control:

- To perform chemically selective microscopy, coherent anti-*Stokes Raman* scattering (CARS) spectroscopy was implemented, using only the single beam of shaped femtosecond pulses and relying on coherent control techniques to extract spectroscopic information. In this context, a scheme relying on multipulse sequences, based on the pioneering work on **single-beam CARS** by the group of *Silberberg*, was applied. This scheme is known to have some drawbacks, which have again been elaborated theoretically, especially ambiguities in measured spectra. To mitigate this and open up further applications of single-beam CARS, a novel approach unambiguously relying on a **time-resolved CARS** measurement (5.2) was developed in the course of this thesis. The advantage of this scheme, in addition to yielding unique spectral information, is the possible incorporation of additional function into the laser pulse sequence used. Like this, single-beam polarization control has been introduced and has been shown to perform spectroscopy with superior robustness and signal quality. Additionally, selective excitation using coherent control was successfully combined with a time-domain probing of the molecular vibration using CARS. First applications were successfully demonstrated, including chemical imaging and selective identification of model substances for hazardous bacterial spores (anthrax).

- Even more functionality can be integrated in the shaped femtosecond beam, which was shown in the last experimental chapter. To increase analytical sensitivity of CARS, **interferometric detection** of the coherent signal was also incorporated into the broadband excitation pulses (6.1), providing signal amplification of more than three orders of magnitude while retaining the simplicity of the single-beam approach. Also, the linear signal dependence on the analyte concentration greatly facilitates microanalytical applications, already arriving at $<10^{-7}$ detected molecules in a sampled volume of only 80×10^{-18} liters. In the future, even better sensitivities can be expected. The robustness of this single-beam interferometric scheme is complemented by the full phase control given by the pulse shaper, allowing computer controlled implementation of sophisticated interferometric detection schemes. This combination was demonstrated for the first time for a new compact fibre laser source, which only became possible by exploiting interferometry and very efficiently processing processing the acquired data. This achievement promises a dramatic further simplification of single-beam CARS and shows the feasibility of all-fibre implementations.

In total, as can be seen from the developments described, a complete toolbox was developed for coherently controlled microscopy in a simplified, holistic approach. This will serve to promote hitherto impractical advanced spectroscopy methods for real-life microscopic imaging, chemical analytics in microenvironments and also rapid detection schemes, *e. g.* for online-monitoring of potentially hazardous substances, such as anthrax spores (5.5.2). The possibility to easily incorporate multi-parameter spectroscopy, by correlating different spectroscopic signals recorded at each spatial position simply by applying a series of designed pulse shapes, also cannot be underestimated (Fig. 7.1).

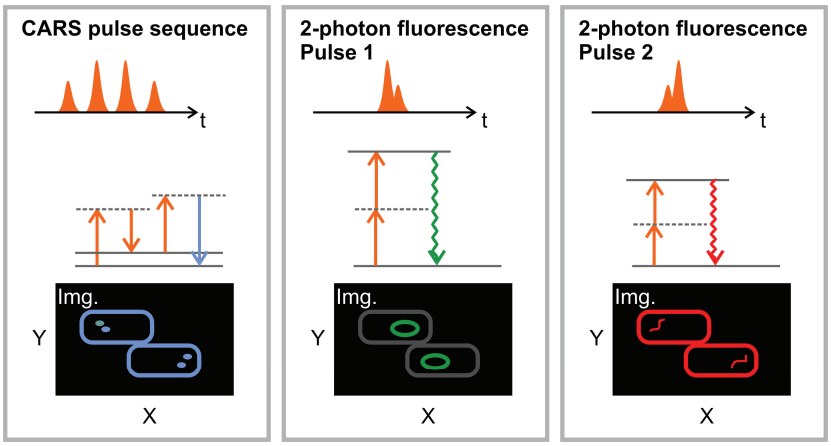

Fig. 7.1: Schematic representation of correlation imaging in nonlinear microscopy with shaped broadband laser pulses. For each pixel signal is recorded, which is created by a single-beam CARS pulse sequence (left) as well as selective two photon fluorescence excitation (middle and right). Like this, microscopic structures can be imaged with very high contrast and selectivity. The complete process is realized solely by appropriate computer control of the fs-pulse shaper.

Future work will have to focus on three aspects. First of all, the measurement time has to be reduced further for single-beam CARS schemes. This can be achieved either by applying multiplex strategies, *e. g.* mapping a time-resolved signal into the spectral domain (Fig. 7.2) by using a chirped probe pulse,[178] or by speeding up the update rate of different pulse shapes, which presently is the limiting bottleneck. Several viable options have already been discussed in section 5.8.

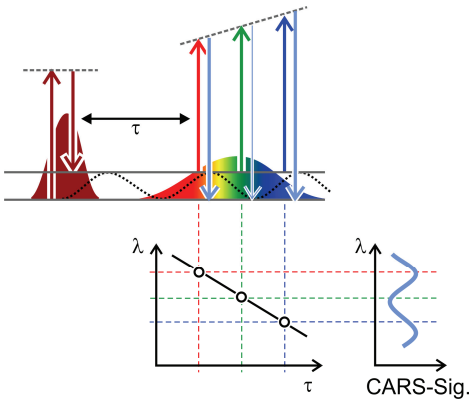

Fig. 7.2: Single-beam implementation of time-resolved multiplex CARS. A first, short fs-pulse creates a coherent excitation of a *Raman* level. The oscillating response is then probed by a second, chirped pulse of the sequence. This temporarily stretched pulse performs a mapping of time (τ) into the wavelength scale. A thus rapidly acquired CARS spectrum reflects the temporal behaviour without scanning the delay τ.

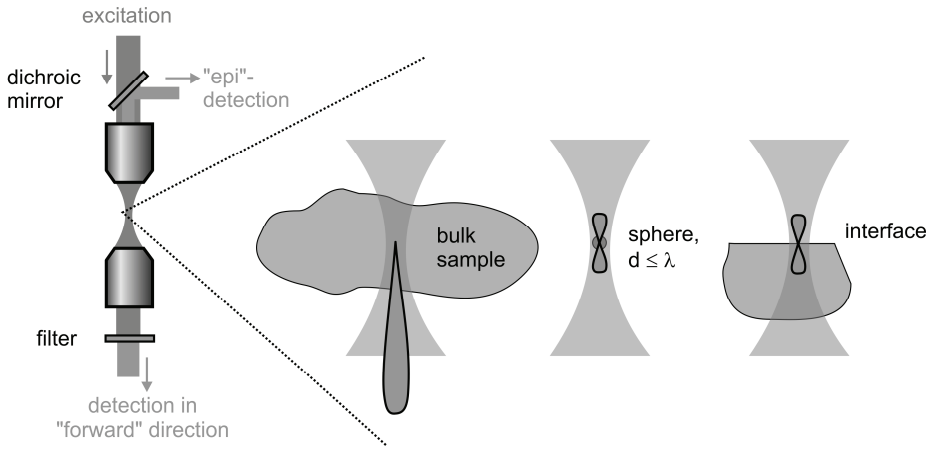

Fig. 7.3: Detection schemes in CARS microscopy. Usually, the forward scattered signal is detected, which in bulk samples always gives the highest far field intensity. In bulk samples, due to the coherent superposition of CARS emission from the entire focal volume, no backward (epi) signal is generated. This is markedly different if the object under study is smaller than the focal dimensions. In this case, signal can also be generated in epi direction, with the far field distribution resembling that of a dipole emitter. The situation is similar for a focus placed directly at an interface between different materials. Epi-CARS therefore yields background-free images of small objects and interfaces with very high contrast.

Secondly, the available bandwidth, currently easily covering more than 1700 cm^{-1} has to be increased. To that end, the laser source pumping the photonic crystal fibre supercontinuum generator should be upgraded from a 100 fs laser to a shorter pulse oscillator. This work is already in progress. In combination with the advanced techniques developed for dispersion compensation, it should thus be possible to use sub 10 fs pulses in the microscope for single-beam spectroscopy. Thirdly, integration based on robust fibre technology holds great promise for further simplification and broader availability for real-life applications. Exploring detection in backscattered (epi-) direction[179] (Fig. 7.3) also holds promise for microscopy applications of non-transparent samples, however the weaker signals might require laser sources with higher pulse energies, as are available *e. g.* by cavity-dumped ultrafast fs-oscillators. Another very promising field of research, especially in order to increase sensitivity, is the use of surface-enhancement effects,[180] which possibly could be exploited very advantageously in conjunction with optimized femtosecond pulses.[181]

The first successful applications of the novel, broadband shaped light source show the great potential for integrated coherent control approaches to study, use and manipulate light-matter interactions in microenvironments. Hence, the foundations seem to be laid and can be expected to nourish fruitful further work in the near future.

8 Zusammenfassung und Ausblick

Diese Arbeit stellt einen neuen, integrierten Ansatz für nichtlineare Spektroskopie im Fokus eines Mikroskops vor. Durch die Kombination eines einzelnen Strahls von Femtosekunden-Impulsen unter 15 fs Dauer, mit einem Impulsformer und dem Mikroskop entstehen völlig neue Möglichkeiten für Spektroskopie mit zuvor unerreichter Flexibilität. Die erste Voraussetzung dafür ist, eine Quelle für solch kurzen Laserimpulse zur Verfügung zu stellen. Dies wurde hier dadurch erreicht, dass eine neuartige Lichtquelle entwickelt wurde, die auf einem Standard-100 fs-Oszillator basiert, dessen Spektrum in einer **photonischen Kristallfaser** (PCF, 2.2.2) kohärent verbreitert wird. Nur durch den Impulsformer, der später für die kohärente Kontrolle der Spektroskopie verwendet wird, ist es möglich, die Phase der neuen Lichtquelle präzise zu steuern und sie damit erst voll einsetzbar zu machen.

Auch wenn das Licht aus der Kristallfaser in einem ersten Schritt noch nicht komprimiert wurde, konnte es dennoch bereits sehr gewinnbringend für eine Umsetzung der in Kapitel 3 vorgestellten multiplex-CARS (coherent anti-*Stokes Raman* scattering) Mikroskopie, abgekürzt **MCARS**, verwendet werden. Durch die Frequenzkonversion in der PCF genügt ein einziger fs-Laser! Im Rahmen der vorliegenen Arbeit wurde dieser prinzipiell literaturbekannte Ansatz in einer neuen, optimierten Form umgesetzt. Der Schwerpunkt lag dabei auf der sehr effizienten Nutzung der gesamten Laserenergie, und einer besonders robusten Implementierung für zukünftige Anwendungszwecke. Im Gegensatz zu allen früheren Arbeiten mit einem solchen Breitband-MCARS-Mikroskop wurden hier erstmals gemessene Spektren von Mischproben durch Anpassung eines physikalischen Modells quantitativ in die Einzelkomponenten zerlegt. Dadurch gelang chemisch selektive Bildgebung und eine quantitative, ortsaufgelöste Analyse von Polymer-Proben, wie beispielhaft untersuchten ternären Polymer-Blends.

Während MCARS bereits deutlich von den neuen Möglichkeiten einer PCF-basierten Laserquelle profitierte, war die Funktion der Strahlung doch allein durch ihr Spektrum definiert. Erst wenn der **Impulsformer** (4.1) verwendet wird und **kohärente Kontrolle** (Kapitel 1) zum Einsatz kommt, kann das ganze Potenzial der Breitband-Femtosekundenanregung ausgeschöpft werden. Dabei konnte gezeigt werden, dass der Impulsformer nicht nur in der Lage ist, die breitbandige kohärente Strahlung aus der PCF zu ultrakurzen Impulsen zu komprimieren, sondern darüber hinaus auch noch alle schädlichen Dispersionseffekte im Mikroskop auszugleichen. Um dazu in der Lage zu sein, muss jedoch die genaue Art der Impulsverzerrungen durch PCF und Dispersion im Mikroskop sehr exakt bekannt sein. Da für diese Messung keine geeignete Methode bekannt war, die in der Lage gewesen wäre, Impulse mit Dauern unter 15 fs in Echtzeit im Fokus eines Mikroskops zu charakterisieren, musste ein neues Schema entwickelt werden, das genau dies leistet. Dazu wurde die **SPIDER-Methode** (4.3) zur Impulscharakterisierung auf die Anforderungen kollinearer Strahlführung im Mikroskop angepasst, und gleichzeitig weitest möglich allein durch Einsatz des Impulsformers umgesetzt. Dieser übernimmt hier also, als zentraler Baustein des Experimentes, auch noch die Aufgabe der Impulscharakterisierung. Eine gründliche Validierung der neuen Methode zeigte die hervorragende Eignung der neuen Methode für die nichtlineare Mikroskopie und die dadurch erfolgreiche Bereitstellung von sehr präzise geformten Laserimpulsen im Fokus des Mikroskops. Genau dies war die unabdingbare Voraussetzung für kohärente Kontrolle.

Kohärente Kontrolle zielt im Allgemeinen auf die Beeinflussung einer Licht-Materie-Wechselwirkung durch Manipulation des anregenden Laserfeldes. Im Kontext nichtlinearer Spektroskopie kann die Phase der anregenden Femtosekundenimpulse dergestalt geformt werden, dass aus der Vielzahl überlagerter Signale der Breitbandanregung nur ein gewünschter Prozess ausgewählt wird. Solche Phasenformung von Laserimpulsen wird computergesteuert mit einem **Impulsformer** (4.1) vorgenommen. Dies macht das Schema außerordentlich flexibel, da verschiedene Spektroskopien allein durch Wechsel der Ansteuerung realisiert werden:

- Um chemisch selektive Mikroskopie zu ermöglichen, wurde kohärente anti-*Stokes Raman* Streuung als nichtlinearer Prozess (coherent anti-*Stokes Raman* scattering, CARS) implementiert; innerhalb des geformten Einzelstrahls durch den Einsatz von Kohärenter Kontrolle. In diesem Kontext wurde zunächst ein auf einer Multipuls-Sequenz basierendes Schema verwendet, das auf den grundlegenenden Arbeiten der Gruppe um *Silberberg* zu Einzelstrahl-CARS beruht. Dieses Schema hat einige Nachteile, insbesondere mögliche Uneindeutigkeiten in gemessenen Spektren, die in Kapitel 5 ausführlich diskutiert wurden. Um solche Uneindeutigkeiten zu vermeiden und eine breitere Anwendbarkeit zu erschließen, wurde ein neuer, spektroskopisch eindeutiger Ansatz für **zeitaufgelöstes Einzelstrahl-CARS** entwickelt (5.6.2). Der große Vorteil dieses Schemas, zusätzlich zu seiner Eindeutigkeit, ist die Möglichkeit, noch weitaus mehr Funktionalität in die verwendeten Laserimpuls-Sequenzen aufzunehmen. Dies wurde genutzt, um durch zusätzliche Kontrolle des Polarisationszustandes einzelner Impulse im verwendeten Anregungsstrahl die Robustheit gegenüber Störungen und die Signalqualität zu steigern. Außerdem wurde gezeigt, dass sich so eine kohärent kontrollierte, selektive und unabhängige Anregung mit der eindeutigen zeitaufgelösten Abfrage molekularer Schwingungen kombinieren lässt.

- Darüber hinaus kann der einzelne Strahl geformter fs-Laserimpulse sogar noch mehr Funktionen übernehmen. Um die analytische Empfindlichkeit von CARS drastisch zu steigern, wurde eine interferometrische Detektion des kohärenten Signals im selben Anregungsstrahl verwirklicht (6.1). Dies erlaubt eine Verstärkung des Signals um mehr als drei Größenordnungen, ohne dass der Aufbau komplizierter wird. Die gesamte Interferometrie wird allein durch dein Impulsformer übernommen, und per Software programmiert. Die interferometrische Detektion sorgt außerdem dafür, dass das gemessenen chemisch selektive Signal direkt linear von der Konzentration des Analyten abhängt, was Voraussetzung für empfindliche Mikroanalytik im Fokus des Mikroskops ist. Dieses robuste, interferometrische Einzelstrahl-CARS-Schema machte es auch zum ersten Mal möglich, einen kompakten Faserlaser als Anregungsquelle zu verwenden, der zwar nur sehr wenig Anregungsintensität zur Verfügung stellen kann, zusammen mit dem empfindlichen Detektionsschema jedoch erfolgreiche zeitaufgelöste nichtlineare Spektroskopie in einem drastisch vereinfachten Aufbau, bei deutlich niedrigeren Kosten, ermöglicht.

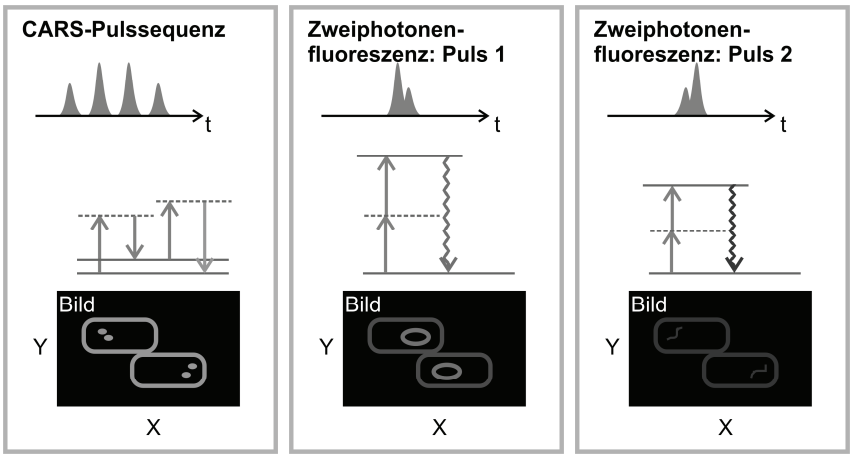

Fig. 8.1: Schematische Darstellung von Korrelations-Bildgebung in der nichtlinearen Mikroskopie mit geformten Ultrabreitband-Femtosekunden-Laserimpulsen. Für jeden Bildpunkt wird das Signal registriert, das eine Einzelstrahl-CARS-Pulssequenz (links), sowie Pulse, die selektiv die Zweiphotonenfluoreszenz zweier verschiendener Farbstoffe anregen (Mitte und rechts), erzeugen. Dadurch können mikroskopische Strukturen mit sehr hohem Kontrast und großer Selektivität abgebildet werden. Alle dargstellten Prozesse lassen sich nur durch unterschiedliche computergesteuerte Ansteuerung des Femtosekunden-Pulsformers verwirklicken.

Zusammenfassend betrachtet lassen sich all die beschriebenen Entwicklung als Module für den neuen, umfassenden Ansatz nichtlinearer Mikroskopie mit einem einzigen Strahl geformter Femtosekundenimpulse betrachten. Damit besteht die Aussicht, bisher durch ihre Komplexität und eingeschränkte Anwendbarkeit nicht praktikabel anwendbare Spektroskopie-Methoden für die mikroskopische Bildgebung zu erschließen. Darüberhinaus ergeben sich auch höchst interessante Perspektiven für chemische Analytik auf der Mikrometerskala und neuen Verfahren zur schnellen on-line Detektion z.B. von Gefahrstoffen (5.5.2). Die Möglichkeit, auf sehr einfache Art und Weise Multiparameter-Untersuchungen vorzunehmen, bei denen verschiedene Spektroskopiesignal korreliert werden, ist weiterhin sehr vielversprechend. In diesem Fall wird in jeder räumlichen Position der Probe eine Serie von Impulsformen eingestrahlt, und die unterschiedlichen Signale verrechnet (Fig. 8.1).

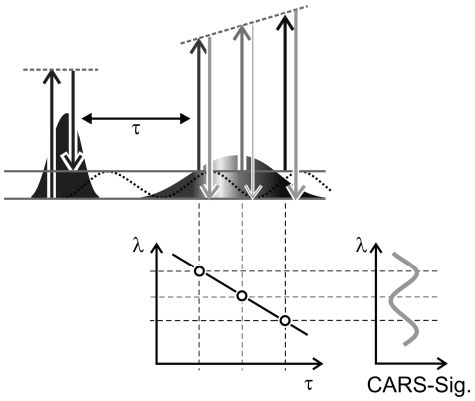

Fig. 8.2: Darstellung der Einzelstrahl-Implementierung von zeitaufgelöstem Multiplex-CARS. Ein erster komprimierter Femtosekunden-Sub-Impuls erzeugt eine kohärente Anregung der Vibrationsniveaus. Die oszillierende CARS-Antwort wird dann durch einen zweiten, gechirpten Sub-Impuls der Sequenz abgefragt. Dieser in der Zeit gestreckte Laserimpuls leistet eine Abbildung der Zeitskala der Molekülschwingung (τ) in die Wellenlängen-Skala. Das auf einmal gemessene Spektrum des CARS-Prozesses repräsentiert daher das zeitaufgelöste CARS-Signal.

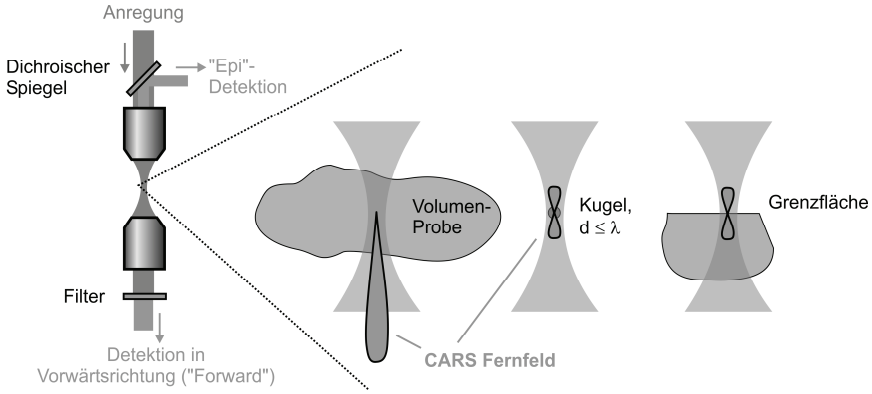

Fig. 8.3: Detektionsschemata in der CARS-Mikroskopie. Das übliche Verfahren ist die Detektion in Vorwärtsrichtung, das aus Volumenproben das stärkste CARS-Fernfeld-Signal liefert. In Volumenproben gibt es wegen der kohärenten Überlagerung der CARS-Emission aus dem gesamten Fokalvolumen praktisch kein in Epi-Richtung zurückgestreutes Signal. Ganz anders ist die Situation, wenn das Objekt im Fokus kleiner ist als die Fokusdimensionen. Nun wird kann auch Signal in Epi-Richtung entstehen - das CARS-Fernfeld ähnelt dem eines Dipolstrahlers. Ähnlich ist die Situation, wenn der Fokus gerade auf einer Grenzfläche zwischen verschiedenen Materialien positioniert ist. Epi-CARS liefert daher sehr kontrastreiche, hintergrundfreie Bilder von kleinen Objekten und von Grenzflächen.

Weitergehende Arbeiten werden sich vorteilhaft auf drei Aspekte konzentrieren: Zunächst müssen Schritte unternommen werden, die Messzeiten für Einzelstrahl-CARS zu reduzieren. Das könnte z. B. durch eine Multiplex-Strategie in der Zeitdomäne erfolgen, bei der das zeitaufgelöste CARS-Signal durch einen Abfrageimpuls mit zeitlich variabler

instantaner Frequenz abgefragt[178] und somit in den Frequenzraum abgebildet wird. (Fig. 8.2), oder auch durch Beschleunigung der Impulsformung, die bisher das technische Limit für die Messgeschwindigkeit im Aufbau darstellt (siehe Diskussion in 5.8).

Zweitens ist es lohnenswert, die zur Verfügung stehende Bandbreite weiter zu vergrößern. Im Moment werden Impulse mit spektralen Breiten ausreichend für die Untersuchung von Schwingungsmoden bis ca. 1700 cm^{-1} erzeugt. Um dies zu erweitern, sollte der bisher verwendete 100 fs-Laser, der die photonische Kristallfaser pumpt, durch einen Oszillator mit bereits kürzeren Impulsen ersetzt werden. Diese Arbeiten haben bereits begonnen. Zusammen mit den entwickelten Methoden zur Pulskompression und Dispersionskompensation sollte es möglich sein, Impulse mit Dauern noch unter 10 fs im Fokus des Mikroskops zu verwirklichen. Diese bieten dann auch genug Bandbreite, um interferometrische Detektion für hochfrequente Moden zu ermöglichen.

Drittens ist die weitere Vereinfachung und Integration in ein rein Faser-basiertes Lasersystem von großer Bedeutung für zukünftige Anwendungen. Für viele Anwendungen ist es auch wichtig, zu untersuchen inwiefern die Detektion auch in Rückwärtsrichtung ("Epi") erfolgen kann, da sich so das Spektrum untersuchbarer Proben deutlich erweitert, und Transparenz keine Voraussetzung mehr ist. (Fig. 8.3). Allerdings sind dort nochmals deutlich schwächere Signale zu erwarten, so dass für diese Untersuchungen Laser mit gleichzeitig sub-20 fs Impulsen und höheren Impulsenergien (>20 nJ) zur Anwendung kommen müssten, die als "cavity-dumped" fs-Oszillatoren bereits kommerziell verfügbar sind.

Die neuartige, hier gezeigte Kombination von nichtlinearer Spektroskopie und kohärenter Kontrolle in einem einzelnen Strahl geformter Femtosekunden-Impulse eröffnet im Kontext der Mikroskopie aufregende Möglichkeiten, Licht-Materie-Wechselwirkungen in mikroskopischen Volumina zu studieren, für Spektroskopie zu nutzen, oder gezielt beeinzuflussen.

Appendix

In chapter 3 a compact description of the fitting routine for quantitative decomposition of broadband MCARS spectra was given. This procedure shall be resumed here from a more practical point of view. The prerequisite is to have obtained suitable broadband CARS spectra, such as Fig. 3.8 in chapter 3, which is again shown in Fig. 0.1a.

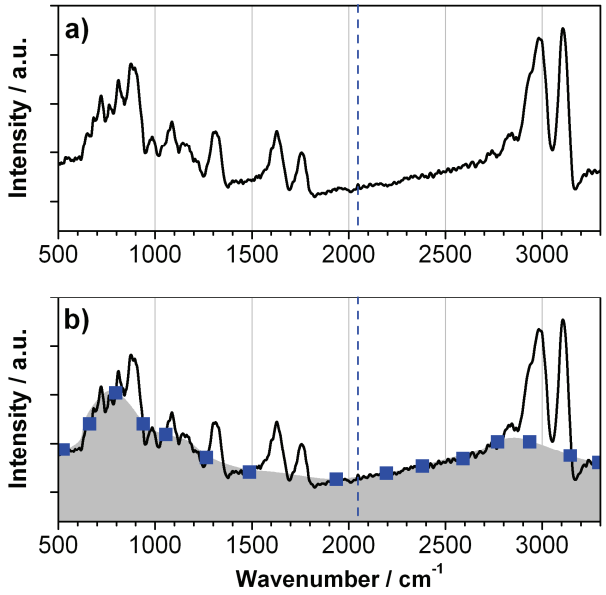

Fig. 0.1: a) Measured MCARS raw spectrum of pure PET. **b)** Nonresonant background fitted manually as baseline to the raw data.

As was shown in chapter 3, a general MCARS spectrum $|S_{mix}(\omega_p + \Omega)|^2$ from a mixture of components is the modulus square of a coherent sum over all complex spectra S_i:

$$\left|S_{mix}\left(\omega_p+\Omega\right)\right|^2=\left|\sum_i c_i\cdot S_i\left(\omega_p+\Omega\right)\right|^2, \tag{6.7}$$

where the coefficients c_i are the relative contents of the components i in the sample, which ultimately are to be determined by the fitting routine. To disentangle the measured CARS intensity spectrum, all interferences have to be taken into account. This requires fitting of pure spectra S_i, still containing amplitude and phase information, which is lost upon forming the modulus. As even S_i cannot be measured directly (without interferometry) even from pure samples, the first step is to find a reasonable solution for S_i by comparing $|S_i|^2$ with the measured data. This indirect fitting is necessary, as the squaring and the modulus do not allow a direct inversion, *e. g.* by simply taking the square root. However, it is simple to make use of a physical model to describe S_i, based on a simple *Lorentzian* resonance term for the susceptibility $\chi^{(3)}_{res,i}(\Omega)$ and a constant $\chi^{(3)}_{NR,i}$:

$$S_i\left(\omega_p+\Omega\right)\propto\left[\chi^{(3)}_{res,i}(\Omega)+\chi^{(3)}_{NR,i}\right]\cdot E_s^*\left(\omega_p-\Omega\right), \tag{6.8}$$

with the resonant susceptibility, according to chapter 3, described as

$$\chi_{res,i}^{(3)}(\Omega) = \sum_n \frac{f_n}{\Omega_n - \Omega + i\Gamma_n}. \tag{6.9}$$

What remains to be described in Eq. (6.8) is the shape of the *Stokes* electric field, entering as envelope for the measured CARS spectrum. Remember that the Stokes spectrum determines the measureable range and the relative strength of the accessible vibrational resonances in MCARS. In Eq. (6.8), the Stokes field still is a complex quantity, bearing a phase. As seen in chapter 3, this can typically be chirp acquired by material dispersion. However, for our purposes this phase does not matter at all, as it is a general phase for all components at the same frequency of the CARS signal, be they resonant or nonresonant: In interferometric terms, only phase differences show up. As Eq. (6.8) will never give rise to phase differences for a given Ω, it can be neglected:

$$S_i(\omega_p + \Omega) \propto \left[\chi_{res,i}^{(3)}(\Omega) + \chi_{NR,i}^{(3)}\right] \cdot \left|E_s(\omega_p - \Omega)\right|. \tag{6.10}$$

The first step necessary to perform a physical fitting of the MCARS data is to obtain the effective $|E_s(\omega_p\text{-}\Omega)|$. This is most directly performed by measuring a signal S_{glass} from a material which has an almost purely nonresonant response, such as glass:

$$\left|S_{glass}(\omega_p + \Omega)\right|^2 = \left|\chi_{NR,glass}^{(3)}\right|^2 \cdot I_s(\omega_p - \Omega). \tag{6.11}$$

Knowing that $\chi_{NR,i}^{(3)}$ only is a scalar, the effective *Stokes* spectrum $I_s(\omega_p\text{-}\Omega)$ is easily calculated, and $|E_s(\omega_p\text{-}\Omega)|$ obtained as its square root. Another, similar approach needs some spectroscopic intuition and knowledge of the general spectral shape of the *Stokes* continuum. If the latter is smooth, a baseline corresponding to the nonresonant background can be found by linear (or spline) interpolation for measured spectra, which already contain resonant CARS lines. This procedure is demonstrated in Fig. 0.1b, where sample points have tentatively been placed to trace the nonresonant background, which is expected to have two peaks due to the spectrum being composed of data taken at two different temporal delays between pump and *Stokes* (dashed vertical line, see chapter 3 for details). To sum it up, the effective Stokes spectrum $I_s(\omega_p\text{-}\Omega)$ can be obtained in three different ways:

- By measuring purely nonresonant CARS signal from a suitable sample, *e. g.* glass. This is the preferred approach.

- The nonresonant background can be fitted to spectral data containing resonances, if the Stokes spectrum is known to be smooth and the density of resonances is low enough to allow a reasonable tracing of the baseline (Fig. 0.1b).

- Fully knowledge-based, if the NIR-*Stokes* spectrum in the excitation is measured precisely. However, this seemingly trivial solution requires perfect consideration of all the spectral detector sensitivity dependencies, which typically cannot be assumed at all constant in the broad spectral range of the Stokes excitation (800 – 1100 nm) and the signal detection (600 – 800 nm)!

For the further fitting procedure, the measured spectra $|S_i(\omega_p + \Omega)|^2$ are normalized by $I_s(\omega_p\text{-}\Omega)$, very similar to the simple data evaluation procedure described in section 3.5.1, or the trial susceptibility $\left[\chi_{res,i}^{(3)}(\Omega) + \chi_{NR,i}^{(3)}\right]$ is multiplied by $I_s(\omega_p\text{-}\Omega)$ in the fitting routine. Here, the latter approach will be pursued.

The fitting itself can either be performed by hand, with a table of the expected spontaneous *Raman* resonances at hand, obtained either from literature, or by a separate spontaneous *Raman* measurement of the pure sample (Fig. 0.2b, grey solid curve). Alternatively, the complete spectrum can be fitted automatically, e. g. using an evolutionary algorithm, with the literature resonances given as starting values for Ω_n [according to Eq. (6.9)]. In the fitting routine, the instrumental spectral resolution is automatically considered using a convolution with a *Gaussian* of width 60 cm^{-1}. While this allows for realistically narrow *Raman* line widths, the sensitivity to line widths much smaller than the instrumental resolution is not very high, hence fitted line widths cannot be expected to be overly precise. The result of the successful fit to the PET MCARS raw spectrum (Fig. 0.1a) was shown in chapter 3 (Fig. 3.9) together with a table summarizing the found fitting parameters. From these parameters, the effective CARS susceptibility can directly be plotted, as shown in Fig. 0.2 decomposed in the single *Lorentzian* resonances *n*. Comparison with a measured sponanteous *Raman* spectrum (Fig. 0.2b, grey solid curve) shows very good qualitative agreement, although the relative line intensities and some line widths of minor peaks vary. This, however, is not very surprising as most importantly the MCARS detector is not intensity calibrated, emphasizing the CARS signal at higher wavenumbers and rather suppressing low-wavenumber modes. Secondly, it was already mentioned that line widths cannot be expected to be fitted with utter perfection.

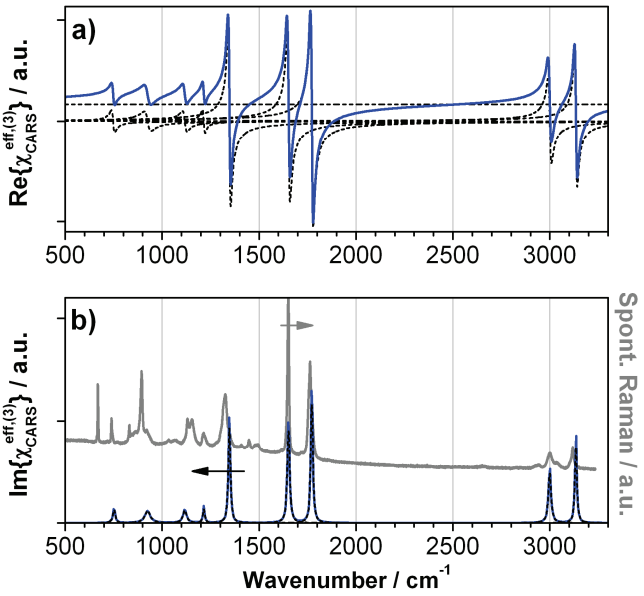

Fig. 0.2: Fitting result of effective CARS susceptibility as real (a) and imaginary part (b). Comparison of the imaginary part with a spontaneous Raman spectrum shows good agreement, although the line intensities vary. This is due to the missing correction of detector spectral sensitivity in the case of the MCARS data, and uncertainties concerning the very same correction in the spontaneous *Raman* instrument.

With all this information obtained, *i. e.* the real and imaginary part of the CARS fields S_i for each component, mixtures of the components can immediately described by Eq. (6.7), which read

$$\left|S_{mix}\left(\omega_p+\Omega\right)\right|^2=\left|\sum_i c_i\cdot S_i\left(\omega_p+\Omega\right)\right|^2. \tag{6.7}$$

Therefore, $|S_{mix}|^2$ has again to be fitted to the measured MCARS spectrum of the mixture to analyze. For a demonstration of two components with S_i determined from experimental MCARS spectra and the above fitting procedure to retrieve the complex field, a comparison of a pure sample of PET and PS, and a 1:1 mixture of the two is presented in Fig. 0.3. The respective real (solid curves) and imaginary (dashed curves) parts of S_i simply add up linearly, which is not the case for the spectra $|S_{mix}|^2$ (grey hatched curves). It can also be seen that due to the stronger overall signal of PS, the spectrum of the mixture resembles more the PS case. This again demonstrates that the complex nonlinear signal dependency requires careful analysis to be able to obtain quantitative information.

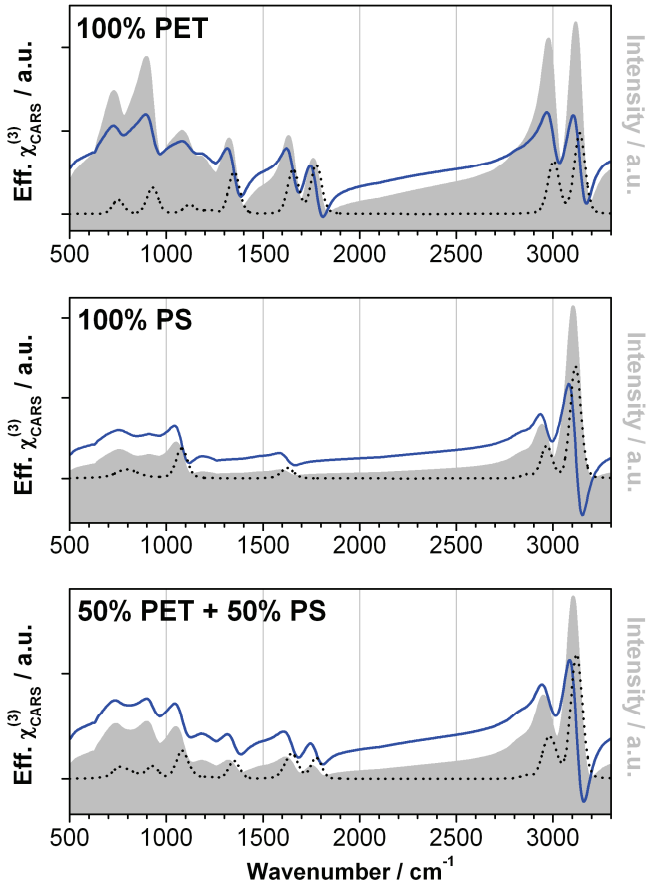

Fig. 0.3: Demonstration of pure polymer samples PET and PS, and a numerically "synthesized" 1:1 mixture thereof. The real (solid curves) and imaginary (dashed curves) parts of the CARS fields S_i are shown, and simply add up linearly in the mixture. The detected signal (grey hatched curves) is however the modulus square of the CARS field. See text and chapter 3 for details.

References

1. S. W. Hell, Science **316**, 1153 - 1158 (2007).
2. J. M. Chalmers, N. J. Everall, M. D. Schaeberle, I. W. Levin, E. N. Lewis, L. H. Kidder, J. Wilson, R. Crocombe, Vibrational Spectroscopy **30**, 43-52 (2002).
3. R. Bhargava, S.-Q. Wang, J. L. Koenig, Advances in Polymer Science **163**, 137-191 (2003).
4. W. R. Zipfel, R. M. Williams, W. W. Webb, Nature Biotechnology **21**, 1369-1377 (2003).
5. X. S. Xie, J. Yu, W. Y. Yang, Science **312**, 228-230 (2006).
6. C. S. Johnson, D. A. Gabriel, *Laser light scattering* (Dover Publications, New York 1994).
7. C. K. Sun, "Higher harmonic generation microscopy," in *Microscopy Techniques*, (2005), 17-56.
8. R. Gauderon, P. B. Lukins, C. J. R. Sheppard, Optics Letters **23**, 1209-1211 (1998).
9. P. J. Campagnola, L. M. Loew, Nature Biotechnology **21**, 1356-1360 (2003).
10. Y. Barad, H. Eisenberg, M. Horowitz, Y. Silberberg, Applied Physics Letters **70**, 922-924 (1997).
11. J. X. Cheng, X. S. Xie, Journal of Physical Chemistry B **108**, 827-840 (2004).
12. A. Volkmer, Journal of Physics D-Applied Physics **38**, R59-R81 (2005).
13. N. Dudovich, D. Oron, Y. Silberberg, Nature **418**, 512-514 (2002).
14. N. Dudovich, D. Oron, Y. Silberberg, J. Chem. Phys. **118**, 9208-9215 (2003).
15. S.-H. Lim, A. G. Caster, S. R. Leone, Physical Review A - Atomic, Molecular, and Optical Physics **72**, 1-4 (2005).
16. B. von Vacano, W. Wohlleben, M. Motzkus, Journal of Raman Spectroscopy **37**, 404-410 (2006).
17. B. von Vacano, W. Wohlleben, M. Motzkus, Optics Letters **31**, 413-415 (2006).
18. K. Bergmann, H. Theuer, B. W. Shore, Reviews of Modern Physics **70**, 1003-1025 (1998).
19. H. Rabitz, R. de Vivie-Riedle, M. Motzkus, K.-L. Kompa, Science **288**, 824-828 (2000).
20. S. A. Rice, M. Zhao, *Optimal Control of Molecular Dynamics* (John Wiley & Sons, New York 2000).
21. M. Shapiro, P. Brumer, *Principles of the Quantum Control of Molecular Processes* (John Wiley & Sons, Hoboken 2003).
22. B. Broers, H. B. V. Vandenheuvell, L. D. Noordam, Optics Communications **91**, 57-61 (1992).
23. F. G. Omenetto, A. J. Taylor, M. D. Moores, D. H. Reitze, Optics Letters **26**, 938-940 (2001).
24. D. Zeidler, T. Witte, D. Proch, M. Motzkus, Optics Letters **26**, 1921-1923 (2001).
25. D. Meshulach, Y. Silberberg, Nature **396**, 239-242 (1998).
26. T. Hornung, R. Meier, D. Zeidler, K. L. Kompa, D. Proch, M. Motzkus, Applied Physics B-Lasers and Optics **71**, 277-284 (2000).
27. A. M. Weiner, D. E. Leaird, G. P. Wiederrecht, K. A. Nelson, Science **247**, 1317-1319 (1990).

28. T. Brixner, G. Gerber, Chemphyschem **4**, 418-438 (2003).

29. J. L. Herek, W. Wohlleben, R. J. Cogdell, D. Zeidler, M. Motzkus, Nature **417**, 533-535 (2002).

30. W. Wohlleben, T. Buckup, J. L. Herek, M. Motzkus, ChemPhysChem **6**, 850-857 (2005).

31. A. H. Buist, M. Muller, R. I. Ghauharali, G. J. Brakenhoff, J. A. Squier, C. J. Bardeen, V. V. Yakovlev, K. R. Wilson, Optics Letters **24**, 244-246 (1999).

32. J. M. Dela Cruz, V. V. Lozovoy, M. Dantus, Journal of Physical Chemistry A **109**, 8447-8450 (2005).

33. D. Meshulach, Y. Silberberg, Phys. Rev. A **60**, 1287 (1999).

34. J.-C. Diels, W. Rudolph, *Ultrafast Laser Phenomena* (Academic Press, San Diego 1996).

35. M. Wollenhaupt, A. Assion, T. Baumert, "Femtosecond Laser Pulses: Linear Properties, Manipulation, Generation and Measurement," in *Springer Handbook of Lasers and Optics*, F. Träger, ed. (Springer Science and Business Media, New York 2007), 937-983

36. R. Paschotta, "Encyclopedia of Laser Physics and Technology", (2007)

37. U. Keller, Nature **424**, 831-838 (2003).

38. J. Canning, Optics and Lasers in Engineering **44**, 647-676 (2006).

39. M. Fermann, A. Tünnermann, J. Opt. Soc. Am. B **24**, special issue (No. 8) on fiber lasers (2007).

40. *Conference proceedings CLEO Europe - IQEC*, Optical Society of America, European Physical Society, Munich (2007)

41. P. Russel, Science **299**, 358 (2003).

42. J. M. Dudley, G. Genty, S. Coen, Reviews of Modern Physics **78**, 1135-1184 (2006).

43. J. K. Ranka, R. S. Windeler, A. J. Stentz, Optics Letters **25**, 25-27 (2000).

44. T. Udem, R. Holzwarth, T. W. Hänsch, Nature **416**, 233 (2002).

45. E. O. Potma, D. J. Jones, J. X. Cheng, X. S. Xie, J. Ye, Optics Letters **27**, 1168-1170 (2002).

46. M. Hashimoto, T. Araki, Optics Letters **25**, 1768-1770 (2000).

47. A. M. Zheltikov, Journal of Raman Spectroscopy **31**, 653-667 (2000).

48. J.-X. Cheng, A. Volkmer, L. D. Book, X. S. Xie, Journal of Physical Chemistry B **106**, 8493-8498 (2002).

49. G. W. H. Wurpel, J. M. Schins, M. Müller, Optics Letters **27**, 1093-1095 (2002).

50. M. Müller, J. M. Schins, Journal of Physical Chemistry B **106**, 3715-3723 (2002).

51. P. S. J. Russell, Science **299**, 358-362 (2003).

52. T. A. Birks, W. J. Wadsworth, P. S. J. Russell, Optics Letters **25**, 1415-1417 (2000).

53. W. J. Wadsworth, A. Ortigosa-Blanch, J. C. Knight, T. A. Birks, T.-P. M. Man, P. S. J. Russell, Journal of the Optical Society of America B: Optical Physics **19**, 2148-2155 (2002).

54. H. N. Paulsen, K. M. Hilligsoe, J. Thogersen, S. R. Keiding, J. J. Larsen, Optics Letters **28**, 1123-1125 (2003).

55. T. W. Kee, M. T. Cicerone, Optics Letters **29**, 2701-2703 (2004).

56. H. Kano, H. Hamaguchi, Applied Physics Letters **86**, (2005).

57. H. Kano, H. Hamaguchi, Applied Physics B-Lasers and Optics **80**, 243-246 (2005).

58. L. Meyer, "Entwicklung und Aufbau eines Femtosekunden-Multiplex-CARS Mikroskops", Diplomarbeit Fachbereich Chemie, Philipps-Universität Marburg (2006).

59. K. M. Hilligsøe, T. V. Andersen, H. N. Paulsen, C. K. Nielsen, K. Mølmer, S. Keiding, R. Kristiansen, K. P. Hansen, J. J. Larsen, Optics Express **12**, 1045-1054 (2004).

60. E. R. Andresen, H. N. Paulsen, V. Birkedal, J. Thøgersen, S. R. Keiding, Journal of the Optical Society of America B: Optical Physics **22**, 1934-1938 (2005).

61. H. Kano, H.-O. Hamaguchi, Journal of Raman Spectroscopy **37**, 411-415 (2006).

62. B. von Vacano, T. Buckup, M. Motzkus, Optics Letters **31**, 1154-1156 (2006).

63. M. D. Schaeberle, C. G. Karakatsanis, C. J. Lau, P. J. Treado, Analytical Chemistry **67**, 4316-4321 (1995).

64. R. L. Morgan, M. J. Hill, P. J. Barham, A. Van Der Pol, B. Kip, J. Van Ruiten, L. Markwort, Journal of Macromolecular Science - Physics **38**, (1999).

65. R. Appel, T. W. Zerda, W. H. Waddell, Applied Spectroscopy **54**, 1559-1566 (2000).

66. S. López Quintana, P. Schmidt, J. Dybal, J. Kratochvic l, J. M. Pastor, J. C. Merino, Polymer **43**, 5187-5195 (2002).

67. S. Huan, W. Lin, H. Sato, H. Yang, J. Jiang, Y. Ozaki, H. Wu, S. Guoli, R. Yu, Journal of Raman Spectroscopy, (2006).

68. H. A. Rinia, M. Bonn, M. Müller, Journal of Physical Chemistry B **110**, 4472-4479 (2006).

69. A. H. Kuptsov, G. N. Zhizhin, *Handbook of Fourier Transform Raman and Infrared Spectra of Polymers* (Elsevier Science Publishers, B.V., Amsterdam 1998).

70. D. Zeidler, S. Frey, K. L. Kompa, M. Motzkus, Physical Review A **64**, 023420 (2001).

71. A. Horneber, Diplomarbeit Fachbereich Chemie, Philipps-Universität Marburg (2008).

72. C. Pohling, "Dreidimensionale Multiplex-CARS Mikroskopie", Diplomarbeit Fachbereich Chemie, Philipps-Universität Marburg (2008).

73. J. Squier, M. Muller, Review of Scientific Instruments **72**, 2855-2867 (2001).

74. G. J. Brakenhoff, M. Muller, J. Squier, Journal of Microscopy **179**, 253-260 (1995).

75. C. Soeller, M. B. Cannell, Pflugers Archiv European Journal of Physiology **432**, 555-561 (1996).

76. R. Wolleschensky, T. Feurer, R. Sauerbrey, U. Simon, Applied Physics B: Lasers and Optics **67**, 87-94 (1998).

77. M. Muller, J. Squier, R. Wolleschensky, U. Simon, G. J. Brakenhoff, Journal of Microscopy **191**, 141-150 (1998).

78. D. Yelin, D. Meshulach, Y. Silberberg, Optics Letters **22**, 1793-1795 (1997).

79. T. Baumert, T. Brixner, V. Seyfried, M. Strehle, G. Gerber, Applied Physics B-Lasers and Optics **65**, 779-782 (1997).

80. G. Stobrawa, M. Hacker, T. Feurer, D. Zeidler, M. Motzkus, F. Reichel, Applied Physics B-Lasers and Optics **72**, 627-630 (2001).

81. A. M. Weiner, Review of Scientific Instruments **71**, 1929-1960 (2000).

82. F. Verluise, V. Laude, Z. Cheng, C. Spielmann, P. Tournois, Optics Letters **25**, 575-577 (2000).

83. J. P. Ogilvie, D. Débarre, X. Solinas, J.-L. Martin, E. Beaurepaire, M. Joffre, Optics Express **14**, 759-766 (2006).

84. T. Brixner, G. Gerber, Optics Letters **26**, 557-559 (2001).

85. M. M. Wefers, K. A. Nelson, Journal of the Optical Society of America B-Optical Physics **12**, 1343-1362 (1995).

86. T. Hornung, "Amplituden- und Phasenmodulation von ultrakurzen Lichtimpulsen mit einer Flüssigkristallmaske und ihre Anwendung zur Kontrolle von Photonenübergängen in Na", MPQ report 247 (1999).

87. J. C. Vaughan, T. Feurer, K. W. Stone, K. A. Nelson, Optics Express **14**, 1314-1328 (2006).

88. M. M. Wefers, K. A. Nelson, IEEE Journal of Quantum Electronics **32**, 161-172 (1996).

89. R. Trebino, *Frequency-Resolved Optical Gating: The Measurement of Ultrashort Laser Pulses* (Kluwer Academic Publishers, Dordrecht 2000).

90. R. Trebino, K. W. DeLong, D. N. Fittinghoff, J. N. Sweetser, M. A. Krumbugel, B. A. Richman, D. J. Kane, Review of Scientific Instruments **68**, 3277-3295 (1997).

91. D. N. Fittinghoff, J. A. Squier, C. P. J. Barty, J. N. Sweetser, R. Trebino, M. Muller, Optics Letters **23**, 1046-1048 (1998).

92. I. Amat-Roldan, I. G. Cormack, P. Loza-Alvarez, E. J. Gualda, D. Artigas, Optics Express **12**, 1169-1178 (2004).

93. I. Amat-Roldan, I. G. Cormack, P. Loza-Alvarez, D. Artigas, Optics Letters **29**, 2282-2284 (2004).

94. A. Monmayrant, M. Joffre, T. Oksenhendler, R. Herzog, D. Kaplan, P. Tournois, Optics Letters **28**, 278-280 (2003).

95. V. V. Lozovoy, I. Pastirk, M. Dantus, Optics Letters **29**, 775-777 (2004).

96. B. Xu, J. M. Gunn, J. M. Dela Cruz, V. V. Lozovoy, M. Dantus, Journal of the Optical Society of America B: Optical Physics **23**, 750-759 (2006).

97. C. Iaconis, I. A. Walmsley, Optics Letters **23**, 792-794 (1998).

98. C. Iaconis, I. A. Walmsley, Ieee Journal of Quantum Electronics **35**, 501-509 (1999).

99. T. M. Shuman, M. E. Anderson, J. Bromage, C. Iaconis, L. Waxer, I. A. Walmsley, Optics Express **5**, 134-143 (1999).

100. M. Takeda, H. Ina, S. Kobayashi, Journal of the Optical Society of America **72**, 156 (1982).

101. P. Baum, S. Lochbrunner, E. Riedle, Optics Letters **29**, 210-212 (2004).

102. M. E. Anderson, L. E. E. de Araujo, E. M. Kosik, I. A. Walmsley, Applied Physics B-Lasers and Optics **70**, S85 (2000).

103. D. N. Fittinghoff, A. C. Millard, J. A. Squier, M. Muller, Ieee Journal of Quantum Electronics **35**, 479 (1999).

104. C. Dorrer, Journal of the Optical Society of America B: Optical Physics **16**, 1160-1168 (1999).

105. J. Wemans, G. Figueira, N. Lopes, L. Cardoso, Optics Letters **31**, 2217-2219 (2006).

106. T. Hornung, R. Meier, M. Motzkus, Chemical Physics Letters **326**, 445-453 (2000).

107. J. M. Dela Cruz, I. Pastirk, V. V. Lozovoy, K. A. Walowicz, M. Dantus, Journal of Physical Chemistry A **108**, 53-58 (2004).

108. J. P. Ogilvie, E. Beaurepaire, A. Alexandrou, M. Joffre, Optics Letters **31**, 480-482 (2006).

109. N. Dudovich, D. Oron, Y. Silberberg, Nature **418**, 512-514 (2002).

110. X. Gu, L. Xu, M. Kimmel, E. Zeek, P. O'Shea, A. P. Shreenath, R. Trebino, R. S. Windeler, Optics Letters **27**, 1174-1176 (2002).

111. S. Linden, H. Giessen, J. Kuhl, Physica Status Solidi B-Basic Research **206**, 119-124 (1998).

112. S. Linden, J. Kuhl, H. Giessen, Optics Letters **24**, 569-571 (1999).

113. M. Cui, M. Joffre, J. Skodack, J. P. Ogilvie, Optics Express **14**, 8448-8458 (2006).

114. M. E. Dickinson, G. Bearman, S. Tille, R. Lansford, S. E. Fraser, Biotechniques **31**, 1272-+ (2001).

115. R. Lansford, G. Bearman, S. E. Fraser, Journal of Biomedical Optics **6**, 311-318 (2001).

116. R. A. Schultz, T. Nielsen, J. R. Zavaleta, R. Ruch, R. Wyatt, H. R. Garner, Cytometry **43**, 239-247 (2001).

117. M. Müller, A. Zumbusch, "Coherent anti-Stokes Raman Scattering Microscopy", (2007), 2156-2170.

118. B. von Vacano, L. Meyer, M. Motzkus, Journal of Raman Spectroscopy **38**, 916-926 (2006).

119. S. Nath, D. C. Urbanek, S. J. Kern, M. A. Berg, Physical Review Letters **97**, 267401 (2006).

120. M. Schmitt, G. Knopp, A. Materny, W. Kiefer, Chemical Physics Letters **270**, 9-15 (1997).

121. T. Lang, K. L. Kompa, M. Motzkus, Chemical Physics Letters **310**, 65-72 (1999).

122. H. Skenderovic, T. Buckup, W. Wohlleben, M. Motzkus, Journal of Raman Spectroscopy **33**, 866-871 (2002).

123. M. Heid, S. Schlucker, U. Schmitt, T. Chen, R. Schweitzer-Stenner, V. Engel, W. Kiefer, Journal of Raman Spectroscopy **32**, 771-784 (2001).

124. S. Nath, D. C. Urbanek, S. J. Kern, M. A. Berg, Physical Review Letters **97**, (2006).

125. B. D. Prince, A. Chakraborty, B. M. Prince, H. U. Stauffer, Journal of Chemical Physics **125**, (2006).

126. D. Pestov, R. K. Murawski, G. O. Ariunbold, X. Wang, M. C. Zhi, A. V. Sokolov, V. A. Sautenkov, Y. V. Rostovtsev, A. Dogariu, Y. Huang, M. O. Scully, Science **316**, 265-268 (2007).

127. X. J. G. Xu, S. O. Konorov, S. Zhdanovich, J. W. Hepburn, V. Milner, Journal of Chemical Physics **126**, (2007).

128. D. C. Urbanek, M. A. Berg, Journal of Chemical Physics **127**, 044306 (2007).

129. A. Volkmer, J. Phys. D: Appl. Phys. **38**, R59-R81 (2005).

130. S. Mukamel, *Principles of Nonlinear Optical Spectroscopy* (Oxford University Press, New York 1995).

131. B. von Vacano, M. Motzkus, Phys. Chem. Chem. Phys. **10**, 681 (2008).

132. M. D. Levenson, S. S. Kano, *Introduction to Nonlinear Laser Spectroscopy* (Academic Press, San Diego 1988).

133. M. Motzkus, S. Pedersen, A. H. Zewail, Journal of Physical Chemistry **100**, 5620-5633 (1996).

134. B. Lavorel, H. Tran, E. Hertz, O. Faucher, P. Joubert, M. Motzkus, T. Buckup, T. Lang, H. Skenderovic, G. Knopp, P. Beaud, H. M. Frey, Comptes Rendus Physique **5**, 215-229 (2004).

135. M. Schmitt, G. Knopp, A. Materny, W. Kiefer, Chemical Physics Letters **280**, 339-347 (1997).

136. S. Fujiyoshi, S. Takeuchi, T. Tahara, Journal of Physical Chemistry A **107**, 494-500 (2003).

137. T. Hornung, H. Skenderovic, M. Motzkus, Chemical Physics Letters **402**, 283-288 (2005).

138. J. Hauer, T. Buckup, M. Motzkus, J. Phys. Chem. A **in press**, (2007).

139. T. Hornung, J. C. Vaughan, T. Feurer, K. A. Nelson, Optics Letters **29**, 2052-2054 (2004).

140. G. C. Bjorklund, IEEE J. Quantum Electronics **QE-11**, 287-296 (1975).

141. A. Zumbusch, G. R. Holtom, X. S. Xie, Physical Review Letters **82**, 4142-4145 (1999).

142. B. Schmidt, M. Hacker, G. Stobrawa, T. Feurer, http://www.lab2.de (2007).

143. N. Dudovich, D. Oron, Y. Silberberg, Journal of Chemical Physics **118**, 9208-9215 (2003).

144. B. von Vacano, M. Motzkus, Optics Communications **264**, 488-493 (2006).

145. B. von Vacano, T. Buckup, M. Motzkus, Optics Letters **31**, 2495-2497 (2006).

146. D. Oron, N. Dudovich, Y. Silberberg, Physical Review Letters **89**, (2002).

147. D. Oron, N. Dudovich, Y. Silberberg, Physical Review Letters **90**, (2003).

148. S. H. Lim, A. G. Caster, S. R. Leone, Physical Review A **72**, (2005).

149. M. Renard, R. Chaux, B. Lavorel, O. Faucher, Optics Express **12**, 473-482 (2004).

150. B. von Vacano, T. Buckup, M. Motzkus, Journal Opt. Soc. America B **24**, 1091-1100 (2007).

151. M. O. Scully, G. W. Kattawar, R. P. Lucht, T. Opatrny, H. Pilloff, A. Rebane, A. V. Sokolov, M. S. Zubairy, Proceedings of the National Academy of Sciences of the United States of America **99**, 10994-11001 (2002).

152. E. Frumker, D. Oron, D. Mandelik, Y. Silberberg, Optics Letters **29**, 890-892 (2004).

153. E. Frumker, Y. Silberberg, Optics Letters **32**, 1384-1386 (2007).

154. D. Zeidler, S. Frey, W. Wohlleben, M. Motzkus, F. Busch, T. Chen, W. Kiefer, A. Materny, Journal of Chemical Physics **116**, 5231-5235 (2002).

155. J. Hauer, H. Skenderovic, K. L. Kompa, M. Motzkus, Chemical Physics Letters **421**, 523-528 (2006).

156. J. Konradi, A. K. Singh, A. Materny, Journal of Photochemistry and Photobiology A **180**, 289-299 (2006).

157. J. Konradi, A. K. Singh, A. Materny, Physical Chemistry Chemical Physics **7**, 3574-3579 (2005).

158. B. von Vacano, M. Motzkus, Optics Communications **264**, 488-493 (2006).

159. T. Polack, D. Oron, Y. Silberberg, Chemical Physics **318**, 163-169 (2005).

160. P. Brumer, M. Shapiro, Chem. Phys. Lett. **126**, 541-546 (1986).

161. S. Postma, P. van der Walle, H. L. Offerhaus, N. F. van Hulst, Review of Scientific Instruments **76**, (2005).

162. J. W. Wilson, P. Schlup, R. A. Bartels, Optics Express **15**, 8979-8987 (2007).

163. D. Oron, N. Dudovich, Y. Silberberg, Physical Review A **70**, 023415 (2004).

164. X. L. Nan, J. X. Cheng, X. S. Xie, Journal of Lipid Research **44**, 2202-2208 (2003).

165. C. L. Evans, E. O. Potma, X. S. N. Xie, Optics Letters **29**, 2923-2925 (2004).

166. D. L. Marks, C. Vinegoni, J. S. Bredfeldt, S. A. Boppart, Applied Physics Letters **85**, 5787-5789 (2004).

167. M. Greve, B. Bodermann, H. R. Telle, P. Baum, E. Riedle, Applied Physics B-Lasers and Optics **81**, 875-879 (2005).

168. E. O. Potma, C. L. Evans, X. S. Xie, Optics Letters **31**, 241-243 (2006).

169. T. W. Kee, H. Zhao, M. T. Cicerone, Optics Express **14**, 3631-3640 (2006).

170. M. Jurna, J. P. Korterik, C. Otto, H. L. Offerhaus, Optics Express **15**, 15207-15213 (2007).

171. M. E. Fermann, A. Galvanauskas, G. Sucha, D. Harter, Applied Physics B-Lasers and Optics **65**, 259-275 (1997).

172. J. C. Knight, J. Opt. Soc. Am. B **24**, 1661-1668 (2007).

173. D. A. Akimov, A. A. Ivanov, M. V. Alfimov, A. M. Zheltikov, Vibrational Spectroscopy **42**, 33-40 (2006).

174. D. A. Zheltikova, A. M. Zheltikov, Applied Physics B-Lasers and Optics **83**, 11-16 (2006).

175. E. R. Andresen, C. K. Nielsen, J. Thogersen, S. R. Keiding, Optics Express **15**, 4848-4856 (2007).

176. B. Schmidt, M. Hacker, G. Stobrawa, T. Feurer, (2007).

177. L. Lepetit, G. Cheriaux, M. Joffre, Journal of the Optical Society of America B-Optical Physics **12**, 2467-2474 (1995).

178. T. Lang, M. Motzkus, Journal of the Optical Society of America B: Optical Physics **19**, 340-344 (2002).

179. J. X. Cheng, A. Volkmer, L. D. Book, X. S. Xie, Journal of Physical Chemistry B **105**, 1277-1280 (2001).

180. T. W. Koo, S. Chan, A. A. Berlin, Optics Letters **30**, 1024-1026 (2005).

181. J. M. Gunn, M. Ewald, M. Dantus, Nano Letters **6**, 2804-2809 (2006).

Danksagungen

An erster Stelle möchte ich mich bei Marcus Motzkus für die stets begeisterte, fördernde und menschlich ausgesprochen angenehme Betreuung dieser Arbeit bedanken. Ohne die großen Freiräume zum Forschen, die er eingeräumt und die Ressourcen, die er immer wieder aufgetan hat, wäre diese Dissertation nicht in der vorliegenden Form entstanden. Prof. Dr. Ulrich Höfer danke ich für die freundliche Übernahme des Zweitgutachtens.

Weiterhin schulde ich einer Vielzahl von Menschen Dankbarkeit, die zum Gelingen beigetragen haben. Zunächst zu nennen sind hier die Marburger Mitstreiter noch aus Garchinger Zeiten, die mir zu guten Freunden geworden sind: Tiago Buckup für die fortwährende Unterstützung bei allen neuen Projekten, die gemeinsamen Labornächte bei der Bezwingung der spektralen Interferometrie, sowie für seine Begeisterungsfähigkeit und die unzähligen wissenschaftlichen und nichtwissenschaftlichen Diskussionen. Dann meinem langjährigen Mitdoktoranden und Bürogenossen Jürgen Hauer, mit dem ich wissenschaftlich die Leidenschaft für Vier-Wellen-Mischen teilte, auch wenn wir uns jederzeit humorvoll über die dafür optimale Anzahl Laserstrahlen auseinandersetzen konnten. Unvergessen bleiben auch seine stets passenden Zitate und die großartigen kulinarischen Beiträge bei Arbeitsgruppentreffen oder den winterlichen Gruppenseminaren. Zuletzt Wendel Wohlleben, mit dem ich bereits im Rahmen meiner Diplomarbeit die ersten Spiegel in Marburg auf den Lasertisch geschraubt hatte, von dem ich LabView, Shaper-, Film- und Fahrradwissen sowie viel nichtlineare Optik gelernt habe, und der mir zu Beginn meiner Promotion noch einen lange vorhaltenden Vorrat an guten Ideen und gemeinsam andiskutierten Experimenten hinterlassen hat. Schnell stießen dann auch „echte“ Marburger dazu, von denen mir Jens Möhring ein weiterer höchst geschätzter Mitdoktorand geworden ist, der mir geholfen hat fantastische, titeltaugliche Abbildungen zu erstellen, immer innovative Vorschläge für mess- oder programmiertechnische Verbesserungen hatte und durch den intensiven wissenschaftlichen sowie sonstigen Austausch auch sehr zur angenehmen Arbeitsatmosphäre beigetragen hat.

Nicht missen möchte ich die Unterstützung der Diplomandinnen und Diplomanden, die ich betreuen durfte. Mit Lars Meyer, Christoph Pohling und Anke Horneber konnte MCARS erschlossen und weiterentwickelt werden, und auch Christina Müller beginnt gerade, ihren CARS-Beitrag zu leisten. Die Zusammenarbeit hat mir ausnahmslos große Freude gemacht, und ich möchte mich für die große Motivation, Geduld und das nette Miteinander herzlich bedanken! Für ein anregendes und unterhaltsames halbes Jahr durfte ich zudem mit Jean Rehbinder als Gaststudent von der École Polytechnique an der Umsetzung von interferometrischem Einzelstrahl-CARS mit dem Faserlaser arbeiten, die ja auch direkt Eingang in diese Arbeit gefunden hat. Aus der Vielzahl weiterer Kollegen möchte ich den Diplomanden der Gruppe Alexander Weigel, Timo Lebold, Annette Brunsen, Jan Dorn und Volker Settels für das angenehme Gruppenklima danken, sowie „meinen“ Vertiefern Meike Roskamp, Christoph Erk, Matthias Fritsch, Volker Gatterdam, Anke Horneber, Ramona Ronge, Marcel Drüschler und Claudia Mattheis. Für die gute technische und administrative Unterstützung in Marburg danke ich Marco Hill, Rigobert Donner, Jutta Hennen - auch Constanze Steffen, mit der zusammengearbeitet zu haben eine Bereicherung war - sowie den Werkstätten.

Ohne die Unterstützung meiner Eltern und den wochenendlichen Ausgleich durch meine Freunde wäre diese Arbeit nicht möglich gewesen. Nicht in Worte fassen kann ich den Dank an meine Freundin Anja, die mich in den Jahren immer unterstützt hat und mich glücklich macht!